Aero

THE EFFECT OF UPSTREAM ROTOR VORTICAL DISTURBANCES ON THE TIME-AVERAGE PERFORMANCE OF AXIAL COMPRESSOR STATORS

by

Theodore V. Valkov

GTL Report #227   August 1997

GAS TURBINE LABORATORY
MASSACHUSETTS INSTITUTE OF TECHNOLOGY
CAMBRIDGE, MASSACHUSETTS

The Effect of Upstream Rotor Vortical Disturbances on the Time-Average Performance of Axial Compressor Stators

by

Theodore V. Valkov

GTL Report #227   August 1997

The Effect of Upstream Rotor Vortical Disturbances on the Time-Average Performance of Axial Compressor Stators

by

Theodore V. Valkov

Abstract

Time-accurate Reynolds-averaged Navier-Stokes simulations have been carried out to investigate the impact of upstream rotor wakes and tip leakage vortices on the loss of a compressor stator. The objective is to (1) identify the unsteady flow mechanisms responsible for performance changes, (2) quantify these changes, and (3) extract useful design information.

There are two generic mechanisms with significant impact on performance: reversible recovery of the energy in the disturbances (beneficial) and non-transitional boundary layer response (detrimental). For both wakes and tip leakage vortices, the impact of these mechanisms can be described in the same two-dimensional terms. In presence of unsteady flow, the efficiency of the design under consideration is 0.2 points higher than that obtained using a mixing-out steady flow approximation (0.5 points recovery benefit minus 0.3 points from boundary layer response). The effects of tip vortices and wakes are of comparable importance.

The impact of stator interaction with upstream wakes and vortices depends on the following parameters: axial spacing, loading, and the frequency of wake fluctuations in the rotor frame. At reduced spacing, this impact becomes significant. For a spacing of 0.07 chords, stage efficiency is 0.6 points higher relative to the steady flow (1.2 points recovery benefit minus 0.6 points from boundary layer response). About 1/2 to 2/3 of the efficiency gain observed experimentally can be attributed to the interaction with upstream wakes and vortices. In the relative frame, wakes fluctuate in time. For fluctuation frequencies between 0.3-0.8 times the blade passing frequency, recovery does not occur, and there is a significant difference between the effects of fluctuating and steady wakes (with the same ensemble-averaged properties). The most important aspect of the tip vortex is the velocity defect, which is perceived by the stator in the same manner as a wake.

A model of recovery and boundary layer response in an embedded stage indicates that a mixing-out steady flow approximation underestimates stage efficiency by 0.3-0.5 points (for typical designs) and by 0.6-1.0 points (for closely-spaced blade rows). A region in design space exists where interaction has a beneficial and relatively constant impact on efficiency. Outside this region, interaction benefits rapidly disappear. For a typical blading diffusion factor of 0.45, the beneficial region is approximately delimited by the de Haller criterion. The detrimental aspects of boundary layer response may be mitigated by (a) selective removal of boundary layer fluid from the suction surface, or (b) tailoring of the blade loading to reduce loss in the front part of the blade.

Acknowledgements

As the time to depart the Gas Turbine Lab draws near, I look back and realize how much I owe to my mentors and colleagues here.

First, I would like to express my special gratitude to Dr. Choon S. Tan for his friendship, as well as for his patient guidance, which he constantly provided in his quality of academic advisor.

I also wish to extend these special thanks to the members of the thesis committee. The contagious enthousiasm of Professor Ian A. Waitz made research easier, and his suggestions proved invaluable. To Professor Marten Landahl, I owe a solid foundation in fluid mechanics. I am also indebted to Professor Peter Belobaba for endorsing Management of Technology as my academic minor.

I greatly value Professor Jack L. Kerrebrock's feedback on my work, and would like to express my gratitude to him and to Professor Mark Drela for being my thesis readers. Many thanks are also due to Professor Edward M. Greitzer and to Professor Frank E. Marble, for their friendly suggestions and criticisms.

This work provided a pleasant opportunity to interact with the people at the Cambridge University Whittle Lab. My discussions with Professor William Dawes and Professor N.A. Cumpsty were beneficial to the project, and are much appreciated.

I am particularly grateful to Dr. John Adamczyk, Senior Aerospace Scientist at the NASA Lewis Research Center, for his special interest in the project and for the useful exchange of ideas that ensued. Our collaboration with NASA provided also the cutting-edge computational resources that made this work possible.

Finally, special thanks are due to Professor Alan Epstein for arranging a field trip to Southern France for the author (fine cuisine and wine included). To him, as well as to my fellow students, I wish the best of luck in exploring new horizons.

Table of Contents

Notation

a_r	Reversible velocity attenuation factor
A	Passage cross-sectional area
A_j	Velocity excess of the upstream disturbance "jet" in the stator frame
A_r	Velocity defect in the relative rotor frame (as fraction of V_{2r})
$A^+(s)$	Pressure gradient function in the Baldwin-Lomax model.
$A^{ox,oy}_{jkpq,i}$	Elemental integro-differential operators
$A_{jkpq,i}()$	Elemental quadratic integro-differential operator
AR	Blading aspect ratio (H/c)
$\tilde{B}_{abc}$	Local third-order integral operator
$B^+_{jpkq,i}()$	Elemental surface integral operator
$B^-_{jpkq,i}()$	Elemental auxiliary surface integral operator
$B^o_{jpkq,i}$	Elemental pseudointegral operator
c, c_S	Stator blade chord
c_R	Rotor blade chord
c_x	Length of the chord projection on the x-axis
C_d	Drag coefficient
C_K, C_W	Constants in the Baldwin-Lomax model ($C_W = 0.25; C_K = 0.3$)
$C^{i,m}_g$	Elementally condensed global system matrix
$C_{gg}...C_{ee}$	Subpartitions of the elemental system matrix
$C_{G,m}$	Condensed global system matrix for m-th mode
$C^i_{jkpq,m}$	Elemental system matrix for m-th mode and i-th element
$C^{i,m}_{pp}$	Elementally condensed partition matrix for m-th mode and i-th element
C_p	Dimensionless static pressure coefficient, $C_p = 2\frac{P-P_1}{\rho U_\infty}$
C_P	Working fluid specific heat at constant pressure
C_t	Dimensionless total pressure coefficient, $C_t = 2\frac{P_t-P_{t,1}}{\rho U_\infty}$

C_x	Absolute axial velocity
C_θ	Absolute tangential velocity
$C_{\theta,1r}, C_{\theta,2r}$	Absolute tangential velocities at the inlet and exit of the rotor
d	Axial gap between rotor and stator
D_G	Condensed global system matrix diagonal
D_{jk}	Discretized local differential operator
DF	Diffusion factor (Cumpsty 1989, p.153)
e	Neper constant, $e = 1 + 1 + 1/2 + 1/3 + ...1/n$
E	Exit boundary of the computational domain
f	Upstream disturbance profile function
$\mathbf{F}$	Convective forcing vector
$F(n)$	Shape function appearing in the Baldwin-Lomax model.
F_m	Velocity eigenfunctions
F_K	Klebanoff intermittency factor
F_W	Wake factor
$(G)_e^i$	Global pointer table
$\mathbf{G}$	Dissipative forcing vector
$\frown$	Pressure eigenfunctions
	Specific enthalpy
h_n	N-th order Lagrangian interpolating polynomial
H	Hub-to-casing height
I	Inlet boundary of the computational domain
$(\mathbf{i,j,k})$	Axial/tangential/spanwise unit vectors in the absolute frame
J	Jacobian of the (η, ζ) blade-to-blade elemental coordinate system
k	Von Karman constant (k=0.41)
K_1, K_2	Constants in the Baldwin-Lomax model (K$_1$=0.0168; K$_2$=1.6)
$L_{i/e}$	Length of disturbance segment at entrance/exit of blade row
$L_{jkrs,i}$	Elemental x-y Laplacian operator
$\dot{m}$	Dimensional mass flux vector
m_n	N-th moment of the upstream disturbance profile
$\dot{M}$	Average mass flux through passage
M	Mach Number
$M_{jk,i,m}^L$	Discretized boundary source term
n_c	Cross-over locus of inner and outer regions

N	Order of the local spectral expansion in the blade-to-blade plane
N_B	Global matrix bandwidth
N_E	Number of spectral elements in the blade-to-blade plane
N_H	Number of spectral elements in the axial direction
N_I	Number of spectral elements along the inlet boundary
N_M	Number of spanwise modes ($N_M = N_Z - 2$)
N_P	Number of spectral elements along the blade surface
$N_{R|S}$	Number of rotor or stator blades
N_V	Number of spectral elements in the blade-to-blade direction
N_Z	Order of the global spectral expansion in the spanwise direction
P_s, p_s	Static pressure
P_t, p_t	Total pressure
$(P)^i_{jk}$	Set of spectral collocation points on the blade-to-blade plane
Q, q	Dynamic head
$\dot{Q}$	Rate of heat addition or removal
r_c	Vortex core radius
R	Perfect gas constant
R	Computational Reynolds Number (§A.4)
Re	Cascade Reynolds Number
R_a	Dimensionless annulus radius
s	Specific entropy
$(\mathbf{s}, \mathbf{n}, \mathbf{b})$	Streamwise/vortical normal/binormal coordinate system unit vectors
S	Blade-to-blade spacing at pitchline
$S, \delta S, dS$	Control surface, boundary and infinitesimal element thereof
t	Dimensionless time (cf.§A.4)
t_w	Wake thickness (at 99% velocity in relative frame)
t^*	Characteristic thickness of the incoming disturbances
t_0	Instant of wake interception
T	Temperature
$\mathbf{T}_k$	Unsteady vorticity production terms
T^i_{jk}	Coordinate transform matrix
T_n	N-th order Chebycheff polynomial
Tu	Turbulence intensity
(u, v, w)	Dimensionless axial/tangential/spanwise velocity vector components

$\mathbf{u}$	Dimensionless absolute velocity vector
(u_r, v_r, w_r)	Velocity components in the rotor exit relative yawed coordinate system (§G.1)
(u_t, v_t, w_t)	Velocity components in the rotor exit relative axial coordinate system (§G.1)
U, V, W	Base flow axial/tangential/spanwise velocity components
U_∞	Reference total velocity component upstream of stator
u_D, v_D, w_D	Mixed-out velocity components downstream of cascade
U_e	Velocity at the edge of the boundary layer
U_m	Mean absolute velocity in the blade row
$U_x, U_{x,\infty}$	Reference axial velocity component upstream of stator cascade
$V, \delta V, dV$	Control volume, boundary and infinitesimal element thereof
V_R	Rotor blade tangential velocity at pitchline
V_1, V_2	Relative velocities at the inlet and exit of the rotor blade row
(x, y, z)	Absolute cartesian coordinate system (centered at stator midspan LE)
(x_r, y_r, z_r)	Rotor exit relative yawed coordinate system (§G.1)
(x_t, y_t, z_t)	Rotor exit relative aligned coordinate system (§G.1)
X	Midgap-to-midgap axial length of the blade row
$(Z)_l, (z)_l$	Spanwise collocation spectral planes

Greek Symbols.

β	Stagger angle at pitchline
$\gamma_{1,r}/\gamma_{1,r}$	Disturbance centerline inclination at the inlet/exit of the rotor
$\gamma_{1,s}/\gamma_{2,s}$	Disturbance centerline inclination at the inlet/exit of the stator
Γ	Circulation
$\delta u, \delta v, \delta w$	Biases added to the upstream disturbance (§G.1)
δ^*	Boundary layer displacement thickness
δ_{mn}	Kronecker Delta function
$(\Delta C_p)^+$	Peak amplitude of the leading edge static pressure pulses
ΔP	Pressure rise
Δt	Dimensionless time step
ΔV_n	Local time-averaged velocity disturbance normal to the boundary layer
(ζ, η)	Elemental coordinate system in the blade-to-blade plane
η	Stage adiabatic efficiency
θ	Gaussian distribution angle in the local (η, ζ) coordinate system
$\theta_{1,r}, \theta_{2,r}$	Relative flow angle at the inlet/exit of the rotor

$\theta_{1,s}, \theta_{2,s}$	Relative flow angle at the inlet/exit of the stator
$\lambda_{m,v}, \lambda_{m,p}$	Velocity/Pressure eigenvalues
μ	Working fluid viscosity
ν	Dimensionless net viscosity ($\nu = 1/R + \nu_t$)
ν_t	Dimensionless eddy viscosity
Ξ_H, Ξ_V	Arclength ratio matrices
π_s	Stage total pressure ratio
Π	Stator static pressure recovery coefficient
$\Pi_m(x)$	Π from mixing the flow at station "x" of the stator passage
Π_p	Π between inlet and exit of the stator passage
ρ	Working fluid density (here constant$=\rho_\infty$)
ϱ_d	Characteristic length scale of the upstream disturbance
ϱ_e	Characteristic size of the computational subdomains
σ	Blading solidity (c/S)
$\sigma^{p/v}_{jk,i,m}$	Discretized pressure/velocity source terms
τ	Dimensionless time
τ^*	Kolmogoroff time scale
ϕ	Stage flow coefficient at pitchline
Φ^L	Line integral over $\mathcal{L}$ (§**C.10**)
χ	Disturbance impingement angle relative to stagger direction
ψ	Stage pressure coefficient defined as $\Delta P_t/\rho V^2$
Ψ	Stage pressure coefficient defined as $\Delta P_t/1/2\rho U^2$
Ψ^N	Flux or surface integral of type "N" (§**C.11-C.14**)
ω	Scalar magnitude of vorticity
$\boldsymbol{\omega}$	Absolute vorticity vector
$\boldsymbol{\omega}_n, \omega_n$	Normal vorticity vector and magnitude thereof)
$\boldsymbol{\omega}_s, \omega_s$	Streamwise vorticity vector and magnitude thereof)
$\omega_x, \omega_y, \omega_z$	Axial, blade-to-blade and spanwise vorticity components
Ω	Base flow spanwise vorticity
Ω_r	Rotor dimensionless angular velocity

Calligraphic Symbols.

$\mathcal{C}^n$	Continuity of n-th derivative
$\mathcal{E}(x)$	Integer part of x.

$\mathcal{E}$	Disturbance secondary kinetic energy
$\mathfrak{S}$	Real-to-modal mapping in the spanwise direction
$\mathcal{H}(x)$	Heavyside step function
$\mathcal{I}$	Inlet boundary of the computational domain
$\mathcal{I}_m$	Non-stationary mixing loss term
ℓ	Arclength
$\mathcal{M}(\mathbf{u}, p, t)$	Turbulence model
$\mathcal{M}^L$	Dimensionless mass flux through the domain defined by $\mathcal{L}$
$\mathcal{O}$	Exit boundary of the computational domain
$\mathcal{P}$	Pressure surface of the stator blade
$\mathcal{R}$	Stage reaction
$\mathcal{S}$	Suction surface of the stator blade
$\mathcal{T}_p$	Blade passing time period
$\mathcal{T}_i$	Time period of fluctuations within vortices and wakes
$\mathcal{Y}$	Time and mass averaged total pressure loss coefficient (§I.1)
$\mathcal{Y}_i$	$\mathcal{Y}$ from mixing the flow at the inlet of the stator passage
$\mathcal{Y}_e$	$\mathcal{Y}$ from mixing the flow at the exit of the stator passage
$\mathcal{Y}_p$	$\mathcal{Y}$ between inlet and exit of the stator passage
$\wp_{G,m}$	Condensed global source term for m-th mode

Subscripts and Superscripts.

$()_{avg}$	Area-averaged quantity at the inlet of the stator
$()_b$	Referring to a node on the periodic boundary of the computational domain.
$()_{c.v.}$	Referring to control volume boundaries
$()_e$	Referring to the e-th internal node in a given spectral element
$()_g$	Referring to the g-th global node in a given spectral element
$()_{g,i}$	Unique global index of the g-th global node on the i-th element
$()_G$	Referring to the G-th uniquely-indexed global node
$()_I, ()^I$	Referring to the inlet boundary of the computational domain.
$()_{i,*}$	Referring to the subindex set "*" on the i-th spectral element
$()_{jk}$	Referring to the (j,k)-th node in a given spectral element
$()_l$	Referring to the l-th spanwise collocation plane
$()_L$	Referring to the hub (lower endwall)
$()_{LE}$	Referring to the leading edge

$()_m$	Referring to the m-th spanwise mode
$()_m$	Referring to a mixed-out flow quantity
$()_{min\|max}$	Referring to the minimum or maximum value of a variable.
$()_O, ()^O$	Referring to the outflow boundary of the computational domain
$()_p$	Limited to the stator passage
$()_R$	Designates a flow quantity relative to the rotor
$()_s$	Designates a flow quantity in the steady (base) flow
$()_S$	Designates a flow quantity relative to the stator
$()_t$	Stagnation quantity
$()_{PS}$	Relative to the pressure surface
$()_{SS}$	Relative to the suction surface
$()_{TE}$	Referring to the trailing edge
$()_s$	Designates a flow quantity in the unsteady flow
$()_U$	Referring to the casing (upper endwall)
$()_1$	Designates a quantity at the inlet of the blade row
$()_2$	Designates a quantity at the exit of the blade row
$()_\infty$	Referring to mixed-out flow conditions upstream of the stator
$()^i$	Referring to the spectral element i.
$()^n$	Referring to the flowfield at time step n.
$()'$	Randomly fluctuating quantity (in turbulent flow).
$()'$	Final state following an isentropic process (§**2.2**)
$()''$	Second spanwise derivative
$()^*$	Referring to the outcome of the convective step
$()^{**}$	Referring to the outcome of the pressure step
$()^+$	Normalized in the law-of-the-wall sense (White, 1974)

Operators and Special Notation.

$\tilde{()}$	Spanwise mode of operand
$\tilde{\tilde{()}}$	Spectral expansion mode of operand in blade-to-blade plane
$\bar{()}$	Time-averaged value of operand
$\bar{\bar{()}}$	Spanwise-averaged value of operand
$()^T$	Transpose of operand
$<>$	Ensemble average of operand
$\|\|$	Cartesian norm

δ	Variational operator
$\Delta()$	Difference operator between unsteady and base flows (cf.§**F.1**)
∇	Gradient operator
$\nabla_{jkrs,i}^{x,y}$	Discretized elemental partial differential operators
$\sum^{i \in Q}$	Sum taken over all the spectral elements in the set Q
$\displaystyle\sum_{i,j,k,l...}$	$\displaystyle\sum_i \sum_j \sum_k \sum_l \cdots$
$\displaystyle\sum_{i=\pm 1} q_i$	$q_1 + q_{-1}$
$A \to B$	Transition from state "A" to state "B"

Acronyms

BL	Boundary Layer
BLD	Boundary layer distortion
LE	Leading edge
LHS	Left-hand side of an equation
LSRC	Low-Speed Research Compressor
N-BLD	Boundary layer disturbances containing normal vorticity
PS	Pressure surface
RHS	Right-hand side of an equation
S-BLD	Boundary layer disturbances containing streamwise vorticity
SS	Suction surface
TE	Trailing edge
TL	Rotor tip leakage vortex
SW	Rotor streamwise vortex
ID	Inviscid design-point base flow
VD	Viscous design-point base flow
VH	Viscous high-loading base flow
VS	Viscous high-shear base flow

Chapter 1

Introduction

1.1. Background and Motivation.

It has been known for almost three decades that the performance of axial compressors depends on the axial spacing between blade rows. Smith (1970) obtained a one-point efficiency gain and a two to four percent stage pressure rise increase in a low-speed research compressor, by reducing blade row spacing from 0.37 to 0.07 chords. Similar results were obtained later by Mikolajczak (1977), while Hetherington and Moritz (1977) achieved a 2-point efficiency gain by increasing the spacing in front of the the rotor blade rows in a multistage compressor. As shown in **Figure 1.1**, the experiments of Smith and Mikolajczak suggest that reduced spacing improves performance, while Hetherington and Moritz' work indicates that increased spacing may be also beneficial. Such behavior is not limited to compressors. Data for axial turbines also shows the existence of optimal spacing with regard to efficiency (Gostelow 1984).

The unsteady flow arising from the interaction between moving and stationary blade rows is thought to be the most likely cause for these observations. One of the earliest connections between performance and blade row interaction was established in Smith's (1966) model of wake recovery. In essence, the recovery process can be described by assuming constant-density, inviscid flow. As shown in **Figure 1.2**, upstream wakes undergo an increase in length when convected by the core flow in the passage. By virtue of Kelvin's theorem, the velocity non-uniformity and the thickness of the wake decrease in inverse proportion to the increase in length. In this manner, some of the secondary kinetic energy in the wakes is reversibly converted into pressure.
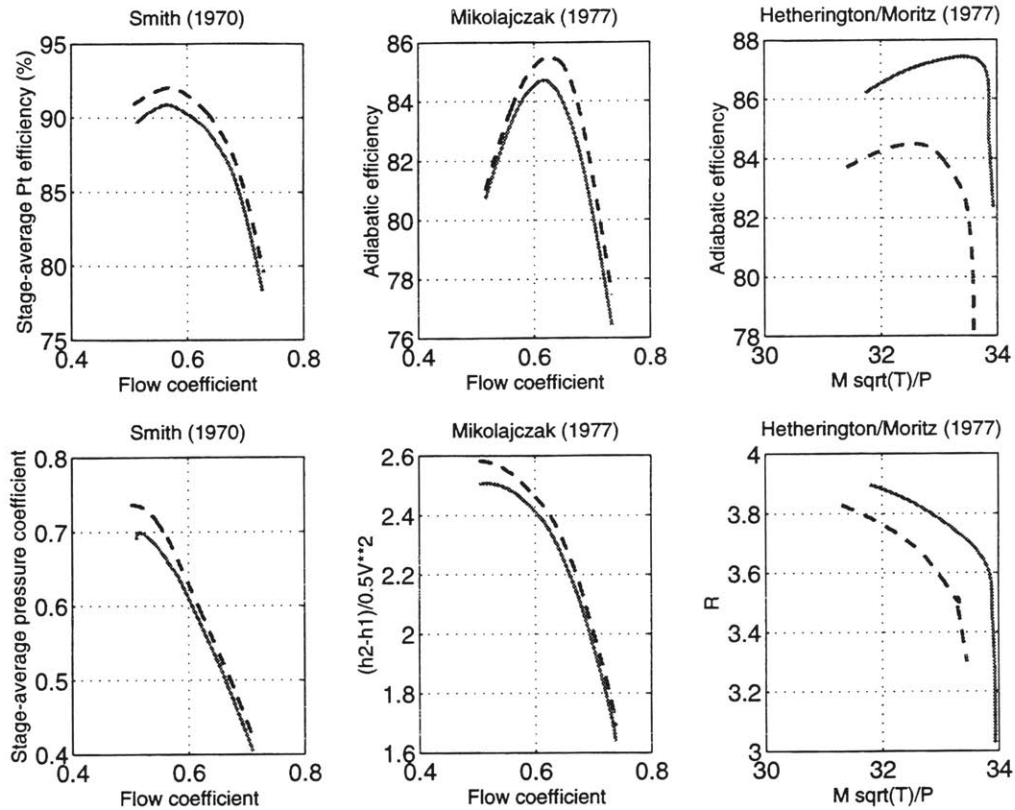
Figure 1.1. Variation of compressor efficiency (top row) and pressure rise (bottom row) for closely (dashed lines) and widely (solid lines) coupled blade rows. In modern core compressors, the spacing is typically between 0.20 and 0.40 blade chords, and primarily determined by structural and mechanical reasons.
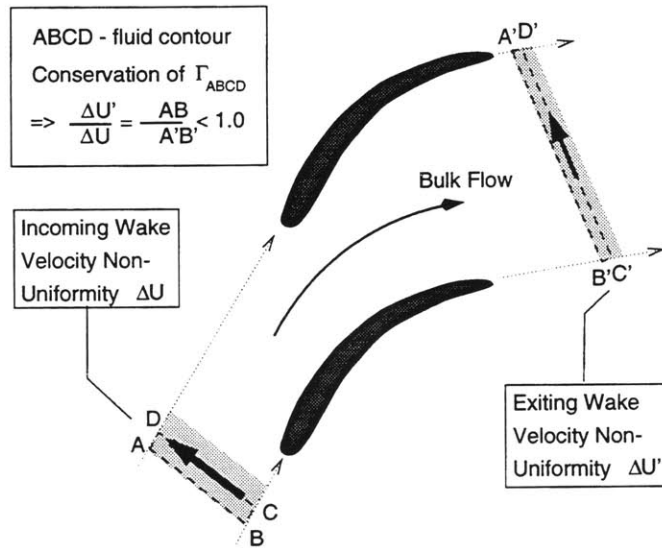
Figure 1.2. Smith's (1966) reversible attenuation and recovery mechanism for 2D wakes. Stretching of the wake segments causes a proportional decrease of their velocity non-uniformity without an increase in entropy. Therefore, the mixing loss of a wake that has passed through the stator is decreased.

The effect of recovery on efficiency can be assessed by considering the mixing loss associated with the wakes. Wake mixing represents 20-25% of the total loss produced by a cascade, and up to 75% of the wake mixing loss is realized within half a chord past the trailing edge (Denton 1993). The potential benefit from recovery is therefore significant. It is not clear though what fraction thereof is actually achieved, since viscous dissipation of the wakes starts immediately at the trailing edge and is present throughout their transport. A recent discussion by Smith (1996) indicates that reversible wake attenuation accounts for only 25 to 50 percent of the efficiency gains observed in the 1970 experiments.

Given the complexity of blade row interaction, there is no shortage of other mechanisms that can be invoked to provide alternative explanation for the data. **Table 1.1** lists some of the unsteady flow mechanisms that have been associated with compressor performance in the past. Despite the substantial experimental and computational work reviewed in §1.2, it is still unclear (1) how most of these mechanisms lead to changes in performance, (2) how significant is their effect in a given compressor. and (3) how this effect depends on design and operating parameters. This is particularly true with respect to three-dimensional and transitional aspects of the unsteady flow.

Mechanism	Discussed in
1. Boundary layer response to backpressure variation	§1.2.2
2. Tip leakage flow response to backpressure variation	§1.2.2
3. Unsteady (bypass) transition in boundary layers	§1.2.3
4. Passage-scale boundary layer disturbances	§1.2.4
5. Unsteady vortex shedding from blades	§1.2.4
6. Transport of upstream wakes (**Figure 1.2**)	§1.2.5
7. Transport of upstream vortices	§1.2.5
8. Induction of unsteady secondary flows	§1.2.6
9. Alteration of endwall and corner flows	§1.2.6

Table 1.1. Unsteady flow mechanisms resulting from blade row interaction and possibly influencing axial compressor performance. The first two mechanisms operate primarily in the upstream direction, while the rest involve the action of upstream vortical disturbances on downstream blade rows.

A number of engineering problems arise from this lack of knowledge. Traditionally, compressor design has been based on boundary-layer/streamline curvature methods with extensive use of published (Lieblein et al. 1953, NASA 1965, Koch and Smith 1976, Adkins and Smith 1982) and proprietary correlations to account for viscous and three-dimensional effects. The initial design is followed by scaled component testing (Wisler, 1985) prior to

engine integration. Computational fluid dynamics (CFD) is an increasingly important element of the design process. Recently, CFD has been successfully used to shorten the design cycle and validate innovative design ideas leading to substantial performance improvement (LeJambre 1995, Rhie et al. 1995). However, it is still not feasible to directly account for unsteady flow in design CFD codes on a sound physical basis. A number of steady-flow approximations are currently used instead (Adamczyk 1985 and 1992, Dorney and Sharma 1996). Mixing-out the non-uniform flow in the space between the blade rows is an example of such a frequently-used approximation.

It is not clear how well such approximations represent actual blade row performance in the presence of the unsteady phenomena listed in **Table 1.1**. This uncertainty may limit the confidence in new designs. Furthermore, it remains to be shown that enhanced knowledge about unsteady flow can be translated into improved performance. Therefore, elucidating the impact of the unsteady flow phenomena in **Table 1.1** on performance may help in the development of more efficient multistage compressors.

1.2. Unsteady Flow and Compressor Performance: A Review.

In the following, the term "performance" shall be used to denote stage adiabatic efficiency and pressure rise. Early investigations of blade row interaction by Kemp and Sears (1953, 1955), Von Karman and Sears (1938), Horlock (1968) and Hawthorne (1970) provided much useful insight regarding blade loading and lift fluctuations. This work was subsequently followed upon by Gallus (1979), Capece and Fleeter (1987), Schultz et al. (1990b) and Wisler (1992). The effect of unsteady flow on other figures of merit, such as durability or aeromechanical robustness, is discussed by Greitzer et al. (1994).

1.2.1. Sources of blade row interaction in compressors.

Blade row interaction is primarily the result of individual blades encountering the flow non-uniformities produced by other blade rows. According to the type of non-uniformities involved, it is useful to distinguish between potential, vortical and shock-wave interaction (Dorney and Sharma, 1996). The three types of interaction are described below, with a particular emphasis on vortical interaction, which is the subject of this thesis.

Potential interaction is associated with the influence of the pressure field of individual blades on other blade rows. Since static pressure gradients are usually highest in the leading edge region, the blade row immediately downstream is considered the principal source of potential interaction. According to Graf (1996), the peak-to-peak backpressure fluctuation at the rotor-stator midgap location can be a significant percentage of the core flow local

dynamic head (0.20% at mid-span, up to 0.40% near casing for the compressor considered).
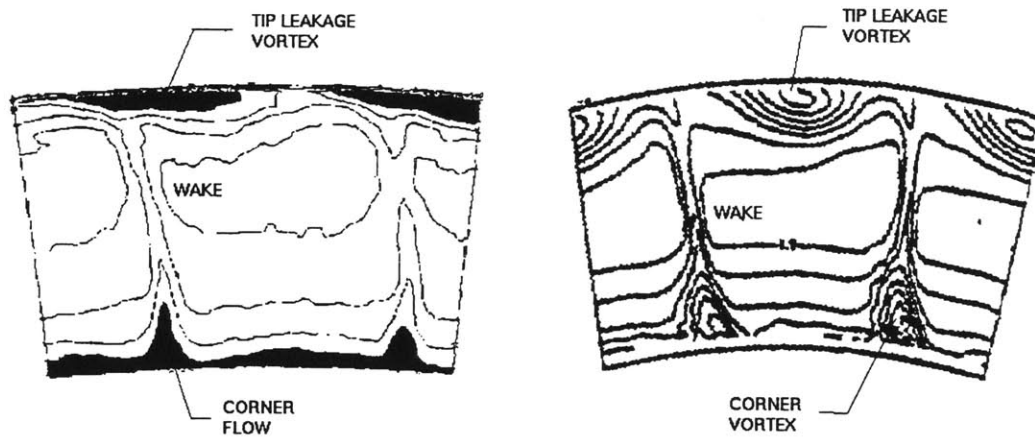
Figure 1.3. Ensemble-averaged relative velocity contours at the exit of a compressor rotor. Left: from Silkowski (1995). Right: from Nikolaou et al. (1996) adaptation of Wagner et al. (1983) data. Rotor wakes, tip vortex and corner vortices are clearly visible. Wakes and tip vortex fluctuate in the relative frame.

Vortical interaction involves wakes and vortices shed from upstream blade rows. **Figure 1.3** provides a typical illustration of these disturbances in the rotor relative frame, based on ensemble-averaged flow data.

- Wakes. Ensemble-averaged measurements of compressor rotor wakes have been obtained by Stauter et al. (1991), Prato and Lakshminarayana (1993), Zierke and Okiishi (1982), Lakshminarayana and Ravindranath (1982), and Manwaring and Wisler (1991) among others. The wake profile can be characterized by a relative velocity defect and thickness, which depend primarily on how far behind the rotor the data is taken. At the mid-gap axial location, measured mid-span defects in different research compressors range between 15-33% of the core flow velocity. Based on the data, the "average" mid-gap mid-span wake has a 20% defect and a thickness of 0.2 chords. The variation of wake defect as a function of axial distance has been quantified by Schlichting (1968, isolated cascade) and Stauter et al. (1991, multistage compressor) among others. The data indicates that the wake defect decays substantially over a distance of half a chord. Wake decay rates are highest immediately behind the rotor, and decrease rapidly in the downstream direction.

  Time-resolved data indicates that (1) there may be substantial variability from wake to wake, and (2) the wake defect fluctuates in time. Gertz (1986), and Kotidis and Epstein (1991), have proposed that these fluctuations are due to a vortex street in the wake. The amplitude of the fluctuations may be as large as the ensemble-averaged defect (Brookfield 1996). The fluctuation frequencies may be between 3 to 8 times the blade passing frequency. It appears that one frequency component of the fluctuations is related to the Strouhal number based on trailing edge wake thickness.

In swirling flows, vorticity disturbances such as wakes are coupled to pressure distur-
bances, and may show oscillations as a function of downstream distance (Kerrebrock
1977, Tan and Greitzer 1986).

- The rotor tip leakage vortex is the principal flow non-uniformity in the tip region
  (Wisler, 1985). The structure and physics of this flow have been investigated by Hunter
  and Cumpsty (1982), Storer and Cumpsty (1991), Khalid (1995) and Nikolaou et al.
  (1996) among others. For unshrouded blades, the tip leakage flow downstream of the
  rotor appears as a slowly swirling core of low-velocity fluid. This core is the result of
  mixing between the leakage flow and the free-stream. The core bears more similarity
  to a wake than to a streamwise vortex, a fact that can be appreciated in **Figure 1.3**.
  The blockage associated with the core is a function of tip loading and tip clearance
  (Khalid 1995), and the velocity defect can be a substantial fraction of the relative ve-
  locity ($\sim$50%). The velocity defect component is about twice as large as the leakage
  crossflow component in the present case.

  Recent unsteady calculations by Graf (1996) indicate that the tip vortex is modulated
  by the periodic fluctuations of backpressure from the downstream stator. The vortex
  response has a time period between 1.6-1.8 times that of the stator blade passing. Thus,
  the total pressure defect of the tip vortex core in the rotor frame also fluctuates in time.

- Rotor streamwise vortices may be present at the hub of the rotor in some axial fans.
  They appear as a round core of swirling flow (Nurzia and Puddu 1994). An idealized
  representation of such a streamwise vortex has been considered here as an interesting
  contrast to the above tip leakage vortex.

Shock-wave interaction is caused by the shock system of a given blade row extending
into neighboring passages. Shock wave interaction may influence boundary layer develop-
ment (Johnson et al. 1990). Although shock waves and compressibility are important in
aeronautical turbomachinery (Kerrebrock, 1992), the flow in the embedded stages of core
compressors is usually subsonic (Wisler, 1985). For this reason, low-speed or incompressible
models are often used in compressor studies.

1.2.2. The effect of backpressure fluctuations.

Simulations of unsteady flow in a core compressor stage by Graf (1996) indicate that
backpressure fluctuations influence performance and tip leakage flow development. The tip
vortex low-P_t core is modulated by the stator at a frequency that is 1.6-1.8 times smaller
than the relative blade passing frequency. Rotor midspan wakes are also modulated to
some extent, but at the same frequency. From a performance standpoint, the tip vortex
modulation is linked to a reduction of the loss in the tip region of the rotor. However, the
imposed backpressure fluctuations also lead to a higher rotor midspan loss. The net effect
of the downstream stator is thus to increase the time-averaged loss of the rotor with respect

to the case where a mixing plane is used between the blade rows. Relative to the same case, the time-average entropy production in the stator passage also increases in presence of the rotor. These unsteady phenomena are present over a wide range of design parameters.

From a design standpoint, these results indicate that increased unsteadiness is beneficial in the tip region of a compressor rotor, and detrimental in the midspan. However, they also suggest that the efficiency gain observed by Smith (1970, 1996) cannot be attributed to the influence of the downstream stator on the rotor.

1.2.3. The effect of unsteady transition.

Early work by Walker (1974) and Pfeil et al. (1983) revealed that boundary layers undergo forced transition under the effect of upstream wakes. Substantial progress has since been achieved in describing wake-driven bypass transition (Dong and Cumpsty 1990, Addison and Hodson 1990b in turbines, Mayle's 1991 turbulent intermittency unified approach, Walker 1993, Orth 1993, Halstead et al. 1994). Nevertheless, its impact on compressor performance remains unclear (Walker 1993).

Dong and Cumpsty (1990a, 1990b) surveyed the undisturbed and wake-excited boundary layers in a facility designed to reproduce the Reynolds number and loading on a representative supercritical (controlled-diffusion) compressor blade. Wakes create a self-sustaining "turbulent spot" where they impinge on the blade. The spot grows and propagates at a slower velocity than the free-stream. In spite of causing early transition, wake interaction has a stabilizing effect on the boundary layer, thus extending the region of laminar flow on the suction surface. In the absence of wakes, boundary layer development is influenced by the level of freestream turbulence. For levels below 1 percent, laminar separation occurs on the suction surface at 0.32 chords, followed by transition and re-attachment. At a turbulence level of 6 percent, laminar separation is suppressed and transition starts at about 0.2 chords. This suggests that bypass transition might be irrelevant at free-stream turbulence levels representative of an embedded stage.

Recent multistage compressor boundary layer surveys by Halstead et al. (1994a,b) in a multistage research compressor, show the existence of a calmed region in the boundary layer. This region is apparently generated by transitional strips initiated at the leading edge by the penetration of wake turbulence. Such regions are known to occur immediately behind turbulent spots (Schubauer and Klebanoff, 1956) regardless of the origin of the turbulence. They are resistant to flow separation due to elevated shear stress and low shape factor. A comparison of shear stress distribution on the suction surface between the first and third stage rotors indicates that the calmed regions are effective in suppressing flow separation

and delaying the onset of transition. This result agrees with Dong and Cumpsty (1990) observations. The effectiveness of the calmed region appears related to the level of intermittency in the turbulent strips induced by the wakes, and their closeness to the leading edge. At lower Reynolds numbers, transition via laminar separation increasingly replaces bypass transition as the calmed region weakens.

On a quantitative basis, the performance effects of wake-induced bypass transition are still unknown. Although suppression of laminar separation is beneficial in principle, Dong and Cumpsty (1990a, 1990b) found that the boundary layer parameters at the suction side trailing edge were similar in both the undisturbed and wake-excited cases; and rather insensitive to wake frequency, blade solidity or free-stream turbulence within the range of the experiment. The authors concluded that midspan loss levels for supercritical compressor blading are not significantly affected by the interaction between wakes and the boundary layer. On the other hand, Schultz et al. (1990a) have observed that wakes cause up to 30% midspan loss increase in a downstream compressor stator.

There is better quantitative information of wake effects on loss in a turbine-like environment. Measurements by Speidel (1951-1957) indicate that upstream wakes cause the profile loss to increase, while data by Yurinskiy and Schestachenko (1974) indicates that the increase is largest for closely-spaced blade rows. Hodson's (1990) area-based model is capable of capturing the trends in Speidel's loss data.

1.2.4. Non-transitional aspects of boundary layer response.

To a compressor blade row, upstream wakes appear as "jets" directed away from the suction surface (Kerrebrock and Mikolajczak 1970, Hodson's "negative jet" 1985). This jet imposes a peak velocity on the boundary layer sometimes exceeding 20 percent of the bulk flow (cf.§F.3). Such strong disturbances may influence boundary layer properties by mechanisms unrelated to transition. For instance, boundary layer thickness and skin friction on a flat plate can be significantly altered by perpendicular flow disturbances associated with an upstream longitudinal vortex (Sankaran and Russel, 1990). The role of similar non-transitional, wake-driven disturbances on profile loss has not been addressed.

In a three-dimensional context, Navier-Stokes simulations by Dawes (1994) show that the tip leakage vortex causes an increase of boundary layer thickness and loss in the tip region of a downstream stator (relative to midspan). As much as 29% of the stator endwall loss was attributed to unsteady flow. Dawes observed a three-dimensional vortical disturbance associated with the interception of the rotor tip vortex by the stator, and conjectured that it constitutes a 3D equivalent of the boundary layer distortions (B-vortices) predicted by Valkov

and Tan (1993) in a two-dimensional simulation. Experimentally, Howard et al. (1994) found that the loss in the tip region of the stator significantly increases when the tip clearance of the upstream rotor is increased from 1.2% to 3% chord. This increased stator loss causes 30% of the stage efficiency reduction associated with increased tip clearance.

Boundary layer vorticity is shed from the trailing edge of the blades in response to the time-varying blade circulation. Losses occur when the kinetic energy associated with this vorticity is dissipated. Fritsch (1992) found that such "unsteady circulation" losses are negligible for a two-dimensional compressor cascade.

1.2.5. Transport of wakes and vortices.

The transport of wakes and vortices can have an impact on performance by mechanisms other than boundary layer response. The efficiency benefit from Smith's (1966) mechanism of reversible wake recovery depends on the balance between attenuation by stretching and attenuation from turbulent mixing. To date, it is not known how much of the energy recovery benefit suggested by Smith's inviscid description is actually realized in the presence of turbulent mixing. Annular cascade data by Poensgen and Gallus (1991a) indicates that in the presence of a downstream stator, wakes are attenuated twice as fast as without a stator. This suggests that reversible recovery effects are significant even when turbulent mixing is present.

Another aspect of wake transport is the migration of wake fluid and the segregation of total temperature downstream of the stators. These phenomena were first identified by Kerrebrock and Mikolajczak (1970), and do not appear to have a substantial effect on efficiency. A third aspect of wake transport has been recently proposed by Adamczyk (1994). It involves the rectification of rothalpy non-uniformities, and is associated with the interaction between wakes and the leading edge pressure field. The effect of rothalpy rectification on compressor efficiency is not clear.

It is reasonable to assume that upstream vortices also undergo some form of reversible processing. Denton (1993) notes that stretching a streamwise vortex filament amplifies its secondary kinetic energy proportionally to the stretching squared. Such amplification is detrimental for performance, because the energy taken from the core flow in this process may be irreversibly dissipated by turbulent diffusion of the vortex. However, rotor tip leakage vortices are structurally more similar to wakes, for which stretching recovers part of the kinetic energy. It is not known whether some of the tip vortex secondary kinetic energy can be recovered or not.

1.2.6. The effect of unsteady secondary and corner flows.

Adamczyk (1992) noted that tilting and stretching of unsteady vorticity lines through their interaction with the unsteady velocity field can result in the production of time-average secondary vorticity, and conjectured that a significant portion of secondary flow development in a multistage machine may be due to unsteady flow. Tip leakage vortices were identified as likely candidates for this process. The effect of secondary flow induced by upstream rotor disturbances on stator performance is presently unknown.

The use of bowed stators has been successful in virtually eliminating stator corner flow separation (LeJambre et al. 1995). In more traditional designs though, corner separation may be a significant source of loss. Schultz et al. (1990a) have observed that cylinder rotor wakes cause stator endwall losses to decrease in a manner that reduces overall passage loss by up to 40%. This improvement was attributed to reduced stator hub corner separation, possibly linked to energizing of the separated region by wake turbulence. Poensgen and Gallus (1991a,b) confirmed the decrease in loss, but pointed out that unsteady secondary flows can also explain the reduction of corner stall.

1.3. Problem Statement and Research Objectives.

This thesis examines the impact of upstream rotor vortical disturbances on the performance of a representative core compressor stator. This investigation has the following objectives:

- Quantify the effect of upstream rotor tip leakage vortex and wake on the loss of the stator (relative to the commonly used steady flow approximation in which wakes and vortices are mixed out in the space between blade rows).

- Identify the unsteady phenomena of significance and explain how they cause loss to increase or decrease.

- Determine what parameters influence the performance impact of wakes and tip vortices.

- Translate this knowledge into design recommendations. In particular, find (1) which design choices lead to enhanced performance, and (2) what are the potential benefits.

A number of yet-unresolved questions in compressor aerodynamics has been addressed during the course of this work:

- Is the rotor tip vortex recovered or not? What is the effect on loss from transporting the tip vortex through the stator?

- What is the effect on loss of the non-transitional response of the stator boundary layer to upstream vortices and wakes?

- What is the effect of wake and tip vortex fluctuations on loss, relative to considering ensemble-averaged wakes and vortices?

- What is the effect of unsteady secondary flows on loss?

- How much of the energy in upstream disturbances is actually recovered by Smith's (1966) dispersion mechanism? Do the mechanisms considered here add up to the amount of efficiency benefit measured by Smith (1970)?

The issue of unsteady transition and its relation to performance is beyond the capability of the numerical experiments executed. This investigation focused instead on the unknown and important three-dimensional and non-transitional aspects of rotor-stator interaction.

1.4. Contributions of Thesis.

Mechanistic understanding. The unsteady flow computations conducted here provide for the first time a detailed picture of how upstream rotor vortices and wakes influence the loss in a core compressor stator. Two generic causal mechanisms, with significant impact on performance, have been identified. These are reversible recovery of energy in the disturbances (beneficial) and non-transitional boundary layer response (detrimental).

- Tip vortex recovery constitutes a new finding. It involves intrinsically three-dimensional vorticity kinematics. However, the energy benefit from tip vortex recovery scales in the same manner as that associated with wake recovery, and can be thus described on a 2D basis. Wake recovery is not new, and occurs in the manner postulated by Smith (1966). For a stator such as the one examined here, most (70-80%) of the energy in the upstream wake/tip vortex is recovered.

- Non-transitional boundary layer response is a new loss mechanism, that can be described in the same 2D terms for both tip vortices and wakes. The mechanism involves the normal displacement of boundary layer vortex lines under the "suction" effect of the upstream disturbances. The resulting redistribution of vorticity leads to an increase in passage loss.

Importance and parametric dependency. The effect of upstream wakes and vortices on stator loss has been quantified. This effect is important, and depends on the following parameters: axial spacing, loading and the frequency of wake/vortex fluctuations in the relative frame.

- At design point, interaction between the stator and the rotor wake/tip vortex results in an efficiency that is 0.2 points higher than obtained using the forementioned steady-state flow approximation. This number represents the sum of 0.5 points efficiency benefit from recovery and 0.3 points efficiency drop from boundary layer response. The individual effects of the wake and of the tip vortex are comparable.

- The effect of tip vortices and wakes on stator loss becomes significantly more important at reduced axial spacing. For a spacing of 0.07 chords, stage efficiency is 0.6 points higher relative to the steady flow (1.2 points recovery benefit minus 0.6 points from additional loss due to boundary layer response).

- For the present geometry, an increase in loading redistributes boundary layer vortical fluid in a manner that decreases the additional loss from boundary layer response.

- The role of fluctuations within the wakes has never been considered before. There is a range of fluctuation frequencies ($\sim$0.3-0.8 times the blade passing frequency) for which recovery does not occur. Outside this range, there is no difference between the effects of fluctuating and ensemble-averaged wakes.

- The most important aspect of the tip vortex is the velocity defect, which is perceived by the stator in the same manner as a wake. Stator flow three-dimensionality is not an important parameter.

Design implications. A model of recovery and boundary layer response has been used to explore how the blade row interaction effects change from design to design. The model considers the effects of rotor wake/stator, rotor tip vortex/stator, and stator wake/rotor interaction in a repeating embedded stage environment. It was found that:

- Steady flow approximations based on mixing the disturbances between the blade rows, underestimate stage efficiency by 0.3-0.5 points (for typical designs) and by as much as 0.6-1.0 points (for designs with closely-spaced blade rows).

- A region in design space was identified where interaction has a beneficial and relatively constant impact on efficiency. Outside this region, interaction benefits rapidly disappear. The extent of this "beneficial" region is determined by the choice of blading diffusion factor DF. For typical values of DF$\sim$0.45, the "beneficial" limits coincide approximately with the de Haller criterion (Cumpsty, 1989).

- The detrimental aspects of boundary layer response may be mitigated by (a) selective removal of boundary layer fluid, or (b) by tailoring the blade loading to reduce steady-state losses in the front part of the blade. For typical designs, the maximum efficiency gain from such measures is about 0.3 points.

Bearing in mind that this is not a back-to-back comparison with Smith (1970) compressor, the results indicate that about one-half to two-thirds of the efficiency gain observed by Smith can be attributed to interaction with upstream wakes and vortices. This suggests the existence of other mechanisms with strong impact on performance. Corner flow response is one such mechanism deserving examination.

1.5. Organization of Thesis.

The main body of the thesis presents the central ideas and results of the investigation in seven chapters, listed below, plus a final chapter of conclusions and recommendations.

Chapter	Topic
2	Method for assessment of unsteady effects on performance. Derivation of figures of merit and mechanistic relationships. Validation of the computational procedure. Description of the computational experiments.
3	Unsteady flow and impact on performance from 2D upstream rotor wakes.
4	Unsteady flow and impact on performance associated with upstream rotor tip leakage (TL) and streamwise (SW) vortices in a baseline inviscid flow situation. Addresses the effects of vortex transport.
5	Unsteady flow and impact on performance associated with upstream rotor TL and SW vortices in fully viscous flow at design point. Focuses on non-transitional boundary layer response and its effect on loss.
6	Sensitivity study, considering the effect of flow three-dimensionality and operating point.
7	Implications for compressor design. Efficiency impact of generic flow processes across the design parameter space. Mitigation of detrimental unsteady mechanisms.

Supporting material developed in the course of the investigation is presented in the following appendices.

Appendix	Topic
A	General Electric Company LSRC/E^3 compressor geometry, coordinate system and dimensionless units.
B-E	The NS3D spectral element computational procedure: validation and assumptions, discretization of the flow equations, efficient implementation and turbulence modeling.
F	Disturbance flow, its governing equations, and numerical implementation.
G-H	Description of the time-varying inlet boundary conditions representing the effect of the upstream rotor; and of the stator base flows serving as a medium for the propagation of the disturbances.
I	Mechanistic relationships for time-averaged changes in stator loss and pressure rise in terms of disturbance flow features
J	Modeling of the generic unsteady flow mechanisms and their effects.

Chapter 2

Method of Investigation

This chapter describes (1) a framework for assessing the effects of upstream disturbances on blade row performance, (2) the selection of a representative compressor geometry, (3) the computational procedure, and (4) the computational experiments to be carried out. For reasons of clarity, most details and supporting data are included as **Appendices A to I**.

2.1. Framework for Assessing the Unsteady Flow Effects.

In the multistage environment, the flow in a given blade row is influenced to some extent by all other blade rows upstream and downstream of it (**Figure 2.1**, top). It would be difficult to get a clear answer to the questions of interest if all the interactions taking place in the compressor were represented. For this reason, the study considers the case of a single stage, where the stator is subjected to the vortical disturbances from the upstream rotor, but no information from the stator reaches the rotor (**Figure 2.1**, middle).

Such a simplification is commonly employed (Dorney and Sharma, 1996), on a basis that the rotor immediately upstream is the strongest source of vortical disturbances to the stator. However, it cannot capture two aspects of unsteady interaction: (1) fluctuation of the wakes/vortices due to the stator pressure field, and (2) disturbances from blade rows other than the upstream rotor. The first aspect is accounted herein by oscillating the velocity defect of the wakes. The second aspect is not accounted for, and might be noticeable. For instance, Huber et al. (1995) have observed that clocking of the first vane of a blowdown turbine with respect to the second vane leads to efficiency variations of about 0.3 points.

In order to assess the "effects of unsteadiness" on stator performance, the time-averaged figures of merit in the unsteady case need to be compared to reference values relevant to

design. A commonly used approximation of blade row interaction is to mix out the flow non-uniformities in between blade rows (Dorney and Sharma, 1996). As shown in **Figure 2.1**, the unsteady results obtained here shall be compared against this steady-state approximation.
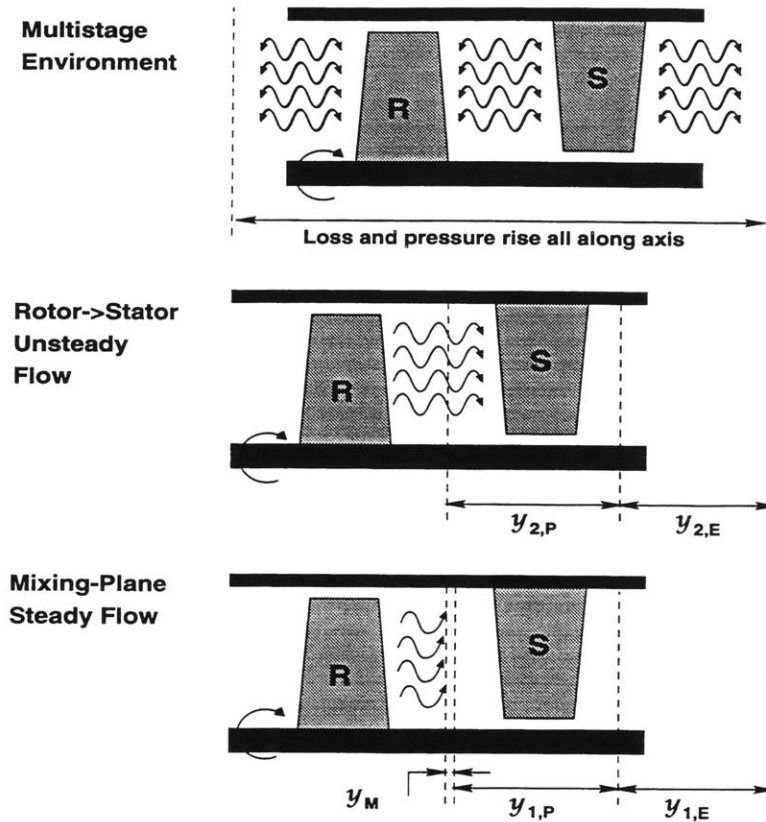
Figure 2.1. Unsteady interaction in the multistage environment (top), effect of rotor on stator as considered here (middle), and reference steady flow (bottom). The figures of merit used in the comparison are also shown, as well as the mid-gap mixing planes. Steady and unsteady flow quantities are denoted as $()_s$ and $()_u$ hereafter, while their difference is represented by the symbolic operator $\Delta()$.

Time-averaged loss ($\mathcal{Y}$) and pressure recovery (Π) coefficients, defined in §**2.2**, are used in the comparison between steady and unsteady stator performance. For instance, the loss change due to unsteady flow within the stator passage is quantified by the difference $\Delta \mathcal{Y}_p = \mathcal{Y}_{p,u} - \mathcal{Y}_{p,s}$ between time-averaged unsteady and steady-state loss coefficients.

The secondary kinetic energy of upstream wakes and vortices may be recovered in the stator without an increase in entropy (Smith 1966, cf.§**1.1**). Vortices shed in response to upstream disturbances carry kinetic energy that is eventually dissipated. The performance effects of recovery and vortex shedding are not captured by the passage loss change coefficient $\Delta \mathcal{Y}_p$ above. These effects can be quantified by comparing the time-averaged disturbance

mixing losses between the exit and the inlet of the stator, and are embodied in the coefficient $\Delta \mathcal{Y}_m$ shown in **Table 2.1** below. The net effect of upstream wakes and vortices on stator loss is thus obtained by adding $\Delta \mathcal{Y}_p$ and $\Delta \mathcal{Y}_m$.

Measure of unsteady effect	Physical meaning
$\Delta \mathcal{Y}_p = \mathcal{Y}_{p,u} - \mathcal{Y}_{p,s}$	Change in loss associated with additional entropy rise within the stator passage
$\Delta \mathcal{Y}_m = \mathcal{Y}_{i,u} - (\mathcal{Y}_{e,u} - \mathcal{Y}_{e,s})$	Change in "potential" loss associated with attenuation (or amplification) of the unsteady flow non-uniformity secondary kinetic energy
$\Delta \mathcal{Y}_n = \Delta \mathcal{Y}_p - \Delta \mathcal{Y}_m$	Net loss change due to upstream disturbances

Table 2.1. Two complementary measures of stator loss changes due to upstream disturbances used here, and definition of net effect. **Figure 2.1** shows the locations at which the component loss coefficients are evaluated. The same method is applied to the stator pressure recovery coefficient.

The stage geometry used in this investigation is that of the General Electric Low Speed Research Compressor. This geometry is representative of an embedded stage in a modern aeronautical compressor (Wisler 1985). It is described in **Appendix A**, along with information on the coordinate system and on the dimensionless units used here.

There has been a substantial interest in explaining Smith's (1970) efficiency data in a quantitative manner. The framework presented in **Figure 2.1** is not identical to that underlying Smith's experiments. Smith compared the performance at design axial gap (0.37 chords for the present LSRC geometry) against the performance at significantly reduced axial gap (0.07 chords). Such small gaps are not used in practice (typical jet engine axial gaps are usually between 0.2 and 0.4 chords). Herein, the performance at design axial gap is compared against a steady state approximation that is equivalent to an infinite gap between the blade rows. This approach is motivated by the need to assess the importance of unsteadiness relative to a simplification commonly used in the design practice, and to determine if improvements are possible within the constraints of practical axial gaps.

Nevertheless, the present framework does not preclude investigating the effects of axial spacing and connecting them to Smith's (1970) data. This has been accomplished by using two categories of wakes and vortices - baseline and "strong". Baseline wakes and vortices have a velocity profile that corresponds to blade rows separated by a distance of 0.37 chords (the same as in Smith's baseline experiment). This value is in the upper range of axial spacings used in existing compressors (typically between 0.2-0.4 chords). "Strong" wakes and vortices have a velocity profile that corresponds to a blade row separation of 0.07 chords.

2.2. Figures of Merit in Unsteady Flow.

The purpose of this section is to derive stator loss and pressure recovery coefficients that are (1) physically related to the compressor efficiency and pressure ratio, and (2) used in the design practice. The details of the derivation can be found in §I.1. It was found that at low Mach numbers, the mass and time-averaged total pressure loss coefficient :

$$\mathcal{Y}_{I \to E} = \frac{1}{A} \left[\iint_E \overline{uc_t} dA - \iint_I \overline{uc_t} dA \right] \tag{2.01}$$

provides an adequate measure of compressor adiabatic efficiency based on entropy rise of the working fluid between inlet (I) and exit (E). Specifically, the drop in stage efficiency due to irreversible flow in the stator is given by :

$$(1 - \eta)_S = \frac{P_{t,\text{avg,stator inlet}} - P_{\text{avg,stator inlet}}}{P_{t,\text{avg,stage inlet}} - P_{t,\text{avg,stage exit}}} \mathcal{Y} \tag{2.02}$$

In steady flow, (2.01) yields the total pressure loss coefficient traditionally used in cascade testing and stage design (Lieblein et al. 1953, Cumpsty 1989, Kerrebrock 1992, Denton 1993). Equation (2.02) can be used to determine the effect of unsteadiness on compressor efficiency, denoted as $\Delta\eta$, by inserting $\Delta\mathcal{Y}$ for $\mathcal{Y}$.

The stator does not perform mechanical work leading to pressure rise, but serves to reduce the swirl from the rotor and convert it into static pressure. In unsteady flow, this capability can be quantified by a time-averaged pressure coefficient:

$$\Pi = \frac{\iint_E \overline{P} dA - \iint_I \overline{P} dA}{Q_{\text{avg, stator inlet}}} = \frac{\iint_E \overline{C_p} dA - \iint_I \overline{C_p} dA}{A} \tag{2.03}$$

For steady cascade flow, (2.03) is equivalent to the pressure coefficient used to characterize diffuser performance (Kerrebrock, 1992). This correspondence is appropriate, since a compressor stator is basically a curved diffuser. Mass-averaging of static pressure coefficients it not justified from momentum conservation standpoint (cf. §I.4).

It is to be noted that the effect of unsteadiness on compressor pressure rise ψ, is related to the change in stator loss ($\Delta\mathcal{Y}$) and not to the change in static pressure coefficient ($\Delta\Pi$). This is so because the pressure rise of the machine is the result of work done on the fluid by the rotors. The stators do not perform work, but total pressure losses therein are equivalent to reducing the work done by the rotors. In this light, a change in stator loss $\Delta\mathcal{Y}$ leads to a proportional change in stage pressure coefficient given by:

$$\Delta\psi = \frac{2Q}{\rho U^2} \Delta\mathcal{Y} \tag{2.04}$$

For this reason, changes in static pressure coefficient $\Delta\Pi$ are examined in less detail than changes in stator loss.

2.3. Mechanistic Relationships.

For incompressible adiabatic flow, the above loss and pressure coefficients can be expressed in terms of unsteady vorticity and velocity fields. The resulting *mechanistic relationships* are helpful for identifying and modeling those unsteady flow features that impact performance. The first relationship, derived in §I.2 connects the time-average passage loss coefficient to the unsteady vorticity field in the stator. It states that the only source of time-averaged loss is the vorticity in the boundary layers, secondary flows and upstream disturbances:

$$A\mathcal{Y}_p = -\frac{2}{Re}\iiint_p \overline{\omega^2}dV \qquad (2.04a)$$

Equation (2.04a) is applicable to both laminar and turbulent unsteady flows, provided that the vorticity in all small-scale eddies is taken into account. In engineering applications, it is often impractical to resolve these small eddies. A Reynolds-averaged form of the Navier-Stokes equations (cf. §B.3.1) is used instead, in which the dissipative effect of small eddies is represented through the use of an eddy viscosity. In this case, the loss depends also on the distribution of eddy viscosity:

$$A\mathcal{Y}_p \approx -2\iiint_p \overline{\nu\omega^2}dV \qquad (2.04b)$$

Time-average losses from mixing the unsteady non-uniform flow to a uniform state are computed by means of a mass and momentum balance under constant area conditions (cf.§I.3). This method of mixing was selected among several available (Greitzer, 1994) because it is physically realizable in the interblade environment. The second mechanistic relationship expresses mixing loss in terms of velocity and pressure fields:

$$A\mathcal{Y}_m(x) = u_D\iint_x(\overline{C_p} + \overline{2u^2} - u_D^2)dA - \iint_x \overline{u(C_p + u^2 + v^2 + w^2)}dA$$

$$+ \frac{1}{u_DA}\overline{\left\{\iint_A uvdA\right\}}^2 + \frac{1}{u_DA}\overline{\left\{\iint_A uwdA\right\}}^2 \qquad (2.06)$$

Equations (2.04)-(2.07) are useful for expressing loss and pressure coefficient changes due to unsteadiness in terms of the fluctuating part of the flowfield. For instance, the change in passage loss $\Delta\mathcal{Y}_p$ of **Table 2.1** can be directly related to the time-average vortical structure of the unsteady flow, expressed as a disturbance relative to the base flow:

$$A\Delta\mathcal{Y}_p = -\frac{4}{Re}\iiint \boldsymbol{\omega}_s \cdot \overline{\Delta\boldsymbol{\omega}}dV - \frac{2}{Re}\iiint \overline{(\Delta\boldsymbol{\omega})^2}dV \qquad \text{(Exact)}$$

$$A\Delta\mathcal{Y}_p \approx -6\iiint \nu_s\boldsymbol{\omega}_s \cdot \overline{\Delta\boldsymbol{\omega}}dV - 2\iiint \nu_s\overline{(\Delta\boldsymbol{\omega})^2}dV \qquad \text{(Reynolds-averaged)}$$

$$\text{(2.07)}$$

The loss benefit from attenuating (or detriment from amplifying) upstream disturbances in the stator, $\Delta\mathcal{Y}_m$ (**Table 2.1**), is related to the energy thickness of velocity fluctuations before and after the stator :

$$A\Delta\mathcal{Y}_m \approx \iint_{\mathcal{E}}\overline{(1+\Delta u)(\Delta u^2 + \Delta v^2 + \Delta w^2)}dA - \iint_{\mathcal{I}}\overline{(1+\Delta u)(\Delta u^2 + \Delta v^2 + \Delta w^2)}dA$$

$$+\frac{1}{A}\overline{\left\{\iint_{\mathcal{I}}(1+\Delta u)\Delta v dA\right\}^2} - \frac{1}{A}\overline{\left\{\iint_{\mathcal{E}}(1+\Delta u)\Delta v dA\right\}^2}$$

$$+\frac{1}{A}\overline{\left\{\iint_{\mathcal{I}}(1+\Delta u)\Delta w dA\right\}^2} - \frac{1}{A}\overline{\left\{\iint_{\mathcal{E}}(1+\Delta u)\Delta w dA\right\}^2}$$

$$\text{(2.08)}$$

The net static pressure recovery coefficient change (passage+mixing) due to unsteady flow in the stator is directly related to a change in time-average blade axial force. The latter is due to static pressure and skin friction redistribution:

$$A\Delta\Pi_n = \int_{x_{LE}}^{x_{TE}}\int_{-H/2}^{H/2}\left[(\overline{\Delta C_p})_{PS} - (\overline{\Delta C_p})_{SS}\right]dydz \qquad \text{(Pressure redistribution)}$$

$$-\frac{2}{Re}\int_{x_{LE}}^{x_{TE}}\int_{-H/2}^{H/2}\left[(\overline{\Delta\omega_z})_{PS} - (\overline{\Delta\omega_z})_{SS}\right]dxdz \qquad \text{(Blade friction redistribution)}$$

$$-\frac{2}{Re}\int_{x_i}^{x_e}\int_{SS}^{PS}\left[(\overline{\Delta\omega_y})_{L} - (\overline{\Delta\omega_y})_{U}\right]dxdy \qquad \text{(Endwall friction redistribution)}$$

$$\text{(2.09)}$$

The utility of (2.08)-(2.10) shall be illustrated in **Chapters 3-6**, in which unsteady flow features are connected to changes in performance. It is the first time that such a unified approach to treating the effects of unsteadiness on blade row loss has been presented. It is to be noted that the relationships are strictly valid for incompressible flow, and are in dimensionless terms (e.g. the density, $\rho=1$, has been omitted from the notation). In unsteady flows where the Mach number approaches or exceeds unity, there are new mechanistic aspects

to loss and pressure rise not addressed in the above. Such cases are beyond the scope of the present investigation.

2.4. Computational Approach.

It is often difficult to characterize a specific unsteady flow aspect from multistage data, because of the many interrelated factors and flow features involved. In addition, the short time scales of the phenomena, and the high cost of operation place logistical constraints on experimental work. Carefully controlled numerical experiments are free of such complexities, and form the basis of this investigation.

Several methods for calculating inviscid and viscous unsteady flow in turbomachinery have been developed over the last two decades (Erdos et al. 1977, Koya and Kotake 1985, Whitehead's 1987 LINSUB, Rai 1987a 1987b, Gibeling et al. 1988, Ni and Sharma 1990, Chen and Chakravarthy 1990, Saxer 1992, Giles and Haimes' 1993 UNSFLO, Dawes 1992). Time-accurate spectral-element techniques for direct simulation of viscous flows have also emerged in the last decade (Patera 1984, Korczak 1985, Tan 1989, Renaud 1991). The computational method employed here is an extension of these high-order techniques.

2.4.1. Numerical method.

At free-stream turbulence levels, Mach, and Reynolds numbers typical of embedded core compressor stages, the unsteady flow in the stator passage can be adequately described by means of the time-dependent Reynolds-averaged Navier-Stokes equations (cf. §B.3.1):

$$\frac{\partial \mathbf{u}}{\partial t} - \mathbf{u} \times \boldsymbol{\omega} = -\nabla p_t + \nabla(\nu \nabla \mathbf{u}) \quad ; \quad \nabla \cdot \mathbf{u} = 0 \qquad (2.11)$$

The present investigation is concerned with the unsteadiness of the flow, which can be represented as a *disturbance* flowfield, superimposed upon the pre-mixed steady (base) flow used as a reference:

$$\Delta \mathbf{u}(x, y, z, t) = \mathbf{u}_u(x, y, z, t) - \mathbf{u}_s(x, y, z)$$

$$(2.12)$$

$$\Delta p(x, y, z, t) = p_u(x, y, z, t) - p_s(x, y, z) \qquad \text{...etc.}$$

The computational procedure employed here does not solve (2.11) directly. Instead, the disturbance flow is obtained by solving the following form of the Navier-Stokes equations (derived by inserting 2.12 into 2.11), and added to the base flow to obtain the full viscous unsteady flow.

$$\frac{\partial \Delta \mathbf{u}}{\partial t} = \mathbf{u}_s \times \Delta \omega + \Delta \mathbf{u} \times \omega_s + \Delta \mathbf{u} \times \Delta \omega - \nabla \Delta p_t + \nabla \left[(\nu_s + \Delta \nu) \nabla \Delta \mathbf{u} + \Delta \nu \nabla \mathbf{u}_s \right] \quad (2.13)$$

Equation (2.13) is mathematically and numerically equivalent to solving the full Navier-Stokes equations (2.11). Unlike standard linearised perturbation approximations, this equation takes fully into account non-linear and viscous effects. The base flow employed must be a solution of the Navier-Stokes equations. For these reasons, the time-average of the disturbance flow $(\overline{\Delta \mathbf{u}}, \overline{\Delta p})$ will not be nil in general.

A fractional time-stepping procedure, using fully-spectral expansion in the spanwise direction and spectral-element expansion in the blade-to-blade plane, is employed to solve (2.13). It is based on the idea of dividing the computational domain into a number of regularly-sized regions, and then proceeding to a high-order expansion of the flowfield within each region to achieve both geometric flexibility and higher accuracy. As described in **Appendices C** and **D**, the procedure also solves the full-flow Navier-Stokes equations.

2.4.2. Application of the computational tools.

The use of the disturbance form of the Navier-Stokes equations (2.13) offers several advantages in terms of isolating and manipulating specific aspects of blade row interaction. In particular, the unsteady flow obtained in each computational experiment is completely defined by the following two inputs:

- A representative disturbance profile from the upstream rotor (e.g. a tip leakage vortex) at the inlet of the stator. The parameters of this disturbance (e.g. displacement thickness) can be held constant or varied independently of other parameters.

- A steady base flow in the stator, obtained beforehand at given operating conditions. Aspects of the base flow (such as loading, three-dimensionality or presence of boundary layers) can be precisely controlled or altogether eliminated to reveal the role of a specific mechanism (e.g. boundary layer interaction) in altering the stator performance.

The disturbances and base flows used here are described in §**2.5** and §**2.6** respectively. The combinations of these as computational experiments addressing issues of interest, are presented in §**2.7**. For each computational experiment, disturbance flow visualization shows the principal features of the unsteady flow, while the mechanistic relationships of §**2.3** explain their role in changing stator performance. Useful design information can be obtained by considering which aspects of the steady flow maximize the beneficial aspects of the unsteadiness. This thought process, shown in **Figure 2.2**, forms the core of the study.
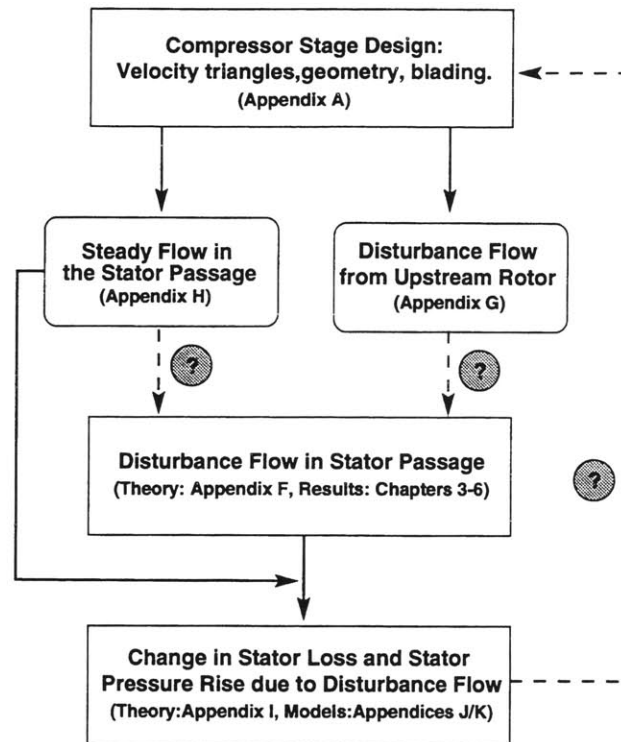
Figure 2.2. Causal relationships between compressor design parameters, unsteady flow, and performance impact thereof. Solid lines indicate links that are understood in principle and can be quantified. Dashed lines are links that remain to be elucidated.

2.4.3. Validation and assumptions.

Ideally, CFD results should be validated by comparison with experimental data taken in a representative environment. Qualitatively, the results of this investigation agree with observations made by Smith (1970) and Howard et al. (1994), as well as with simulations by Dawes (1994) and Graf (1996). However, there is no experimental data about the unsteady flowfield inside the stator that allows direct confirmation of the unsteady mechanisms identified. For this reason, three issues have been addressed to ensure that the results are representative: (1) solver accuracy, (2) the effect of eddy viscosity on the computed results; and (3) the effect of simplifying assumptions.

For reasons of conciseness, supporting material from this assessment has been placed in **Appendix B**. Section **B.2** demonstrates the instrinsic accuracy of the computational procedure. Section **B.3** justifies the use of a turbulence model by comparing scales of unsteadiness and turbulence, and by examining the role of free-stream turbulence levels on transition in embedded stages. This section also considers the sensitivity of the results to the particular turbulence model used. Eddy viscosity does not appear to be an important parameter, given

that (1) recovery occurs over a shorter lengthscale than diffusion, and (2) those unsteady mechanisms that impact performance are of convective nature.

Certain assumptions have been made to make the problem tractable. These assumptions are (1) incompressible flow; (2) planar cascade; (3) straight stator blades; and (4) one-to-one rotor/stator blade ratio. Section B.4 concludes that the essential effects of wakes and vortices can be captured under these assumptions. To fully appreciate the discussion, the reader should first become familiar with the unsteady flow results in **Chapters 3-6**.

2.5. Inlet Disturbances.

Three generic types of inlet disturbances, described in **Appendix G**, are used in the investigation: wakes, rotor tip leakage vortices, and simple streamwise vortices. These disturbances are based on observations of the interblade unsteady flow environment.

- **Rotor Wakes** are represented by a Gaussian velocity defect profile in the rotor frame. The profile is characterized by a peak relative velocity defect (A_r) and by a 99% velocity thickness (t_w). In a first set of computations, A_r and t_w are kept steady in time but varied from experiment to experiment in a manner representative of different degrees of "mixedness" of a baseline LSRC rotor wake at nominal loading (**Table 2.2**). This approximates the effect of changing the axial separation between blade rows.

A_r (%)	12	25	37	50	65
t_w (chords)	0.33	0.20	0.15	0.12	0.10

Table 2.2. Set of mid-gap wake defects and 99% thicknesses used to characterize interaction with ensemble-averaged wakes. Axial spacing decreases left to right.

In a second set of computational experiments, the wake defect is varied in time with a time period ranging from 1/7 to 2 times the rotor blade passing period. This sheds light on the role of velocity fluctuations within the wakes.

- **Rotor Tip Leakage (TL) Vortices** are represented as a core of steady, slowly-swirling low-energy fluid. Two TL vortices are used in the computational experiments: "nominal" and "strong". The "nominal" vortex velocity profile is extracted from Khalid's (1995) Navier-Stokes simulation of tip leakage flow in an isolated LSRC rotor at design loading with 3 percent tip clearance. The peak P_t defect in the nominal vortex core at the exit of the rotor is 45% of the local dynamic head. The core extends roughly over 60% of the blade-to-blade spacing and over 15% of the span.

The "nominal" and "strong" vortices differ by the magnitude of the velocity defect in the vortex core. For the strong vortex, this defect is scaled up by using a wake decay relationship proposed by Stauter et al. (1991). Since the inlet computational boundary (where disturbances are prescribed) is fixed at 0.25 chord units ahead of the stator, this scaling helps simulate the effect of reducing axial spacing.

- **Rotor Streamwise (SW) Vortices** are represented by an exponential viscous core with a diameter of 15% of span and dimensionless circulation of 0.45 units. Such vortices are not seen in core compressors, but may be present in other types of turbomachinery (Nurzia and Puddu, 1994). In addition, they illustrate how tip leakage vortex processing differs from what Denton (1993) conjectured.

It is to be noted that these disturbances assume a different appearance when passing from the rotor into the stator frames. This is due to the relative stacking orientation between rotor and stator blade sections. In a compressor stage such as that of the LSRC, rotor and stator blades are approximately perpendicular. As a result, rotor disturbances associated with blockage (wakes, TL vortex core) appear as "jets" directed away from the suction surface and towards the pressure surface of the stator. On the other hand, crossflow disturbances in the rotor frame (SW vortex) appear to the stator as fluctuations in the plane of the blade. This situation is shown in **Figure 2.3.**
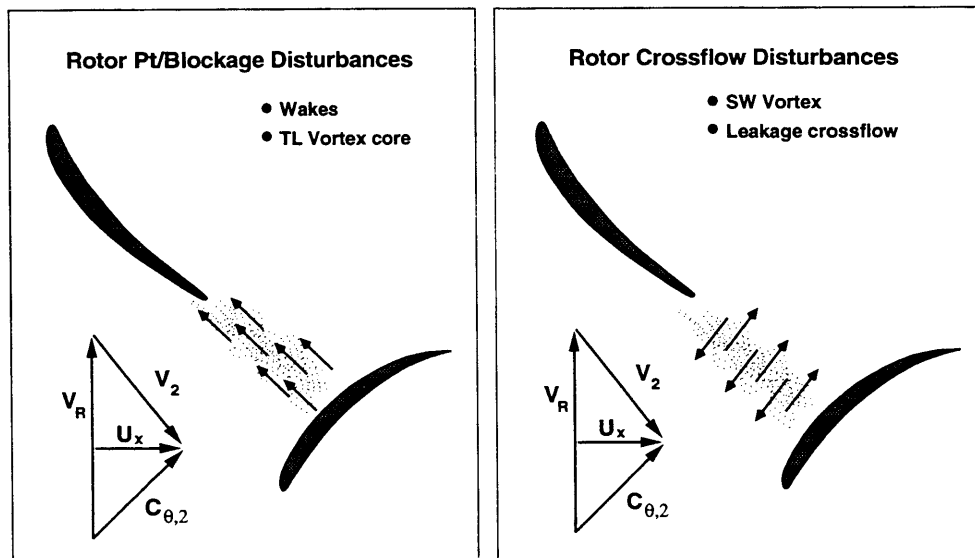
Figure 2.3. Two generic types of disturbances perceived by a downstream blade row: normal "jets" (total pressure/blockage in the rotor frame) and planar perturbations (crossflow disturbances in the rotor frame). Note that the disturbance flow shown is invariant under change of reference system.

2.6. Steady (Base) Flows.

The foregoing disturbances propagate and interact with the following four steady (base) flows in the stator passage, described in detail in **Appendix H**:

- **Nominal** base flow (denoted by "VD") at a flow coefficient of 0.45 and a Reynolds number of 250,000 (design). The spanwise velocity distribution at the inlet of the stator is based on an idealized representation of Khalid's (1995) circumferentially-averaged rotor solution. The midspan inlet flow angle is 46°, and the diffusion factor is 0.43.

- **High-loading** base flow (denoted by "VH"), at a flow coefficient of 0.38. As shown in **Figure A.1**, this is close to the peak of the characteristic but the flow is not stalled. At midspan, the inlet flow angle is 51 degrees, and the diffusion factor is 0.52.

- **Embedded-stage** base flow (denoted by "VS"). The nominal flow above is not highly three-dimensional. In this respect, it differs from the core flow in a deeply embedded stator. The "VS" base flow has the same loading characteristics as "VD" flow above, but is obtained using an inlet shear profile that is more representative of the flow at the inlet of an embedded stage.

- **Inviscid** base flow (denoted by "ID") at the same flow coefficient as flow ("VD") above. This flow is irrotational, and thus free of loss, secondary flow and boundary layers.

The viscous base flows are obtained by means of the three-dimensional Reynolds-averaged Navier-Stokes flow solver described by Adamczyk et al. (1989). The inviscid flow is obtained by stacking PCPANEL (McFarland, 1984) solutions in the spanwise direction.

2.7. Computational Experiments Performed.

The computational experiments are described in terms of inlet disturbances and base flows used. Three groups of computational experiments have been carried out. In the first, the wakes described in §2.5 interact with a midspan section of the stator on a two-dimensional basis and at design point conditions. The purpose of the wake calculation is to answer unresolved issues about the amount of wake recovery and the role of non-transitional boundary layer response. Moreover, the wake calculations shall prove helpful in understanding better some aspects of tip leakage vortex interaction.

The second group of computational experiments is summarized in **Table 2.3**. Its purpose is to identify key loss-producing mechanisms associated with tip leakage and streamwise vortices. The first two calculations shown in **Table 2.3** are inviscid in the sense that (1) the base flow is inviscid; and (2) the disturbances propagate in a slip-free manner. Turbulent diffusion is still retained in the bulk of the disturbance flow however. This allows to distinguish losses due to mixing of the vortex from losses associated with boundary layer response in the subsequent viscous flow calculations.

The third group of computational experiments explores the sensitivity of TL vortex interaction to operating parameters, vortex structure and axial spacing. The experiments are described in **Table 2.4**. The 2D/TL experiment deserves particular attention. Baseline calculations strongly suggest that the effects of tip vortex-stator interaction can be described on a locally two-dimensional basis, similar to that of wake interaction. The 2D/TL experiment is designed to verify this claim by using a two-dimensional formulation of the disturbance equations of motion, in which each computational plane is independent (cf. §C.17).

Designation	Description and Purpose
ID/SW	Interaction of a streamwise vortex (SW) with an inviscid base flow (ID). Determine loss impact from transport of streamwise vortices without the complications due to boundary layer response.
ID/TL	Interaction of a tip leakage vortex (TL) with an inviscid base flow (ID). Find if the vortex energy is reversibly recovered without the complications due to boundary layer response.
VD/SW	Interaction of a SW vortex with a viscous base flow at design loading (VD). Compare to ID/SW to show (1) how SW vortex transport is affected by the boundary layer, (2) how the boundary layer responds to the disturbance, and (3) what are the loss effects thereof.
VD/TL	Interaction of a TL vortex with a viscous base flow at design loading (VD). Compare to ID/TL to show (1) how TL vortex transport is affected by the boundary layer, (2) how the boundary layer responds to the disturbance, (3) what are the loss effects thereof under baseline conditions, and (4) how interaction with the tip vortex differs from that with a streamwise vortex.

Table 2.3. Computational experiments aimed at revealing key features and mechanisms of interaction with upstream rotor tip and streamwise vortices.

Designation	Description and Purpose
VH/TL	Interaction of a nominal TL vortex with a high-loading base flow (VH). Compare to VD/TL to show (1) how vortex transport is affected by loading, (2) how higher pressure gradients affect boundary layer response. Note that the vortex strength is the same as in case VD/TL.
VS/TL	Interaction of a nominal TL vortex with a viscous base flow with high-shear inlet profile (VS). Compare to VD/TL to show (1) how vortex transport is affected by base velocity gradients, (2) what is the effect of unsteady secondary flows, and (3) what is the effect of increased base flow three-dimensionality.
VD/TS	Interaction of a "strong" TL vortex with a design-point loading viscous base flow (VD). Compare to VD/TL to determine the effect of reduced axial spacing on unsteady flow and losses.
VD/TP	Interaction with a tip vortex, from which the crossflow component in the rotor frame has been removed. Compare to VD/TL in order to separate the effects associated with the blockage in the vortex, from those due to leakage crossflow and streamwise vorticity. Determine what is the most important aspect of the tip vortex.
2D/TL	Locally two-dimensional interaction of a TL vortex with a design-point viscous base flow (VD). The disturbance equations of motion are solved over a stack of independent blade-to-blade planes. Determine whether TL interaction is truly a three-dimensional phenomenon, or whether is can be explained in locally 2D terms.

Table 2.4. Computational experiments used in a sensitivity study of stator and upstream tip leakage vortex interaction.

Chapter 3

Two-Dimensional Wake/Stator Interaction

This chapter examines the unsteady flow arising from the two-dimensional interaction of upstream wakes with a midspan section of the stator. The purpose is to identify the mechanisms by which wakes influence time-averaged performance, and quantify the impact thereupon. Three issues are addressed: (1) the role of non-transitional boundary layer response, (2) the importance of wake recovery in the presence of mixing; and (3) the effect of fluctuations inside the wakes. This information shall be of use later, given the similarity between wakes and tip leakage vortices.

Two series of computational experiments are carried out at a design flow coefficient of 0.45, Reynolds number of 300,000, and time step of 0.0005. The first series consists of five computational experiments, using the same wake at different degrees of "mixedness". In these experiments, the wake relative defect A_r at the inlet of the computational domain is varied as shown in **Table 2.2** (but is kept steady in time). This series of experiments shows the effect of changing the blade row axial spacing. The 25% wake is representative of interaction at design axial spacing in the LSRC geometry used here (0.37 chords). The 50-60% wakes are representative of Smith's (1970) closely-coupled blade row interaction in the same compressor.

In the second series of experiments, the wake has constant ensemble-averaged properties, but the defect is sinusoidally varied in time at a fraction of the blade passing frequency. This is a simplified representation of wake fluctuations seen in data (Kotidis and Epstein 1991, Waitz 1996, Brookfield 1996). It is sufficient for the purpose of identifying trends. The role of wake fluctuations has never been considered in interaction studies.

3.1. Constant Wakes: Unsteady Flow Features.

The instantaneous disturbance velocity field associated with the wakes appears as a "jet" directed against the pressure side of the stator blade. Upon interception of this "jet", pressure pulses that are a significant fraction of the inlet dynamic head, appear on the leading edge. As shown in **Figure 3.1**, the pulse on the pressure surface (PS) is positive, while that on the suction surface (SS) is negative.
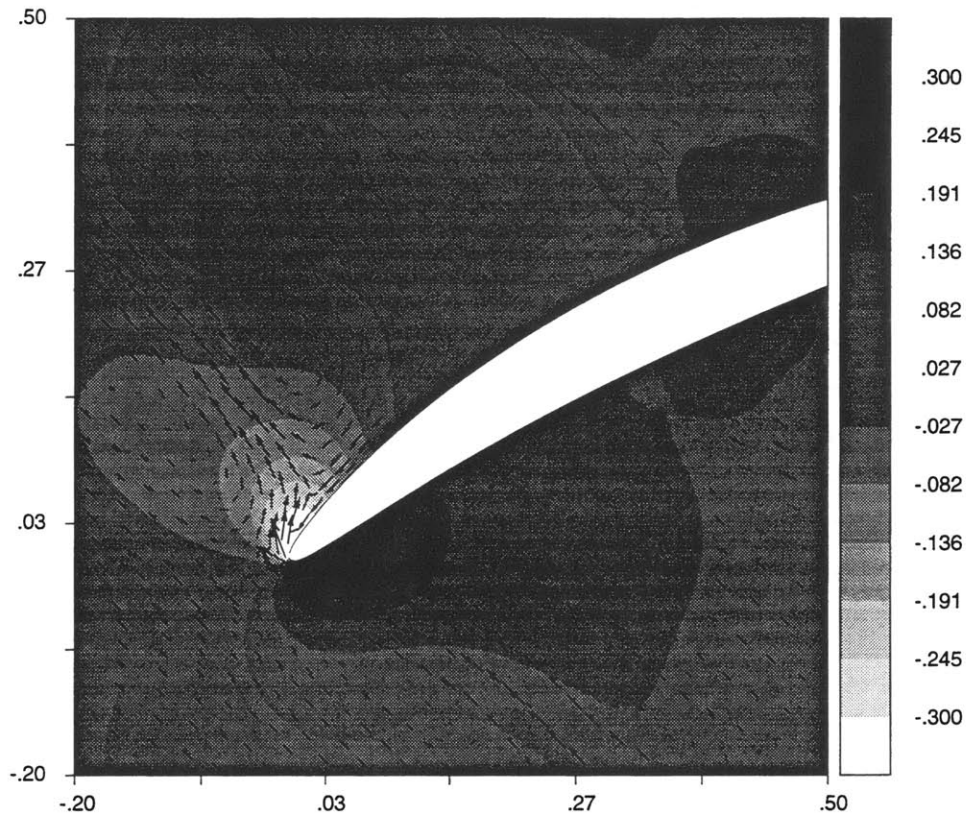
Figure 3.1. Disturbance static pressure isocontours and disturbance velocity field at interception time t_0. Note the (+/-) pressure regions on each side of the leading edge and the "jet" of the upstream wake (baseline 25% wake case).

The static pressure pulses are a potential flow effect, observed in both Navier-Stokes and inviscid calculations (Valkov, 1992). They constitute the most important aspect of the unsteady loading on the blade. Their duration is comparable to the time necessary for the wake to be "cut" by the leading edge. The peak value of the static pressure pulse on the pressure side, $(\Delta C_p)^+$, can be described in quasi-steady inviscid terms as the additional pressure resulting from bringing the "wake jet" to a stagnation point:

$$(\Delta C_p)^+ = 2\tan\theta_1 A_j + A_j^2 \tag{3.01}$$

where A_j is the peak velocity in the wake "jet", and θ_1 is the inlet flow angle. As shown in **Figure 3.2**, this simple model, derived in §**J.2.4**, agrees well with the CFD results.
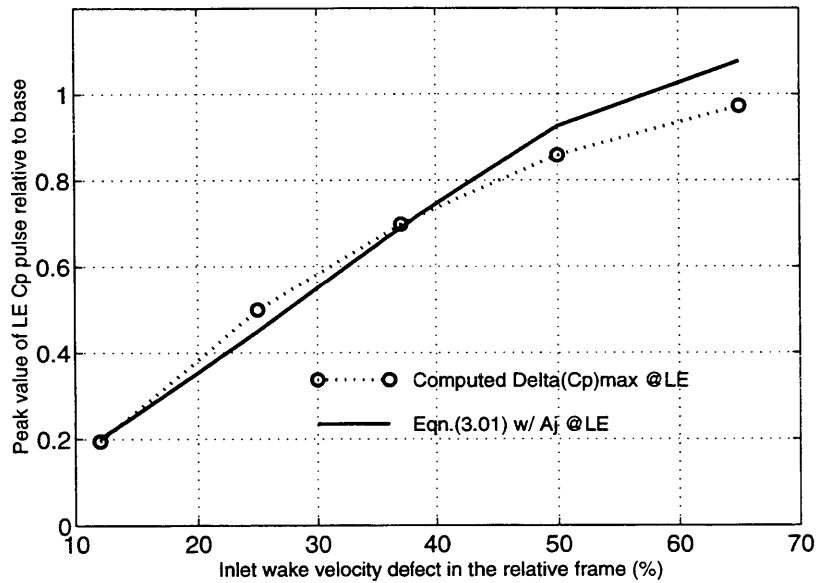
Figure 3.2. Comparison between $(\Delta C_p)^+$ from the simulation and from the quasi-steady inviscid-impingement models in §J.2.4.

According to Equation (2.07), it is useful to describe the unsteady flow in terms of disturbance vorticity $\Delta\omega$, defined as the difference in vorticity between the unsteady flow and the steady base flow. Instantaneous disturbance vorticity fields are shown in **Figure 3.3** for baseline 25% wakes, and in **Figure 3.4** for 65% wakes. The baseline wakes are essentially transported in the manner conjectured by Smith (1966). Individual wake segments are stretched. Their SS and PS ends travel at different speed, and leave the stator with a shift relative to the other wakes. The 65% wakes are characterized by a more pronounced migration.

Figures 3.3 and **3.4** also show vortex shedding from the trailing edge and non-transitional vortical disturbances in the boundary layer. For the present geometry, vortex shedding is not an important source of loss. This can be appreciated by comparing the velocity fluctuations in the boundary layer to the velocity fluctuations associated with the wake in **Figure 3.10** (right). On the other hand, the suction side boundary layer disturbances (referred to as BLDs in the following) are the leading source of passage loss change. This section focuses on the origin of BLDs, while §**3.3.2** examines their connection to loss.
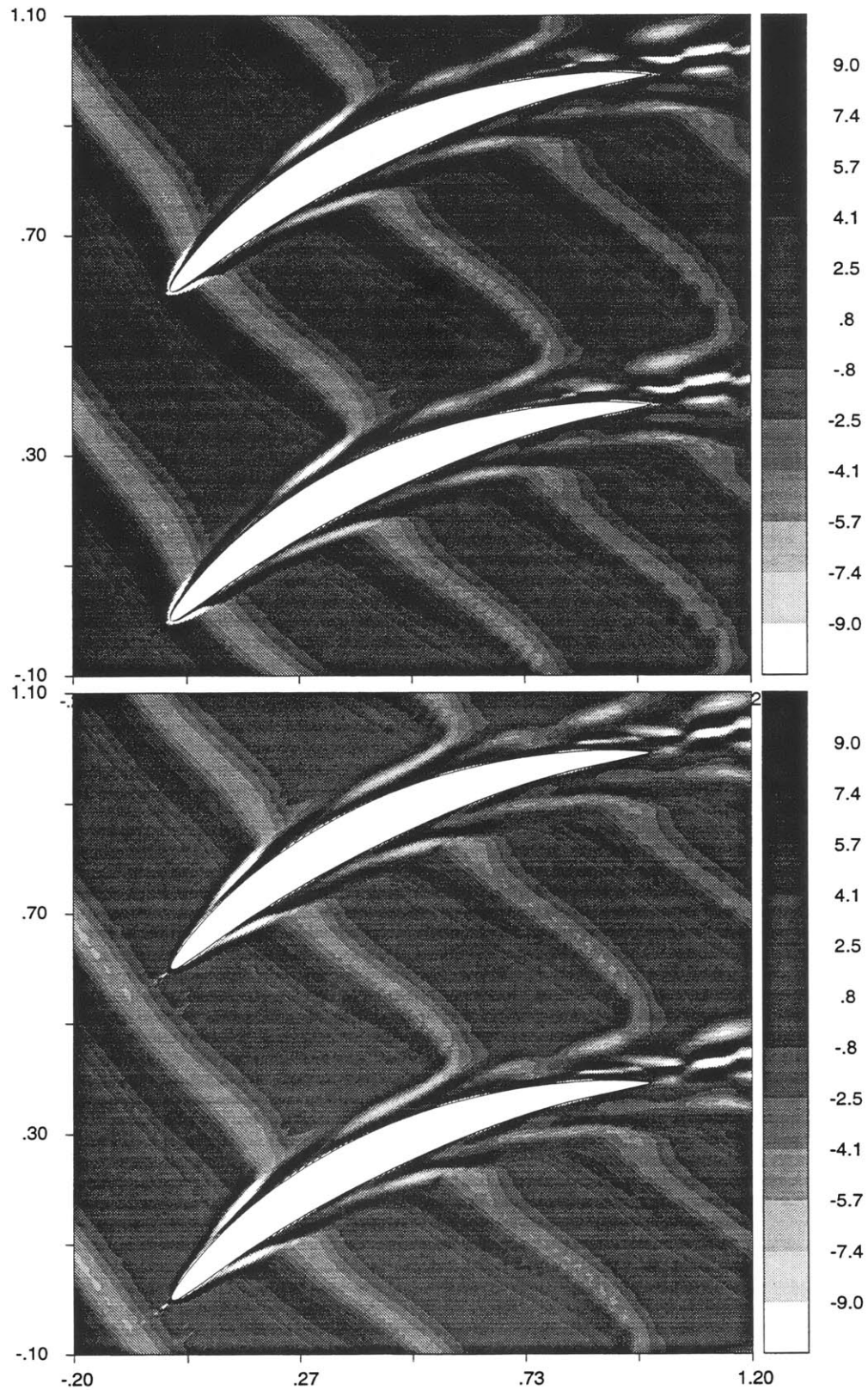
Figure 3.3. Upstream wakes are convected by the core flow while inducing vortical disturbances near the blade surface. Isocontours of disturbance vorticity at the moment of wake interception ($t = t_0$, top) and between interceptions ($t = t_0 + T/2$, bottom). Baseline wakes (25%), two dimensional Navier-Stokes simulation at Re=300,000.
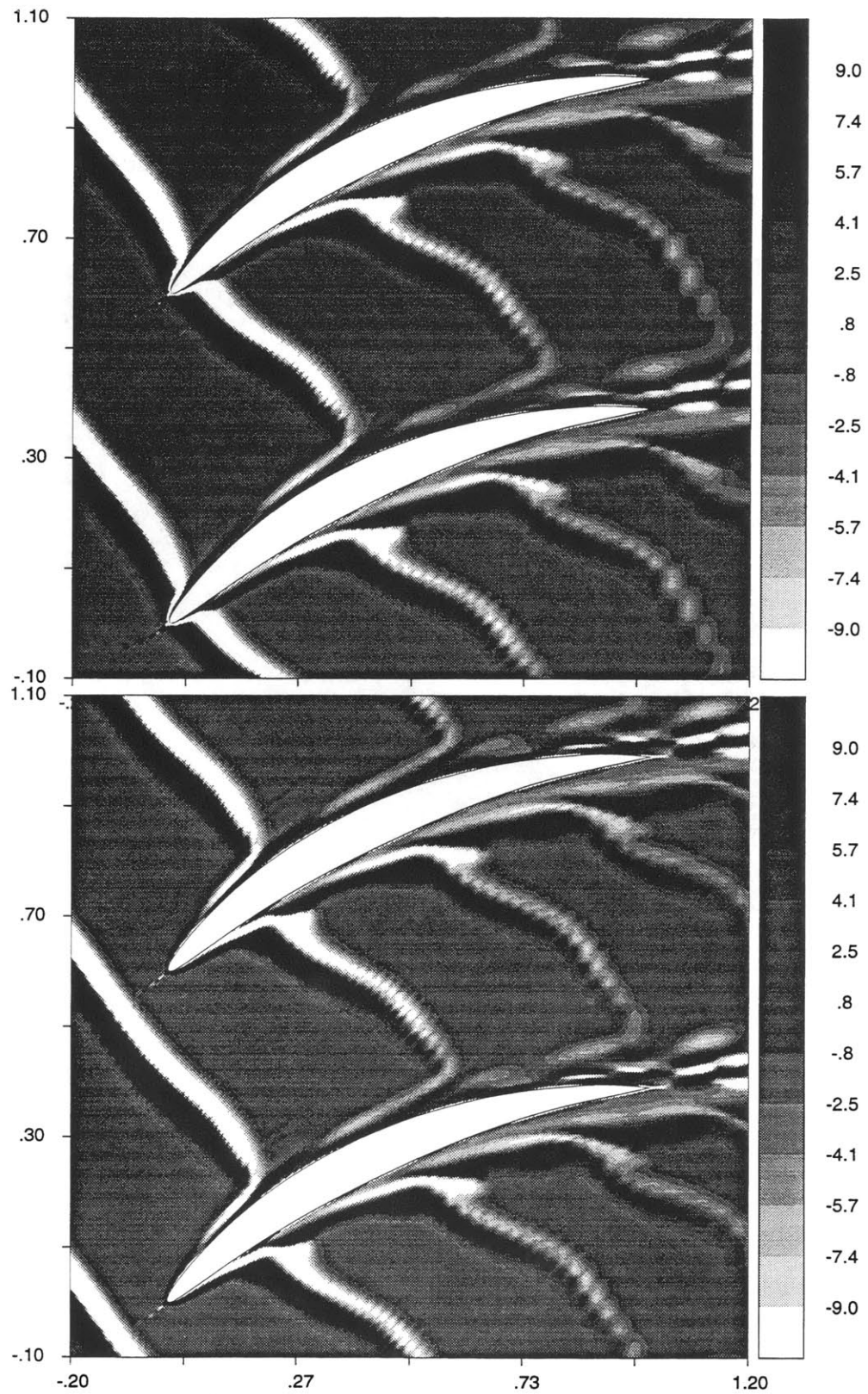
Figure 3.4. Isocontours of disturbance vorticity at the moment of wake interception ($t = t_0$, top) and between interceptions ($t = t_0 + T/2$, bottom). Strong wakes (65%), two dimensional Navier-Stokes simulation at Re=300,000.

The boundary layer disturbances (BLD) seen in wake interaction calculations have a characteristic structure, illustrated in **Figure 3.5**. Each BLD originates on the leading edge at the moment of wake interception. It is composed of two thin regions of high negative and positive shear respectively. These regions are lifted away from the suction surface by the wake jet, and are convected at the edge of the boundary layer.
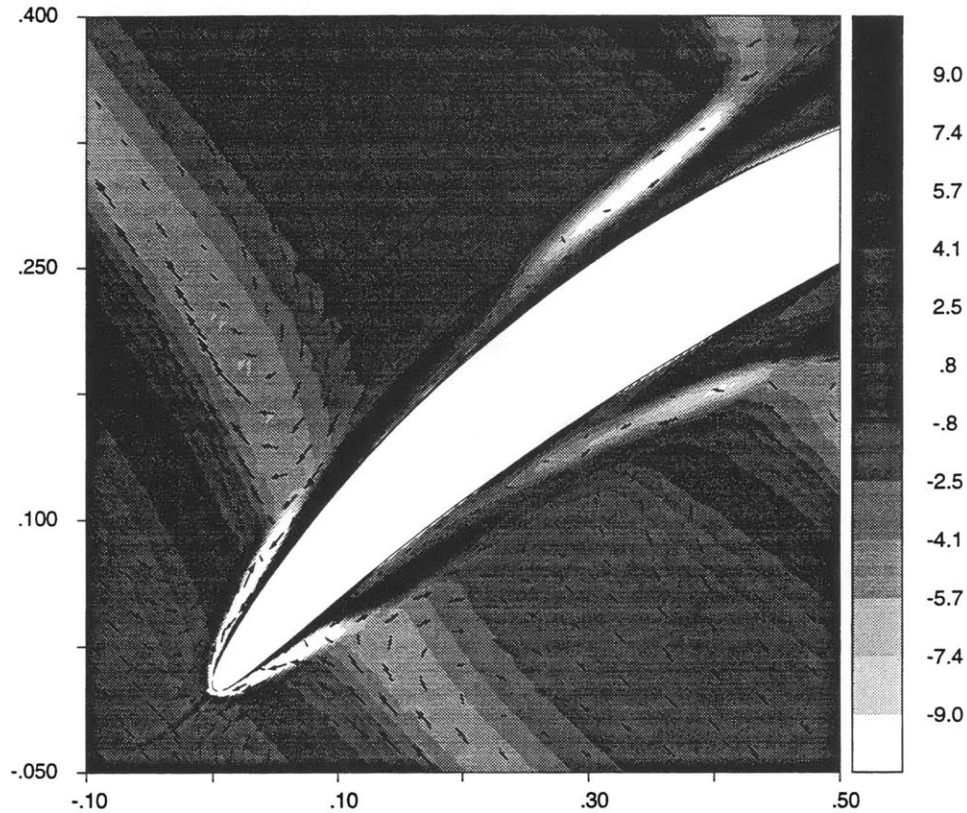
Figure 3.5. Disturbance vorticity isocontours at the leading edge for baseline wakes slightly past interception ($t = t_0 + 0.1T$), showing one incipient and one fully developed BLD (from a previous wake). Vertical scale is exaggerated.

Three computational experiments, where a specific aspect of the unsteady flow dynamics is altered, have been carried out to determine the origin of the BLDs in **Figure 3.5**:

(1) Inviscid base flow + linearized slip-free disturbance equations.
No BLDs are observed (Valkov, 1992).

(2) Viscous base flow + linearized slip-free disturbance equations.
BLDs similar to those above can be observed (Valkov, 1992).

(3) Viscous base flow + non-linear viscous disturbance equations from which the BL distortion term $\mathbf{T}_1$ below has been removed. No BLDs are observed.

$$\mathbf{T}_1 = -(\Delta \mathbf{u} \cdot \nabla)\omega_s \qquad (3.02)$$

These calculations suggest that the vortical disturbances shown in **Figure 3.5** originate from displacement of the boundary layer vortex filaments under the suction effect of the wakes. Calculation (3) provides the strongest support for this conclusion. Calculation (3) is identical in all points to a Navier-Stokes simulation, except that the vortex filaments in the base flow boundary layer are not allowed to move under the effect of the "negative jet" intthe upstream wake. The only mechanisms responsible for disturbance vorticity in such a flow are (a) production and diffusion of vorticity on the blade surface due to fluctuations of the velocity at the surface, and (b) changes in turbulent eddy viscosity due to unsteadiness. As **Figure 3.6** shows, these mechanisms alone do not lead to appreciable boundary layer disturbances (although shear stress fluctuations remain appreciable).
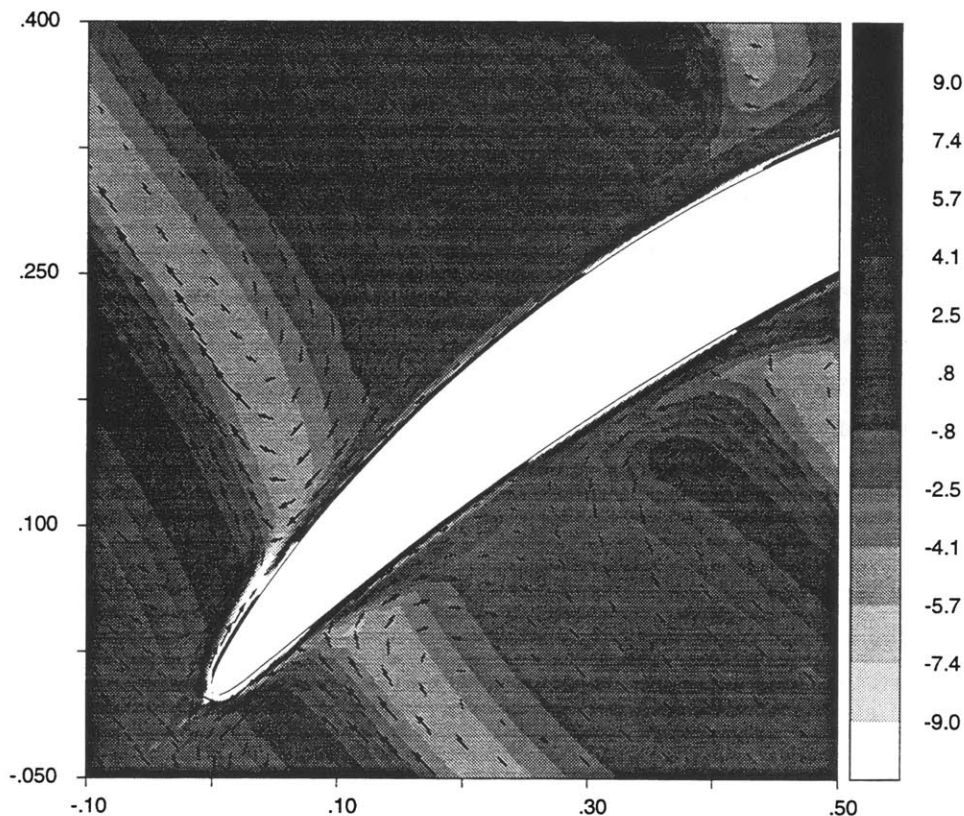
Figure 3.6. Disturbance vorticity isocontours at the leading edge for baseline wakes slightly past interception $(t = t_0 + 0.1T)$ from a disturbance calculation from which the BL distortion term (3.02) has been removed. In comparison to **Figure 3.5**, no significant BLDs are present in this flow.

A simplified model for the distortion of boundary layer vortex filaments is derived in **Appendix J**. The model is based on the premise that the distortion process is an essentially convective process, that occurs on a scale local to the boundary layer, and is governed by the following equation:

$$\frac{\partial \Delta \omega}{\partial t} + \underbrace{U\frac{\partial \Delta \omega}{\partial x} + V\frac{\partial \Delta \omega}{\partial y}}_{\text{transport}} \approx - \underbrace{\Delta v \frac{\partial \Omega}{\partial y}}_{\text{production}} \qquad (3.03)$$

This model embodies a balance between transport of disturbance vorticity $\Delta \omega$, and "production" thereof from convective redistribution of base flow boundary layer fluid under the effect of a transverse velocity disturbance Δv. The model helps explain why (a) BLDs are primarily produced in the boundary layer/bulk flow interface over the foremost part of the blade, and (b) the primary BLDs contain negative disturbance vorticity. A model for the unsteady losses can be derived on the basis of (3.03) and (2.07). As shown in **Figure 3.7**, this model captures the trend in the CFD results.

It is difficult to obtain such a clear illustration of the boundary layer response if the unsteady flow is described in terms of velocity instead of vorticity. For this reason, published compressor flow data cannot be used to provide direct evidence for BLDs. Some indirect evidence can be found in data presented by Wilder et al. (1990). The authors have used time-resolved LDV measurements to infer the vorticity distribution around an airfoil interacting with upstream spanwise vortices. This situation is similar to wake interaction to the extent that the unsteady velocity field has a component normal to the blade. The experimental results show a vortical disturbance in the suction side boundary layer at the moment of vortex interception.

3.2. Constant Wakes: Effects on Performance.

Interaction with constant-strength wakes has two opposite effects on stator loss. First, wakes cause the time-average passage loss to increase by an amount denoted as $\Delta \mathcal{Y}_p$. This increase, shown in **Figure 3.7**, is small for the 25% (baseline-spacing) wakes but becomes noticeable for the 50% (close-spacing) wakes.

On the other hand, mixing the unsteady flow leaving the stator entails less loss than mixing the wakes prior to the stator. The resulting loss benefit, $\Delta \mathcal{Y}_m$, is shown in **Figure 3.8**. It is relatively small for the 25% wakes, but becomes important for the 50% wakes. This benefit is due to a reduction of the non-uniform velocity in the wake. The magnitude of $\Delta \mathcal{Y}_m$ can be captured well by a simplified kinematic model of wake transport and recovery (dashed line in **Figure 3.8**), derived in §J.2.
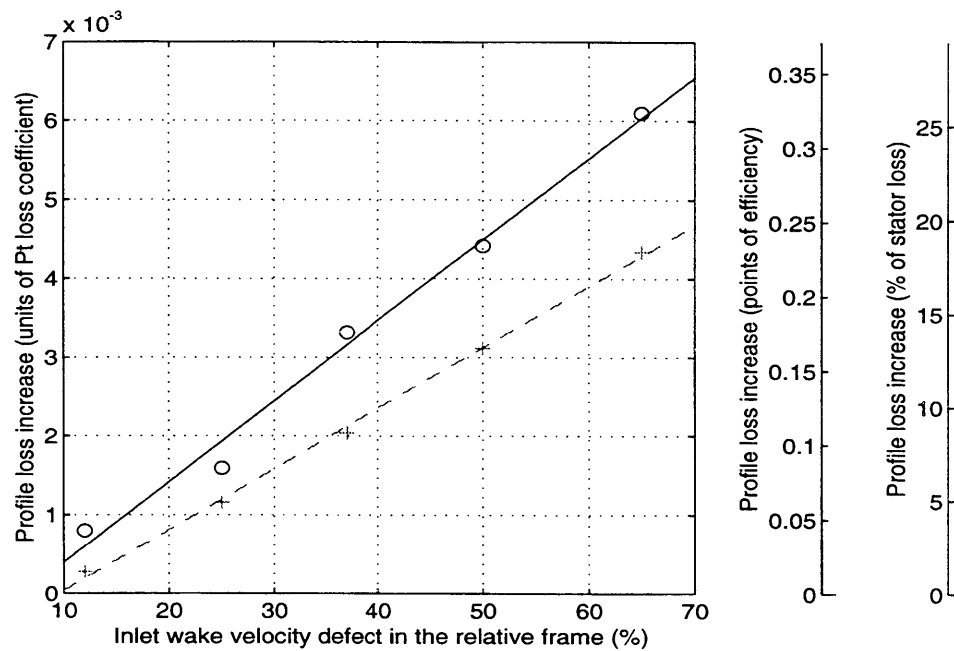
Figure 3.7. Increase in time-averaged stator passage loss $\Delta\mathcal{Y}_p$ for various states of a baseline rotor wake ($\phi = 0.45, \psi = 0.65, Re_s = 3 \times 10^5$). Circles+solid line: Navier-Stokes simulations+linear regression. Crosses+dash line: boundary layer distortion model+linear regression.
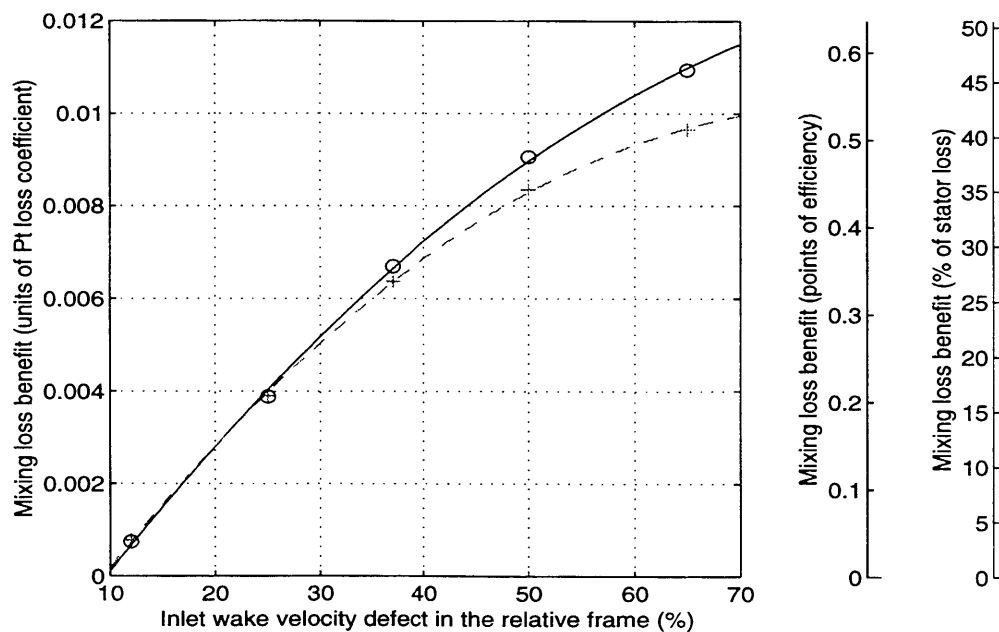
Figure 3.8. Mixing loss benefit from wake processing $\Delta\mathcal{Y}_m$ for various states of a baseline rotor wake ($\phi = 0.45, \psi = 0.65, Re_s = 3 \times 10^5$). Circles+solid line: Navier-Stokes simulations+quadratic regression. Crosses+dash line: Transport model+quadratic regression.

In the range of wake defects surveyed, the benefit from wake recovery $\Delta \mathcal{Y}_m$ outweighs the passage loss increase $\Delta \mathcal{Y}_p$. Consequently, the net effect of wakes on loss, $\mathcal{Y}_n = \mathcal{Y}_p + \mathcal{Y}_m$, is beneficial. The net benefit depends on the degree to which the wake is mixed out, as shown in **Figure 3.9**. Three observations can be made from this figure.

- The 25% baseline wake has a negligible net effect on loss ($\sim$ 0.1 efficiency points). This wake is representative of interaction at design point axial spacing (0.37 chords) for the selected geometry. A steady-state approximation of rotor-stator interaction, where the wakes are mixed prior to entering the stator, is adequate in this case.

- For 50-60% wakes (axial spacing of 0.07 chords), wake interaction has a noticeable net effect on stator loss ($\sim$ 0.3 efficiency points). This value represents only a fraction of the one efficiency point gain observed by Smith (1970) for a similar reduction in blade row separation, and confirms recent estimates of the effect of wakes (Smith, 1996).

- If the increase in passage loss can be mitigated somehow, only the mixing loss benefit shown in **Figure 3.8** would remain (0.2 pts efficiency gain at baseline spacing, 0.5 pts efficiency at close spacing).
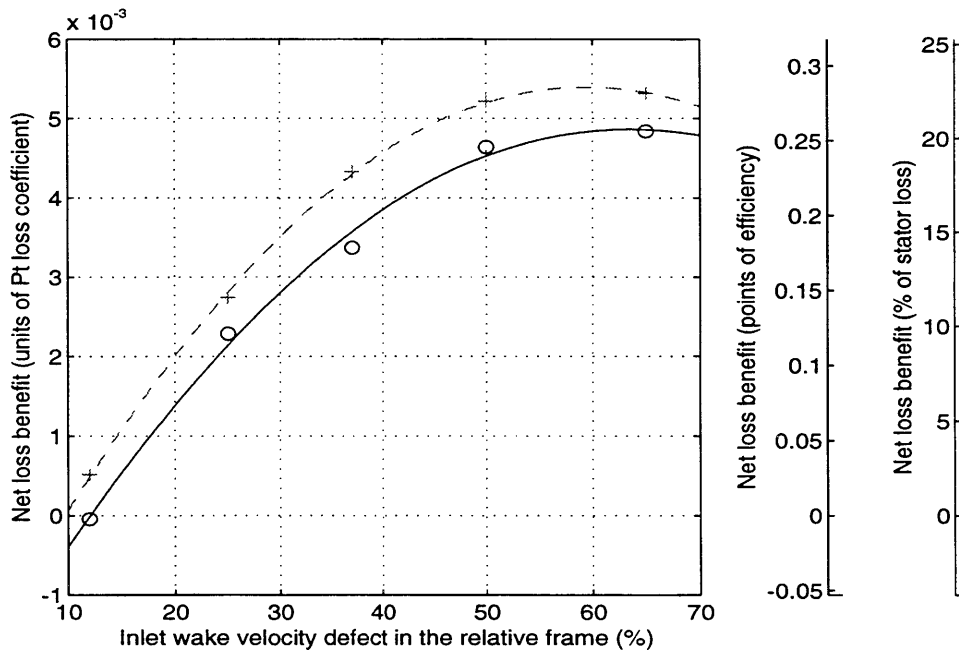
Figure 3.9. Net effect of wake processing $(\Delta \mathcal{Y}_p + \Delta \mathcal{Y}_m)$ for various states of a baseline rotor wake ($\phi = 0.45, \psi = 0.65, Re_s = 2.510^5$). Circles+solid line: Navier-Stokes simulations+quadratic regression. Crosses+dash line: Models (§J.2-J.3)+quadratic regression.

3.3. Causal Mechanisms for the Changes in Performance.

3.3.1. Reversible recovery.

Figure 3.10 shows instantaneous velocity profiles in the blade-to-blade direction on the leading and trailing edge planes respectively. It is apparent that the wakes are strongly attenuated during their transport through the stator in terms of velocity and thickness. This is the principal cause for the mixing loss benefit $\Delta \mathcal{Y}_m$.
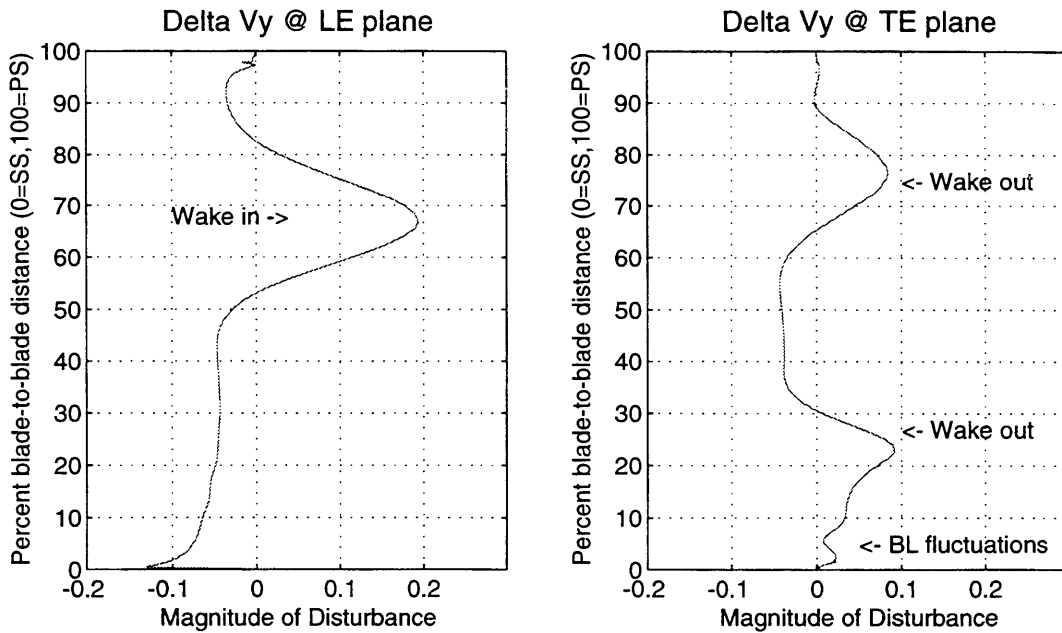
Figure 3.10. Instantaneous tangential velocity distribution on a crossflow "plane" at the leading (left) and trailing (right) edges. The presence of two wakes at the exit is an artifact from wake turning. Baseline 25% wakes.

In principle, wake attenuation is the result of two processes: reversible recovery (Smith 1966) and irreversible mixing. Only the first process is beneficial. What fraction of the wake energy is recovered has been so far an open question. Our results indicate that virtually all of the wake energy is recovered. This finding can be explained by noting that recovery generally occurs over a shorter lengthscale than wake turbulent diffusion.

Recovery lengthscales. A simplified kinematic model of reversible recovery has been developed in **Appendix J** to determine recovery lengthscales. The model assumes inviscid flow and embodies the mechanism proposed by Smith (1966). The exact expression for mixing loss benefit is rather lengthy, but it can be approximated in the following manner:

$$\Delta \mathcal{Y}_m \approx \left(1 - a_r^2\right) \Delta \mathcal{Y}_i \qquad (3.04)$$

where $\Delta \mathcal{Y}_i$ is the mixing loss of the wake at the inlet, and a_r is an attenuation factor (given by the stretching of the wake segments L_i/L_e). This model is in accordance with recent work by Adamczyk (1994), and captures well the computed mixing loss benefit (**Figure 3.8**).

Algebraically, the attenuation a_r is a function of the flow angles, wake ingestion angle and solidity (§(J.2.3)). Physically, a_r is mainly a function of the flow turning in the passage. This is shown in **Figure 3.11**. This figure indicates that, for a typical stator, most of the wake energy is recovered over a distance of 0.25 to 0.33 chords. For instance, in the present stator the flow turns by 10 degrees over the first 0.2 chords. According to **Figure 3.11**, about one-half of the wake energy is recovered in this distance.
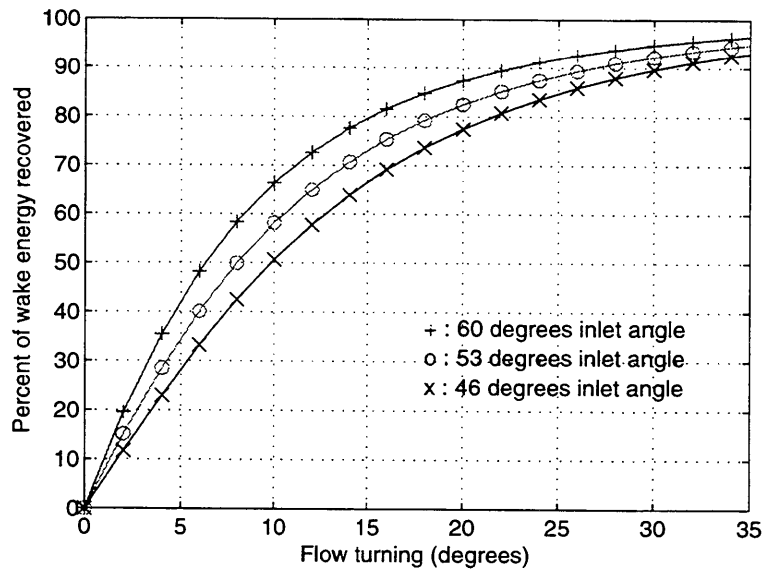
Figure 3.11. The fraction of wake energy $\Delta \mathcal{Y}_m/\mathcal{Y}_{2,i}$ recovered in inviscid flow is mainly a function of the flow turning in the stator. Flow turning is representative of the axial distance traveled by the flow. Most of the wake energy is recovered in the front part of the stator. For this figure, the wake is kept perpendicular to the blade $(\gamma_i = \theta_i)$.

Diffusion lengthscales. The distance required to dissipate the wake energy by means of turbulent diffusion alone, depends primarily on the velocity defect in the wake. For wakes in the asymptotic stage (Abramovich 1965, Schlichting 1968), this distance may be several times the blade chord. For wakes at a typical distance behind the rotor (e.g. 25% baseline wake), this distance appears to be of the order of the blade chord (based on Carta et al. 1991 data). In this case, most of the wake energy is recovered over a shorter distance in the front part of the stator, and turbulent diffusion is not an important loss mechanism. This is indicated by the good agreement between the inviscid recovery model and the Navier-Stokes results in **Figure 3.8** for wake defects of 35% and less.

Even for strong wakes, the inviscid model predicts a recovery benefit that is fairly close to the Navier-Stokes results. For such wakes, energy diffusion lengthscales may be initially as short as those associated with reversible recovery. However, mixing scales are very sensitive to the wake defect, while recovery scales are not. Reversible recovery attenuates the wake defect quite rapidly, and thus outcompetes turbulent diffusion for the energy in the wake.

For this reason, wake diffusion is not a significant loss mechanism over the range of wake defects considered (12-65%). Most of the wake energy is recovered without a significant increase in entropy. As shown below, boundary layer response is the leading cause for the observed passage loss increase.

3.3.2. Boundary layer response.

Regions of increased passage loss can be identified by examining the time-averaged total pressure difference $(\overline{\Delta C_t})$ in **Figure 3.12**. This quantity is practically equivalent to the time and mass-averaged total pressure flux $(\overline{\Delta u C_t})$ used to compute loss. **Figure 3.12** shows two features. First, two regions of high and low $\overline{\Delta C_t}$ respectively develop in the aft part of the passage. Second, there is a thin band of significant low-$\overline{\Delta C_t}$ over the suction surface. This band coincides with the trajectory of the BLDs described in §**3.2**.
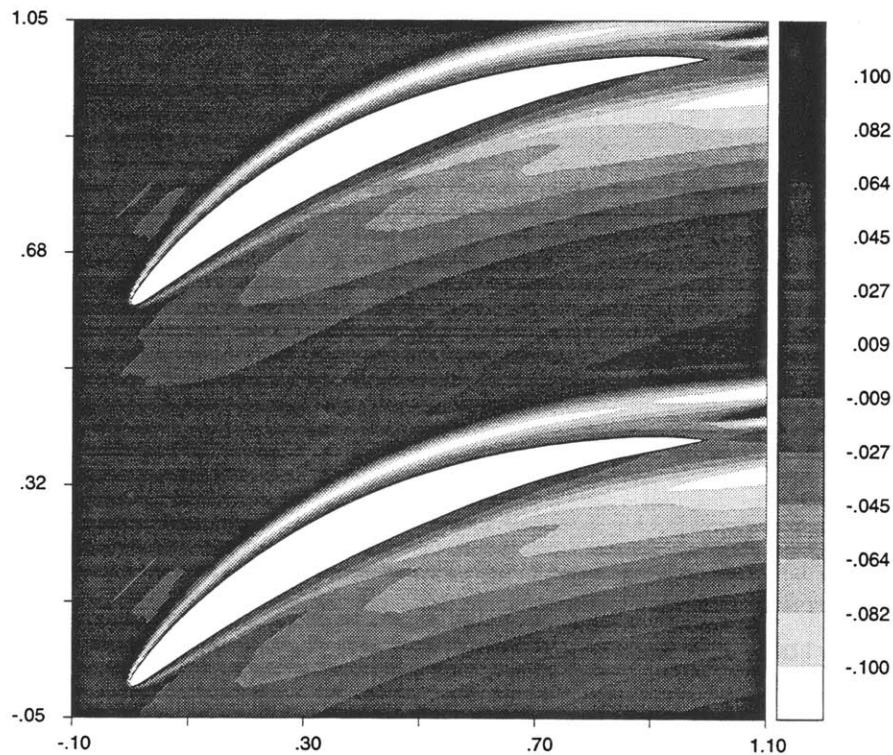
Figure 3.12. Isocontours of time-averaged total pressure difference $\overline{\Delta C_t}$ between unsteady and reference steady flows. Note high-loss band over the suction surface of the stator. Baseline 25% wakes.

Figure 3.13 shows that these total pressure changes are due to the redistribution of passage vorticity on a time-averaged basis, denoted symbolically by $\overline{\Delta\omega_z}$. The connection between $\overline{\Delta C_t}$ and vorticity redistribution is embodied by the following form of the Navier-Stokes equations, derived in §I.7:

$$\frac{\partial \overline{\Delta C_t}}{\partial n} \approx -2U_s\overline{\Delta\omega} \qquad (3.08)$$

Figure 3.13 also shows that the largest passage loss changes occur over the suction surface of the stator. It was established in §3.1, that the vorticity fluctuations in this region are due to the distortion of the boundary layer vortical filaments by the "jet" velocity associated with the upstream wakes.
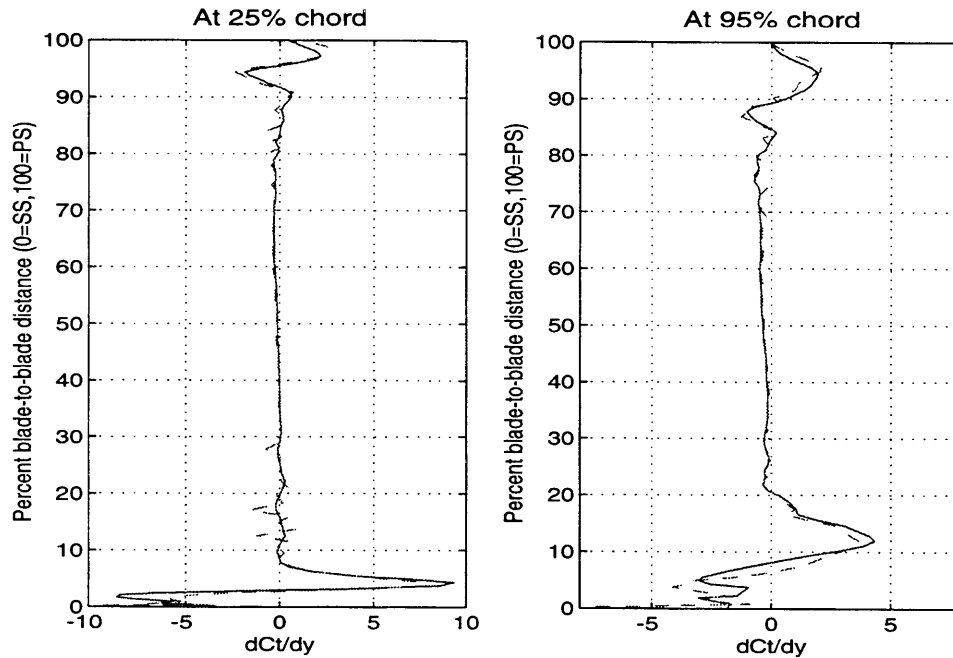
Figure 3.13. Comparison between $\frac{\partial \overline{\Delta C_t}}{\partial n}$ (solid line) and $-2U_s\overline{\Delta\omega}$ (dashed line) from the Navier-Stokes results at two different axial locations. Total pressure changes are due to redistribution of vorticity. Baseline 25% wakes.

In physical terms, the "suction" effect of the wake "jet" transports high-entropy boundary layer fluid from near the wall towards regions of higher mass flux. Mass-averaged entropy flux thus increases, and so do the time-averaged passage losses. This process is essentially convective in nature. Its effect on loss can be captured by a relatively simple model, based on vorticity dynamics, and derived in §J.3:

$$\Delta \mathcal{Y}_p \approx \frac{6}{U} \int_{LE}^{TE} x\overline{\Delta v}\frac{d\mathcal{Y}_{p,s}}{dx}dx \approx \frac{2\Delta V_n}{\cos\theta_1}\mathcal{Y}_{p,s} \qquad (3.09)$$

This model states that the time-average increase in passage loss under the effect of a "jet" disturbance is depends on the base flow passage loss $\mathcal{Y}_{p,s}$, and is proportional to the time-average transverse velocity disturbance ΔV_n at the edge of the boundary layer. The latter is roughly proportional to the wake displacement thickness at the inlet of the stator and to the wake reduced frequency. As **Figure 3.7** shows, the model compares reasonably well with the Navier-Stokes simulations and captures the linear trend in the CFD results. This model, along with the mechanistic understanding of passage loss increase, shall prove useful in describing the effects of tip leakage vortices later on.

3.3.3. Performance of the stator as a diffuser.

The ability of the stator to convert kinetic energy to static pressure is measured by the pressure coefficient Π derived in §2.3. Upstream wakes cause this coefficient to increase by an amount $\Delta\Pi_n$, shown in **Figure 3.14**. The increase is modest, and is due principally an augmentation of the loading on the leading edge. This augmentation, shown in **Figure 3.15**, is a time-averaged effect of the pressure pulses on the leading edge described at the beginning of the chapter.
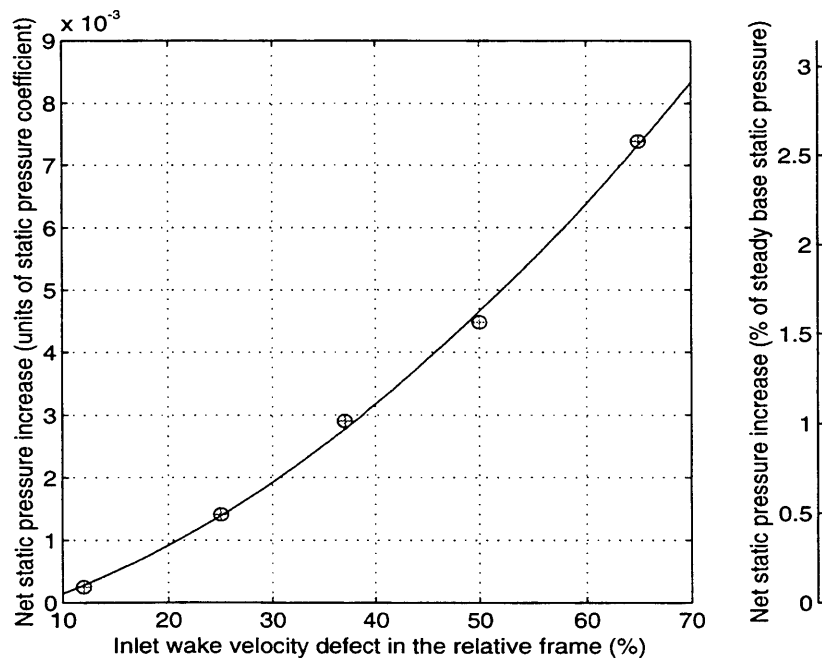
Figure 3.14. Increase in stator pressure coefficient relative to pre-mixed steady flow assumption. ($\phi = 0.45, \psi = 0.65, Re_s = 3 \times 10^5$).
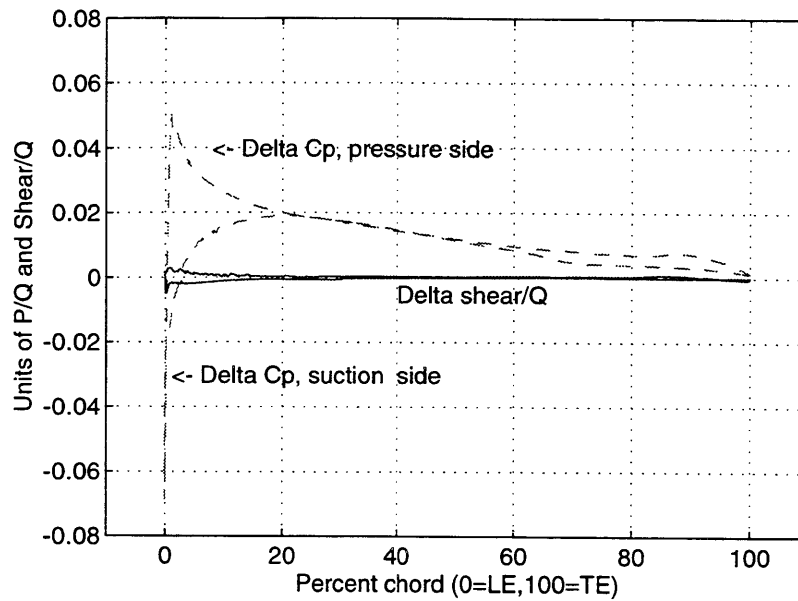
Figure 3.15. Time-average blade surface distribution of static pressure change relative to pre-mixed flow ($\Delta \overline{C_p}$, dash line) and shear stress change ($\nu \Delta \omega \times n$, solid line). Baseline wakes.

3.4. Effect of Fluctuations Within the Wakes.

So far, the wake properties were held constant in time. This is equivalent to "ensemble-averaging" the wakes prior to interaction with the stator. Experimental data shows however the presence of velocity fluctuations within compressor wakes. These fluctuations may be a substantial fraction of the wake velocity defect, and occur at a scale comparable to the wake thickness (Waitz 1996, Brookfield 1996). It is thought they are due to discrete vortical structures in the wake (Gertz 1988,Kotidis and Epstein 1991).

A second series of computational experiments addresses the role of such fluctuations on rotor-stator interaction. Two specific questions are addressed: (1) are the two mechanisms identified of §**3.2** still valid in the presence of a time-varying wake velocity defect; and (2) what is the effect on performance relative to the "ensemble-averaged" case?

The wakes used for this purpose share the same "ensemble-averaged" profile and properties (33% wake relative defect, 0.15 chords thickness at mid-gap, axial gap of 0.2 chords). For each wake, the defect is sinusoidally varied in time with an amplitude equal to the "ensemble-averaged" value, and with an a time period T_i ranging between 1/7 and 2.0 times the blade passing period T_p. The choice of amplitude is representative of fluctuations seen near the rotor trailing edge (Brookfield 1996). The ratio T_i/T_p takes fractional values ensuring that a fixed point on the blade does not experience the same disturbance at every interaction.

Small T_i/T_p ratios (1/7-3/7) constitute a simplified representation of measured wake fluctuations (Kotidis and Epstein 1991, Brookfield 1996). Large ratios (4/3-2) are meant to be representative of fluctuations in the tip vortex seen by Graf (1996).

3.4.1. Unsteady flow features.

Figures 3.16a-d illustrate the vortical structure of the unsteady flowfield for T_i/T_p (wake fluctuation timescale/interaction timescale) increasing from 1/5 to 2. This parameter influences the dynamics of the wake during its transport through the stator. Three regimes can be distinguished : low-frequency $(T_i/T_p \geq 1.3)$ intermediate-frequency $(1/5 \leq T_i/T_p \leq 1.3)$ and high frequency $(T_i/T_p \leq 1/5)$ fluctuations.

For high-frequency fluctuations, the individual vortices comprising the wake appear to coalesce into a steady wake, that is transported through the stator much in the same way as described above (**Figure 3.16a**). For low-frequency fluctuations, the lengthscale over which wake properties vary is larger than the blade-to-blade spacing, and the individual wake segments are also transported as described above (**Figure 3.16d**). For intermediate frequencies however, the wake fluid forms passage vortices that persist far downstream (**Figures 3.16b,c**). Boundary layer disturbances (BLDs), similar to those seen with ensemble-averaged wakes, are present over the suction surface for all frequencies.

3.4.2. Effect of wake fluctuations on loss.

Figure 3.17 shows the net loss change for the stator in the presence of fluctuating wakes, and compares it to that obtained for an ensemble-averaged wake. It is apparent that the timescale ratio parameter T_i/T_p has an important effect on the amount of benefit to be expected from wake interaction.

In the low-frequency regime $(T_i/T_p \geq 1.3)$, fluctuating and ensemble-averaged wakes have basically the same impact on loss. This is because the lengthscale over which wake properties vary is larger than the local scales over which the mechanisms identified in §3.3 operate.

In the high-frequency regime $(T_i/T_p \geq 1.3)$, fluctuating and ensemble-averaged wakes also have similar effects on loss, although the latter produce somewhat higher benefit. This is due to the coalescence of small vortices seen in **Figure 3.16a**, which effectively smooths out variations along the wake. However, there is some loss associated with the coalescence, which slightly reduces the benefit from interaction.
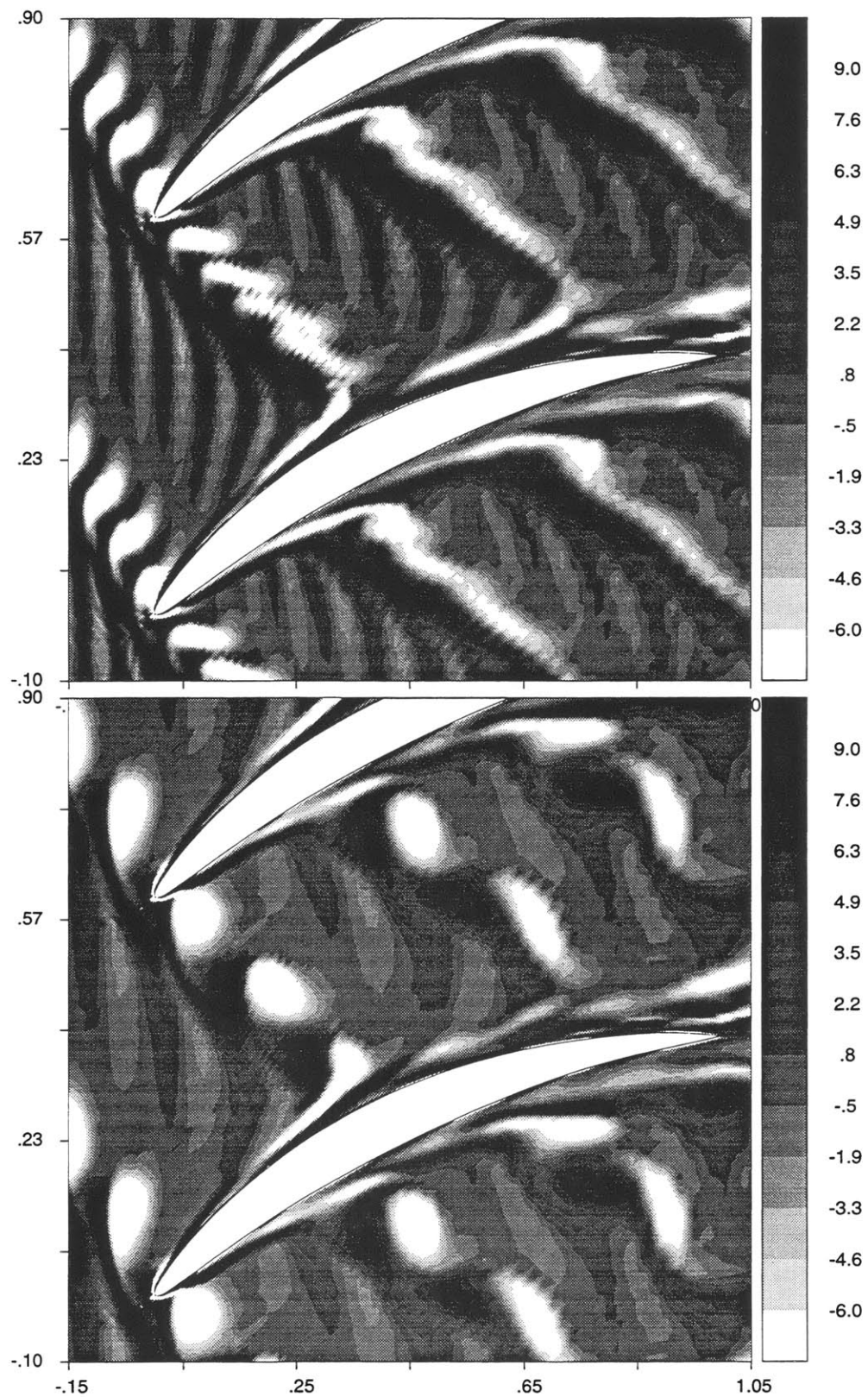
Figure 3.16a(top)/3.16b(bottom). Instantaneous contours of disturbance vorticity in a calculation with time-varying wake defect. Top: $T_i/T_p=1/5$. Bottom: $T_i/T_p=2/5$.
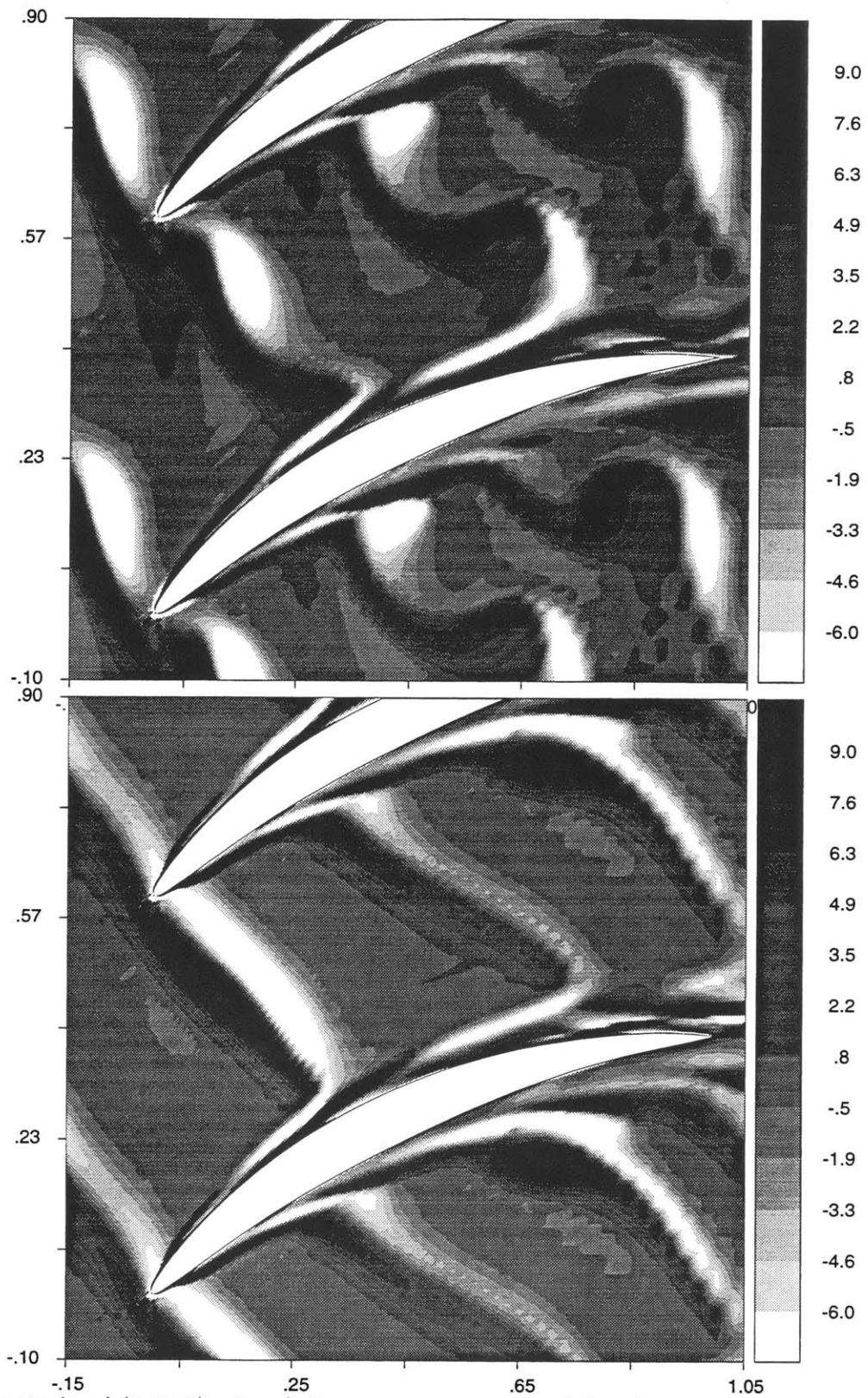
Figure 3.16c(top)/3.16d(bottom). Instantaneous contours of disturbance vorticity in a calculation with time-varying wake defect. Top: $T_i/T_p=3/4$. Bottom: $T_i/T_p=2.0$.
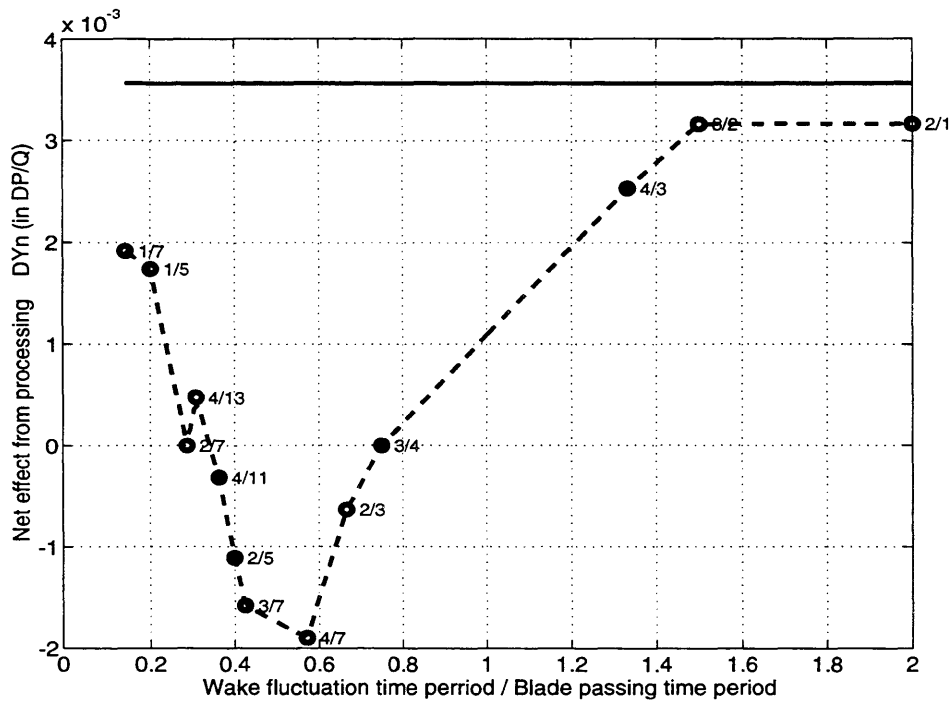
Figure 3.17. Net loss effect $\Delta \mathcal{Y}_n$ from wake interaction for various values of the timescale ratio parameter T_i/T_p shown next to data points. Circles+dashed line: fluctuating wake calculations. Wakes have constant "ensemble-averaged" properties ($A_r=0.33, t=0.15$). Solid line: level of $\Delta \mathcal{Y}_n$ for interaction with a steady wake ($\phi = 0.45, \psi = 0.65, Re_s = 3 \times 10^5$).
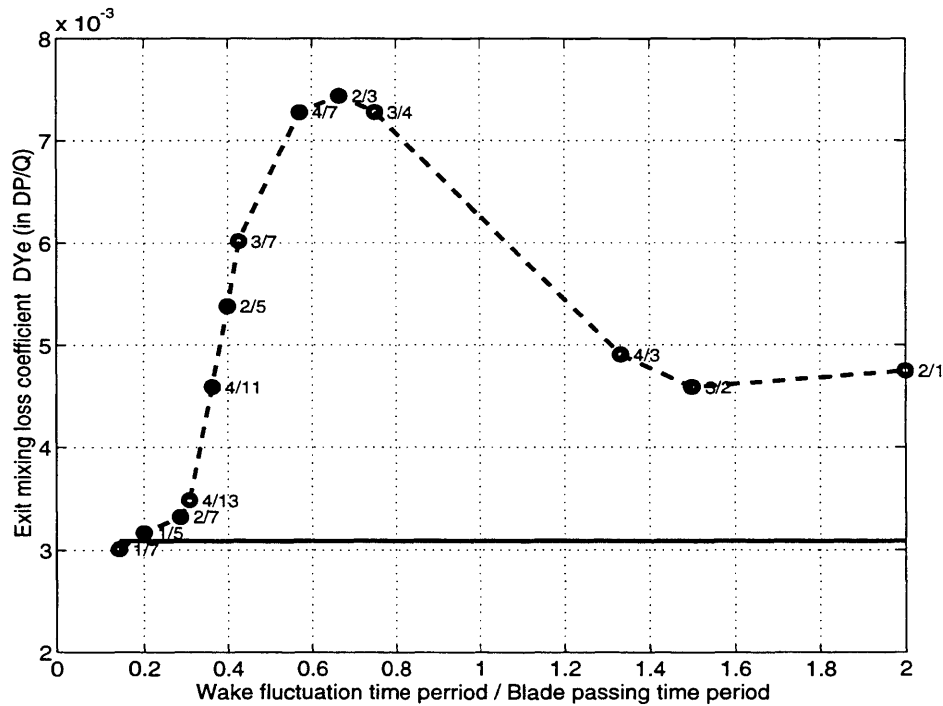
Figure 3.18. Exit mixing loss associated with unsteadiness $\Delta \mathcal{Y}_e$ for various values of the timescale ratio parameter T_i/T_p. Circles+dashed line: fluctuating wake calculations. Solid line: level of $\Delta \mathcal{Y}_n$ for interaction with a steady wake. Wake recovery is not present in the intermediate-frequency range ($1/5 \leq T_i/T_p \leq 1.3$).

In the intermediate-frequency regime ($1/5 \leq T_i/T_p \leq 1.3$), fluctuating wakes have a different effect from that of ensemble-averaged wakes. In this regime, wake interaction is detrimental for stator performance albeit by a small amount. This is due to the formation of passage vortices (**Figures 3.16b,c**), which prevent recovery of the wake energy. As **Figure 3.18** shows, in this frequency range, the wakes leave the stator while retaining a substantial part of their kinetic energy.

3.4.3. Static pressure fluctuations.

Static pressure fluctuations associated with wake interaction are important in engine noise. The present simulations indicate that ensemble-averaged and fluctuating wakes result in different patterns of static pressure fluctuations. The differences can be appreciated by comparing **Figure 3.19a** (steady-defect wakes) to **Figure 3.19b** (fluctuating-defect wakes with the same ensemble-average).

The first difference is associated with the break-up of the wakes into discrete vortices, discussed above. Every vortex core carries a region of low static pressure. Such low static pressure regions are present throughout the stator passage in **Figure 3.19b**.

The second difference appears to be associated with the timing of velocity fluctuations on the blade surface. As shown in **Figure 3.19a**, steady-defect wakes result in a regular train of static pressure fluctuations along the blade surface. These fluctuations have a precise and relatively simple periodicity (Valkov, 1992). On the other hand, fluctuating-defect wakes for which T_p is not an integer multiple of T_i, are associated with increased irregularity of the blade surface static pressure disturbances.
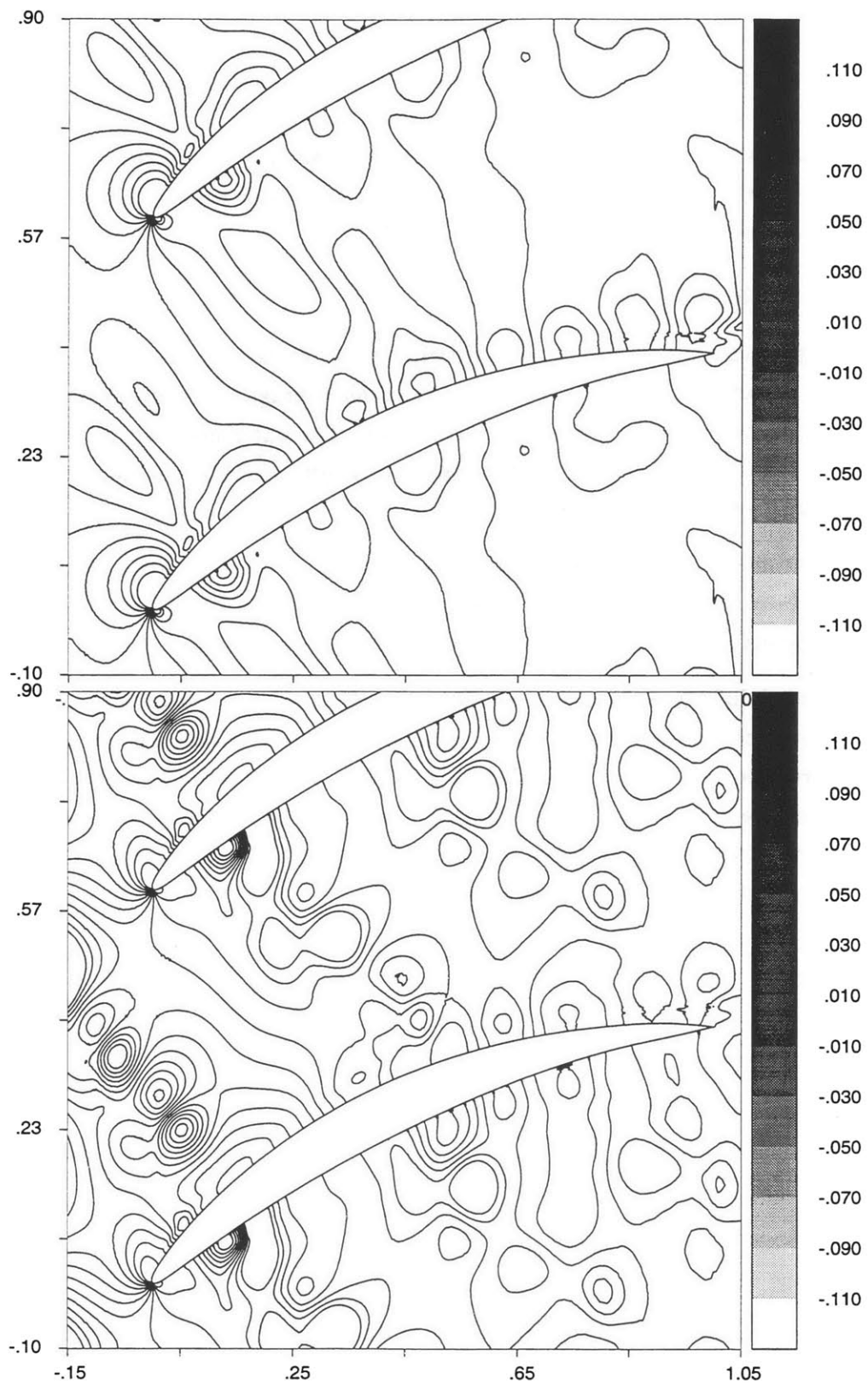
Figure 3.19a(top)/3.19b(bottom). Instantaneous contours of disturbance static pressure. <u>Top:</u> Velocity defect steady in time. <u>Bottom:</u> Fluctuating velocity defect, $T_i/T_p=2/5$.

3.5. Summary.

The foregoing computational experiments addressed three issues that had been previously unresolved with regard to wake-stator interaction: (1) the role of non-transitional boundary layer response for loss, (2) the importance of wake recovery in the presence of mixing, and (3) the effect of wake fluctuations.

- There are two opposing mechanisms by which ensemble-averaged wakes influence performance : reversible recovery and boundary layer distortion. In a stage geometry such as the GE/LSRC, the benefit from reversible recovery is relatively small at typical axial spacings ($\sim$0.1-0.2 efficiency pts, 25% wakes), but becomes significant with tightly-coupled blade rows ($\sim$0.5 efficiency pts, 50% wakes). The recovery occurs in the manner proposed by Smith (1966). Almost all of the kinetic energy of the ensemble-averaged wakes is recovered.

- Boundary layer distortion leads to an increase in passage loss that partly reduces the benefit from reversible recovery. In the LSRC geometry, this loss increase is relatively small at typical axial spacings ($\sim$0.1 efficiency pts, 25% wakes), but becomes non-negligible with tightly-coupled blade rows ($\sim$0.25 pts, 50% wakes). The loss increase is due to "lifting" of high-loss boundary layer vortical fluid into regions of higher mass flow by the "suction" effect of the wakes. A kinematic model of boundary layer vortical filament displacement can capture reasonably well the amount of increase, and shows that it is depends on the steady loss and on the wake displacement thickness.

- For the present stator, the recovery benefit is larger than the passage loss increase. As a result, there is a small net benefit from wake interaction at typical axial spacings ($\sim$0.1 efficiency pts, 25% wakes), and a moderate benefit with tightly-coupled blade rows ($\sim$0.3 pts, 50% wakes). Mixing-plane steady-state approximations to wake interaction are thus adequate (at least for the LSRC geometry employed). Only about 0.25 points of the 1 point efficiency gain observed by Smith (1970) in the LSRC can be attributed to rotor wake-stator interaction alone.

- The level of benefit from wake recovery depends on the frequency of fluctuations in the wake, expressed as a timescale ratio T_i/T_p between fluctuation period T_i and blade passing period T_p. There is an interval of T_i/T_p where the wake forms discrete vortices and no recovery occurs. Outside this interval, wake interaction is beneficial and can be captured using an ensemble-averaged form of the wakes. Experimentally observed values of T_i/T_p appear to be between 1/8 and 1/3. This range partly overlaps with the interval where recovery does not occur.

Representativeness. Two external factors affect the degree to which the above results can be considered indicative of wake interaction in an actual stage. The first is the use of a turbulence model. In this regard, the flow mechanisms having a practical impact on stator performance (boundary layer distortion and reversible wake attenuation) are convection or

pressure-driven. Turbulent viscosity does not appear to play a substantial role in these mechanisms.

The second factor is the assumption of two-dimensional flow. In practice, wakes may contain a spanwise velocity component (Prato and Lakshminarayana, 1993). The wake fluid migrates radially (Kotidis and Epstein, 1991). Blade geometry and flow conditions may be such that wake interception by the stator occurs at different times depending on spanwise location. However, the mechanisms identified here occur on a local basis, and are thus unlikely to be radically different in a three-dimensional situation. This is supported by direct 3D Navier-Stokes simulations of wake-stator interaction at low Reynolds number (2000).

In these computations, the unsteady flow over the middle two-thirds of the span is fundamentally similar to that in the 2D case. In the outer 15-20% of span though, the wakes distort and develop a core of streamwise vorticity. This can be attributed to differential convection of wake fluid within the endwall boundary layer, which tilts the wake vortex filaments away from the spanwise direction. Upstream tip leakage vortices are however the dominant forms of disturbance in this part of the span (e.g. Wisler, 1985). The three-dimensional unsteady flows associated with these vortices are the subject of the next three chapters.

Chapter 4

Inviscid 3D Vortex/Stator Interaction

This chapter examines the unsteady flow and performance changes arising from the interaction between upstream vortices and a stator cascade with an inviscid base flow at design point flow coefficient. Two calculations, each using a different vortex, are carried out

- **ID/SW.** Interaction with an upstream streamwise vortex (SW) with a core radius of 15 percent span and a circulation of $0.5cU_\infty$. The results are described in the first half of this chapter (§**4.1-4.2**).

- **ID/TL.** Interaction with a tip leakage (TL) vortex, based on Khalid's (1995) computed flowfield at the exit of an isolated LSRC rotor at design loading and 3% tip clearance. The results are described in the second half of the chapter (§**4.3-4.4**).

Denton (1993) pointed out that the transport of streamwise vortices through a cascade has a deleterious effect on performance. The primary purpose of the present calculations is to determine whether this applies to rotor tip leakage vortices as well.

The unsteady flows are obtained by means of a slip-free disturbance formulation about an inviscid stator base flow (cf. §**F.4**). The turbulent diffusion term has been retained in the disturbance flow (F.09). In this manner, the vortices are allowed to mix out while interacting in a setting that is free of boundary layers. This approach (1) allows to determine how much of the tip vortex energy is recovered in the presence of mixing; and (2) provides a basis against which subsequent viscous results can be compared to reveal the effects of boundary layer response.

4.1. Case ID/SW: Features of the Unsteady Flow.

4.1.1. Transport of the vortex core.

As shown in **Figure 4.1**, the SW vortex core is transported across the stator without significant change in shape. The vortex core is stretched by an amount $(L_e/L_i = 1.7)$ consistent with the kinematic transport model originally developed for 2D wakes (§**J.2**). According to §**J.4.1**, the vorticity in the core should be intensified in proportion to this stretching. **Figures 4.2** and 4.3 show however that the peak core vorticity at the TE plane is less than that at the inlet (by about 15%). This suggests that turbulent diffusion exerts a noticeable effect during the transport of the SW vortex.
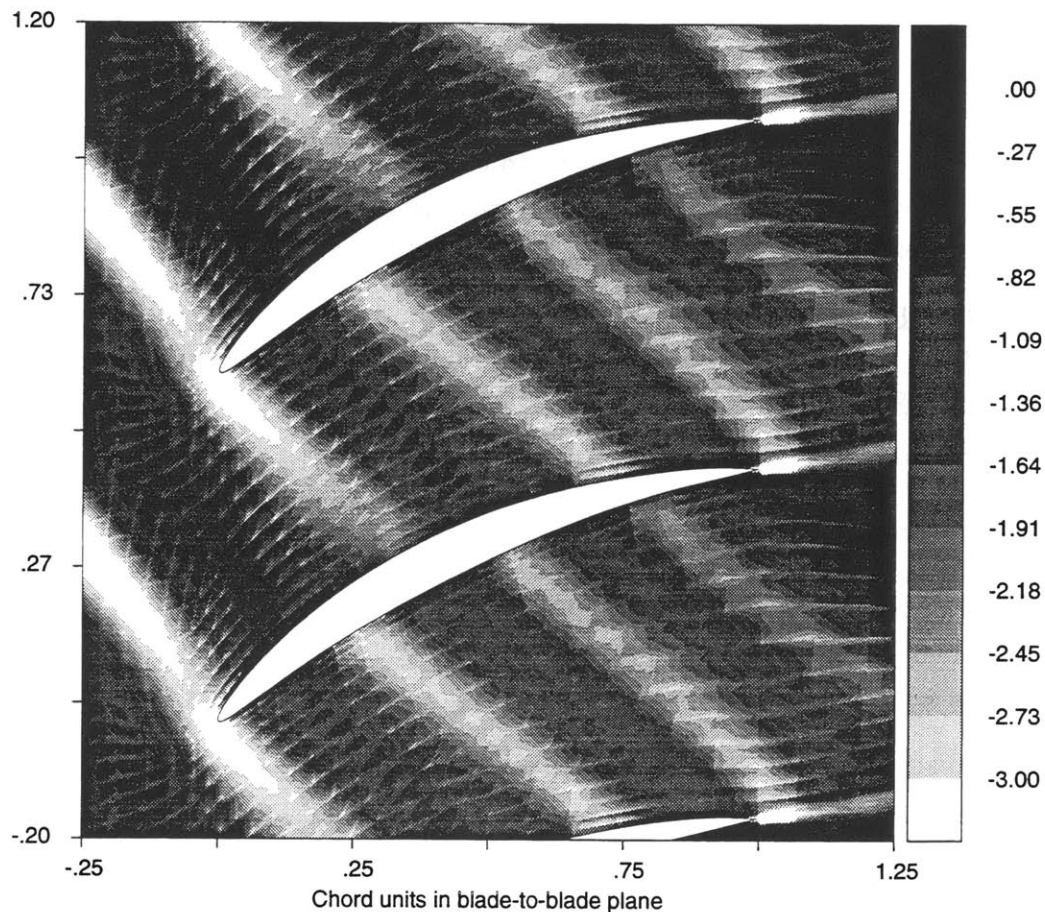
Figure 4.1. Location of vortical fluid in the stator passage at the moment of vortex interception. Perspective view of the entire stator passage in the spanwise direction towards the hub. The SW vortex cores are visible as regions of negative $-|\Delta\omega|$.

Figures 4.2 and **4.3** show the vorticity components at successive cross-sections of the vortex. At the inlet of the stator, the SW vortex core contains virtually no streamwise

vorticity. This can be explained by the relative orientation between the rotor relative and stator absolute coordinate systems (cf.§2.5). Further downstream however, a streamwise vorticity component appears and grows at the expense of the normal component. This is due to the change in angle between the bulk flow and the vortex core. Another consequence of the change in angle is the existence of two vortex cores at the exit of the stator. These are in fact two successive rotor vortices.
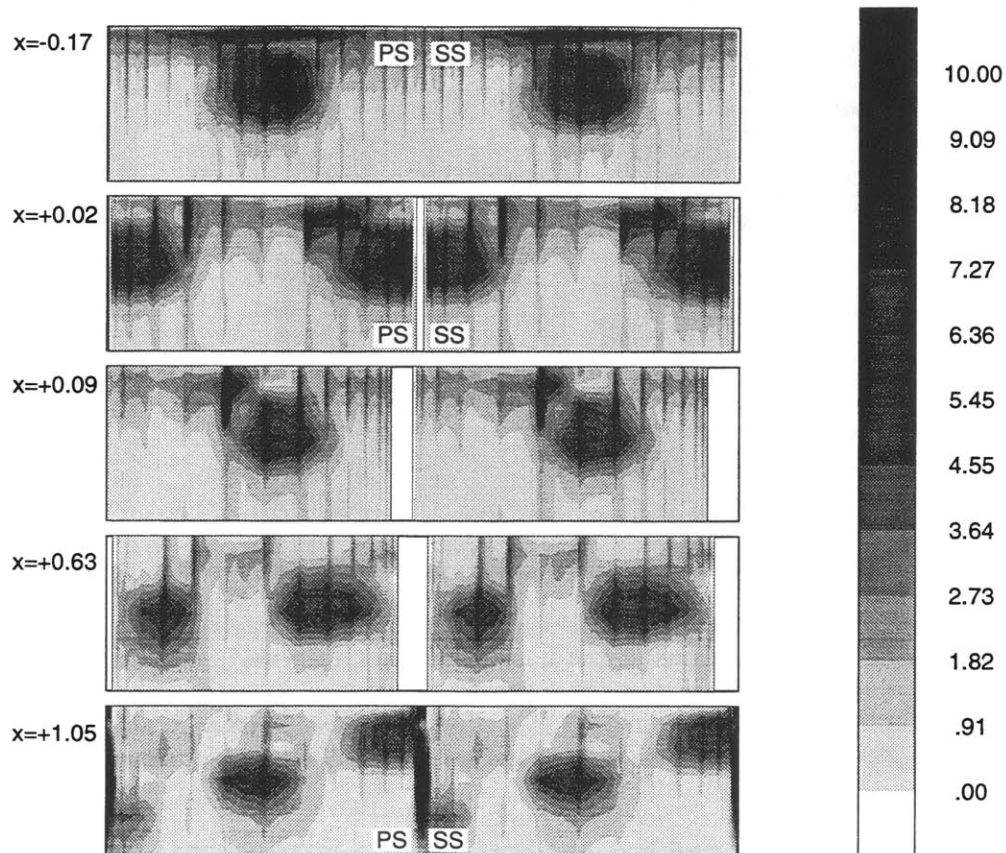
Figure 4.2. Isocontours of normal vorticity on successive crossflow planes, anchored at the axial locations indicated (LE at x=0, TE at x=1). Only the outer quarter of span is shown, since no significant vorticity is present below. Two stator passages are shown. The vortex cores are visible as regions of positive $\Delta\omega_n$. Shed vorticity is also visible on the cross-section at the bottom, as a band of positive $\Delta\omega_n$ along the trailing edge.

Besides the SW vortex core, the only other vortical feature of significance is the shedding of spanwise and trailing streamwise vortices from the trailing edge. These vortices can be seen at the bottom of **Figures 4.2** and **4.3** respectively. Spanwise vortices are shed in response to time-varying circulation about the blade sections. Losses associated with such 2D vortex shedding were investigated by Fritsch (1992) and found to be negligible.
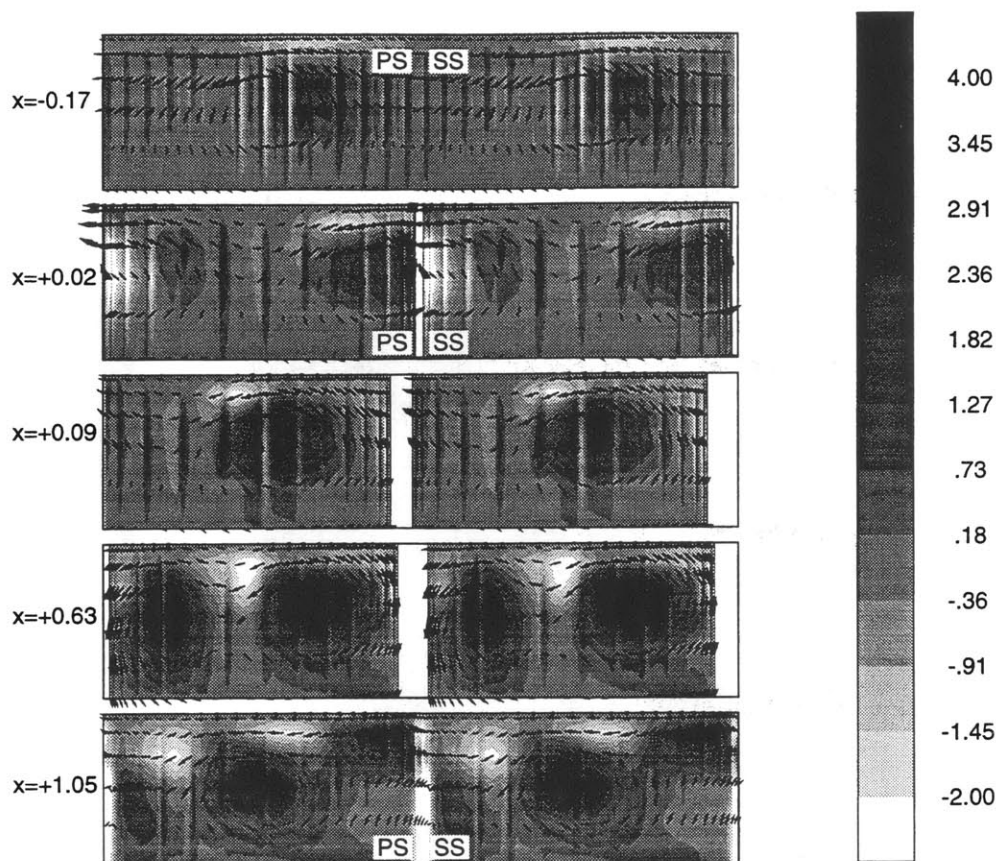
Figure 4.3. Isocontours of streamwise vorticity on successive crossflow planes, anchored at the axial locations indicated (LE at x=0, TE at x=1). Only the outer quarter of span is shown, since no significant vorticity is present below. Two stator passages are shown. The vortex cores are visible as regions of positive $\Delta\omega_s$. Shed vorticity is also visible on the cross-section at the bottom, as a band of negative $\Delta\omega_s$ along the trailing edge.

Streamwise vortices are shed in response to spanwise variation of blade circulation. In the present case, the circulation around these vortices is $0.16Uc$, which is significant when compared to the circulation around the upstream vortex core itself ($0.27Uc$). Therefore, the kinetic energy in the shed streamwise vortices is about one-fourth to one-third that of the incoming SW vortices. Thus, the contribution of 3D trailing vortices to loss is substantially larger than that of 2D shed vortices investigated by Fritsch (1992),

The SW vortex core does not exhibit the behavior observed by Graf (1996) for rotor tip leakage vortices. Graf found that the tip vortex in a full stage moves with a period between 1.6-1.8 times the blade passing frequency. Herein, the period of motion of all vortical structures is precisely equal to the rotor blade passing period.

4.1.2. Pressure fluctuations.

SW vortex interaction leads to a distinctive pattern of static pressure fluctuations in the passage and on the blade surface, characterized by (1) a leading edge pressure pulse, and (2) a train of "tornado-like" regions of low-P_s sweeping over the blade surface. These are shown in **Figure 4.4**.

The pressure pulse appears near the casing at the moment of vortex interception. It can be attributed to the local disturbance velocity component normal to the blade. The time-averaged effect of this pulse is to unload the leading edge over the outer 15-20% span. The train of low-P_s regions sweeping the blade is a reflection of the low static pressure in the SW vortex core (the core is maintained in equilibrium by a static pressure gradient balancing the centrifugal forces associated with vortex swirl).
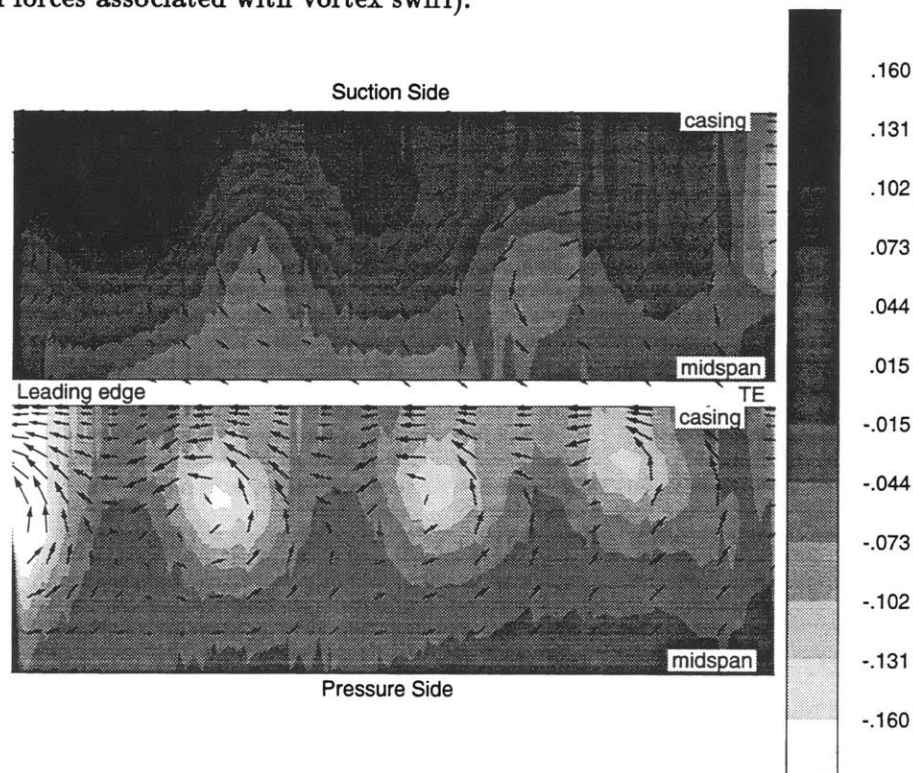
Figure 4.4. Disturbance static pressure contours and disturbance velocity vectors on the blade suction (top) and pressure (bottom) surfaces at the moment of wake interception. The LE pressure pulse and the "tornado" disturbances sweeping the surface are visible.

4.1.3. Validation of the free-slip conditions.

Free-slip boundary conditions have been imposed with the purpose of preventing the disturbance from "adhering" to the solid surfaces, and producing vorticity there. **Figure 4.5** suggests that this has been achieved to an adequate degree in the computed solution. The average RMS spanwise vorticity on the blade surface (excluding interelement boundaries) is

$0.523U/c$. This low value indicates that the disturbance flow is slip-free from a practical standpoint. Similar verification (not shown) has been carried out on the endwalls.
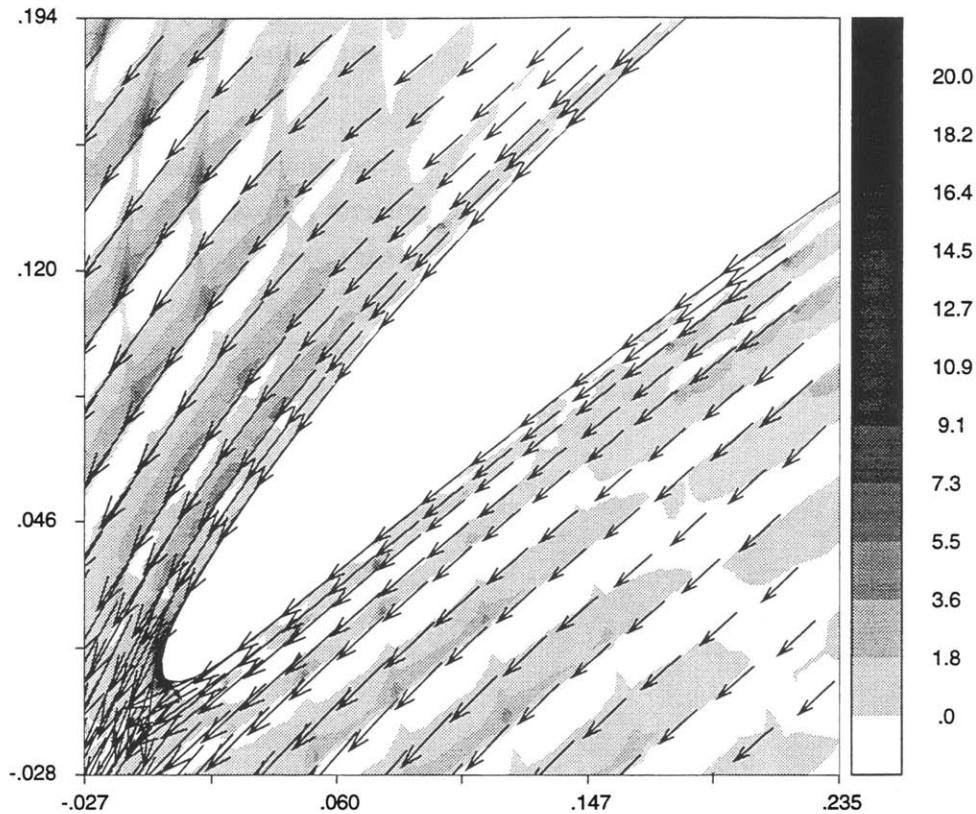
Figure 4.5. Disturbance velocity vectors and spanwise vorticity isocontours in the 91% span blade-to-blade plane, showing that the disturbance flow is slip-free.

A moderate amounts of aliasing noise is present in the vorticity fields shown above. The origin of the noise lies in slight C^1 discontinuities between spectral elements in the blade-to-blade plane (cf. §C.4). In the present case, these discontinuities may become apparent upon differentiation of the flowfield at the inter-element boundaries, However, they are too weak to affect losses, velocity and total pressure fields.

4.2. Case ID/SW: Time-Average Performance Changes.

Table 4.1 shows the change in performance due to SW vortex interaction in the present inviscid context. The figures of merit chosen to quantify the change are described in §2.1. Overall, SW vortex interaction is detrimental for the stator performance, increasing the net loss by about 0.2 efficiency points. Approximately two-thirds of this loss increase is associated with the increase in secondary kinetic energy of the unsteady flow leaving the stator. The other third is due to mixing of the vortex.

Figure of Merit	Change $(\Delta P_t/Q)$	Change (efficiency pts)	Change (% of steady value)
Passage loss $\Delta \mathcal{Y}_p$	−0.0011	−0.07	−3.8
$\Delta \mathcal{Y}_m = \Delta \mathcal{Y}_e - \Delta \mathcal{Y}_i$ $(\Delta \mathcal{Y}_i = 0.0038)$	−0.0023	−0.15	−7.8
Net loss change $\Delta \mathcal{Y}_n = \Delta \mathcal{Y}_p + \Delta \mathcal{Y}_m$	−0.0034	−0.22	−11.6

Table 4.1. Change in time-average stator performance for case **ID/SW** relative to the pre-mixed steady flow. Beneficial changes (leading to increased efficiency) are shown as positive quantities.

The increase in secondary kinetic energy of the unsteady flow leaving the stator is associated with (a) stretching of the SW vortex cores and (b) shedding of trailing vorticity from the TE of the stator blade. Vortex stretching is the dominant mechanism leading to performance deterioration. **Figure 4.6** shows how vortex stretching in the stator causes the mixing loss of the vortex to increase.
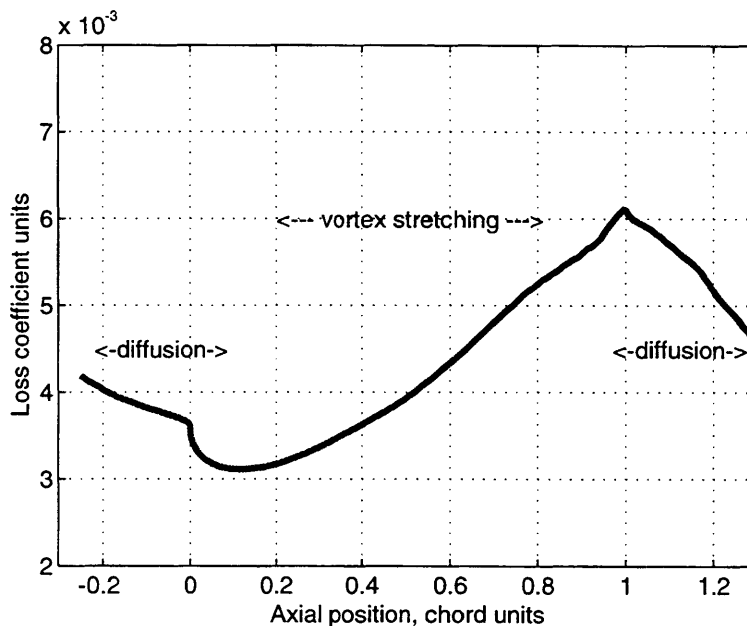
Figure 4.6. Approximate time-average secondary kinetic energy $\mathcal{E}$ of the unsteady flow at different axial locations. Mixing of the vortices causes $\mathcal{E}$ to decrease (x≤0.2 or x≥1), stretching causes $\mathcal{E}$ to increase (0.2≤x≤1) (LE at x=0, TE at x=1, vertical axis shows constant-area mixing loss coefficient).

Processing of SW vortices also decreases the static pressure recovery coefficient Π_n by about 3 percent. As shown in §2.3, this coefficient is directly determined by the axial force

on the stator blade. This force decreases because the pressure pulses from vortex interception (cf. §**4.3.3**) decrease the leading edge loading on a time-averaged basis.

4.3. Case ID/TL: Features of the Unsteady Flow.

4.3.1. Unsteady velocity field.

The velocity disturbance associated with the tip leakage vortex is quite different from that of the streamwise vortex above. At the inlet of the stator, the tip leakage (TL) vortex appears as a core of axial velocity deficit and tangential velocity excess, shown in **Figure 4.7**. In this sense, the incoming disturbance resembles a thick wake limited to the outer 15% of span. Therefore, the TL vortex appears to the stator as a jet of fluid directed away from the suction surface towards the pressure surface. The overall shape of the jet changes little in time. The most significant aspects of the vortex transport appear to be (a) attenuation
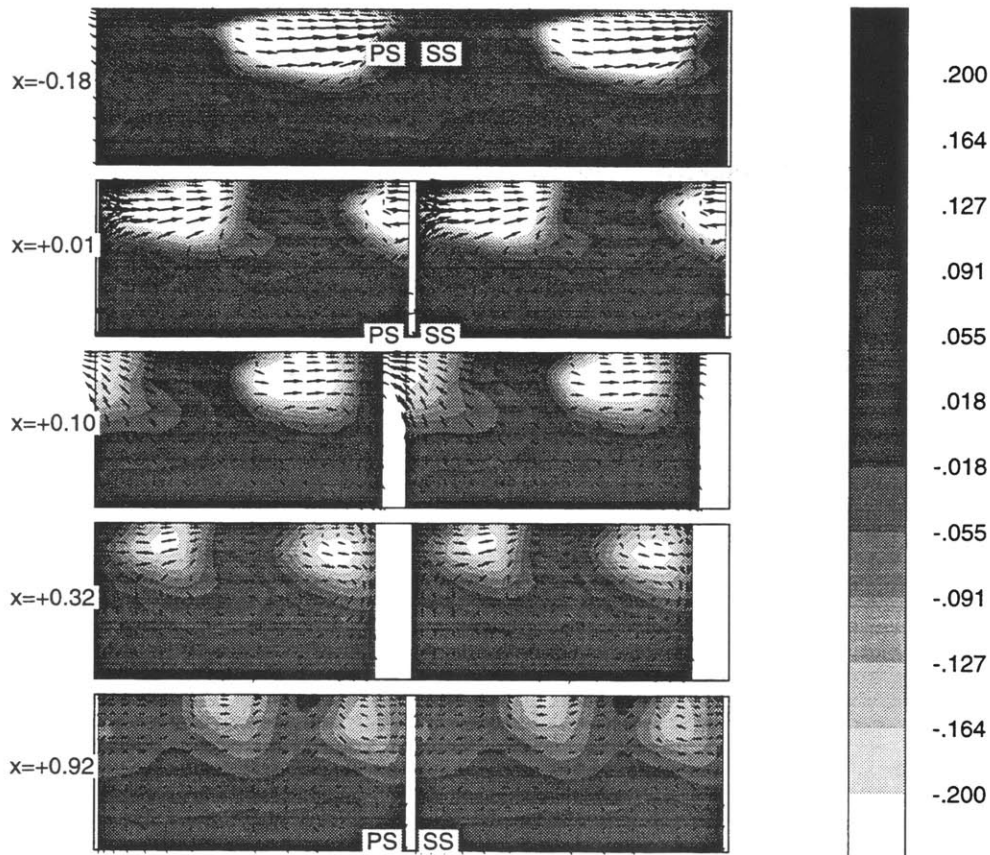
Figure 4.7. Disturbance axial velocity isocontours and disturbance crossflow velocity vectors on successive crossflow planes, anchored at the axial locations indicated (LE at x=0, TE at x=1). Only the outer third of span is shown, as no significant features are present below. More than one vortex core may be present at the exit, owing to change in the vortex tile angle γ..

of the core velocity non-uniformity, and (b) migration of vortical fluid towards the pressure surface. Both aspects can be appreciated in **Figure 4.8**, which emphasizes the wake-like nature of the unsteady flow in the passage. The attenuation mechanisms shall be discussed in the next section. **Figure 4.8** shows that the peak velocity disturbance in the vortex is attenuated by a factor of three between the inlet and the exit of the stator. This attenuation is somewhat higher than that of wakes, and indicates that some recovery of the vortex energy is taking place.
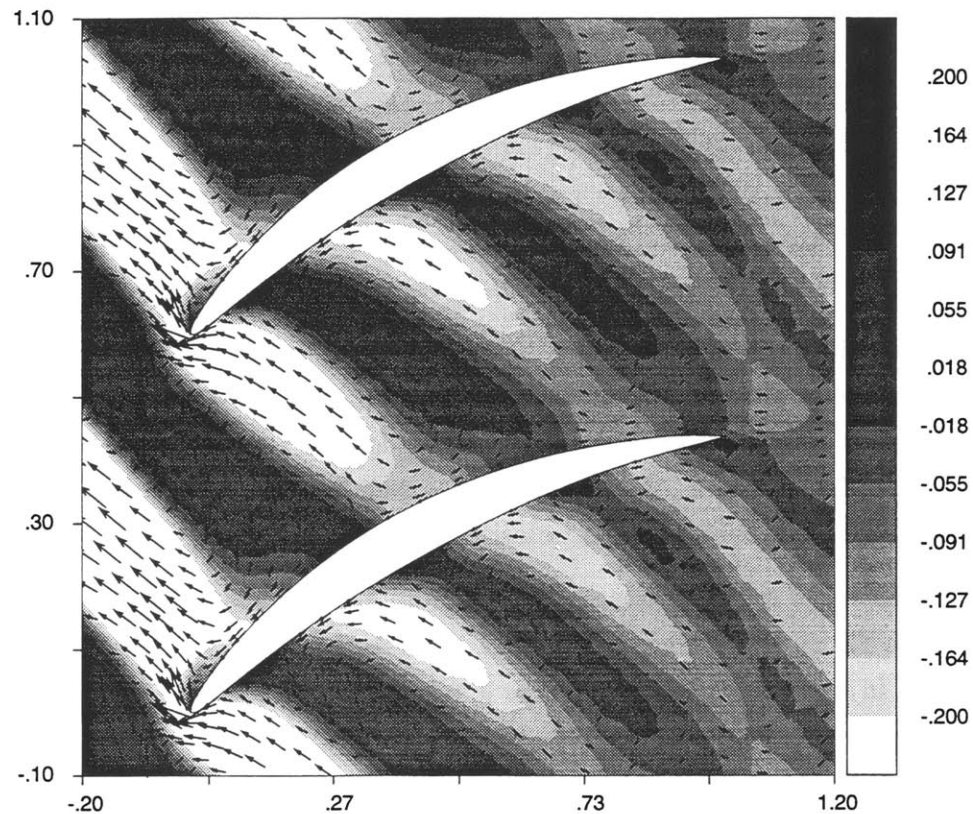
Figure 4.8. Disturbance axial velocity isocontours and disturbance velocity vectors on the blade-to-blade plane at 91% span (passing approximately through the TL vortex core). The velocity field associated with the tip leakage vortex is similar to that of a wake (cf.**Figure 3.1**).

The migration of vortical fluid is due to the excess tangential velocity of the jet in the stator frame. This excess is equal to $0.38U_\infty$ at the inlet of the stator. The physical meaning of this value is that for every 0.1 distance units traveled, the SS "end" of the TL vortex should migrate by 0.038 distance units towards the pressure side.

4.3.2. Structure and recovery of the vortex.

The vortical structure of the tip vortex follows from its appearance as a three-dimensional

jet, noted above. **Figures 4.9** and **4.10** show respectively the normal and streamwise components of the vortex. At the inlet, the normal vorticity component is similar to that of a wake, while the streamwise vorticity component appears as two opposite-sign layers near the casing. Given that the base flow is inviscid and uniform in the spanwise direction, this structure is transported without much distortion.

To help understand how the vortex is attenuated, it is useful to consider the normal and streamwise vortical components separately. The disturbance velocity associated with the normal vorticity component is attenuated in essentially the same manner as a wake (i.e. in proportionality to stretching of the vortex, cf. §3.3). The disturbance velocity associated with the streamwise vorticity component is attenuated in a different manner, illustrated schematically in **Figure 4.11**. The slowing of the flow in the stator leads to "shortening" of the streamwise vortex filaments. This leads to attenuation of the streamwise vorticity component itself. An analogy to a line vortex going through a diffuser, indicates that the attenuation of streamwise vorticity is proportional to the vortex stretching L_i/L_e (cf. §J.4.2).

From a quantitative standpoint, this analogy means that the recovery of the tip vortex scales in the same manner as that of wakes (3.04). This is an important finding, implying that (1) transport of tip vortices is beneficial; and (2) most of the kinetic energy of the vortex can be recovered in the stator. These implications shall be developed further in §4.4, where the contribution of turbulent diffusion to loss is also considered.

The attenuation of streamwise vorticity is the most notable aspect of the unsteady vortical flow in the ID/TL case. As shown in **Figures 4.12a-b** the vortex is simply and cleanly cut by the blade. In itself, this is useful because it will help identify vortical features associated with boundary layer response in the fully-viscous calculations of **Chapter 5**. The period of motion of all vortical features is precisely equal to the rotor blade passing period.

The SW vortices in §4.1-§4.2, appear as "tornado-like" disturbances sweeping the surface of the blade. On the other hand, TL vortices appear as 3D jets of fluid directed towards the pressure side of the stator. Both are convected by the base flow without significant distortion, and are cleanly "chopped" in segments by the blades.
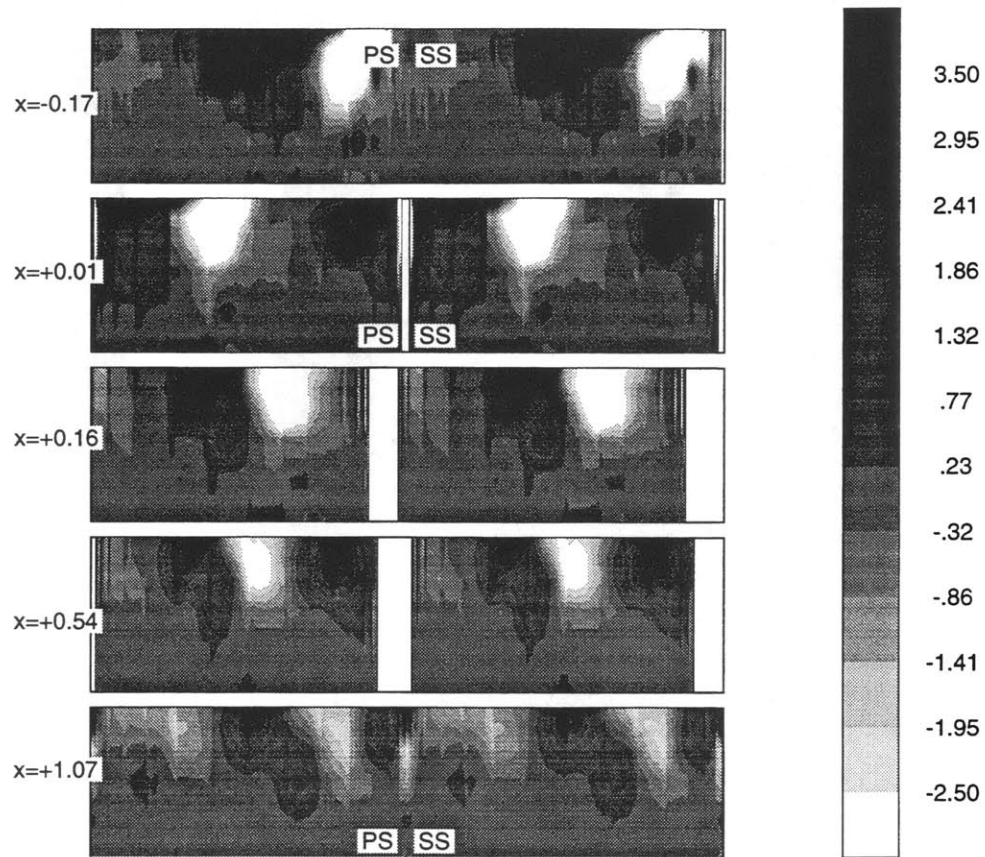
Figure 4.9. Spanwise component of the disturbance normal vorticity, $\mathbf{k} \cdot \Delta\boldsymbol{\omega}_n$, on successive crossflow planes, anchored at the axial locations indicated (LE at x=0, TE at x=1). The reasons for showing $\mathbf{k} \cdot \Delta\boldsymbol{\omega}_n$ instead of $|\Delta\boldsymbol{\omega}_n|$ are as follows: (a) it is a signed scalar, (b) it is pertinent to the wake-like nature of the flow under consideration. Instant of vortex interception $(t = t_0)$, outer one-third of span.
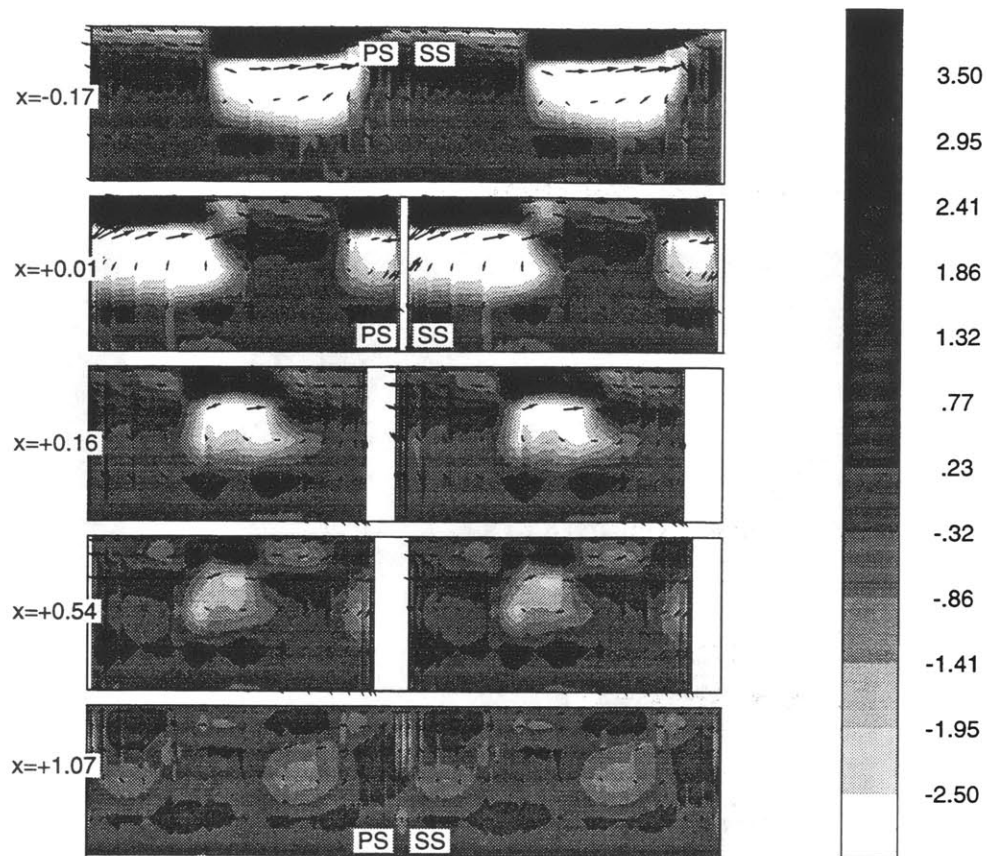
Figure 4.10. Disturbance streamwise vorticity contours on successive crossflow planes, anchored at the axial locations indicated (LE at x=0, TE at x=1). Instant of vortex interception $(t = t_0)$. Only the outer one-third of span is shown.
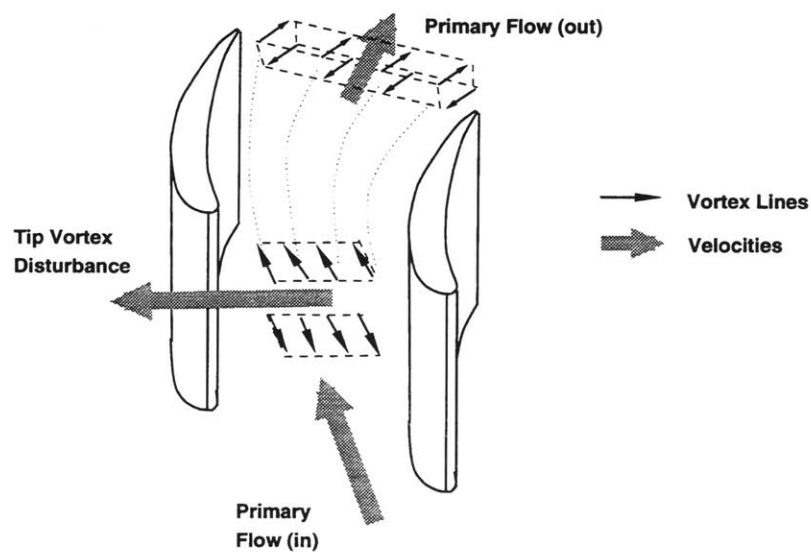
Figure 4.11. Schematic model of recovery associated with the absolute streamwise vorticity component in the incoming tip vortex.
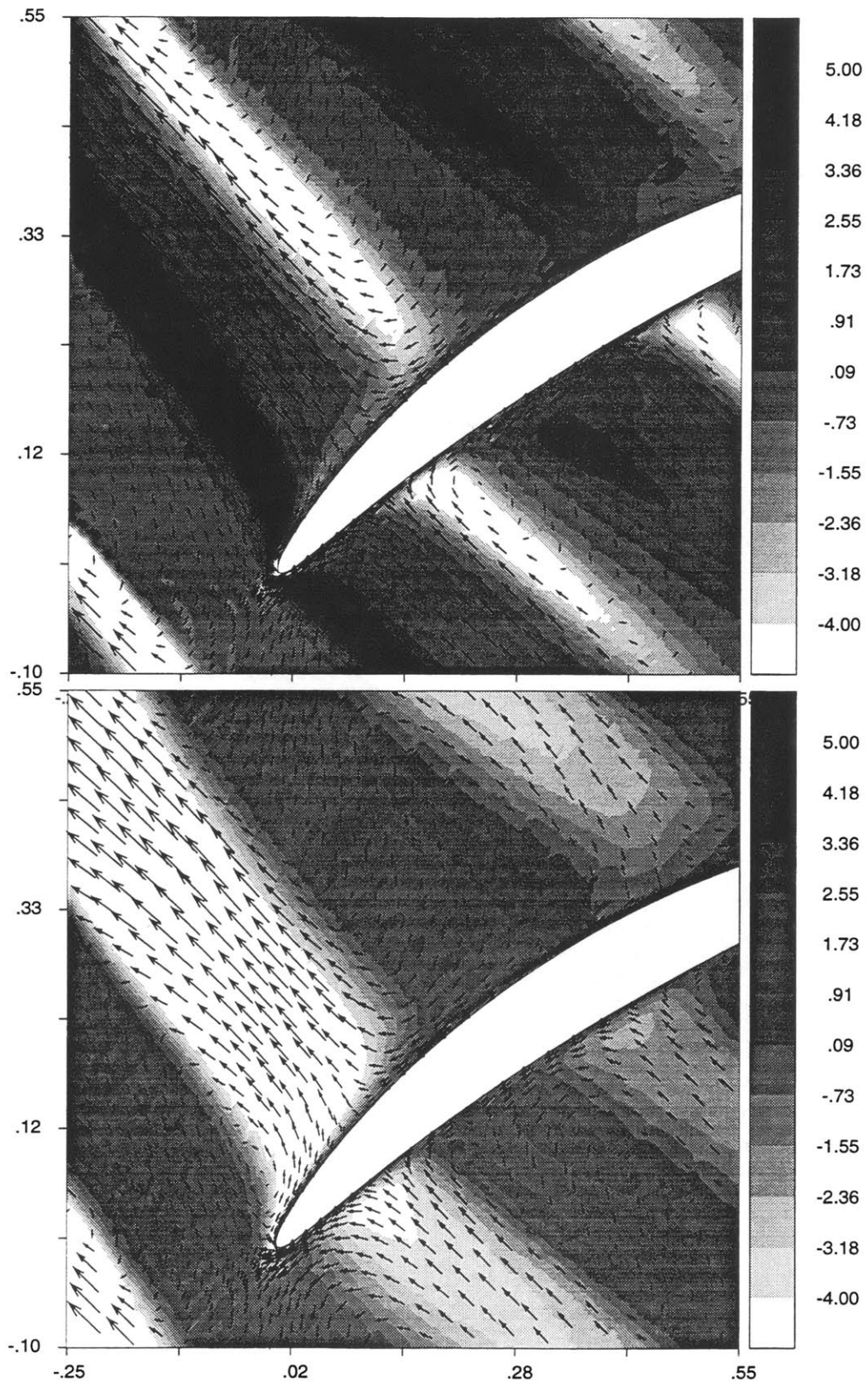
Figure 4.12a (top)/4.12b (bottom). Top: Spanwise component of the disturbance normal vorticity $\mathbf{k} \cdot \Delta\boldsymbol{\omega}_n$, on the 91% span blade-to-blade plane shortly after interception ($t = t_0 + 0.25T$). Bottom: disturbance streamwise vorticity at the same location and time. The plane chosen passes approximately through the center of the vortex, which is cleanly cut by the blade.

4.3.3. Pressure fluctuations.

The upstream tip vortex induces a pattern of static pressure fluctuations that is confined over the outer 15-25% of the span and that is similar to that seen for 2D wakes. This pattern is characterized by a positive pressure pulse on the leading edge PS, and by a negative pressure pulse on the leading edge SS, at the time of vortex interception. **Figure 4.13** shows the unsteady static pressure field at this time. The peak value of the disturbance static pressure at the location shown (0.84 dynamic heads) matches that from the 2D impingement model in §**3.1** (0.93 dynamic heads, using a local jet velocity of 0.38 units). The net effect of the pulses is to increase the blade loading in the leading edge region of the tip of the stator.
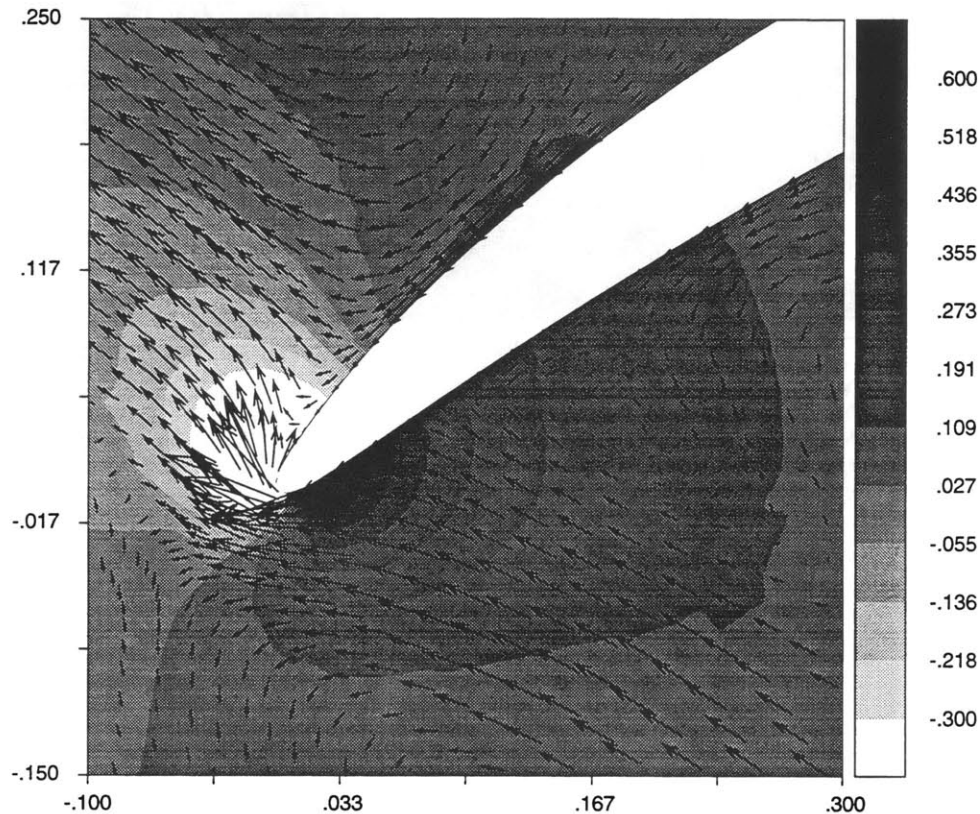
Figure 4.13. Disturbance static pressure contours near the leading edge at the moment of vortex interception. Location: 91% span blade-to-blade plane (passing approximately through the TL vortex core). Low and high C_p regions and jet impingement are clearly visible. Compare to **Figure 3.1**.

4.4. Case ID/TL: Time-Average Performance Changes.

Table 4.2 shows the change in performance due to TL vortex interaction in the present inviscid context. Overall, TL vortex interaction is beneficial for stator performance. The gain in efficiency is about 0.25 points relative to the mixing-plane steady flow approximation.

Figure of Merit	Change $(\Delta P_t/Q)$	Change (efficiency pts)	Change (% of steady value)
Passage loss $\Delta \mathcal{Y}_p$	-0.0010	-0.06	-3.3
$\Delta \mathcal{Y}_m = \Delta \mathcal{Y}_e - \Delta \mathcal{Y}_i$ $(\Delta \mathcal{Y}_i = 0.0049)$	$+0.0043$	$+0.28$	$+14.5$
Net loss change $\Delta \mathcal{Y}_n = \Delta \mathcal{Y}_p + \Delta \mathcal{Y}_m$	$+0.0044$	$+0.22$	$+11.0$

Table 4.2. Change in time-average stator performance for case **ID/TL** relative to the pre-mixed steady flow. Beneficial changes (leading to increased efficiency) are shown as positive quantities.

This gain is due to the reversible recovery of energy in the vortex jet, which scales in the same manner as that of a 2D wake (despite the uniquely three-dimensional aspects discussed in §4.3.2). Since turbulent diffusion is retained in the core flow, the value of $\Delta \mathcal{Y}_p$ (first line of **Table 4.2**) represents the contribution to loss from mixing of the tip vortex within the stator. This contribution is not important. Most of the kinetic energy of the vortex is recovered without an increase of entropy. This can be explained by the argument developed
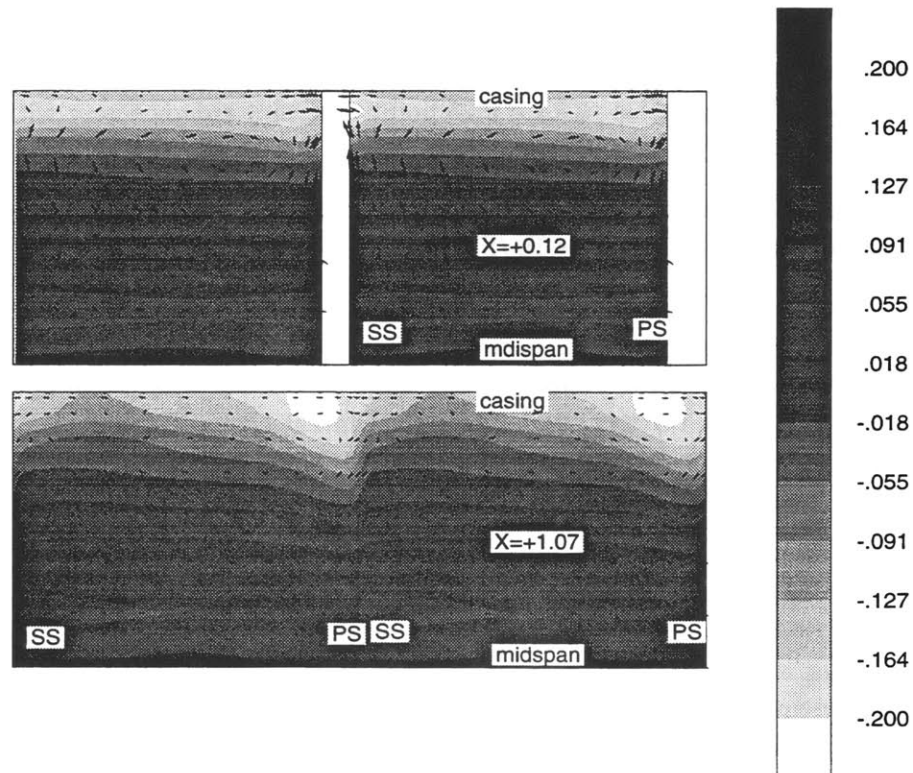
Figure 4.14. Top: Time-averaged disturbance total pressure $\Delta \overline{C_t}$ and disturbance crossflow $\Delta \overline{\mathbf{u}}$ on the inlet and exit plane respectively (LE:x=0,TE:x=1). Note segregation of low-P_t vortical fluid.

for 2D wakes — recovery occurs over shorter lengthscales than turbulent diffusion.

There is one aspect of tip vortex interaction that cannot be directly appreciated from the time-resolved data. Time-averaging of P_t fluctuations at the inlet of the stator yields a distribution that is nearly uniform circumferentially. However, as shown in **Figure 4.14**, a core of low-$\overline{P_t}$ fluid appears in the pressure side casing corner at the exit of the stator. This "segregation" of total pressure correlates to within a few percent with the time-averaged redistribution of normal vorticity, and is the result of tangential migration of vortex fluid. This redistribution of total pressure in the flow constitutes a three-dimensional equivalent to Kerrebrock and Mikolajczak (1970) total temperature segregation of rotor wakes. It is not however a source of loss by itself, as the first line in **Table 4.2** shows.

4.5. Inviscid Vortex-Stator Interaction: Summary.

Two computational experiments are carried out, in which upstream TL and SW vortex disturbances propagate in an inviscid steady base flow without adhering to the solid surfaces. Turbulent mixing of the disturbances is retained however. This approach allows to determine the effect of vortex core transport on loss in the presence of turbulent diffusion. It was found that the effects of SW and TL vortices are markedly different:

- Most of the TL vortex energy is recovered in the stator without an increase in entropy. In the ID/TL case, this yields a 0.25 point efficiency enhancement with respect to the mixed-out steady flow approximation.

- On the other hand, transport of SW vortices is detrimental for stator performance. (by 0.20 efficiency points for the ID/SW case).

- Recovery of the TL vortex energy is due to stretching of the TL vortex. The recovery process is three-dimensional in nature (it involves compression of streamwise vortical filaments) but happens to scale in the same way as 2D wake recovery. Thus, recovery of wakes and tip vortices can be described in 2D terms. Turbulent diffusion of wakes and tip vortices is far less important for loss than previously thought (resulting in a loss of 0.06 efficiency points in the ID/TL case). This is because recovery lengthscales are shorter than diffusion lengthscales, and independent of the velocity non-uniformity.

- Stretching of the SW vortex core is the primary reason for efficiency degradation in the ID/SW case. This is in accordance with Denton (1993). While unsteady vortex shedding might not be important in a 2D flow (Fritsch 1992), this is not the case for the present 3D flow. In the ID/SW case, shedding of streamwise vorticity from the TE of the blades is a noticeable source of loss.

The next chapter considers how these conclusions hold in fully viscous flow. In particular, the role of vortical structures arising from boundary layer response shall be examined.

Chapter 5

Viscous 3D Vortex/Stator Interaction

This chapter examines the unsteady flow and performance changes in a stator cascade subjected to the following two types of upstream vortices at design point loading and Reynolds number (**Figure A.1**, ϕ=0.45, Re=3.10^5):

- Nominal tip leakage (TL) vortex, based on Khalid's (1995) computed flowfield at the exit of a single LSRC rotor at design loading and 3% tip clearance. This computational experiment is designated as case VD/TL. The results are discussed in §**5.1-5.2**.

- Simple streamwise vortex (SW) with a core radius of 12 percent span and a circulation of $0.5cU_\infty$ in the rotor frame. This computational experiment is designated as case VD/SW. The computed results are discussed in §**5.3**

The difference between the computational experiments in this chapter, and their ID/TL and ID/SW counterparts in **Chapter 4**, is the presence of boundary layers. A back-to-back comparison with ID/TL and ID/SW shall be used to show (a) how vortex transport is affected by the presence of boundary layers, (b) how the boundary layer responds to vortices and (c) what the effects on stator performance are at design point conditions.

5.1. Case VD/TL: Features of the Unsteady Flow.

This section focuses on the vortical features of the unsteady flow. The pressure fluctuations induced by the upstream tip leakage vortex are similar in nature and amplitude to those seen in the "inviscid" ID/TL (cf. §**4.3**), and appear primarily as an instantaneous increase of the loading on the leading edge in the stator tip region upon vortex interception. This

confirms that the unsteady pressure fields are in large extent a potential flow effect from the interference between the blade and the upstream velocity disturbances.

5.1.1. Structure and attenuation of vortex cores.

In viscous flow, the vortex core velocity non-uniformity is still strongly attenuated in the stator. There are two differences with respect to the inviscid ID/TL case however: (1) distortion of the vortex core and (2) more pronounced migration. Both can be attributed to the presence of an endwall boundary layer in the base flow.

Distortion. Vortex core "filaments" closer to the casing are convected at a slower rate than those away from it. This leads to "skewing" of the TL vortex core in the crossflow plane, illustrated in **Figure 5.1**. Albeit interesting, this "skewing" does not appear to be important as far as vortex energy recovery is concerned (cf. §**5.2**). It is to be noted that all vortical structures in the flow move with a period equal to the rotor blade passing period.
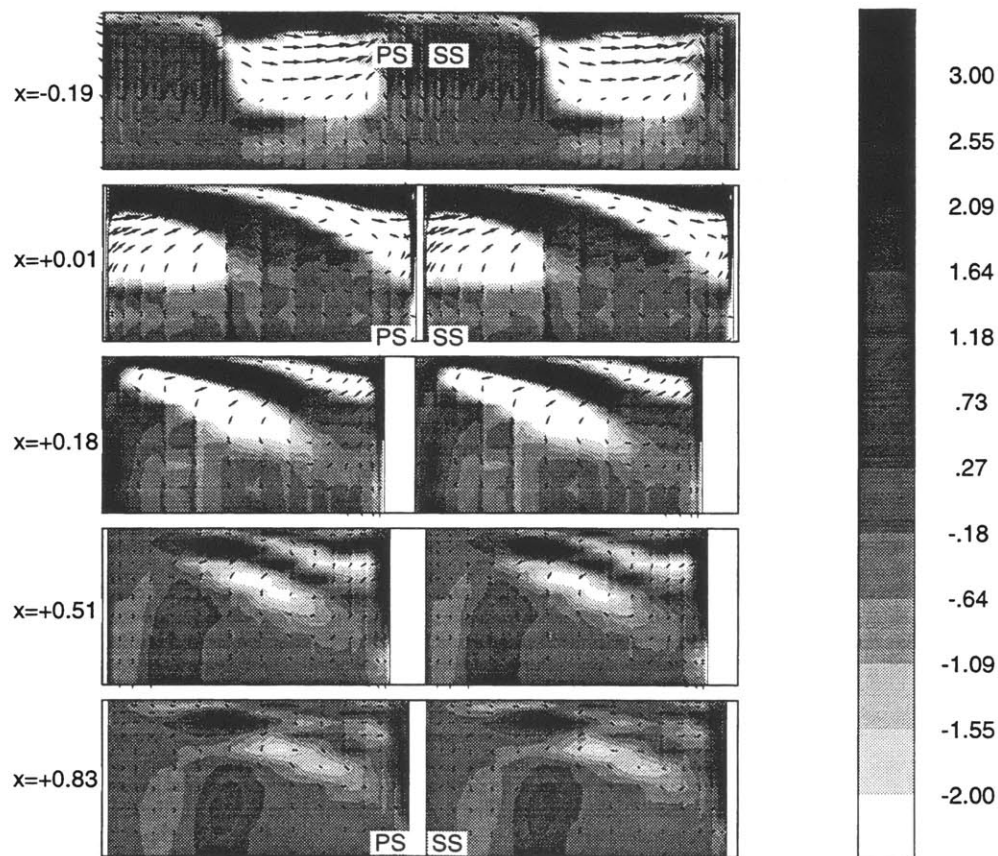
Figure 5.1. Disturbance streamwise vorticity isocontours at $t = t_0$. Crossflow planes are selected to avoid intersection with BLDs (to give a clearer image of the core structure). A comparison with **Figure 4.10** shows skewing of the TL vortex core.

Vortex migration can be appreciated by comparing **Figure 5.2** to **Figure 4.8**. The same representation of the tip vortex is used in the ID/TL and VD/TL cases. However, at the spanwise location shown in **Figure 5.2**, the base flow velocity in case VD/TL is about 25% less than in case ID/TL. Therefore, the vortex fluid in case VD/TL migrates closer to the pressure surface for the same distance traveled.
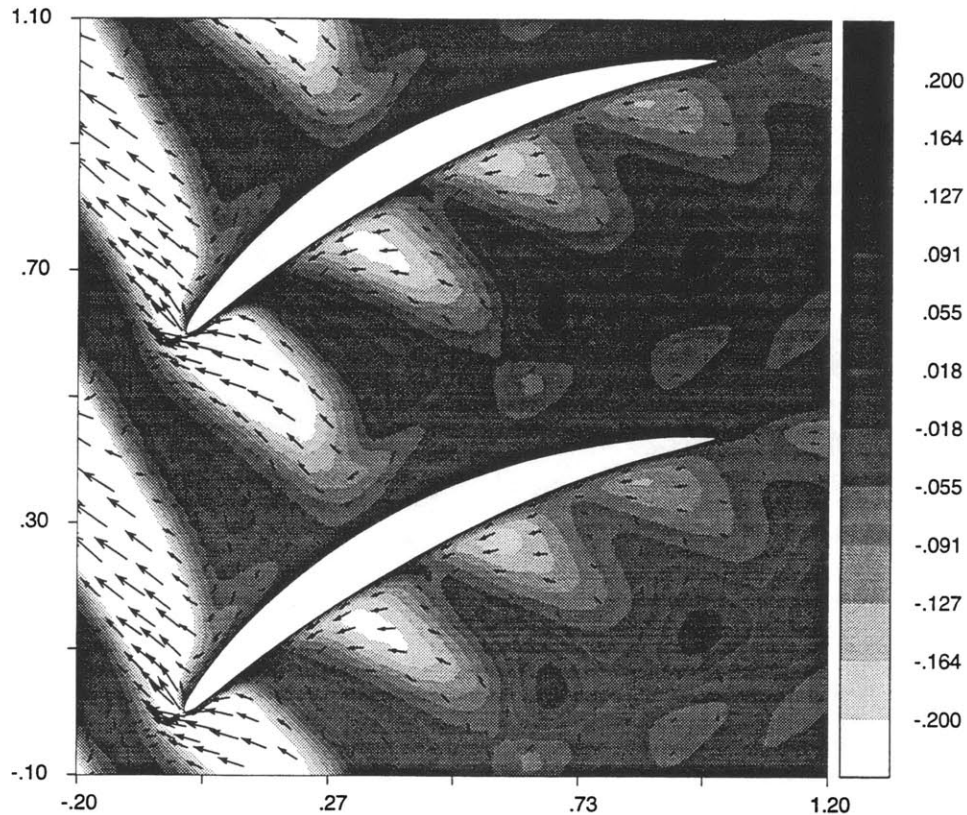
Figure 5.2. Disturbance axial velocity contours in the 91% span blade-to-blade plane. This plane passes though the vortex core and is immersed in the endwall boundary layer.

5.1.2. Non-transitional boundary layer response.

The interaction between the tip leakage vortex and the boundary layers results in vortical disturbances not seen in the inviscid case. These disturbances originate on the leading edge at the time of vortex interception, and are located in the tip region of the stator blade ($\sim$75%-95% span). Each disturbance has normal as well as streamwise vorticity components. Each of these will be examined separately.
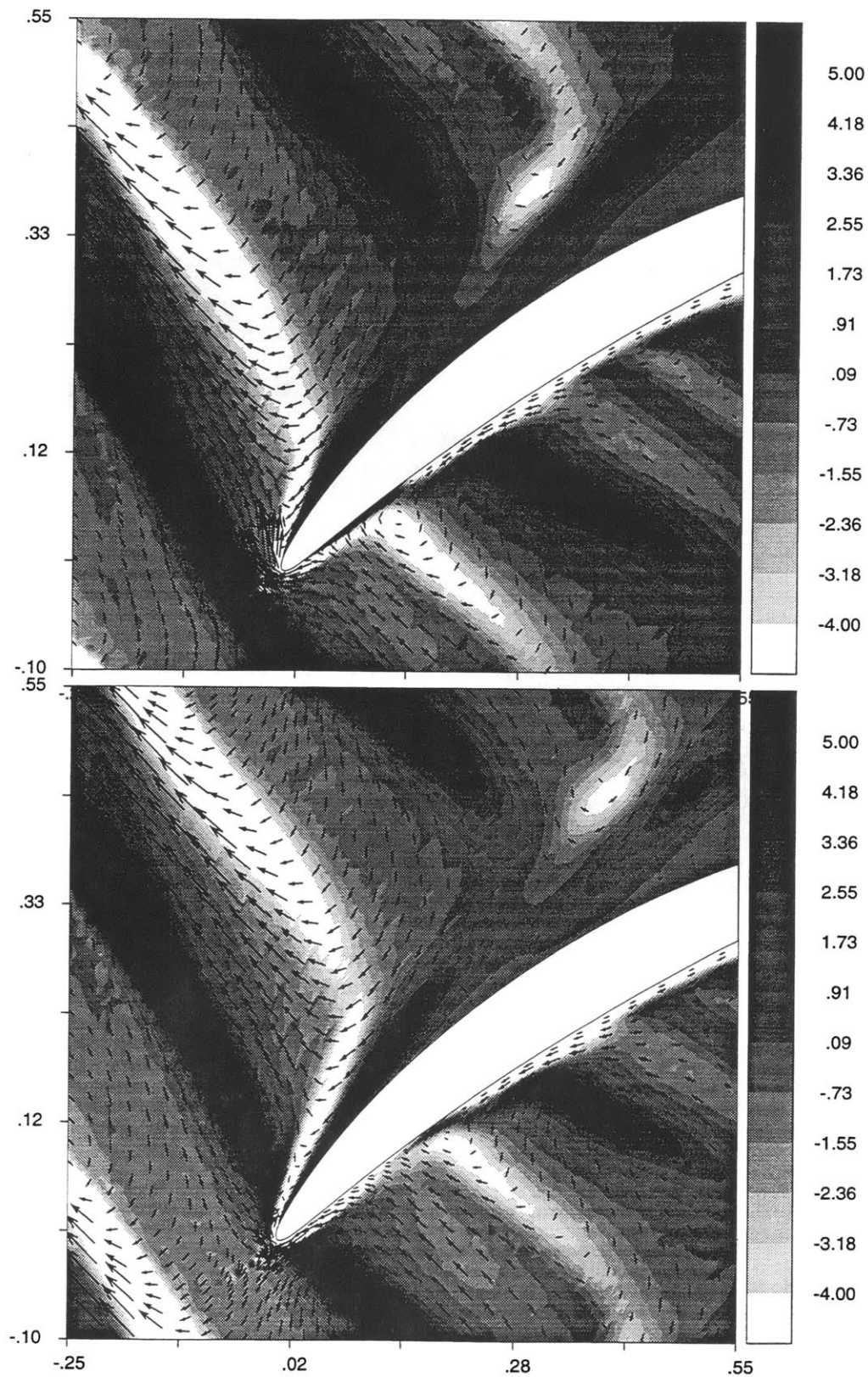
Figure 5.3a/5.3b. Spanwise component of the disturbance normal vorticity $\mathbf{k} \cdot \Delta\boldsymbol{\omega}_n$ and velocity vectors $\Delta\mathbf{u}$ on the 91% span blade-to-blade plane, passing approximately through the center of the vortex. Similar features are observed between 80-95% span. Outside this range, the flow is virtually free of vortical fluctuations. Top (a) at time $t = t_0$. Bottom (b) at time $t = t_0 + 0.25T$ Compare to **Figure 4.12a.**
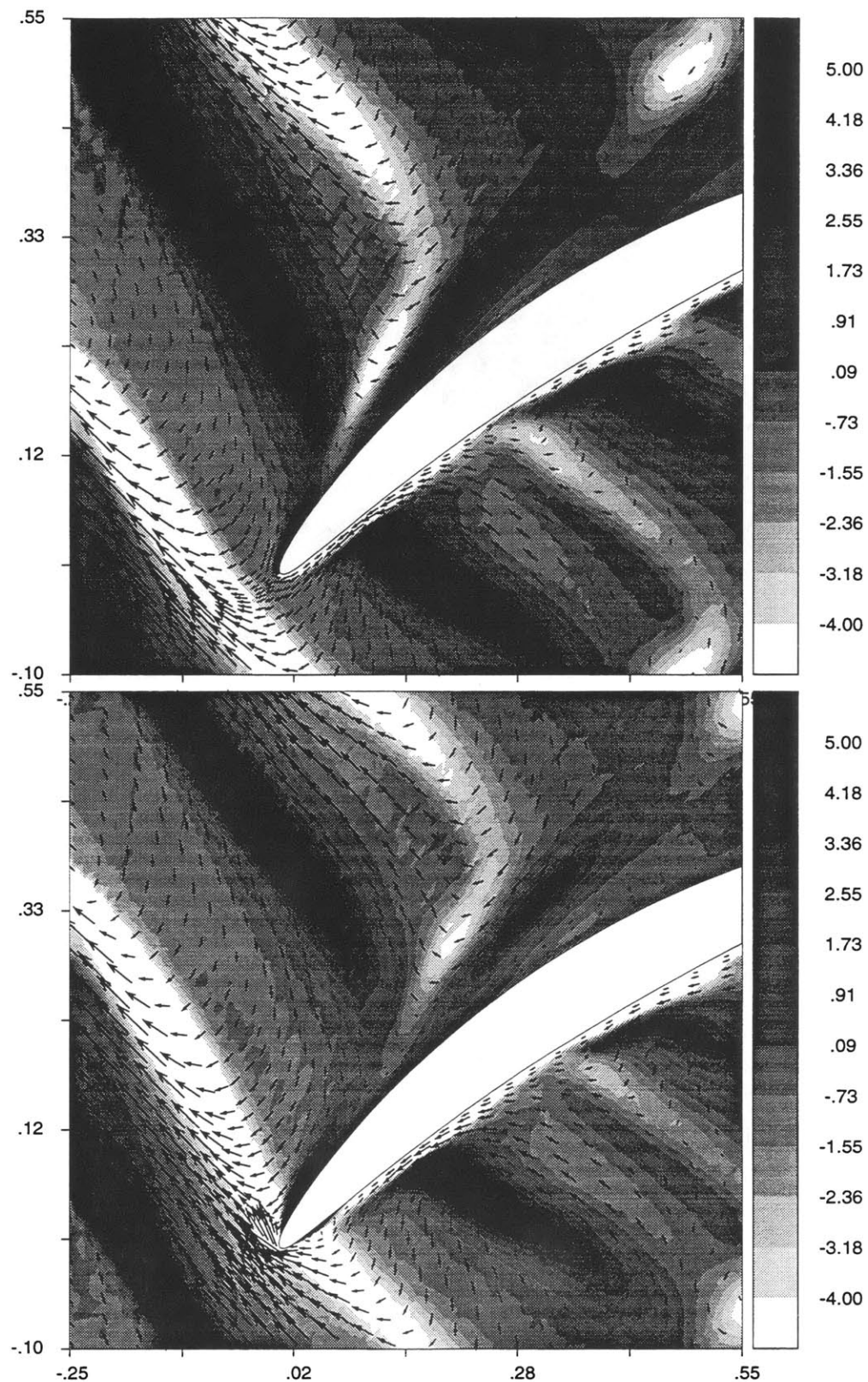
Figure 5.3c/5.3d. Spanwise component of the disturbance normal vorticity $\mathbf{k} \cdot \Delta\boldsymbol{\omega}_n$ and velocity vectors $\Delta\mathbf{u}$ on the 91% span blade-to-blade plane. Top (c) at time $t = t_0 + 0.50T$. Bottom (d) at time $t = t_0 + 0.75T$. Compare to **Figure 4.12a**.
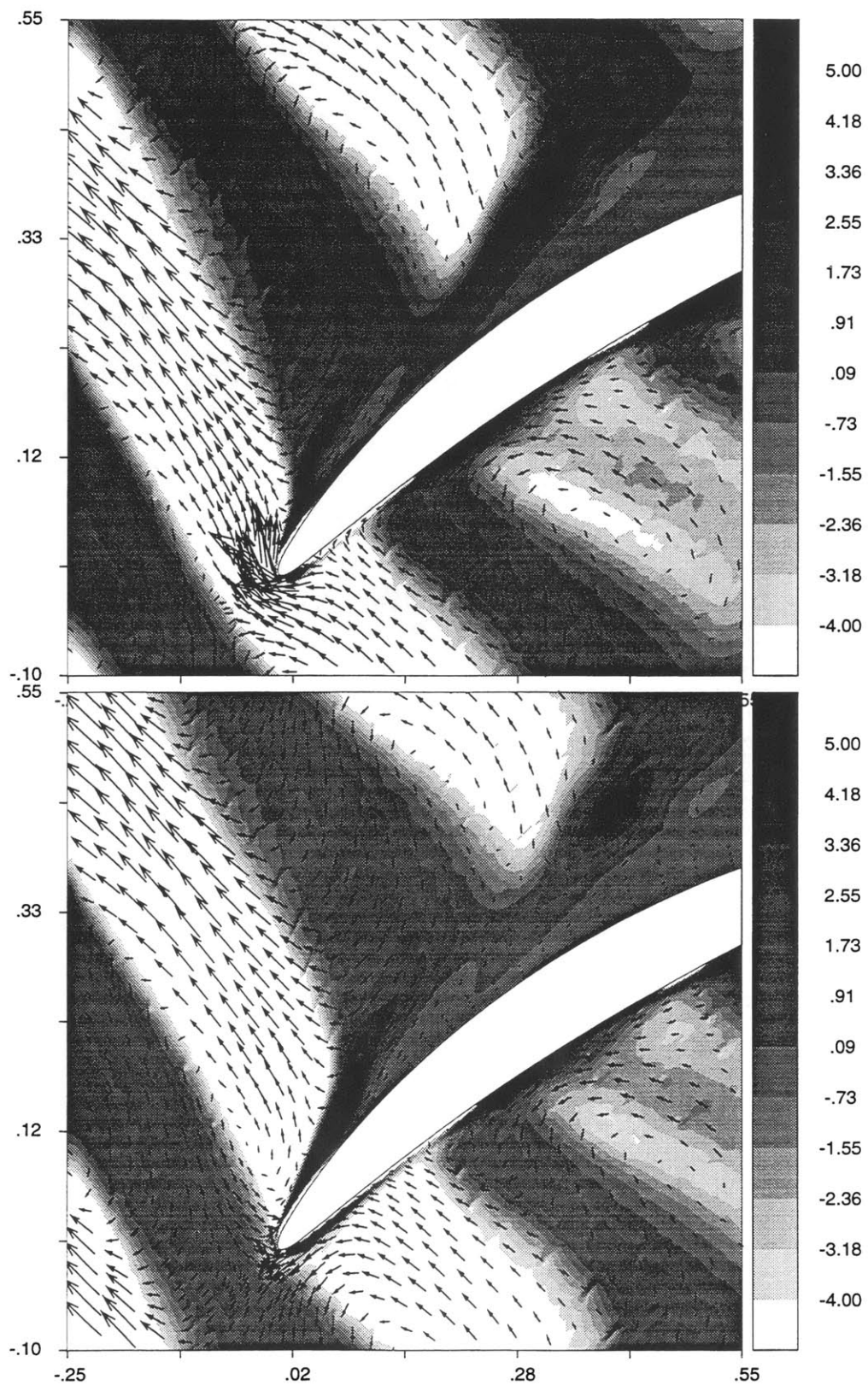
Figure 5.4a/5.4b. Disturbance streamwise vorticity $\Delta\omega_s$ levels and velocity vectors $\Delta\mathbf{u}$ on the 91% span blade-to-blade plane. Top (a) at time $t = t_0$ (defined as moment of wake interception). Bottom (b) at time $t = t_0 + 0.25T$. Compare top to **Figure 4.12b**.
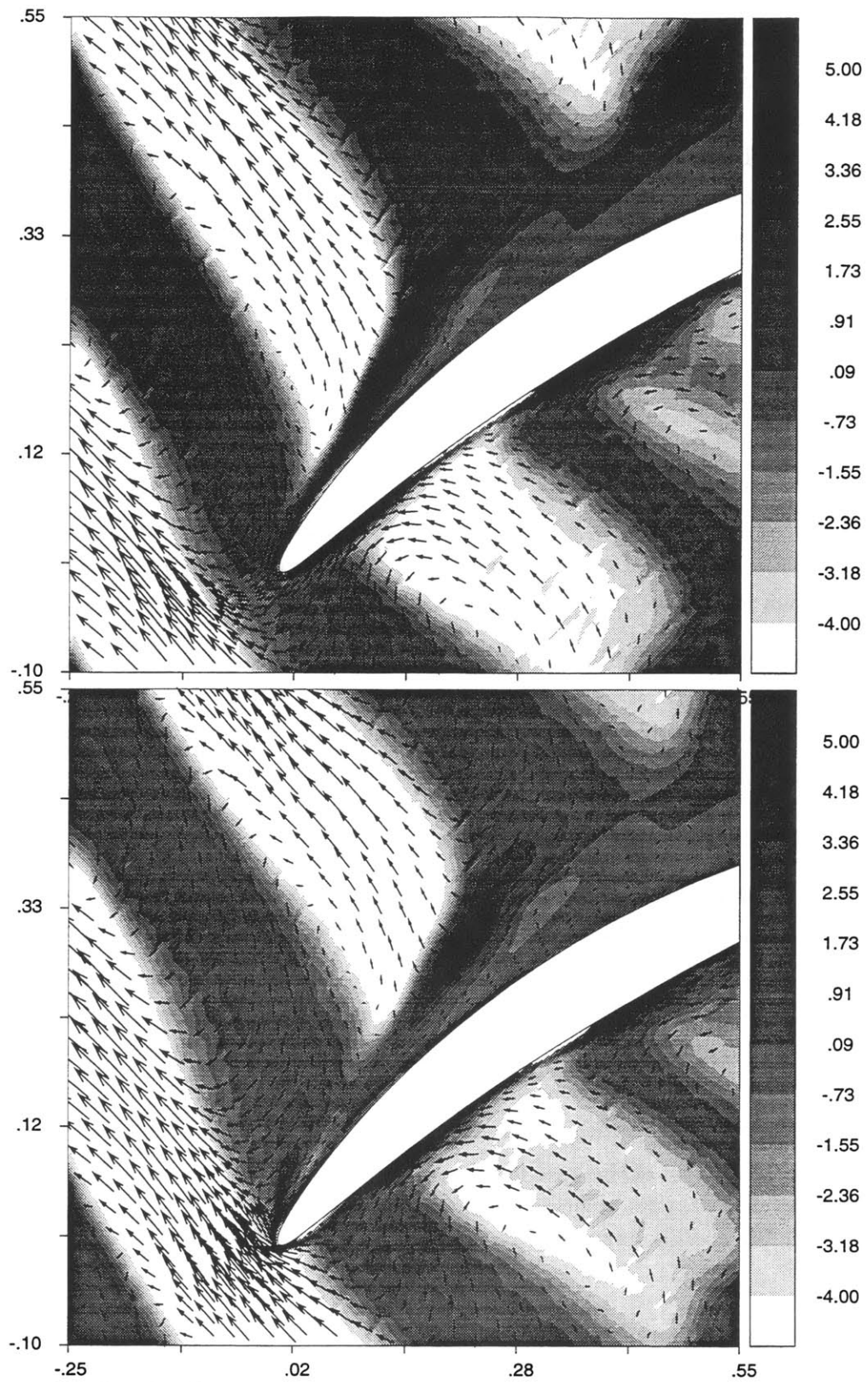
Figure 5.4c/5.4d. Disturbance streamwise vorticity $\Delta\omega$, levels and velocity vectors $\Delta\mathbf{u}$ on the 91% span blade-to-blade plane. Top (c) at time $t = t_0 + 0.50T$. Bottom (d) at time $t = t_0 + 0.75T$. Compare top to **Figure 4.12b**.

Normal vorticity disturbances are the component of $\Delta\omega$ that is perpendicular to the local flow direction. **Figure I.3 (Appendix I)** shows the convention used to decompose the vorticity vector into streamwise and normal components. **Figure 5.3** shows the spanwise component of the normal vorticity disturbances, $\mathbf{k} \cdot \Delta\omega_n$, at four successive time instants within one vortex passing period. This is the dominant component of the disturbance normal vorticity, and the most appropriate one to illustrate the wake-like nature of the flow.

In this context, the disturbances shown in **Figure 5.3** are morphologically similar to the boundary layer distortions (BLDs) seen in two-dimensional calculations with wakes. For this reason, these disturbances shall be referred to as N-BLDs (short for "normal vorticity boundary layer disturbances"). N-BLDs are present over both pressure and suction surfaces. Pressure side N-BLDs remain flattened against the blade surface. Suction side N-BLDs on the other hand, are more prominent. They are lifted away from the surface, and are convected in the downstream direction behind the suction side end of the tip vortex. Each N-BLD has a characteristic vortical structure, that consists of two opposite-sign vortical regions. The positive region is closer to the blade surface and somewhat smaller than the negative region.

Streamwise vorticity disturbances originate on the suction side leading edge upon vortex interception. These disturbances are shown in **Figure 5.4**. They appear as an elongated core of positive $\Delta\omega_s$, transported under the suction side end of the TL vortex. These disturbances shall be referred to as S-BLD in the following.

5.1.3. Mechanisms for boundary layer response.

From a theoretical standpoint, any change in the vorticity field can lead to a change in loss (Equation 2.07). In the present case, the foregoing N-BLDs do lead to a noticeable increase in passage loss (cf. §5.2.1). It is therefore useful to elucidate what mechanisms are involved in their production. The similarity between N-BLDs and disturbances from 2D wake calculations, implies that the redistribution of boundary layer vortical filaments is one such mechanism. This hypothesis shall be verified by comparing the contributions of the four mechanisms through which disturbance vorticity can appear in the flow (cf. §F.6):

(1) Normal distortion of the base flow boundary layer vortex filaments under the effect of velocity disturbances associated with wakes and vortices. This mechanism is present in both 2D and 3D flows, and is represented by the following term:

$$\mathbf{T}_1 = (\Delta\mathbf{u} \cdot \nabla)\omega_1 \qquad (5.01)$$

(2) Stretching and tipping of base flow boundary layer vortex filaments by the same velocity disturbances. Although similar to above, this mechanism exists only in 3D flows, and is represented by the following term:

$$\mathbf{T}_2 = (\omega \cdot \nabla)\Delta\mathbf{u} \qquad (5.02)$$

(3) Stretching and tipping of vortex filaments present in the upstream disturbances by the base flow velocity gradients. This mechanism also exists only in 3D flows, and is represented by the following term:

$$\mathbf{T}_3 = (\Delta\boldsymbol{\omega} \cdot \nabla)(\mathbf{u}_1 + \Delta\mathbf{u}) \qquad (5.03)$$

(4) Diffusion of additional vorticity produced on the solid surfaces and changes in vorticity diffusion rates due to velocity disturbances from wakes and vortices. This mechanism is represented by the following term:

$$\mathbf{T}_4 \approx \nu_u\nabla\times\Delta\boldsymbol{\omega} + \Delta\nu\nabla\times\boldsymbol{\omega}_s \qquad (5.04)$$

The above hypothesis can be verified by extracting these terms from the unsteady solution, and comparing their magnitude throughout the flowfield. This is done in **Figures 5.5-5.8** at the instant of vortex interception. A comparison between these figures indicates that normal displacement of the base boundary layer vortical filaments (mechanism "1" above) is the leading cause of disturbance vorticity production from blade-vortex interaction. Tipping and stretching of <u>disturbance</u> vortical "filaments" (mechanism "3" above) is a close second contributor, while tipping and stretching of base boundary layer vortical lines (mechanism "2" above) is somewhat less important. At the other extreme, diffusion does not appear to be a factor in the dynamics of the unsteady vortical features.
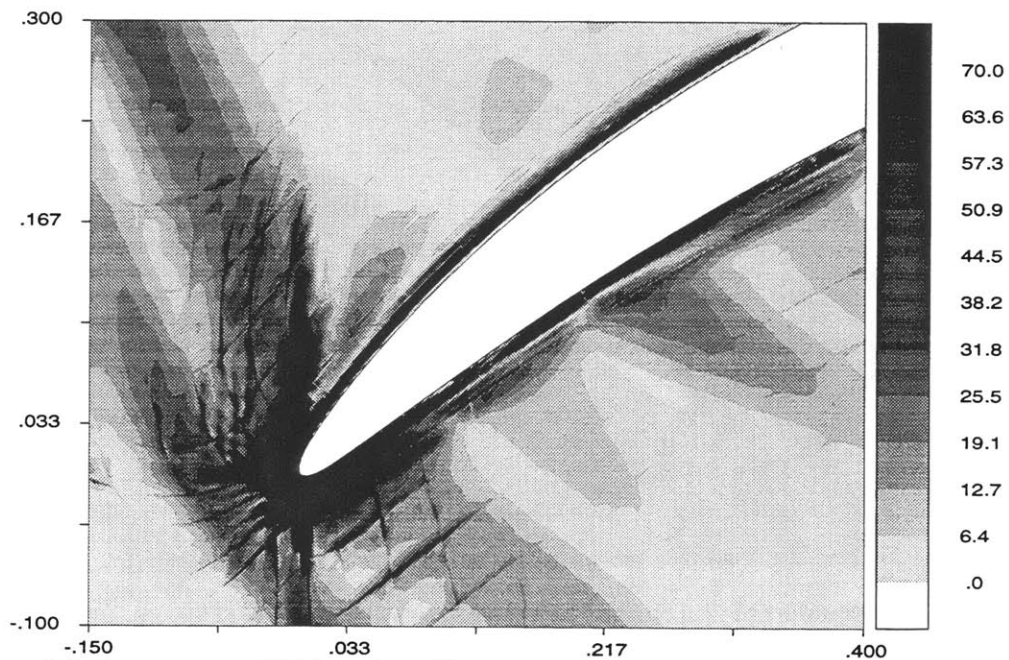
Figure 5.5. Isocontours of $|\mathbf{T}_1|$ on the 92% span blade-to-blade plane at time t_0. This quantity represents the rate of disturbance vorticity production by means of normal displacement of base flow vortical "filaments". Such production occurs near the blade surface (involving spanwise filaments), and to a lesser extent near the casing (involving endwall BL vortex filaments). A correlation with **Figure 5.3** shows this term to be dominant in regions that produce normal vortical disturbances.
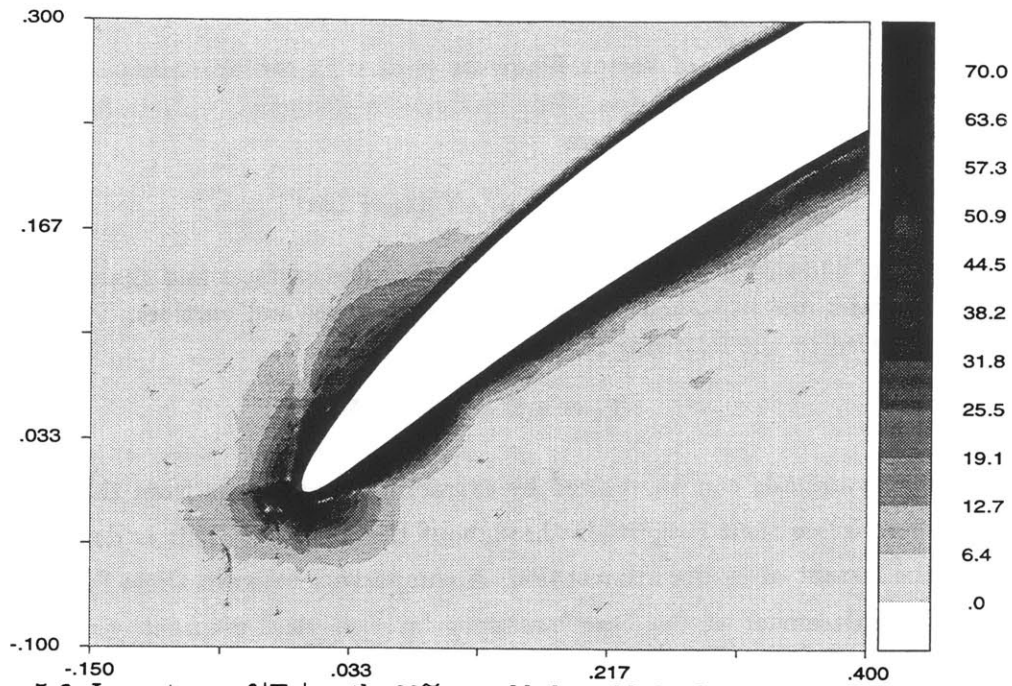
Figure 5.6. Isocontours of $|\mathbf{T}_2|$ on the 92% span blade-to-blade plane at time t_0. This quantity represents the rate of disturbance vorticity production by means of tipping and stretching of base flow vortical "filaments". Compare to **Figure 5.5**.
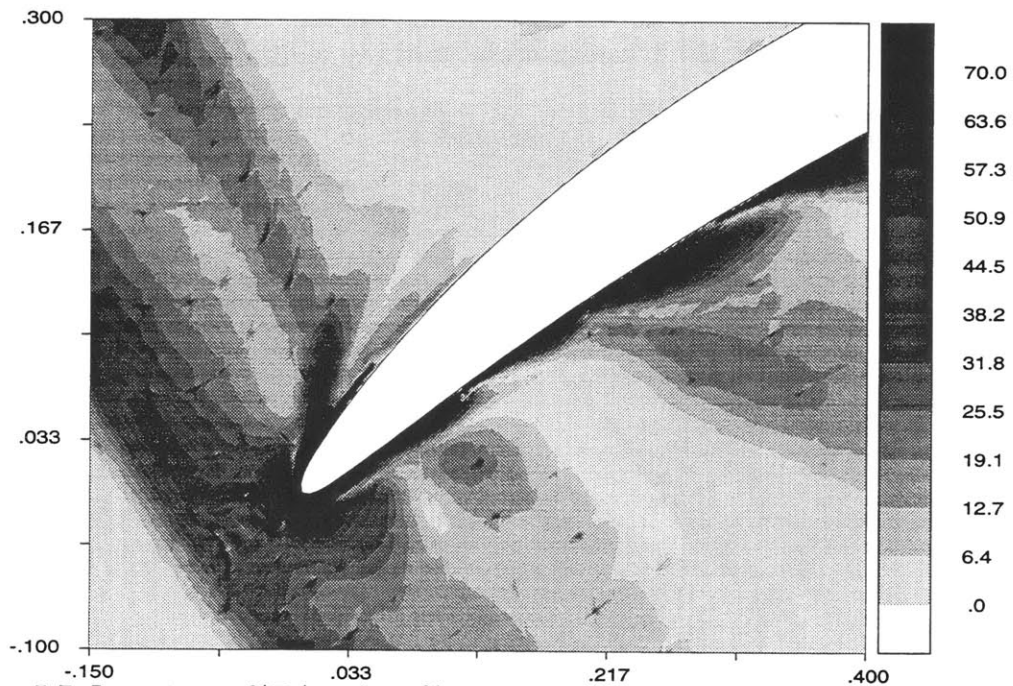
Figure 5.7. Isocontours of $|\mathbf{T}_3|$ on the 92% span blade-to-blade plane at time t_0. This quantity represents the rate of disturbance vorticity production by means of tipping and stretching of disturbance vortical "filaments". Figure shows that such production occurs at the SS leading edge, near the PS, and within the TL vortex core. Correlate with **Figure 5.3** and compare to **Figure 5.5**.
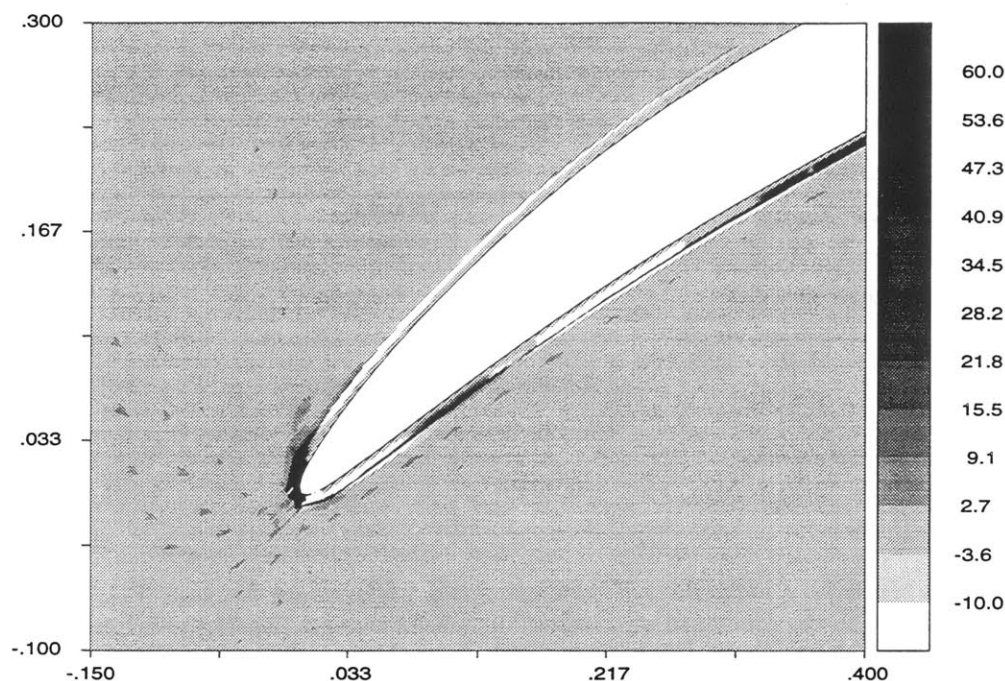
Figure 5.8. Isocontours of $|\mathbf{T}_4|$ on the 92% span blade-to-blade plane at time t_0. This quantity represents disturbance vorticity production by means of diffusion of the fluctuating shear stresses on the blade surface. Compare to **Figure 5.5**.

This comparison does not allow to identify which vortical filaments in particular are distorted to give rise to the vortical disturbances. Such information can be however obtained by comparing the components of $\mathbf{T}_1...\mathbf{T}_3$ in the spanwise and streamwise directions respectively. The comparison in the spanwise direction indicates that N-BLDs are produced by redistribution of spanwise vortical filaments in the blade boundary layers under the "suction" effect of the TL vortex "negative jet". This mechanism is essentially the same as in 2D wake interaction. It explains (1) the morphological similarity between 2D and 3D disturbances, and (2) the absence of such disturbances in computations where the base flow is inviscid (**Figure 4.12a**). The comparison in the streamwise direction shows that S-BLDs are produced primarily by tipping of spanwise vortical filaments in the vortex itself by the velocity gradients in the endwall corner of the base flow.

5.2. Case VD/TL: Time-Average Performance Changes.

Table 5.1 shows the change in performance due to interaction with the tip leakage vortex at design point conditions. The principal difference with respect to the ID/TL case is that the passage loss difference between steady and unsteady flow, $\Delta \mathcal{Y}_p$, increases from 0.0010 to 0.0033 units of $\Delta P_t/Q$. This can be seen by comparing **Table 5.1** to **Table 4.2**.

Both ID/TL and VD/TL cases use a turbulent diffusion model to account for mixing of the disturbances during their transport through the stator. However, they differ because of

the presence of boundary layers in case VD/TL. Therefore, the additional 0.0023 points of loss relative to ID/TL is associated with the response of the boundary layer.

Figure of Merit	Change $(\Delta P_t/Q)$	Change (efficiency pts)	Change (% of steady value)
Passage loss $\Delta \mathcal{Y}_p$	−0.0033	−0.20	−11.0
$\Delta \mathcal{Y}_m = \Delta \mathcal{Y}_e - \Delta \mathcal{Y}_i$ ($\Delta \mathcal{Y}_i = 0.0049$)	+0.0045	+0.29	+15.0
Net loss change $\Delta \mathcal{Y}_n = \Delta \mathcal{Y}_p + \Delta \mathcal{Y}_m$	−0.0012	+0.09	+4.0

Table 5.1. Change in time-average stator performance for case VD/TL relative to the pre-mixed steady flow. Beneficial changes (leading to increased efficiency) are shown as positive quantities.

As shown in **Figure 5.9**, the increase in passage loss is confined to the tip region of the stator (75-95% span). Locally, the increase is rather significant ($\sim$30-50%), and warrants a more detailed analysis of the underlying causes. Howard et al. (1994) have noted a similar increase in stator tip loss when the tip clearance of the upstream rotor is opened up. From a qualitative standpoint, their observations supports our results.

The passage loss increase nearly cancels the loss benefit from reversible recovery of the tip leakage vortex. As a result, there is only about 0.1 efficiency points difference between the time-averaged unsteady flow and the steady flow obtained by mixing the tip vortex at the mid-gap axial plane.

5.2.1. Role of boundary layer response.

There is a strong resemblance between tip leakage vortex and 2D wake interaction, noted above in terms of boundary layer vortical response. The change in time-averaged total pressure $\Delta \overline{C_t}$, is also very similar to that due to 2D wakes when examined on blade-to-blade planes between 80-95% span. This can be appreciated by comparing **Figure 5.10** to **Figure 3.12**. Both figures show the existence of (a) a band of high-loss fluid over the suction side of the stator, and (b) two wide regions of high and low-loss fluid that progressively develop in the middle of the passage. These features are localized between 75-95% span. No significant vortical or total pressure disturbances occur below 75% span. In the ID/TL case, where no boundary layers are present, only feature (b) is observed.

In the 2D wake interaction case, total pressure changes and the subsequent increase in passage loss were attributed to redistribution of spanwise vorticity in the stator passage (cf.

§**3.3.2**). For the present tip vortex interaction case, the same explanation, written below in symbolic form:

$$\frac{d\Delta\overline{C_t}}{dy} \overset{?}{\approx} -2u_s\Delta\overline{\omega_z} \tag{5.05}$$

fits the computed results very well. The agreement is shown in **Figures 5.12a-c** at several axial and spanwise locations, and holds even fairly close to the casing. **Figures 5.11a-c** confirm that the total pressure changes in **Figure 5.10** are due to a re-arrangement of vortex filaments normal to the flow direction. On the basis of correlating total pressure and vorticity changes using (5.05), two mechanisms involving different vortex filaments can be identified in the unsteady flow:

1) Spanwise vorticity fluctuations in the suction surface boundary layer (N-BLDs, §**5.1.2**) are associated with a high-loss band over the suction surface of the stator.

2) Migration and piling of vortical fluid against the pressure surface of the stator leads to the two regions of low and high P_t that progressively develop in the middle of the passage. It leads to segregation of high-entropy vortex fluid in the circumferential direction.

Mechanism (2) above is present in both ID/TL and VD/TL computational experiments, while mechanism (1) is present in the VD/TL case only. This indicates that normal distortion of the suction side boundary layer is the cause for the noticeable passage loss increase in case VD/TL. In physical terms, the "suction" effect of the tip leakage vortex transports high-entropy boundary layer fluid from near the wall towards regions of higher mass flux. This leads to increased loss in the tip region of the stator.

The normal distortion mechanism is the same as the one responsible for the passage loss increase in 2D wake interaction. In the VD/TL case, this mechanism appears to be operating on a locally two-dimensional basis. The common origin of passage loss increase suggests that the 2D model of §**3.3.2** can be extended to the three-dimensional tip vortex interaction. This extension, carried out in §**J.4.2**, relates the increase in passage loss $\Delta\mathcal{Y}_p$, to the steady flow loss distribution on the blade $\mathcal{Y}_p$, and to the time-average disturbance velocity transverse to the boundary layer $\overline{\Delta V_n}$:

$$\Delta\mathcal{Y}_p \approx 2\frac{\Delta V_n}{U}\mathcal{Y}_{ps} \tag{5.06}$$

From a design standpoint, it can be shown that ΔV_n is proportional to the clearance-related blockage A_b/A_e as defined by Khalid (1995). It also depends on the angle between the vortex core and the stator stagger axis (5.07).
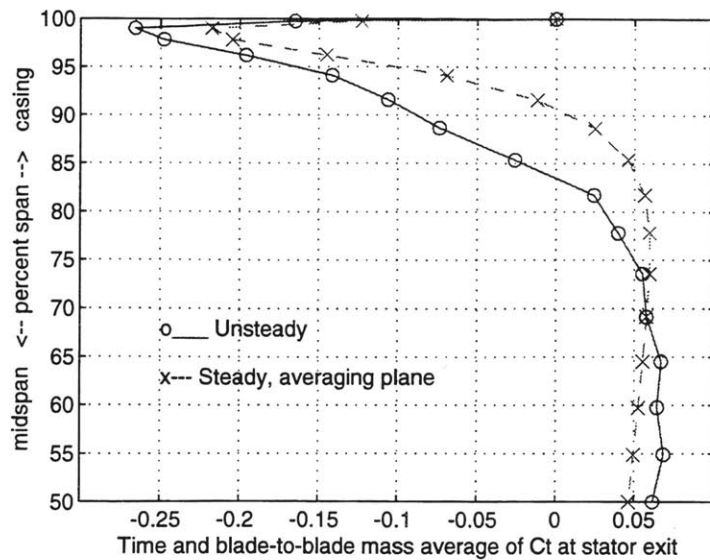
Figure 5.9. Distribution of time and blade-to-blade mass averaged flux of total pressure $\int \overline{uC_t} dy$ leaving the stator at various spanwise locations, for both unsteady and steady pre-mixed flows. Large negative values are indicative of high loss. Note the increase of loss in the tip region in the unsteady case.
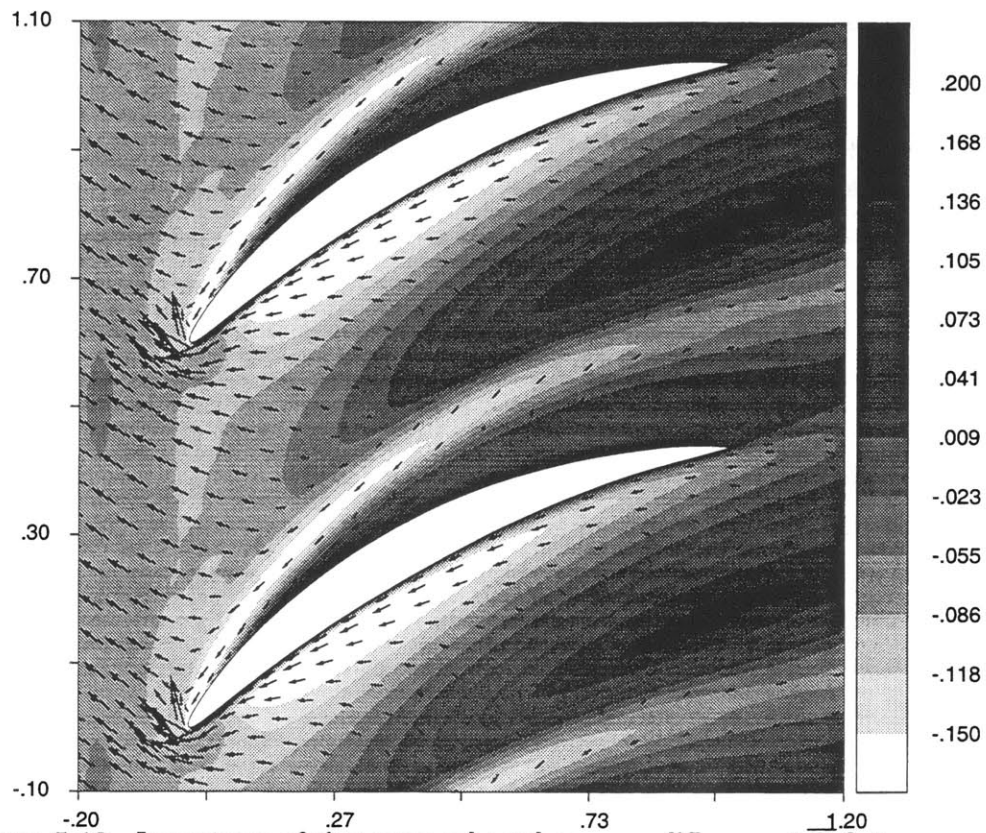
Figure 5.10. Isocontours of time-averaged total pressure difference $\Delta \overline{C_t}$ between unsteady and steady flow on the 91% blade-to-blade plane. This plane passes approximately through the center of the TL vortex core. Figure shows an area with distinct C_t decrease coincident with the trajectory of the BLDs. Compare with **Figure 3.12**.
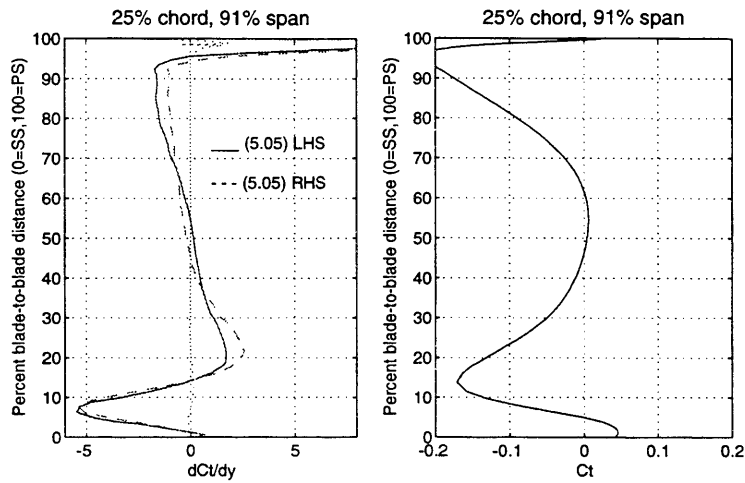
Figure 5.11a. Right: Blade-to-blade profile of $\Delta \overline{C_t}$ at 91% span and 25% axial chord. Left : Correlation with time-averaged redistribution of spanwise vorticity $\Delta \overline{\omega_z}$ for the profile at right.
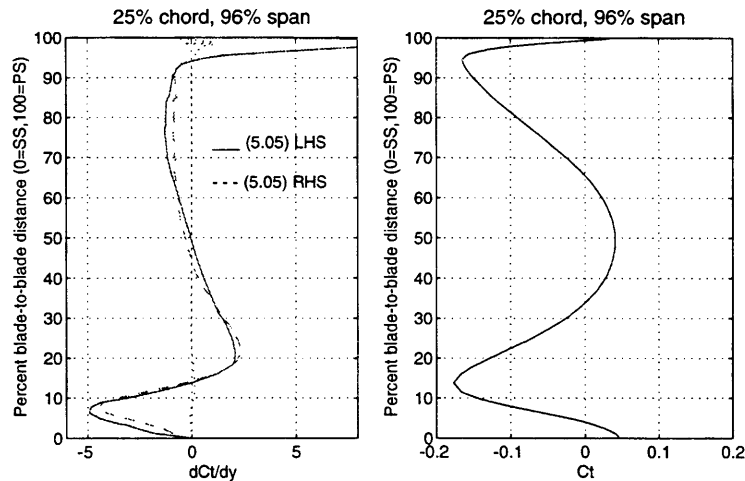
Figure 5.11b. Right: Blade-to-blade profile of $\Delta \overline{C_t}$ at 96% span and 25% axial chord. Left : Correlation with time-averaged redistribution of spanwise vorticity $\Delta \overline{\omega_z}$ for the profile at right.
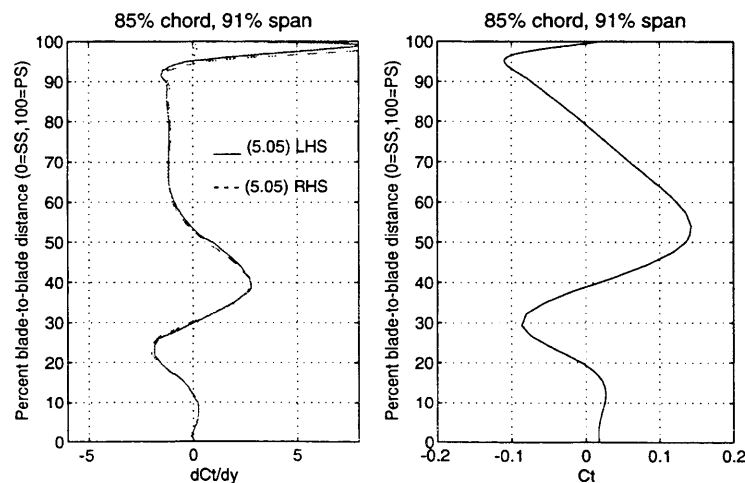
Figure 5.11c. Right: Blade-to-blade profile of $\Delta \overline{C_t}$ at 91% span and 85% axial chord. Left : Correlation with time-averaged redistribution of spanwise vorticity $\Delta \overline{\omega_z}$ for the profile at right.

$$\Delta V_n \sim V_2 \frac{A_b}{A_e} \sin \chi \tag{5.07}$$

In the present case, $A_b/A_e = 0.04, \sin \chi \approx 1, \mathcal{Y}_{p,s} = 0.03$. With these values, (5.06) yields a passage loss increase of 0.0021 units of dynamic head. This is reasonably close to the increase computed here (0.0033 units, from which 0.0010 units due to vortex turbulent diffusion need to be taken out). Equation (5.06) can be used to determine how $\Delta \mathcal{Y}_p$ scales with changes in design. For this purpose, one may use Khalid's (1995) finding that the tip clearance flow blockage in compressors scales (a) proportionally to tip clearance size, and (b) as a power of a rotor tip loading parameter.

5.2.2. Role of unsteady secondary flows.

The foregoing analysis indicates that the main mechanism for passage loss increase, $\Delta \mathcal{Y}_p$, in the VD/TL case is the normal distortion of spanwise vortex filaments. This section shows that unsteady streamwise vorticity in the stator is not important for loss production. This is accomplished by splitting the vorticity vector in streamwise and normal components, and making use of (I.46) to separate their contributions to $\Delta \mathcal{Y}_p$.

$$A \frac{d \Delta \mathcal{Y}_p}{dx} = \iint_x \overline{\Delta \nu \omega_n^2} dA + \iint_x \overline{\Delta \nu \omega_s^2} dA \tag{5.08}$$

The ratio of normal to streamwise vorticity terms in (5.08) can be used to express the relative importance of unsteady streamwise vorticity for loss. **Figure 5.12** shows the distribution of this ratio as a function of axial location.
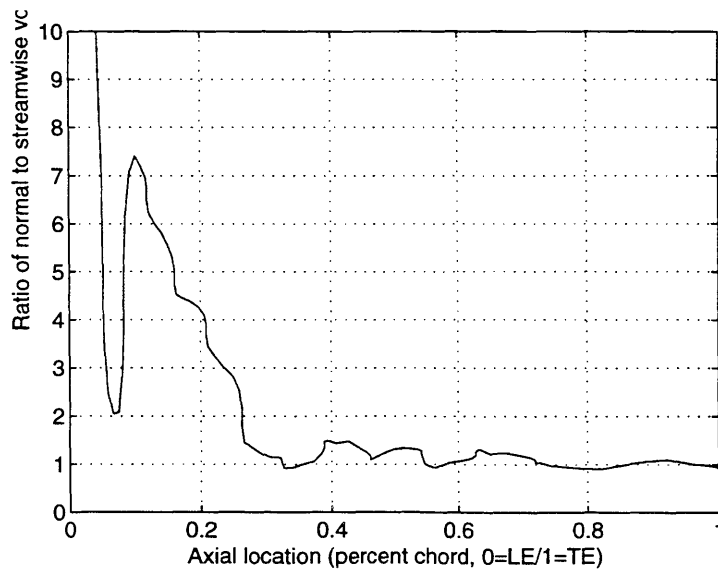
Figure 5.13. Absolute value of $\iint \overline{\Delta \nu \omega_n^2} dA / \iint \overline{\Delta \nu \omega_s^2} dA$ vs. axial location.

Over the critical front third of the stator, the contribution of $\Delta\bar{\omega}_n$ is 2-10 times larger than that of $\Delta\bar{\omega}_s$, despite the presence of significant streamwise vorticity fluctuations. Equation (2.07) provides an answer to this apparent paradox. When disturbance vorticity vectors are aligned with the base flow vorticity, their contribution to loss may be far larger, relative to the case where disturbance and base flow vortex filaments are at right angles. Although normal and streamwise vorticity fluctuations observed in the flow are of similar magnitude, the latter are perpendicular to the boundary layer vorticity. As a result, the contribution of streamwise vorticity fluctuations to passage loss is relatively small.

5.2.3. Role of reversible recovery.

Recovery of the tip leakage vortex energy is the main beneficial aspect of rotor-stator interaction. The performance benefit from recovery in the VD/TL case is virtually identical to that in the ID/TL case. The loss figures indicate that this recovery is not significantly affected by turbulent diffusion of the vortex core, or by distortion of core vortical filaments due to the presence of endwall boundary layers.

It is to be noted that recovery of the vortex energy proceeds at the same rate as that of 2D wakes (cf. §4.3.2). This explains the recovery of a substantial fraction ($\sim 75\%$) of the kinetic energy present at the inlet in the TL vortex. For 2D wakes, **Figure 3.11** indicates that most of the energy is recovered over a lengthscale of about 0.25 chords. On the orher hand, distortion takes place over lengthscales comparable to one chordlength. Therefore, vortex energy is recovered before distortion can significantly change the dynamics of recovery.

A similar, albeit subtler, argument can explain why turbulent diffusion does not affect recovery. The argument relies on the assumption that TL vortex diffusion proceeds at a rate similar to that of wakes. Stauter et al. (1991) surveys indicate that the lengthscale over which turbulent diffusion alone would significantly dissipate wakes entering the stator is of the order of 0.5-1.0 blade chords. Therefore, vortex energy is recovered faster than it is dissipated. These considerations offer a plausible explanation for the almost full recovery of the energy in upstream wakes and tip leakage vortices observed.

5.3. Case VD/SW: Time-Average Performance Changes.

The effects of upstream streamwise vortices on stator performance are radically different from those of tip leakage vortices. As shown in **Table 5.2**, streamwise vortices lead to a passage loss increase of about 0.3 efficiency points. While this value is similar to the "inviscid" ID/SW case, a comparison between **Table 5.2** and **Table 4.1** reveals two significant differences. First, the vortex is attenuated instead of being amplified ($\Delta y_e > \Delta y_i$ for ID/SW,

$\Delta \mathcal{Y}_e < \Delta \mathcal{Y}_i$ for VD/SW). Second, the passage loss increase due to unsteadiness, $\Delta \mathcal{Y}_p$, is substantially larger with respect to the ID/SW case.

Figure of Merit	Change $(\Delta P_t/Q)$	Change (efficiency pts)	Change (% of steady value)
Passage loss $\Delta \mathcal{Y}_p$	−0.0062	−0.38	−21.0
$\Delta \mathcal{Y}_m = \Delta \mathcal{Y}_e - \Delta \mathcal{Y}_i$ ($\Delta \mathcal{Y}_i = 0.0045$)	+0.0019	+0.12	+6.5
Net loss change $\Delta \mathcal{Y}_n = \Delta \mathcal{Y}_p + \Delta \mathcal{Y}_m$	−0.0042	-0.26	−14.6

Table 5.2. Change in time-average stator performance for case **VD/SW** relative to the pre-mixed steady flow. Beneficial changes (leading to increased efficiency) are shown as positive quantities.

5.3.1. Role of vortex transport.

The presence of endwall and blade boundary layers is the only difference between the ID/SW and VD/SW cases. While the vortex core was clearly delineated and stretched in the ID/SW case, this does not occur in the VD/SW case. With a viscous base flow, the SW vortex core appears "smeared" in the blade-to-blade direction (**Figure 5.13**). Differential convection rates for vortex filaments inside the endwall boundary layer are the most likely explanation for the vortex core distortion.

This change in core structure makes vortex stretching less effective in adding kinetic energy. As a result of diffusion, the mixing loss at the exit of the stator, $\Delta \mathcal{Y}_e$, decreases with respect to the ID/SW case. This is shown in **Figure 5.14**, and explains the apparent mixing loss benefit from passing the vortex core through the stator.

5.3.2. Role of boundary layer response.

The increase in passage loss $\Delta \mathcal{Y}_p$ in the VD/SW case is about six times larger than that in the ID/SW case. Since the same core flow diffusivity is retained in both cases, this increase suggests that SW vortex interaction induces boundary layer disturbances that lead to net loss. The time-averaged streamwise and normal vorticity components of these boundary layer disturbances are shown in **Figures 5.16** and **5.17**. In these figures, the disturbance vorticity $\Delta \omega_{ID}$ from the ID/SW case, has been subtracted from the viscous flow disturbance vorticity $\Delta \omega_{VD}$. In this manner, only boundary layer disturbance vorticity remains.

Figure 5.15 shows that the BL disturbances induced by the SW vortex are inherently three-dimensional in nature. A strong streamwise vortex is present over the suction surface

of the stator. The spanwise location of this feature is coincident with the position of the SW vortex core (which has been deliberately made "invisible" in the manner described above). A normal vortical component (not shown) is also present along with the streamwise component.

A possible explanation for these features is the uplifting of boundary layer vortical filaments by the "tornado-like" velocity and static pressure fields associated with the SW vortex core.
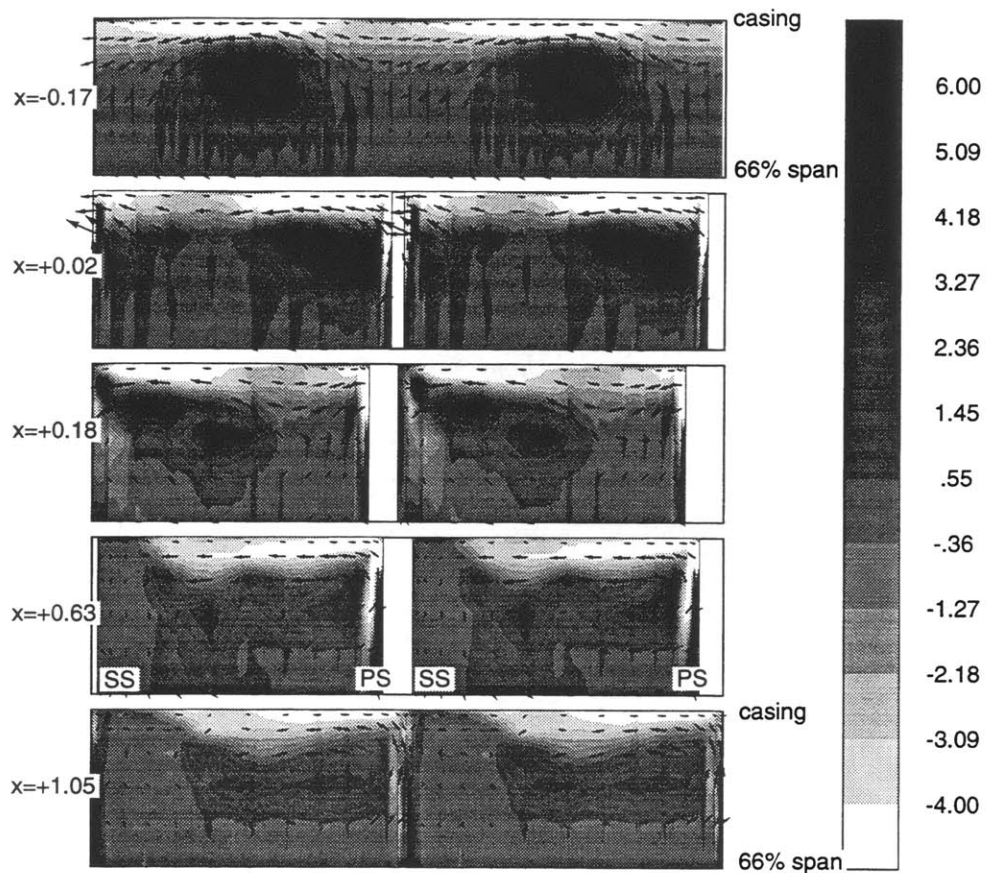
Figure 5.13. Disturbance normal vorticity $\Delta\omega_n$ and crossflow velocity vectors $\Delta\mathbf{u}$ at five successive crossflow planes at the time of vortex interception. Compare to **Figure 4.2** to appreciate the distortion of the streamwise vortex core.
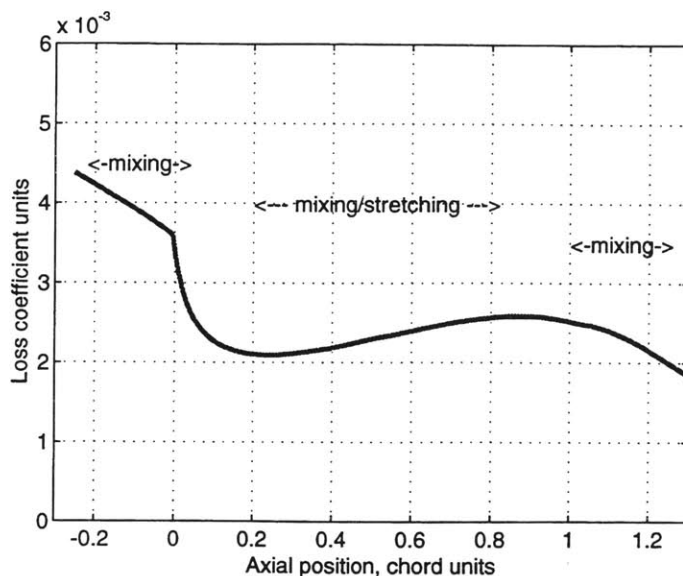
Figure 5.14. Approximate time-average secondary kinetic energy $\mathcal{E}$ of the unsteady flow at different axial locations (LE at x=0, TE at x=1) for case VD/SW. Vortex stretching causes $\mathcal{E}$ to increase, mixing has opposite effect. In comparison to **Figure 4.9**, vortex stretching is not as effective in increasing $\mathcal{E}$..
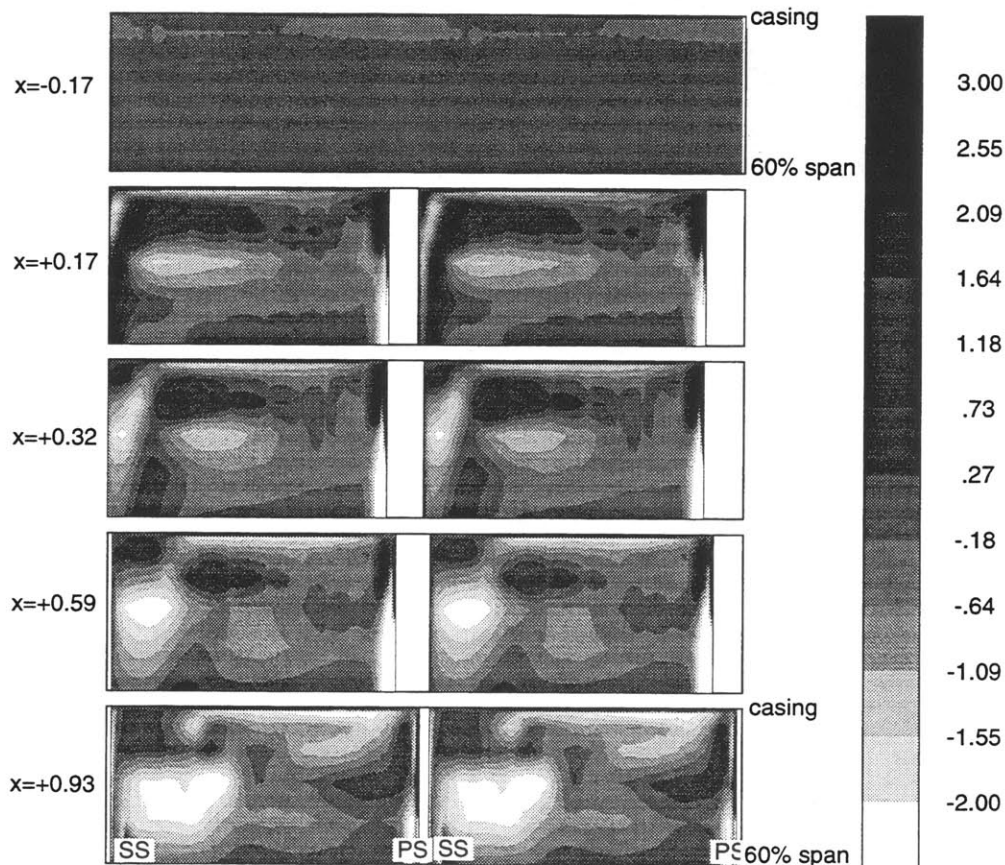
Figure 5.15. Distribution of $\Delta\overline{\omega}_{s,VD/SW} - \Delta\overline{\omega}_{s,ID/SW}$ on successive crossflow planes. Note the development of a streamwise vortex from the SS boundary layer, starting from midchord onwards.

5.4. Viscous Vortex-Stator Interaction: Summary.

The interaction between upstream vortices and base flow boundary layers has an important effect on stator performance and unsteady flow features. Interaction with simple streamwise vortices is detrimental for performance. Rotor tip leakage vortices are processed in a manner different from the simple streamwise vortices. For the geometry and operating conditions considered, it was found that:

- Most of the tip leakage vortex energy is recovered during its transport through the stator ($\sim$75% in the present case). This results in a loss benefit of 0.3 efficiency points. The recovery scales in the same way as that of a 2D inviscid wake (Smith, 1966), and is not significantly affected by diffusion or vortex core distortion.

- A noticeable increase in passage loss ($\sim$0.2 efficiency points) occurs in the tip region of the stator in the presence of a tip leakage vortex. Such an increase is not observed in calculations where the base flow is inviscid. The increase is due to normal displacement of high-entropy boundary layer vortical fluid by the "negative jet" velocity of the tip leakage vortex. This mechanism is identical to that in 2D wake-stator interaction.

- This passage loss increase nearly cancels the benefit from vortex energy recovery. The overall stator passage loss decreases by about 0.1 efficiency points, relative to the mixed-out steady flow assumption. From design standpoint, this is a small effect.

There is no time-resolved flowfield data that allows to assess the computed results. Some indirect assessment is possible though, provided one is careful when using data obtained under different test conditions. The spanwise extent and the magnitude of passage loss increase computed here are in accord with Howard's (1994) measurements of stator loss behind a rotor for two different tip clearances. Dawes' (1994) unsteady simulations indicate the existence of boundary layer disturbances, similar to those shown here. Graf's (1996) full-stage computational study shows a stator passage loss increase relative to the averaging-plane steady flow case. The increase is small at baseline loading, and noticeable ($\sim$30%) at high stage loading.

From a loss standpoint, the upstream tip leakage vortex interacts with the stator in the same manner as a two-dimensional upstream wake. This important finding suggests a unified treatment for those upstream disturbances primarily associated with velocity defect in the relative frame. Processing of such disturbances by the downstream blade row has two opposite aspects. The first is beneficial, and consists of the recovery of the disturbance energy without significant entropy increase. The second is detrimental, and involves an increase of passage loss due to motion of boundary layer vortex filaments normal to the main flow direction under the effect of the disturbance jet-like velocity field. The next chapter examines the sensitivity of these mechanisms to operating parameters and vortex structure.

Chapter 6

Sensitivity Study of Vortex/Stator Interaction

The purpose of this chapter is to examine the sensitivity of tip leakage vortex interaction to axial spacing, vortex structure and stator operating parameters. The following five computational experiments are carried out for this purpose. In each experiment, only a single parameter is changed with respect to the VD/TL case of **Chapter 5**. The VD/TL case corresponds to design-point viscous flow interaction, and serves as a basis for comparison.

- **VD/TM.** Parameter: The disturbance velocity prescribed at the inlet is scaled up by a factor of 1.41 with respect to case VD/TL. Purpose: Assess the effect of axial spacing.

- **VD/TP.** Parameter: Crossflow velocity component of tip leakage vortex in rotor frame set to zero. Purpose: Assess the relative importance of crossflow versus velocity defect in the vortex core for stator loss.

- **VH/TL.** Parameter: Stator loading increased ($\phi = 0.38$, midspan $\theta_1 = 51°$, DF=0.52). Purpose: Assess the ffect of loading on vortex-stator interaction. Note that the TL vortex is the same as in the baseline VD/TL case.

- **VS/TL.** Parameter: Inlet profile to stator (at design point loading). A profile with high shear, representative of an embedded stage, is used. Purpose: Assess the effect of base flow three-dimensionality on interaction.

- **2D/TL.** Parameter: Solver modified to execute two-dimensional simulations of vortex interaction on independent planes stacked along the span. Purpose: Verify the hypothesis that 3D tip leakage vortex and 2D wake interaction with the stator can be described in the same terms.

6.1. Sensitivity to Tip Leakage Vortex Parameters.

6.1.1. Case VD/TM : closely-coupled blade rows.

Since the position of the inlet boundary of the computational domain is held fixed, reduc-
tion of axial spacing between the rotor and the stator is represented by scaling the disturbance
velocity prescribed at the inlet of the stator in the VD/TL case by a factor f_x:

$$f_x = \exp\left[-2.295\frac{d_{reduced} - d_{design}}{2c}\right] \tag{6.01}$$

This equation is based on the assumption that the tip leakage vortex diffuses at the same
rate as rotor wakes, and uses a correlation proposed by Stauter et al. (1991) for wake decay
in a research compressor. Wake data is used to determine the amount by which the nominal
vortex needs to be scaled, since (a) no such information could be found for tip leakage
vortices, and (b) tip leakage and wake flows appear to be related (Khalid, 1995). Equation
(6.01) shows that a factor of 1.41 is required to simulate the reduction in axial spacing from
0.37 to 0.07 chords in Smith's (1970) experiment. The scaled-up tip leakage vortex is then
used as inlet boundary conditions in the computation.

The effects of the stronger tip vortex on stator performance are shown in **Table 6.1**.
First, the amount of energy that is reversibly recovered is significant ($\sim$0.5-0.6 efficiency
points). However, the increase in passage loss is also appreciable ($\sim$0.3-0.4 efficiency points).
As a result, the net performance effect of processing the tip leakage vortex remains small
($\sim$0.2 points relative to the case where the vortex is mixed at the mid-gap axial plane).

Figure of Merit	Change $(\Delta P_t/Q)$	Change (efficiency pts)	Change (% of steady value)
Passage loss $\Delta \mathcal{Y}_p$	−0.0062	−0.39	−20.0
$\Delta \mathcal{Y}_m = \Delta \mathcal{Y}_e - \Delta \mathcal{Y}_i$ $(\Delta \mathcal{Y}_i = 0.0100)$	+0.0094	+0.59	+31.3
Net loss change $\Delta \mathcal{Y}_n = \Delta \mathcal{Y}_p + \Delta \mathcal{Y}_m$	+0.0034	+0.20	+11.3

Table 6.1. Change in time-average stator performance for case **VD/TM**
relative to pre-mixed steady flow. Beneficial changes (leading to increased
efficiency) are shown as positive quantities. Compare to **Table 5.1**.

Examination of the disturbance vorticity and total pressure fields indicates that the larger
performance changes in case VD/TM, relative to the baseline case VD/TL, are simply due

to the larger velocity non-uniformity in the vortex, and not to new causal mechanisms. This is illustrated by comparing **Figure 6.1** to **Figure 5.3a**. The comparison shows unsteady vortical fields that differ in magnitude but not in nature.
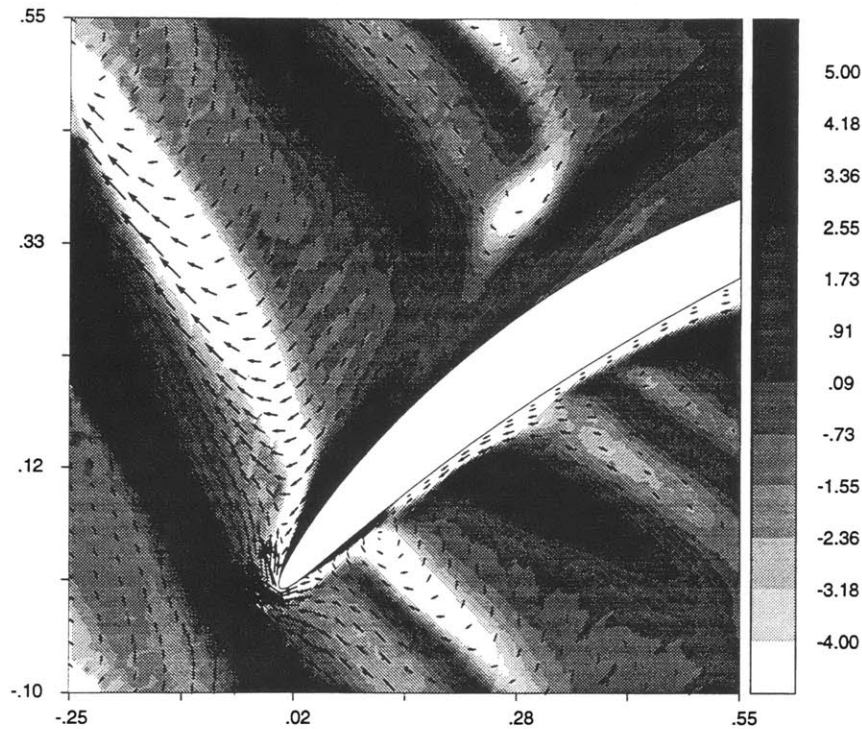
Figure 6.1. Disturbance spanwise vorticity $\Delta\omega_z$ on the 91% span blade-to-blade plane at the instant of vortex interception. Case VD/TM (strong vortex). The flowfield is qualitatively similar to that shown in **Figure 5.3a** (baseline vortex).

In summary, the VD/TM case indicates that bringing the blade rows closer together increases the importance of tip vortex/stator interaction. The increase is however small, and makes up for only a fraction of the overall improvement observed by Smith (1970).

6.1.2. Case VD/TP : effect of TL crossflow.

The purpose of the VD/TP computational experiment is to prove that the velocity defect associated with the vortex core is the main cause for changes in performance. This hypothesis is strongly suggested by the unsteady mechanisms identified in **Chapter 5**. In the VD/TP case, the leakage crossflow associated with the tip vortex in the rotor relative frame is removed. Only the velocity defect is retained, so that the vortex velocity profile is identical in nature to that of a wake.

The effects of the altered vortex can be assessed by comparing the results in **Table 6.2** to those in **Table 5.1**. The increase in passage loss, $\Delta\mathcal{Y}_p$, is not significantly different from

that in the baseline VD/TL case. This is in accord with the model proposed in §5.2.1, which links $\Delta \mathcal{Y}_p$ to the velocity disturbance normal to the boundary layer, ΔV_n. Given the relative orientation between rotor and stator blades, crossflow disturbances in the rotor frame appear parallel to the stator surface, while velocity defect disturbances are perpendicular to the surface. Removing the crossflow component of the vortex does not significantly affect ΔV_n. Consequently, boundary layer vortical disturbances (**Figure 6.2**) and the resulting passage loss changes are similar to those in the baseline VD/TL case.

Figure of Merit	Change $(\Delta P_t/Q)$	Change (efficiency pts)	Change (% of steady value)
Passage loss $\Delta \mathcal{Y}_p$	-0.0040	-0.24	-13.0
$\Delta \mathcal{Y}_m = \Delta \mathcal{Y}_e - \Delta \mathcal{Y}_i$ ($\Delta \mathcal{Y}_i = 0.0036$)	$+0.0030$	$+0.19$	$+10.0$
Net loss change $\Delta \mathcal{Y}_n = \Delta \mathcal{Y}_p + \Delta \mathcal{Y}_m$	-0.0010	-0.06	-3.0

Table 6.2. Change in time-average stator performance for case **VD/TP** relative to the pre-mixed steady flow. Beneficial changes (leading to increased efficiency) are shown as positive quantities.
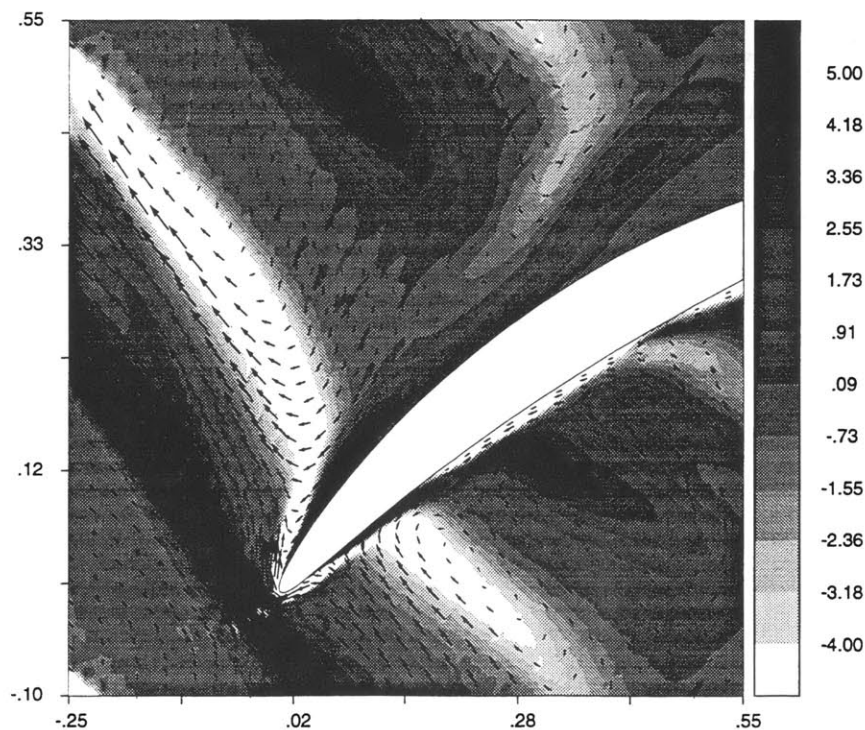
Figure 6.2. Disturbance spanwise vorticity $\Delta \omega_z$ on the 91% span blade-to-blade plane at the instant of vortex interception. Case VD/TP (rotor frame crossflow component in vortex core removed). Compare to **Figure 5.3a** .

On the other hand, the crossflow component accounts for about one-third of the energy in the vortex at the inlet of the stator (second line of **Table 6.2** and **6.1**). As a result, the benefit from reversible recovery is not as large as in the baseline VD/TL case.

In summary, the VD/TP computational experiment indicates that the velocity defect in the tip leakage vortex is the most important factor in inducing unsteady flow and in affecting the performance of the downstream stator.

6.2. Sensitivity to Base Flow Parameters.

6.2.1. Case VH/TL : increased stator loading.

The purpose of the VH/TL computational experiment is to determine the effect of stator loading on the unsteady flow and the performance changes due to upstream tip leakage vortices. This is achieved by using a steady stator base flow at loading that corresponds to unstalled operation near the peak of the characteristic ($\phi = 0.38$, midspan $\theta_1 = 51°$, DF$=0.52$, cf. **Figure A.1**). This base flow is described in §**G.5**. It is characterized by increased boundary layer thickness at the suction side leading edge, and by increased loss relative to the design-point VD base flow.

In practice, increasing the stage loading also results in a "stronger" tip leakage vortex. Here however, the upstream vortex is kept the same as in the baseline VD/TL case. In this manner, stator loading effects are separated from other changes in the flowfield.

Figure of Merit	Change $(\Delta P_t/Q)$	Change (efficiency pts)	Change (% of steady value)
Passage loss $\Delta \mathcal{Y}_p$	-0.0016	-0.1	-5.0
$\Delta \mathcal{Y}_m = \Delta \mathcal{Y}_e - \Delta \mathcal{Y}_i$ ($\Delta \mathcal{Y}_i = 0.0052$)	$+0.0048$	$+0.3$	$+16.0$
Net loss change $\Delta \mathcal{Y}_n = \Delta \mathcal{Y}_p + \Delta \mathcal{Y}_m$	$+0.0032$	$+0.2$	$+11.0$

Table 6.3. Change in time-average stator performance for case **VH/TL** relative to the pre-mixed steady flow. Beneficial changes (leading to increased efficiency) are shown as positive quantities.

Passage loss. The most significant effect of increasing the stator loading is to reduce the increase in passage loss, $\Delta \mathcal{Y}_p$, due to the upstream vortex (**Table 6.3**). The reduction is not substantial, but (at first sight) runs contrary to the simplified loss model for $\Delta \mathcal{Y}_p$

proposed at the end of §J.3. This model states that $\Delta \mathcal{Y}_p$ is proportional to the average velocity disturbance normal to the blade, ΔV_n (identical in cases VD/TL and VH/TL) and to the base flow loss, $\mathcal{Y}_{p,s}$ (higher in VH/TL than VD/TL). According to (6.02), $\Delta \mathcal{Y}_{p,s}$ should increase at high loading. A comparison between **Table 6.3** and **Table 5.1** shows however the opposite.

$$\Delta \mathcal{Y}_p \approx 2\frac{\Delta V_n}{U} \mathcal{Y}_{p,s} \qquad (6.02)$$

This contradiction is resolved if one considers how and where the additional loss $\Delta \mathcal{Y}_p$ is created. According to §5.2.1, $\Delta \mathcal{Y}_p$ arises when the velocity field of the upstream vortex distorts the boundary layer, lifting high-entropy fluid away from the surface into the free-stream. This happens mostly in the front part of the blade where ΔV_n is largest. **Figure 6.3** shows that the VH base flow has actually a lower loss than the VD base flow over that part of the blade. Therefore, the boundary layer distortion process above has less of a performance impact with the VH base flow. The passage loss degradation $\Delta \mathcal{Y}_p$ at high loading is thus smaller than that at design point loading.
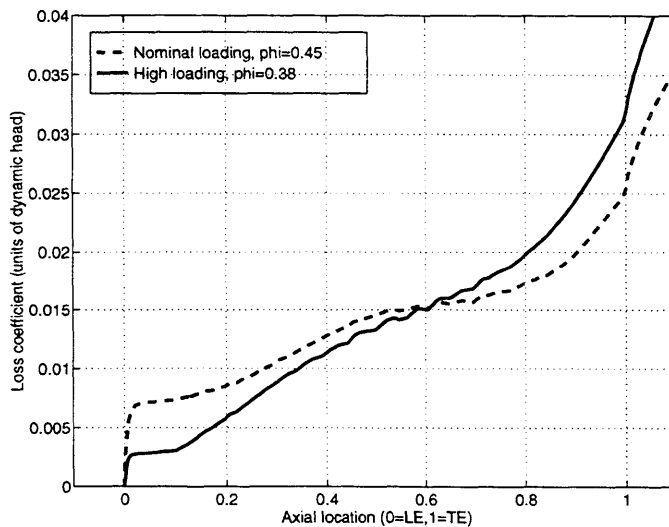
Figure 6.3. Distribution of steady flow passage loss $\mathcal{Y}_{p,s}$ as a function of axial distance into the stator, at high and at design-point loading.

This finding suggests that the passage loss increase due to wakes and tip leakage vortices can be reduced by tailoring the loss distribution on the blade. All other parameters being equal, the passage loss increase would be smaller for geometries where most of the steady-state loss is generated in the aft portion of the blade section. This dependency can be captured by the full equation from which the simplified model (6.02) is derived. The full equation takes into account the axial variation of the loss production rate, $d\mathcal{Y}/dx$.

$$\Delta \mathcal{Y}_p \approx \frac{6}{U} \int_{LE}^{TE} x \Delta V_n(x) \frac{d\mathcal{Y}_{p,s}}{dx} dx \qquad (6.03)$$

Recovery of tip leakage vortices. In principle, the benefit from recovery of wakes and tip vortices is also linked to loading in an indirect manner, through the amount of flow turning. A larger portion of the disturbance energy is recovered for high flow turning angles. With the present geometry however, most of this energy is already recovered at design point flow turning. Therefore, **Table 6.3** shows no change in the mixing loss benefit, $\Delta \mathcal{Y}_m$, with respect to the design-point VD/TL case.

Unsteady flow features. From a qualitative standpoint, the disturbance flowfield $(\Delta \mathbf{u}, \Delta \omega)$ is similar to that at design-point loading. This is illustrated in **Figure 6.4**, and suggests that no new unsteady loss mechanisms arise for highly-loaded unstalled blading.

Figure 6.4. Disturbance spanwise vorticity $\Delta \omega_z$ on the 91% span blade-to-blade plane at the instant of vortex interception. Case VH/TL (high stator loading, $\phi = 0.38$). Compare to **Figure 5.3a** .

In summary, the high-loading computational experiment shows that the increase in passage loss depends on the steady state loss distribution, and that the latter can be tailored to reduce this detrimental aspect of rotor-stator interaction.

6.2.2. Case VS/TL : increased base flow three-dimensionality.

The inlet profile to the stator, used to obtain the baseline VD base flow, is relatively uniform. This profile is based on data from a low-speed research compressor, which has four stages. In multistage machines however, the inlet velocity profiles to embedded blade rows can exhibit substantial spanwise variation (Cumpsty, 1989).

The purpose of the VS/TL computational experiment is to determine the effect of such variation on interaction with tip leakage vortices. This is done by changing the inlet profile of the steady base flow. The inlet profile used, shown in **Figure H.1**, is representative of an embedded stage. The resulting base flow is characterized by stronger secondary flows (produced as the non-uniform flow at inlet is turned by the stator) and by more pronounced spanwise loading variation than the design-point base flow.

The performance effects of the upstream tip leakage vortex with this highly "three-dimensional" base flow are not significantly different from the baseline case. This can be seen by comparing **Table 6.4** to **Table 5.1**. The somewhat larger passage loss increase is due to a higher base flow loss in the tip region of the stator in the VS base flow used. This is in accordance with the unsteady loss passage model discussed above.

Figure of Merit	Change $(\Delta P_t/Q)$	Change (efficiency pts)	Change (% of steady value)
Passage loss $\Delta \mathcal{Y}_p$	−0.0056	−0.35	−19.0
$\Delta \mathcal{Y}_m = \Delta \mathcal{Y}_e - \Delta \mathcal{Y}_i$ $(\Delta \mathcal{Y}_i = 0.0054)$	+0.0051	+0.32	+17.0
Net loss change $\Delta \mathcal{Y}_n = \Delta \mathcal{Y}_p + \Delta \mathcal{Y}_m$	−0.0005	0.	−2.0

Table 6.4. Change in time-average stator performance for case **VS/TL** relative to the pre-mixed steady flow. Beneficial changes (leading to increased efficiency) are shown as positive quantities.

Except for minor changes due to spanwise variation of the velocity at which the vortex is convected, the unsteady flow features are also similar to those observed in the baseline VD/TL computational experiment. This is illustrated by **Figures 6.5a-b** in terms of spanwise and streamwise disturbance vorticity components respectively. It is to be recalled that the disturbance spanwise vorticity is the dominant normal component of the boundary layer disturbances for the unsteady flows considered.
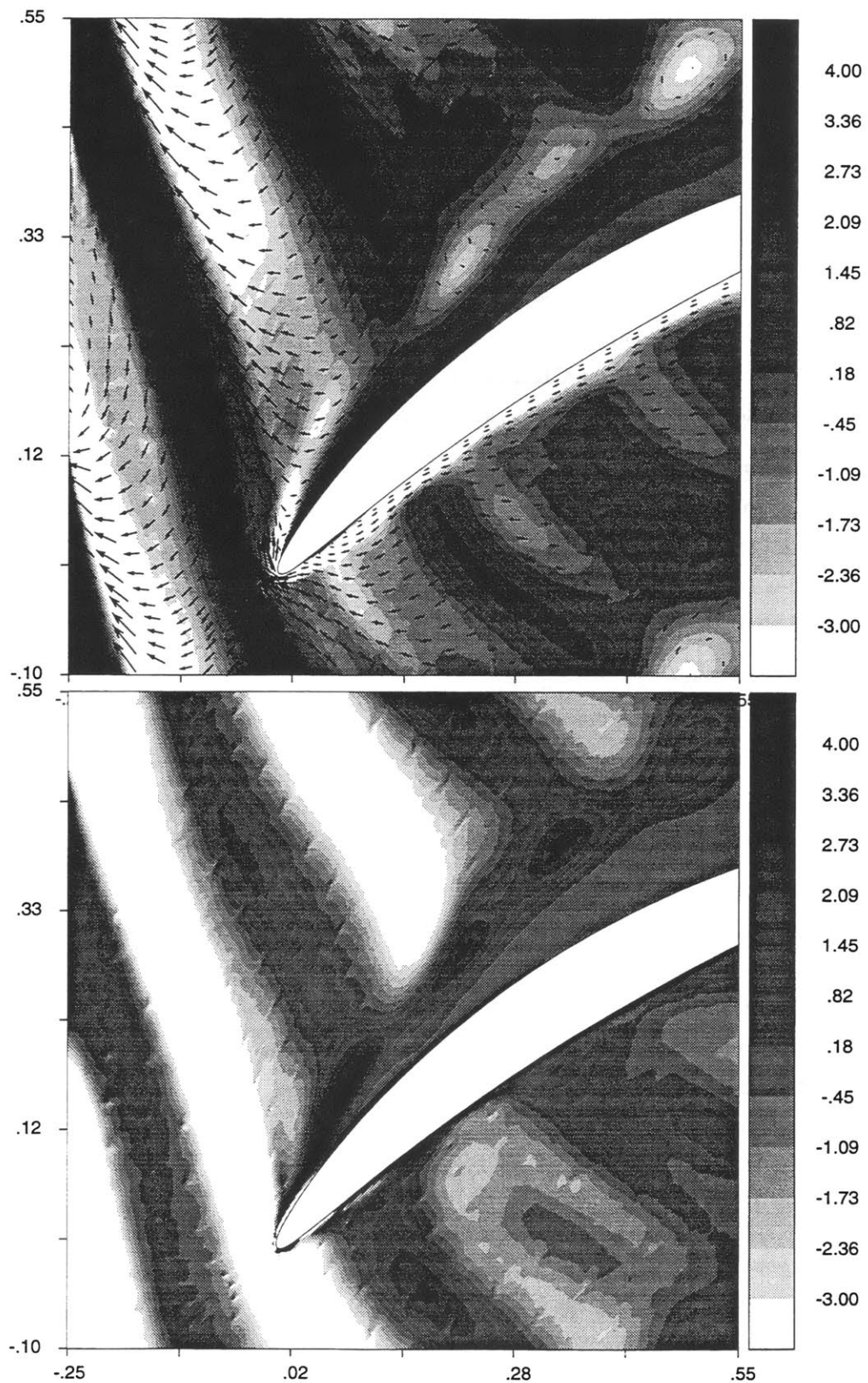
Figure 6.5a (top)/6.5b (bottom). Disturbance flow vortical structure on the 91% span blade-to-blade plane at the instant of vortex interception. Case VS/TL (non-uniform velocity inlet profile to the stator). Top: disturbance spanwise vorticity, compare to **Figure 5.3a**. Bottom: disturbance streamwise vorticity, compare to **Figure 5.5a**.

In summary, the VS/TL computational experiment indicates that the effect of the tip leakage vortex on stator performance is not very sensitive to the three-dimensionality of the base flow. The results also indicate that the detrimental effects of tip vortex interaction might be larger in stators having high tip region loss.

6.3. Effect of Tip Leakage Vortex Fluctuations.

In the results so far, the tip leakage vortex was held steady in the rotor relative frame. However, Graf's (1996) computational study indicates that the vortex core fluctuates in a manner similar to that used in **Chapter 3** for unsteady 2D wakes. For 1:1 blade count, the fluctuation period is 1.6-1.8 times the stator blade passing period.

Due to computational constraints. the effect of such tip vortex fluctuations on the stator performance cannot be assessed in the same direct manner employed for wakes. An indirect argument, drawing on the similarities between wake and tip vortex interaction mechanisms, indicates that such fluctuations are not important with regard to stator performance (It is to be noted that these fluctuations are important for rotor performance, Graf 1996).

Insofar as 2D wake interaction performance effects are concerned, there is no difference between using fluctuating and ensemble-averaged wakes at fluctuation periods larger than 1.5 times the blade passing period (cf. §3.4.2). This is so because the wake properties in such cases vary over a distance larger than the lengthscales associated with the most significant unsteady flow phenomena (reversible recovery, boundary layer distortions).

The results in **Chapter 5**, as well as the VD/TP, VS/TL and 2D/TL computational experiments, suggest that the most important effects of tip leakage vortices on stator performance occur through the same two-dimensional mechanisms that are involved in wake interaction. In this case, the large-period fluctuations in the vortex core would not influence the interaction with the stator. Therefore, the use of an ensemble-averaged vortex that is steady in the rotor frame, is likely to be representative of the effects of interaction with a fluctuating vortex.

6.4. Stacked-Plane Two-Dimensional Approximation.

The purpose of the 2D/TL computational experiment is to confirm the hypothesis that the most important effects of tip leakage vortices on stator performance occur through the same two-dimensional mechanisms that are involved in wake interaction.

This is accomplished by confining the unsteady flow in the stator to a collection of blade-to-blade planes at discrete spanwise locations. While the inlet boundary conditions vary

from plane to plane, the flow on each plane is strictly two-dimensional. This representation of the interaction still retains the three-dimensional geometry of the incoming vortex, but is essentially two-dimensional from a mechanistic standpoint. Thus, the 2D/TL and VD/TL cases differ only in the equations of motion used.

In the aspects relevant to unsteady performance, the unsteady flowfield obtained in this manner is very similar to that of the fully three-dimensional VD/TL simulation. The vortex is attenuated during its transport through the stator. This confirms the conjecture of §4.3.2 that tip vortex recovery can be described in a quasi two-dimensional context. As shown in **Figure 6.6**, the unsteady flow over the suction surface is characterized by spanwise vortical disturbances similar to those discussed in §5.1.2. These disturbances are responsible for the passage loss increase that partly mitigates the benefit from tip vortex recovery.
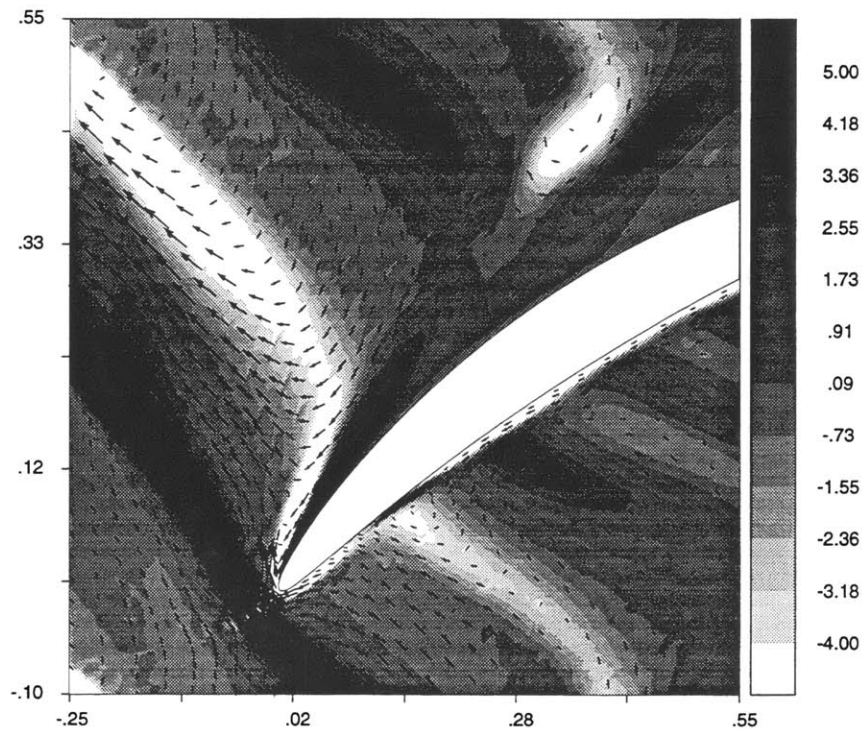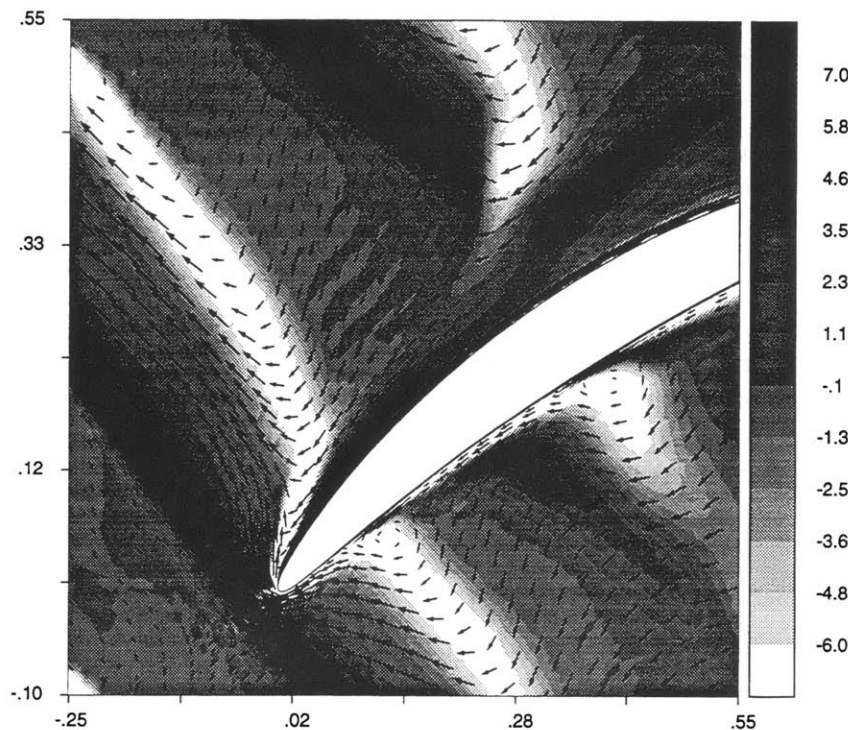

Figure 6.6. Disturbance spanwise vorticity $\Delta\omega_z$ on the 91% span blade-to-blade plane at the instant of vortex interception. Case 2D/TL (disturbances propagate in a two-dimensional manner). Compare to **Figure 5.3a**.

The 2D/TL computational experiment confirms that the tip leakage vortex interacts with the stator in the the same manner as an upstream two-dimensional wake. Together with the results from the VD/TP and VS/TL computations, this finding suggests that unsteady 3D flow phenomena are not significant from a loss standpoint.

6.5. Conclusions from Sensitivity Study.

This chapter examined the sensitivity of tip leakage vortex interaction to axial spacing, vortex structure and stator operating parameters. A representative, unstalled stator geometry was used. The following conclusions can be drawn from this examination:

- The unsteady flow mechanisms through which upstream tip leakage vortices influence stator performance are generic. These mechanisms consist of (a) recovery of disturbance energy by means of vortex stretching (b) increase in passage loss due to boundary layer distortion by the upstream disturbance velocity field.

- Vortex recovery is beneficial for performance. Its benefit is significant ($\sim$0.3-0.6 efficiency points relative to the mixed out steady flow approximation).

- Vortex recovery benefits are mitigated to a large extent by the passage loss increase, which amounts to a loss of 0.2-0.4 efficiency points. As a result, the net effect of tip vortex interaction relative to the mixing-plane steady flow approximation, is between 0.0-0.2 efficiency points over the range of parameters considered.

- Blading design changes may reduce the passage loss increase, and thus capture a larger portion of the recovery benefits. All other factors being constant, stators in which the steady losses are "concentrated" in the tip region or in the front part of the blades will experience a higher passage loss increase from tip leakage vortex interaction.

- The above unsteady flow mechanisms can be described on a locally two-dimensional basis. In this sense, the most important aspect of the tip leakage vortex is the velocity defect associated with the vortex core. Unsteady secondary flows and spanwise variation of steady inlet profiles do not affect these mechanisms and their performance impact in a significant manner.

These conclusions are at the basis of the parametric study in **Chapter 7**. The study examines the influence of compressor design on the performance effects of upstream wakes and tip leakage vortices, and places bounds on these effects.

Chapter 7

Implications for Compressor Performance and Design

The purpose of this chapter is to (a) identify design options leading to enhanced performance by leveraging rotor-stator interaction, and (b) estimate the expected benefit in terms of efficiency. This is accomplished by examining how stage design influences the efficiency change, $\Delta\eta$, associated with interaction between rotors and stators. The interaction in question involves rotor and stator wakes, as well as rotor tip leakage vortices.

The calculation of $\Delta\eta$ for a given design has two aspects. First, the wakes and vortices for this design are characterized using simple correlations. Second, the effect of these wakes and vortices on blade row loss are estimated using models of recovery and boundary layer response based on **Chapters 3-5** and derived in **Appendix J**. These models are be applied in the relative frame of both the rotor and stator blade rows.

The first part of this chapter introduces a framework for making use of such $\Delta\eta$ calculations. The second part shows how $\Delta\eta$ varies throughout the compressor design space. The variation is broken down in terms of individual contributions from wake recovery, tip vortex recovery ...etc. A third part considers design options to maximize $\Delta\eta$. The implications for compressor design are summarized in **Chapter 8**.

7.1. Design Framework.

There is no established framework for translating unsteady fluid mechanics knowledge into design insights. Three issues have been considered to arrive at such a framework here: (1) how to simplify the interaction in the multistage environment, (2) what design parameters to vary, and (3) how to describe the design space.

Simplified representation. We shall consider blade row interaction in the embedded stage shown in **Figure 7.1**. This stage is assumed to be one of several identical upstream and downstream stages. In this manner, the number of design variables is greatly reduced, while the essence of the problem is retained.
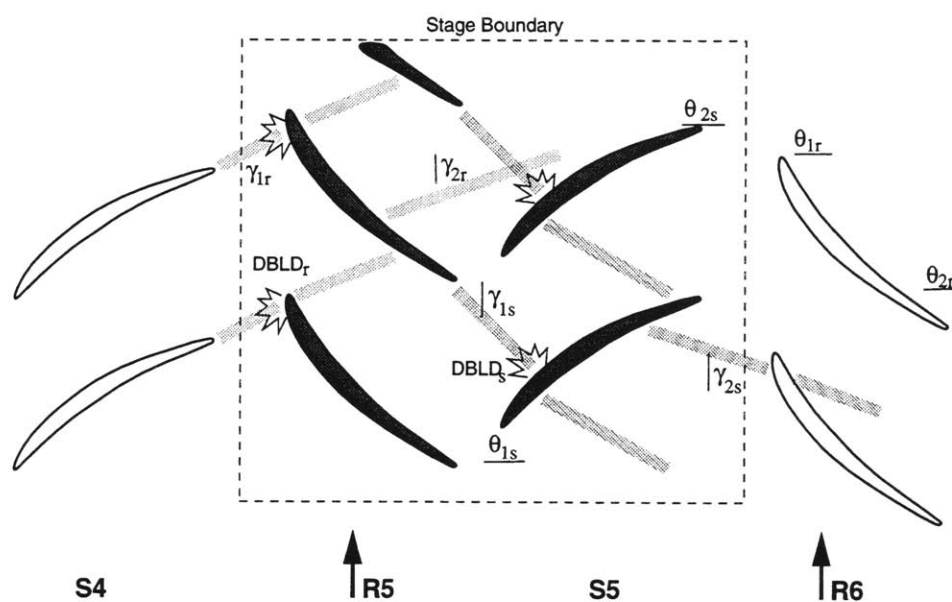
Figure 7.1. Embedded stage used in determining the effect of stage design on "unsteady performance". Flow angles are measured relative to the axial direction, disturbance ingestion angles are measured relative to the tangential direction.

The following interactions are considered (a) stator wake with downstream rotor, (b) rotor wake with downstream stator, and (c) rotor tip leakage vortex with downstream stator. The effect of upstream stator hub leakage vortices has not been considered. Each interaction has a beneficial effect on the loss in the downstream blade row (associated with reversible recovery), as well as a detrimental effect associated with boundary layer distortion. These two effects are quantified for each interaction, using models described in **Appendix J**.

Selection of design parameters. Two unsteady flow mechanisms affecting stator performance were identified in **Chapter 6** – wake/vortex recovery and boundary layer distortion. The parametric study in **Chapter 6** also indicates that these particular mechanisms are not sensitive to the stator flow three-dimensionality, and that their effects can be described on two-dimensional terms, common to both wakes and tip leakage vortices. For this reason, the design parameters selected for the study are those of a two-dimensional cascade. Two types of design parameters are considered – variable and constant.

Variable parameters are (1) flow coefficient ϕ, (2) stage pressure coefficient ψ, (3) reaction $\mathcal{R}$, and (4) blading solidity σ. Once these are specified, the flow angles, wake angles, diffusion

factors and steady losses are readily determined (cf. §J.1). Constant parameters represent geometry features that are normally fixed, such as rotor tip clearance τ, axial spacing d and blading chordlength c. Except as noted, these are held constant while moving around the design parameter space.[1]

Design parameter space. Herein, a simplified design approach described by Cumpsty (1989) has been adopted to explore feasible regions of design space. Of course, this is not the only possible approach. In the present case however, it helps to arrive at a useful conclusion about how design influences the performance impact of rotor-stator interaction. The approach utilises two constraints. The first is to fix the blading diffusion factor:

$$\mathrm{DF} = \left[1 - \frac{\cos\theta_1}{\cos\theta_2}\right] + \frac{\cos\theta_1}{2\sigma}(\tan\theta_1 - \tan\theta_2) \tag{7.01}$$

A useful working range for DF is between 0.35 and 0.6 (Cumpsty, 1989). Herein, a design point pitchline diffusion factor of 0.45 is adopted for both rotor and stator. This choice is representative of modern designs (e.g. Wisler, 1985), and provides a first constraint for exploring the $\{\phi, \psi, \mathcal{R}, \sigma\}$ design parameter space. The second constraint is provided by a form of the de Haller criterion mentioned by Cumpsty (1989):

$$1 - \frac{\cos^2\theta_1}{\cos^2\theta_2} < 0.44 \tag{7.02}$$
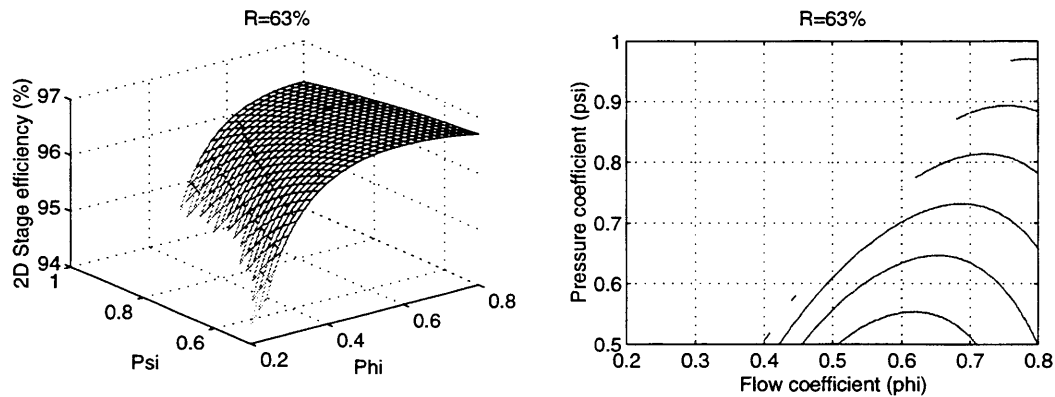
Figure 7.2. Left: 2D steady-state efficiency for DF=0.45 and 63% reaction as a function of design flow and pressure coefficient. Right: contour map of the surface at left within the de Haller limit (7.02). **This plotting convention is used throughout the chapter.** Reaction does not affect the steady efficiency significantly (Cumpsty, 1989).

Cumpsty (1989) points out that the upper limit of (7.02) corresponds approximately to typical stage loading at design. With constraints (7.01-7.02), the design parameter space is

---

[1]$c_r = 1.12, c_s = 1.0, \tau = 0.03, d = 0.32$ (Wisler 1985, Manwaring and Wisler 1992)

restricted to a sub-region of the (ϕ, ψ) plane, where the 2D stage efficiency peaks. Such a region is illustrated in **Figure 7.2**, and can be explained as follows. For a fixed diffusion factor and reaction, higher pressure rise designs require higher solidity. However, this leads to lower efficiency, since loss coefficients for unstalled blades are primarily a function of solidity $(\mathcal{Y} \approx 0.014\sigma/cos\theta_2$, Cumpsty 1989). The onset of the rapid decrease in efficiency coincides with the boundary of the de Haller criterion. This can be appreciated by correlating the left and right plots in **Figure 7.2**. Later in this chapter, we shall see that there is a relation between the de Haller criterion and the effects of rotor-stator interaction.

7.2. Impact of Stage Design on The Effects of Blade Row Interaction.

In this section, the influence of design on the performance impact of blade row interaction shall be examined in the following manner. The diffusion factor DF, tip clearance τ and blade row axial spacing d are held fixed. Using the models of **Appendix J**, the change in stage efficiency, $\Delta\eta$, due to interaction is computed and shown in the (ϕ, ψ) plane for a given reaction $\mathcal{R}$. The results are presented first in terms of individual contributions from each mechanism. This is followed by a summary of their net effect, as shown below.

- **§7.2.1.** $\Delta\eta$ due to recovery of wake energy only

- **§7.2.2.** $\Delta\eta$ due wake/boundary layer interaction only

- **§7.2.3.** Net $\Delta\eta$ due to wakes

- **§7.2.4.** $\Delta\eta$ due to recovery of tip vortex only

- **§7.2.5.** $\Delta\eta$ due tip vortex/boundary layer interaction only

- **§7.2.6.** Net $\Delta\eta$ due to tip leakage vortices

- **§7.2.7.** Total $\Delta\eta$ due to wakes and vortices

7.2.1. Efficiency benefit from wake recovery.

Figure 7.3 shows the variation of the efficiency benefit $\Delta\eta$ from reversible recovery of rotor and stator wakes. Representative blading diffusion factor (DF=0.45) and blade row spacing (d=0.3 chords) are used for this figure. It should be noted that the contour lines at the right show $\Delta\eta$ within the limits of the de Haller criterion, while the surface plot at the left covers a more extensive region of design space (limited by a solidity criterion, $\sigma < 2.5$). This plotting convention shall be used throughout **Chapter 7**.
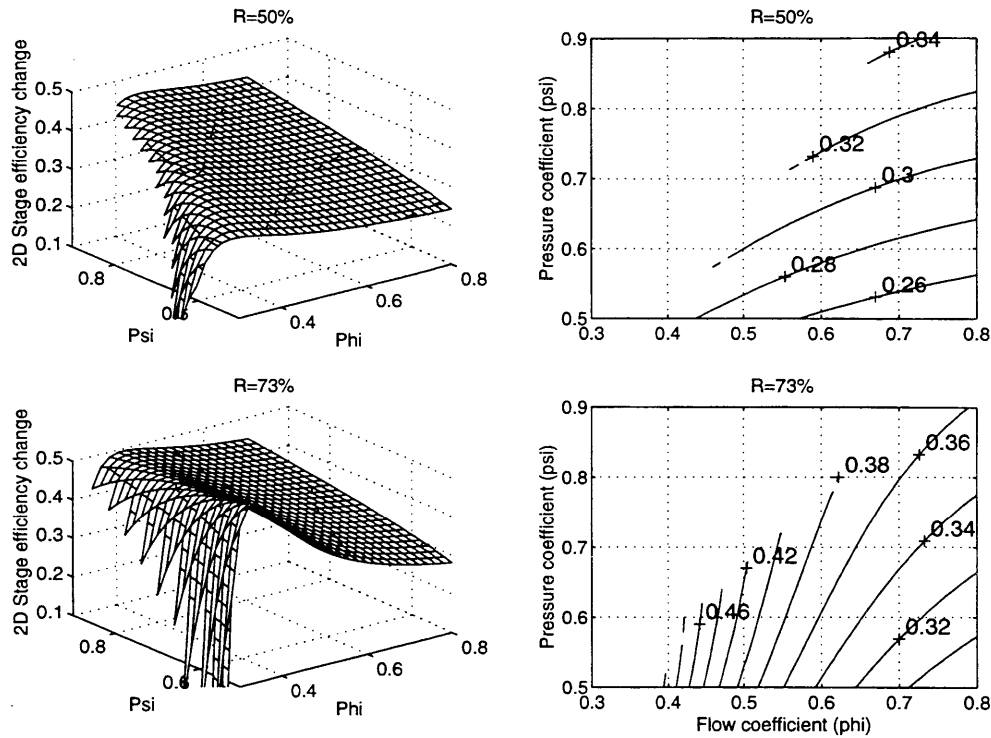
Figure 7.3. Stage efficiency benefit $\Delta\eta_m$ (relative to pre-mixed steady flow) from the recovery of rotor and stator wakes in an embedded stage as a function of design point (DF=0.45,d=0.32,c_r=1.12,c_s=1.0) Reactions of 50% (top) and 73% (bottom). Plots for reactions of 50-P% and 50+P% are identical by virtue of symmetry. At high reactions, most of the benefit comes from recovery of rotor wakes by the stator.

Within the approximate limits of the de Haller criterion, stage design has a relatively small effect on the benefit from wake recovery. For low pressure and flow coefficients however, wake recovery benefits rapidly disappear. This finding can be explained as follows. The loss benefit $\Delta\mathcal{Y}_m$ from wake recovery is proportional to the wake energy thickness $\mathcal{E}$ and to the square of the wake stretching ratio $a_r = L_e/L_i$ (cf. §3.3).

$$\Delta\mathcal{Y}_m \approx \mathcal{E}(1 - a_r^2) \tag{7.03}$$

It follows that the benefit from recovery is highly sensitive to the value of a_r, which primarily depends on the flow turning angle (§J.2.3). For low (ψ, ϕ), high stagger blading with relatively low turning is required. In this case, the wakes are not significantly stretched in the downstream blade row, and a_r is close to unity. The benefit of recovery for such designs is almost non-existent.

7.2.2. Efficiency loss due to wake/boundary layer interaction.

The second generic mechanism by which wakes influence blade row performance is the normal displacement of boundary layer fluid under the effect of the wake disturbance velocity (cf. §3.3,§5.2). This displacement of high-entropy fluid causes passage losses to increase. The resulting efficiency degradation is shown in **Figure 7.4**.
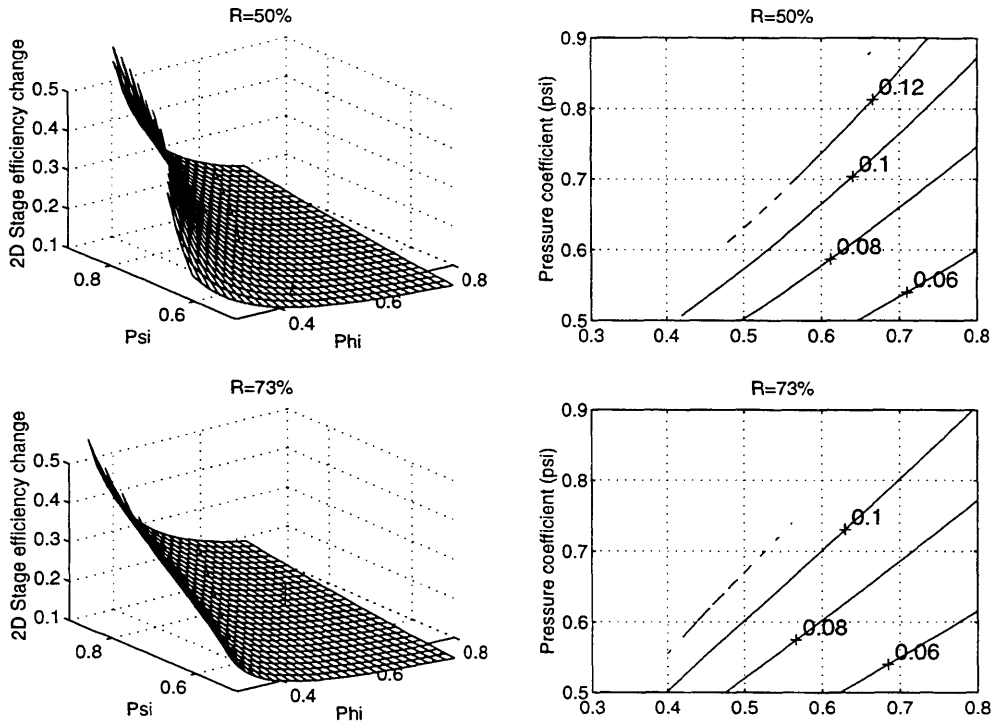
Figure 7.4. Stage efficiency deterioration $\Delta\eta_p$ (shown as positive percentage relative to pre-mixed steady flow) from wake/boundary layer interaction in a full embedded stage $(DF = 0.45, d = 0.32, c_r = 1.12, c_s = 1.0)$.

Figure 7.4 indicates that the efficiency deterioration due to wake/boundary layer interaction is small and constant within the limits of the de Haller criterion. Outside these limits however, this deterioration increases to significant levels ($\sim$0.5 efficiency points). This can be explained as follows. According to §3.3.2, the increase in loss is proportional to the steady-state loss of the blades. Steady-state losses increase outside the limits of the de Haller criterion. The efficiency deterioration due to wake/BL interaction increases correspondingly. It is to be noted that this aspect of the model does not take into account the precise chordwise distribution of loss along the blade, which was shown in §6.2.1 to be important. This simplification is compatible with the exploratory role of the design study in this chapter.

7.2.3. Net efficiency change from interaction with wakes.

The net change in stage efficiency due to wake interaction $\Delta\eta_w$, is equal to the benefit from recovery minus the deterioration associated with boundary layer response. This net change is shown in **Figure 7.5**.
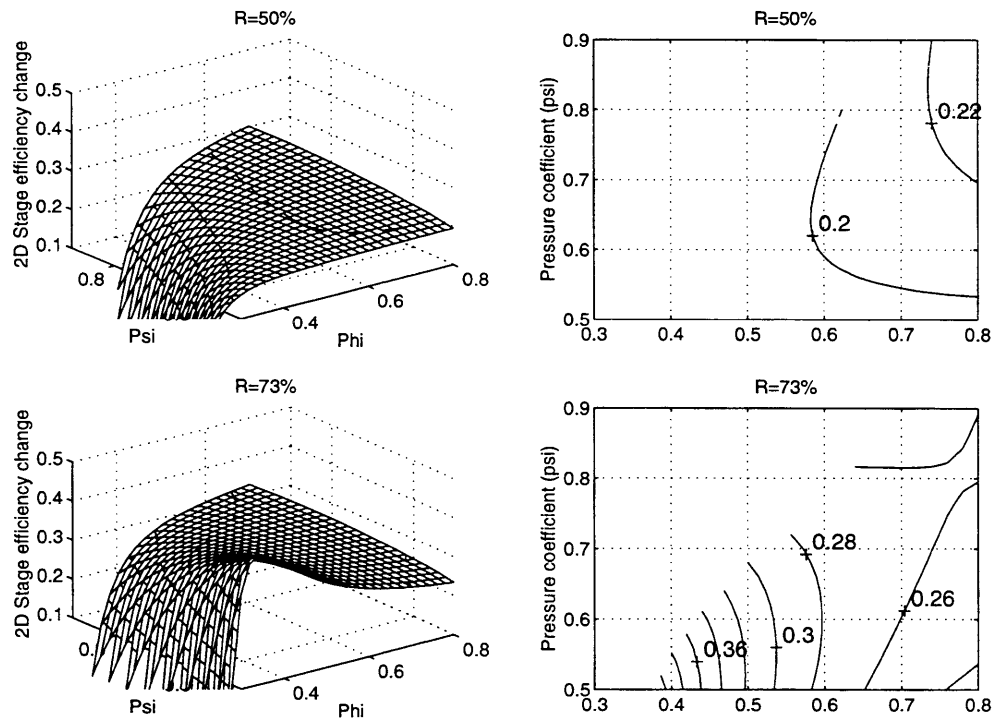
Figure 7.5. Net efficiency change $\Delta\eta_w$ (relative to pre-mixed steady flow) due to wake interaction in a full embedded stage (DF=0.45,d=0.32,c_r=1.12,c_s=1.0).

Within the approximate limits of the de Haller criterion, wake interaction is slightly beneficial. The gain in efficiency is about 0.2-0.35 points relative to the mixing-plane flow assumption. This gain is also practically insensitive to the choice of design, although the use of high reaction is associated with a marginally larger gain.

Outside the approximate limits of the de Haller criterion, wake interaction benefits disappear. For high-pressure rise, low-flow coefficient designs, wake interaction can be detrimental. This can be explained by the drop in recovery benefit, $\Delta\eta_m$, and by the increase in boundary layer response loss, $\Delta\eta_p$, considered separately in §**7.2.1-7.2.2**.

7.2.4. Efficiency benefit from tip leakage vortex recovery.

The mechanisms by which the rotor tip leakage vortex affects the performance of a downstream stator are the same as those identified for wakes - reversible recovery and boundary

layer distortion. Despite their confinement to the tip region of the stator, their effect on performance can be described on a locally two-dimensional basis (cf. §6.4). **Appendix J** addresses the problem of scaling the tip vortex for different designs on the basis of Khalid's (1996) findings.

This section examines the stage efficiency benefit from recovery of the rotor tip leakage vortex (stator leakage vortices exist, but are not considered). As shown in **Figure 7.6**, rotor tip vortex recovery is associated with benefits between 0.1-0.6 efficiency points. The benefits are largest at high pressure and flow coefficients. For a design such as the LSRC, the estimated benefit from the model is 0.25 points (in accordance with the Navier-Stokes results).
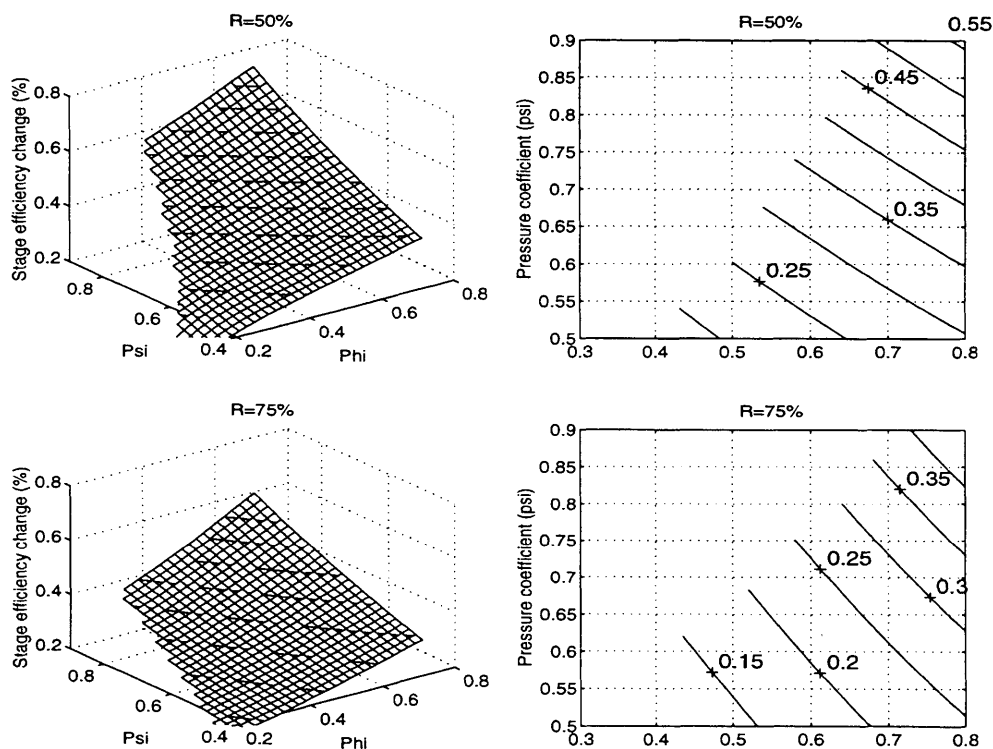
Figure 7.6. Stage efficiency benefit, $\Delta\eta_m$, from recovery of rotor tip leakage vortex in the stator as a function of stage design point (2% chord tip clearance, $DF = 0.45, d = 0.32, c_r = 1.12, c_s = 1.0$).

7.2.5. Efficiency loss due to vortex/boundary layer interaction.

Figure 7.7 shows the efficiency deterioration $\Delta\eta_p$ due to stator boundary layer response to the upstream tip leakage vortex. From a qualitative standpoint, $\Delta\eta_p$ behaves much in the same way as that associated with wake/boundary layer interaction. Within the limits of the de Haller criterion, $\Delta\eta_p$ is small ($\sim$0.1 efficiency points) and relatively independent of design. Outside these limits, $\Delta\eta_p$ grows to significant levels ($\sim$0.5 efficiency points).

This behavior occurs for the same reason as that involved in wake/boundary layer interaction (§7.2.2). For a fixed diffusion factor, high-ψ designs are achieved by increasing solidity and therefore steady-state loss (Cumpsty, 1989). Since $\Delta\eta_p$ is proportional to the steady loss, this increase is reflected in larger efficiency drop from vortex/BL interaction.
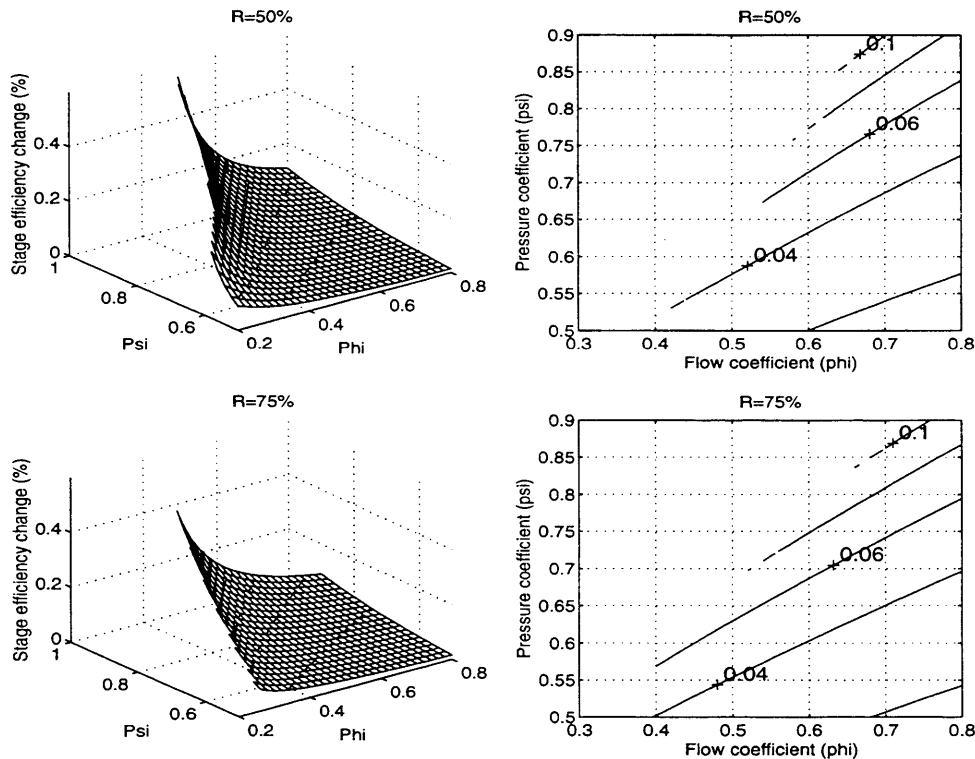
Figure 7.7. Stage efficiency deterioration, $\Delta\eta_p$, from tip leakage vortex/boundary layer interaction as a function of stage design point (2% chord tip clearance, $DF = 0.45, d = 0.32, c_r = 1.12, c_s = 1.0$). Unsteady losses increase sharply outside the approximate limits of the de Haller criterion.

7.2.6. Net efficiency change from interaction with the tip vortex.

The net change in stage efficiency due to tip leakage vortex interaction, is equal to the benefit from recovery minus the deterioration associated with boundary layer response. This net change is shown in **Figure 7.8**. Within the approximate limits of the de Haller criterion, tip leakage vortex interaction yields a modest efficiency improvement that is relatively constant and comparable to that of wakes ($\sim$0.1-0.3 efficiency points).

Outside the approximate limits of the de Haller criterion, vortex interaction benefits disappear. For high-pressure rise, low-flow coefficient designs, vortex interaction may become detrimental. The reasons for this behavior are explained in §7.2.4-§7.2.5 above, and are essentially the same as for wakes.
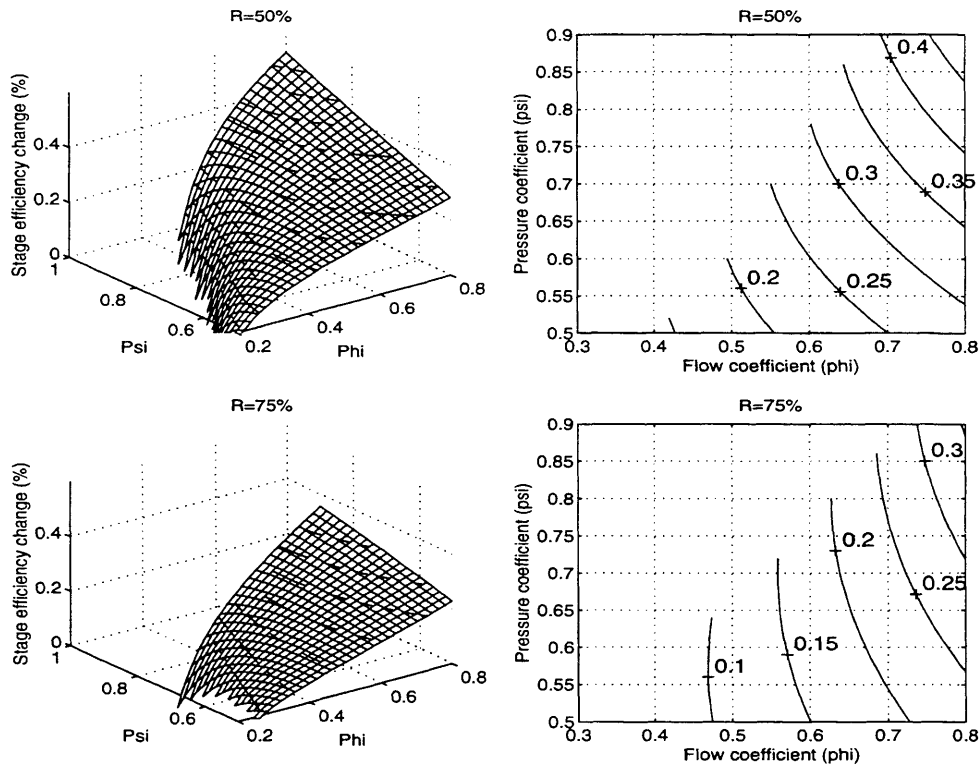
Figure 7.8. Net effect of rotor tip leakage vortex interaction on stage efficiency as a function of stage design point (2% chord tip clearance, $DF = 0.45, d = 0.32, c_r = 1.12, c_s = 1.0$).

7.2.7. Total efficiency change due to blade row interaction.

So far, individual blade row interaction mechanisms were considered separately. This section discusses the sum total of performance changes from these mechanisms, and considers how it is affected by axial spacing and by the choice of blading diffusion.

Figure 7.9 shows the change in stage efficiency due to blade row interaction (wakes+tip leakage vortex) for a nominal axial spacing of 0.32 chords. Within the approximate limits of the de Haller criterion, blade row interaction is moderately beneficial ($\Delta\eta \sim 0.5$ points), and relatively insensitive to stage design. Outside these limits, blade row interaction benefits rapidly disappear. This is due to (a) increase of the loss associated with boundary layer response to unsteadiness, and (b) decrease of the benefit associated with wake recovery.

Blade row interaction effects are moderately sensitive to the choice of diffusion factor. Repeating the efficiency calculations with DF=0.52 yields results that differ from those in **Figure 7.9** by about 0.1-0.2 point. However, the subregion of (ϕ, ψ) in which interaction is beneficial, is extended in the direction of higher pressure rise and lower flow coefficient.
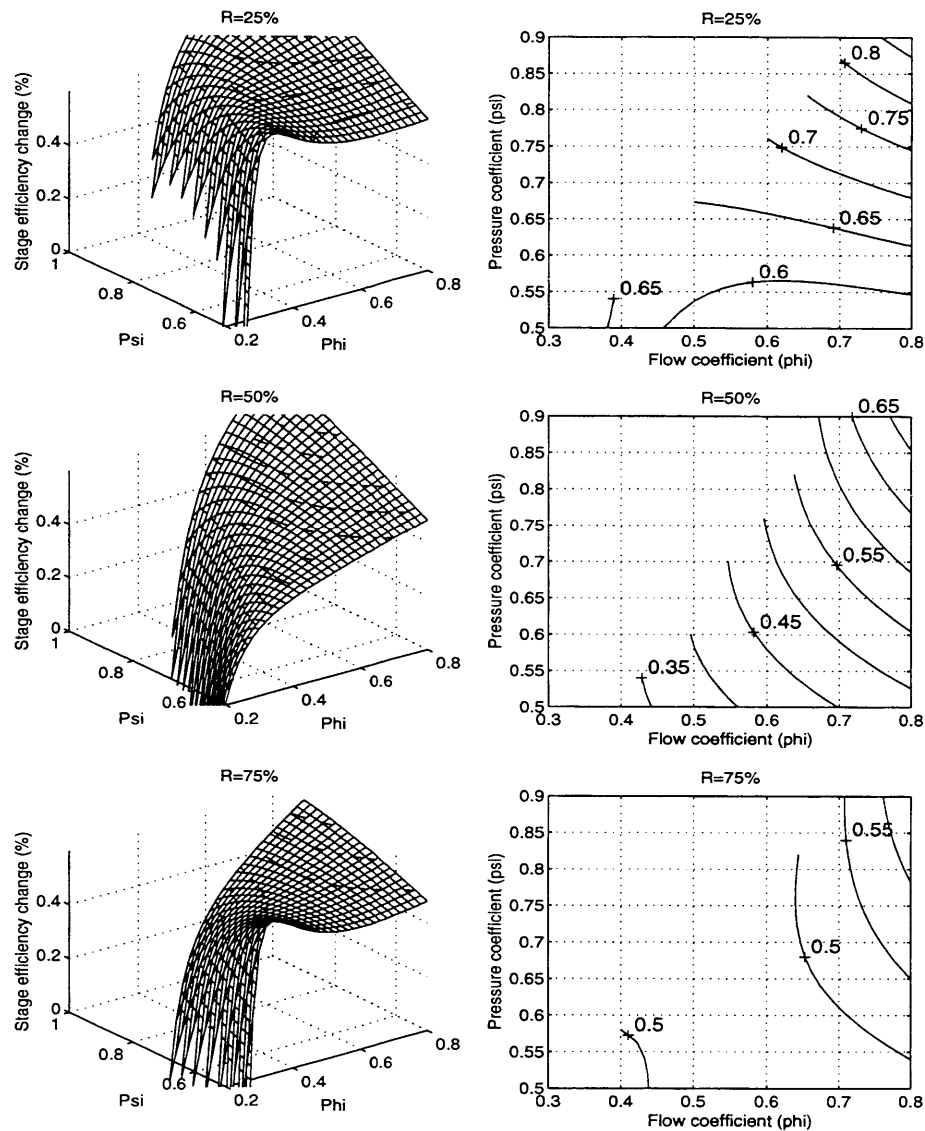
Figure 7.9. Sum total of efficiency changes due to wake and tip vortex interaction in a repreating embedded stage (2% chord tip clearance, $DF = 0.45, d = 0.32, c_r = 1.12, c_s = 1.0$). Efficiency changes shown are with respect to pre-mixed steady flow.

Blade row spacing is an important factor. As shown in **Figure 7.10**, reducing the spacing from 0.32 chords to 0.07 chords increases the net efficiency benefits from blade row interaction to significant levels ($\sim$1 point).

Comparing the efficiencies in **Figures 7.9** and **7.10** at the GE/LSRC compressor design point (ϕ=0.45, ψ=0.65, $\mathcal{R}$=63%) indicates that a reduction of the blade row axial spacing from 0.37 to 0.07 chords yields an efficiency improvement of 0.5-0.6 points. Although the blading and tip clearance used by Smith (1970) are not exactly the same as those chosen above, this difference still does not account for the 1 point efficiency gain in his experiment

(unless the wakes carry twice the amount of energy of the wakes from the correlations used in the model).
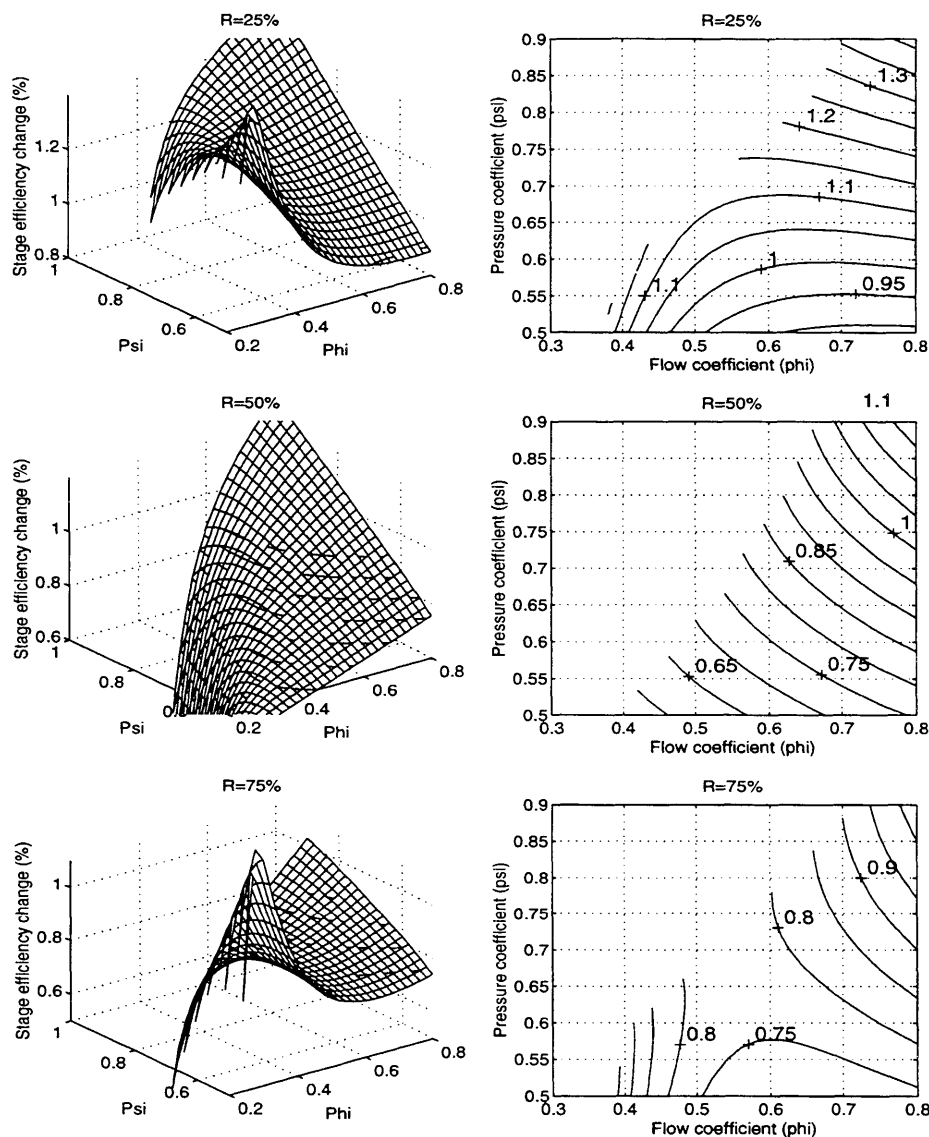
Figure 7.10. Sum total of efficiency changes due to wake and tip vortex interaction for closely-spaced blade rows (2% chord tip clearance, $DF = 0.45, d = 0.07, c_r = 1.12, c_s = 1.0$). Efficiency changes shown are with respect to pre-mixed steady flow. Reduced axial spacing improves stage efficiency, but by a lesser amount than observed by Smith (1970).

This suggests that other mechanisms (see **Table 1.1**) may affect performance significantly. One likely such mechanism is the reduction of corner flow separation in the presence of upstream wakes. Schultz et al. (1990a) have observed that rotor wakes cause stator endwall losses to decrease in a manner that reduces overall passage loss by up to 40%. This improvement was attributed to reduced stator hub separation. The impact of corner separation on efficiency in Smith's compressor is not known.

7.3. Analysis of Design Options.

The results in §7.2 show that the design parameter space can be divided into two regions. The relative extent of these regions depends on the blading diffusion factor. For a typical DF=0.45, the boundary between these regions coincides approximately with the de Haller criterion (7.02).

Within the limits of this criterion, the impact of blade row interaction on efficiency is moderately beneficial with respect to the mixing-plane steady flow approach ($\sim$0.4-0.6 points). There is relatively little variation in efficiency benefit from design to design ($\sim$0.1-0.2 points). Outside the limits of this criterion, blade row interaction benefits rapidly disappear.

Therefore, the primary design option is whether to place a design inside or outside these limits. According to §7.1-§7.2, designs where high pressure ratio is achieved by means of increased solidity might fall outside the region where interaction is beneficial.

Some efficiency improvement can be achieved by mitigating the detrimental effect of non-transitional boundary layer response. For the LSRC design examined here, the maximum potential improvement is of the order of 0.3-0.4 efficiency points. This value assumes that the 0.2 points deterioration from BL response to the rotor tip vortex, and the 0.1 points deterioration from BL response to rotor and stator wakes, can be completely eliminated.

Two methods are available for mitigating the effect of boundary layer response. The first method is suggested by the results in §6.2.1, where a two-fold reduction in the passage loss increase $\Delta\mathcal{Y}_p$ was achieved while increasing the loading. This method consists of using sections for which the loss is "moved" from the front towards the back of the blades.

The second method is suggested by the results in §5.2.1. It consists in the removal of boundary layer fluid from the front portion of the blade suction surface. This eliminates the cause for passage loss increase (normal redistribution of vortical lines in the boundary layer under the effect of upstream velocity disturbances). The suction method entails increased mechanical complexity, as well as losing a certain fraction of the mass flow. At this point, a cost-benefit study of suction is recommended.

Since tip vortex/boundary layer interaction in the tip region of the stator contributes the most to the increase in passage loss, a promising strategy is to apply suction over the outer 75-95% of stator span. The mass flow removed from the stator surface may be used as bleed air. The proposed cost-benefit study should focus on this strategy.

Chapter 8

Conclusions and Recommendations

8.1. Summary and Conclusions.

Time-accurate Reynolds-averaged Navier-Stokes simulations have been carried out to investigate the effect of upstream rotor wakes and tip leakage vortices on the performance of a typical stator, relative to the steady flow approximation of mixing out such disturbances between blade rows. The objectives of this work are to (1) identify the unsteady flow mechanisms responsible for performance changes, (2) quantify these changes, and (3) translate this information into design insights.

Two generic mechanisms with significant impact on performance have been identified. These are the reversible recovery of the energy in the disturbances (beneficial), and the non-transitional boundary layer response (detrimental). These mechanisms appear to be generic.

- Tip vortex recovery involves intrinsically three-dimensional vorticity dynamics. However, the energy benefit from tip vortex recovery scales in the same manner as that associated with wake recovery, and can be described in the same 2D terms.

- Non-transitional boundary layer response involves the normal displacement of boundary layer vortex lines under the "suction" effect of the upstream disturbances. The resulting redistribution of vorticity leads to an increase in passage loss. For tip vortex interaction, the loss increase occurs in the tip region of the stator (in accordance with Howard et al. 1994).

- Both mechanisms are associated with the velocity defect of the disturbances in the relative frame. The effects of these mechanisms can be described in the same two-dimensional terms for both wakes and tip leakage vortices.

Quantitative effect and dependency. The effect of the upstream wakes and vortices on the stator loss is important. It depends on the following parameters: axial spacing, loading and the frequency of wake fluctuations in the relative frame.

- For the present design, passing the rotor wakes and vortices through the stator results in a stage efficiency that is 0.2 points higher than that obtained using the steady flow approximation (0.5 efficiency points recovery benefit minus 0.3 points from boundary layer response). Individually, the effects of rotor tip vortex and wake are comparable.

- The effect of tip vortices and wakes becomes significantly more important at reduced axial spacing. For a spacing of 0.07 chords, the stage efficiency is 0.6 points higher relative to the steady flow (1.2 points recovery benefit minus 0.6 points from boundary layer response).

- For the present geometry, an increase in loading redistributes boundary layer vortical fluid in a manner that decreases the additional loss from boundary layer response.

- There is a range of fluctuation frequencies ($\sim$0.3-0.8 times the blade passing frequency) for which recovery does not occur. Within this range, there is a significant difference between the effects of fluctuating and steady wakes with the same ensemble-averaged properties. Thus, the use of ensemble-averaged wakes in interaction studies is not necessarily correct. Tip vortices are thought to fluctuate at a low frequency outside this range.

- The most important aspect of the tip vortex is the velocity defect, which is perceived by the stator in the same manner as a wake. Stator flow three-dimensionality and unsteady secondary vorticity are not important as far as the performance effects of stator/tip vortex interaction are concerned.

Design implications. A model of recovery and boundary layer response has been used to explore how blade row interaction effects change from design to design. The model considers interaction in a repeating embedded stage environment, and indicates that:

- Steady flow approximations based on mixing the disturbances between the blade rows, underestimate stage efficiency by 0.3-0.5 points (for typical designs) and by as much as 0.6-1.0 points (for designs with closely-spaced blade rows).

- A region in design space exists where interaction has a beneficial and relatively constant impact on efficiency. Outside this region, interaction benefits rapidly disappear. The extent of the beneficial region is determined by the choice of blading diffusion factor DF. For typical values of DF$\sim$0.45, the beneficial limits coincide approximately with the de Haller criterion.

- The detrimental aspects of boundary layer response may be mitigated by (a) selective removal of boundary layer fluid, or (b) tailoring the blade loading to reduce steady-state losses in the front part of the blade. For typical designs, the maximum efficiency gain from such measures is about 0.3 points.

Although differences in compressor design prevent a back-to-back comparison, our results suggest that 1/2 to 2/3 of the efficiency gain obtained by Smith (1970) can be attributed

to interaction with upstream wakes and vortices. Future work should be focused on other mechanisms that may have a strong impact on performance, such as corner flow response.

8.2. Recommendations for Future Work.

This study demonstrates the potential of CFD for connecting complex flow processes to turbomachinery performance and design. Future research should be directed at:

- Physical experiments, to assess the performance trends and flow features found herein. The CFD results indicate what to look for in the data. Time-resolved velocity measurements in the suction side boundary layer should be carried out with a degree of resolution sufficient to visualize the unsteady vorticity fields. Such data can be used to assess the role of non-transitional boundary layer response. Measurements of tip leakage vortex velocity profiles as a function of downstream distance with and without stators would be useful in assessing vortex recovery.

- Investigation of the response of separated corner flow to upstream disturbances. Experimental data suggests that upstream wakes can reduce the extent of corner separation in a significant manner (Schultz et al. . 1990a). Elucidating the causes and the magnitude of this effect would be a useful contribution. Reduction of corner separation could be one of the factors behind Smith (1970) observations.

- The results indicate that the effects of fluctuating and steady wakes with the same ensemble-averaged properties might be different, depending on the period of fluctuations. It would be useful to (1) characterize the time scales and amplitude of these fluctuations in the core compressor environment, and (2) verify experimentally the role of the fluctuation period.

Wake interaction is one of the major sources of broadband and tonal noise in jet engines (Waitz, 1996). The unsteady wake calculations of **Chapter 3** can be used to explore the role of wake fluctuations in generating broadband noise. The results from such a study would be useful for current work in the field of aeroacoustics, and may lead to strategies for controlling broadband noise.

Bibliography

Abramovich G.N. (1965)
The Theory of Turbulent Jets, M.I.T. Press, Massachusetts Institute of Technology.

Abu-Ghannam B.J., Shaw R. (1980)
Natural Transition of Boundary Layers - The Effects of Turbulence, Pressure Gradient and Flow History. J. Mech. Eng. Sci., 22, No.5.

Adamczyk J.J. (1996)
Wake Mixing in Axial Flow Compressors. Presentation Materials for ASME Paper 96-GT-029, Birmingham, United Kingdom, June 1996.

Adamczyk J.J., Celestina M.L., Chen J.P. (1994)
Wake-Induced Unsteady Flows : Their Impact on Rotor Performance and Wake Rectification. ASME Paper 94-GT-219.

Adamczyk J.J. (1992)
Unsteady Aerodynamic Interaction Effects on Turbomachinery Blade Life and Performance. AIAA Paper 92-0149.

Adamczyk J.J., Celestina M.L., Beach T.A., Barnett M. (1989)
Simulation of Three-Dimensional Viscous Flow Within a Multistage Turbine. ASME Journal of Turbomachinery, 112.

Adamczyk J.J. (1985)
Model Equations for Simulating Flows in Multistage Turbomachinery. ASME Paper 85-GT-226.

Addison J.S., Hodson H.P. (1990a)
Unsteady Flow Transition in an Axial Flow Turbine: Part 1 - Measurements on the Turbine Rotor. ASME Journal of Turbomachinery, 112, April 1990.

Addison J.S., Hodson H.P. (1990b)
Unsteady Flow Transition in an Axial Flow Turbine: Part 2 - Cascade Measurement and Modeling. ASME Journal of Turbomachinery, 112, April 1990.

Adkins G.G., Smith L.H. (1982)
Spanwise Mixing in Axial Flow Turbomachines. ASME Journal of Engineering and Power, 104, No.1, pp.97-110.

AGARD (1994)
Turbomachinery Design Using CFD. AGARD Lecture Series No.195, North Atlantic Treaty Organization.

Ashley H., Landahl M. (1965)
Aerodynamics of Wings and Bodies, Dover Publications Inc.

Baldwin B.S., Lomax H. (1978)
Thin Layer Approximation and Algebraic Model for Separated Turbulent Flows. AIAA Paper 78-257.

Batchelor G.K. (1967)
An Introduction to Fluid Dynamics, Cambridge University Press.

Benocci C. (1991)
Modeling of Turbulent Heat Transport: A state of the Art. Von Karman Institute Technical Memorandum TM-47.

Binder A., Forster W., Mach K., Rogge H. (1987)
Unsteady Flow Interaction Caused by Stator Secondary Vortices in a Turbine Rotor. ASME Journal of Turbomachinery, **107**, April 1987.

Book D.L. (1981)
Finite-difference techniques for vectorized fluid dynamics calculations. Springer series in computational physics, Springer-Verlag.

Brookfield J.B. (1996)
Private Communication. Massachusetts Institute of Technology, June 1996.

Bury M. (1996)
Private Communication. Massachusetts Institute of Technology, June 1996.

Capece V.R., Fleeter S. (1987)
Unsteady Aerodynamic Interactions in a Multistage Compressor. ASME Journal of Turbomachinery, **109**, July 1987.

Chen C.L., Chakravarthy S.R. (1990)
Calculation of Unsteady Rotor/Stator Interaction. AIAA Paper 90-1544.

Cumpsty N.A. (1989)
Compressor Aerodynamics, Longman Group Ltd.

Dawes W.N. (1994)
A Numerical Study of the Interaction of a Transonic Compressor Rotor Overtip Leakage Vortex with the Following Stator Blade Row. ASME Paper 94-GT-156.

Dawes W.N. (1992)
Towards Improved Throughflow Capability: The Use of Three-Dimensional Viscous Flow Solvers in a Multistage Environment. ASME Journal of Turbomachinery, **114**, pp.8-17.

Degan D., Schiff L.B. (1986)
Computation of Turbulent Supersonic Flows Around Pointed Bodies Having Crossflow Separation. Journal of Computational Physics, **66**, pp.173-196.

Denton J.D. (1993)
Loss Mechanisms in Turbomachines. ASME Journal of Turbomachinery, 115,No.4.

Denton J.D. (1992)
The Calculation of Three-Dimensional Viscous Flow Through Multistage Turbomachines. ASME Journal of Turbomachinery, 114, pp.18-26.

Dong Y., Cumpsty N.A. (1990a)
Compressor Blade Boundary Layers : Part 1 - Test Facility and Measurements with Incident Wakes. ASME Journal of Turbomachinery, 112, April 1990.

Dong Y., Cumpsty N.A. (1990b)
Compressor Blade Boundary Layers : Part 2 - Measurements With Incident Wakes. ASME Journal of Turbomachinery, 112, April 1990.

Dongarra J.J., Bunch J.R., Moler C.B., Stewart G.W. (1979)
LINPACK Users' Guide. SIAM.

Dorney D.J., Sharma O.P. (1996)
Evaluation of Flow Field Approximations for Transonic Compressor Stages. ASME Paper 96-GT-371.

Erdos J.I., Alzner E., McNally W. (1977)
Numerical Solution of Periodic Transonic Flow Through a Fan Stage. AIAA Journal, ((15)).

Fritsch G, Giles M.B. (1995)
An Assymptotic Analysis of Mixing Loss. ASME Journal of Turbomachinery, 117, pp.367-373.

Fritsch G. (1992)
An Analytical and Numerical Study of The Second-Order Effects of Unsteadiness on the Performance of Turbomachines. MIT Gas Turbine Laboratory Report No.210, Massachusetts Institute of Technology, June 1992.

Gallus H.E. (1979)
High-Speed Blade-Wake Interactions, in "Unsteady Flow in Turbomachines". VKI Lecture Series 1979-3, Von Karman Institute for Fluid Dynamics.

Gertz J.B (1988)
Unsteady Design-Point Flow Phenomena in Transonic Compressors. GTL Report No.188, Massachusetts Institute of Technology

Gibeling H.J., Buggeln R.C., Chen S.Y, McConnaughey H.V. (1988)
Implicit Navier-Stokes Analysis of Turbine Rotor-Stator Interaction. AIAA Paper 88-3090.

Giles M., Haimes R. (1993)
Validation of a Numerical Methods for Unsteady Flow Calculations. ASME Journal of Turbomachinery, 110, January 1993.

Girault V. (1986)
Finite element methods for Navier-Stokes equations : theory and algorithms. Springer series in computational mathematics, Springer-Verlag.

Gostelow J.P. (1984)
Cascade Aerodynamics, Pergamon Press.

Gottlieb D.O., Orszag S.A. (1977)
Numerical Analysis of Spectral Methods : Theory and Applications. NSF-CBMS Monograph
No.26, SIAM.

Graf M.B. (1996)
Effects of Stator Pressure Field on Upstream Rotor Performance. Doctoral Thesis, Depart-
ment of Mechanical Engineering, Massachusetts Institute of Technology, 1996.

Greitzer E.M., Tan C.S., Wisler D.C., Adamczyk J.J., Strazisar A.J. (1994)
Unsteady Flow in Turbomachines : Where's The Beef?. Unsteady Flows in Aeropropulsion,
ASME Publication AD-Vol.40.

Halstead D.E., Wisler D.C., Okiishi T.H., Walker G.J., Hodson H.P., Shin H.W. (1995)
*Boundary Layer Development in Axial Compressors and Turbines. Part 1 of 4: Composite
Picture.* ASME Paper 95-GT-461.

Halstead D.E., Wisler D.C., Okiishi T.H., Walker G.J., Hodson H.P., Shin H.W. (1995)
Boundary Layer Development in Axial Compressors and Turbines. Part 2 of 4: Compressors.
ASME Paper 95-GT-462.

Hawthorne W.R. (1970)
The Flow Through Moving Cascades of Lifting Lines With Fluctuating Lift. Aeronautical
Council Research Paper ARC 32369.

Hebert G.J., Tiederman W.G. (1990)
Comparison of Steady and Unsteady Secondary Flows in a Turbine Stator Cascade. ASME
Journal of Turbomachinery, 112.

Hetherington R., Morritz R.R. (1977)
*The Influence of Unsteady Flow Phenomena on the Design and Operation of Aero Engines,
in "Unsteady Phenomena in Turbomachinery".* AGARD CP-144.

Hodson H.P. (1990)
Modeling Unsteady Transition and Its Effect on Profile Loss. ASME Journal of Turbomachin-
ery, 112, October 1990.

Hodson H.P. (1985)
An Inviscid Blade-to-Blade Prediction of Wake-Generated Unsteady Flow. ASME Journal of
Turbomachinery, 107, pp.337-344.

Horlock J.H. (1968)
Fluctuating Lift Forces on Airfoils Moving Through Transverse and Chordwise Gusts. ASME
Paper 68-FE-28.

Howard M.A., Ivey P.C., Barton J.P., Young K.F. (1994)
*Endwall Effects at Two Tip Clearances in a Multi-Stage Axial Flow Compressor With Controlled-
Diffusion Blading.* ASME Journal of Turbomachinery, 116.

Howard M.A., Gallimore S.J. (1993)
Viscous Throughflow Modeling for Multistage Compressor Design. ASME Journal of Turbo-machinery, 115, April 1993.

Huber F.W., Johnson P.D., Sharma O.P., Staubach J.B., Gaddis S.W. (1995)
Performance Improvements Through Indexing in Turbine Airfoils. Part I - Experimental Investigation. ASME Journal of Turbomachinery, 115, April 1995.

Hunter I.H., Cumpsty N.A. (1982)
Casing Wall Boundary-Layer Development Through an Isolated Compressor Rotor. ASME Journal of Turbomachinery, 104, April 1982.

Jameson A., Schmidt W., Turkel E. (1981)
Numerical Solutions of the Euler Equations by Finite-Volume Methods Using Runge-Kutta Time-Stepping Schemes. AIAA paper 81-1259.

Jeffrey H., Jeffrey B.S. (1972)
Methods of Mathematical Physics, Cambridge University Press.

Johnson A.B., Oldfield M.G., Rigby M.J., Giles M.B. (1990)
Nozzle Guide Vane Shock Wave Propagation and Bifurcation in a Transonic Turbine Rotor. ASME Paper 90-GT-310.

Kemp N.H., Sears W.R. (1953)
Aerodynamic Interference Between Moving Blade Rows. J.Aero.Science, 1953, 20.

Kemp N.H., Sears W.R. (1955)
The Unsteady Forces Due to Viscous Wakes in Turbomachines. J.Aero.Science, 1955, 22.

Kerrebrock J.L. (1992)
Aircraft Engines and Gas Turbines, 2nd ed. Massachusetts Institute of Technology, 1992.

Kerrebrock, J.L. (1977)
Small Disturbances in Turbomachinery Annuli with Swirl. AIAA Journal, 15, June 1977.

Kerrebrock J.L., Mikolajczak A.A. (1970)
Intra-Stator Transport of Rotor Wakes and Its Effect on Compressor Performance. ASME Journal of Engineering and Power, October 1970, pp.359-368.

Khalid S.A. (1995)
The Effects of Tip Clearance on Axial Compressor Pressure Rise. Doctoral Thesis, Department of Mechanical Engineering, Massachusetts Institute of Technology, 1995.

Koch C.C., Smith L.H. (1976)
Loss Sources and Magnitudes in Axial-Flow Compressors. ASME Journal of Engineering and Power, July 1976 (pp.411-424).

Korczak K.Z. (1985)
Development of an Isoparametric Spectral Element Method for Direct Numerical Simulation of the Navier-Stokes Equations. Doctoral Thesis, Department of Mechanical Engineering, Massachusetts Institute of Technology, 1985.

Kotidis P.A., Epstein A.H. (1991)
Unsteady Radial Transport in Radial Compressor Stage. ASME Journal of Turbomachinery, **113**, April 1991.

Koya M., Kotake S. (1985)
Numerical Analysis of Fully Three-Dimensional Flows Through a Turbine Stage. ASME Journal of Engineering for Gas Turbines and Power, **107**, pp.945-952.

Lakshminarayana R., Ravindranath A. (1982)
Interactions of Compressor Rotor Blade Wake With Wall Boundary Layer/Vortex in the End-Wall Region. ASME Journal of Turbomachinery, **104**, April 1982.

Launder B.E., Spalding D.B. (1983)
The Numerical Computation of Turbulent Flows. Numerical Prediction of Flow, Heat Transfer, Turbulence and Combustion - Selected Works of Professor D. Brian Spalding, Pergamon Press.

Lejabmre C.R., Zacharias R.M., Biederman B.P., Gleixner A.J., Yetka C.J. (1995)
Development and Application of a Multistage Navier-Stokes Solver. Part II : Application to a High Pressure Compressor Design. ASME Paper 95-GT-342.

Lewis J.P., Delaney R.A., Hall E.J. (1987)
Numerical Prediction of Turbine Blade-Vane Interaction. AIAA Paper 87-2149.

Lieblein S. Schwenk F.C., Broderick R.L. (1953)
Diffusion Factor for Estimating Losses and Limiting Blade Loading in Axial Flow Compressor Blade Elements. NACA RM E53D01.

Manwaring S.R., Wisler D.C. (1992)
Unsteady Aerodynamics and Gust Response in Compressors and Turbines. ASME Paper 92-GT-422.

Mayle R.E. (1991)
The Role of Laminar-Turbulent Transition in Gas Turbine Engines. ASME Journal of Turbomachinery, **113**.

Mayle R.E., Dullenkopf K. (1990)
A Theory for Wake-Induced Transition. ASME Journal of Turbomachinery, **112**, April 1990.

McFarland E.R. (1984)
A Rapid Blade-To-Blade Solution for Use in Turbomachinery Design. ASME Journal of Engineering for Gas Turbines and Power, 106 (2):376-382.

Mikolajczak A.A. (1977)
The Practical Importance of Unsteady Flow, in "Unsteady Phenomena in Turbomachinery. AGARD CP-144, North Atlantic Treaty Organization.

Moore J., Moore J.G. (1995)
Osbourne Reynolds: Energy Methods in Transition and Loss Production: A Centennial Perspective. ASME Journal of Turbomachinery, **117**, pp.142-153, January 1995.

NASA (1965)
Aerodynamic Design of Axial Flow Compressors. NASA SP-36, Nasa Lewis Research Center,

National Aeronautics and Space Administration.

Nikolaou I.G., Giannakoglou K.C., Papailiou K.D. (1996)
Study of a Radial Tip Clearance Effects in a Low-Speed Axial Compressor Rotor. ASME
Paper 96-GT-37.

Ni R.H., Sharma O. (1990)
Using 3D Euler Flow Simulations to Assess Effects of Periodic Unsteady Flow Through Turbines. AIAA Paper 90-2357.

Nurzia F., Puddu P. (1994)
Experimental Investigation of Secondary Flows in a Low Hub-Tip Ratio Fan. ASME Paper
94-GT-377.

Orth U. (1993)
Unsteady Boundary Layer Transition in Flow Periodically Disturbed by Wakes. ASME
Journal of Turbomachinery, 115, No.4, October 1993.

Patera A.T. (1984)
A Spectral Element Method for Fluid Dynamics: Laminar Flow in a Channel Expansion.
Journal of Computational Physics, 54, No.3.

Pfeil H., Herbst R., Schroder T. (1983)
Investigation of the Laminar-Turbulent Transition of Boundary Layers Disturbed by Wakes.
ASME Journal of Engineering and Power, 105.

Poensgen C., Gallus H.E. (1991a)
*Three-Dimensional Wake Decay Inside of a Compressor Cascade and Its Influence on the
Downstream Unsteady Flow Field. Part I - Wake Decay Characteristics in the Flow Passage.*
ASME Journal of Turbomachinery, 113.

Poensgen C., Gallus H.E. (1991b)
*Three-Dimensional Wake Decay Inside of a Compressor Cascade and Its Influence on the
Downstream Unsteady Flow Field. Part II - Unsteady Flow Field Downstream of the Stator.*
ASME Journal of Turbomachinery, 113.

Prato J., Lakshminarayana B. (1993)
*Investigation of Compressor Rotor Wake Structure at Peak Pressure Rise Coefficient and
Effects of Loading.* ASME Journal of Turbomachinery, 115, July 1993.

Rai M.M. (1987a)
Navier-Stokes Simulations of Rotor-Stator Interaction Using Patched and Overlaid Grids.
AIAA Journal of Propulsion and Power, 3, pp.387-396.

Rai M.M. (1987b)
Unsteady Three-Dimensional Navier-Stokes Simulations of Turbine Rotor-Stator Interaction.
AIAA Paper 87-2058.

Renaud E.W. (1991)
*Secondary flow, total pressure loss and the effect of circumferential distortions in axial turbine
cascades.* Doctoral Thesis, Department of Aeronautics and Astronautics, Massachusetts

Institute of Technology, 1991.

Rhie C.M. et al. (1995)
Development and Application of a Multistage Navier-Stokes Solver. Part I : Multistage Modeling Using Bodyforces and Deterministic Stresses. ASME Paper 95-GT-341.

Sankaran L., Russell D.A. (1990)
A Numerical Study of Longitudinal Vortex Interaction with a Boundary Layer. AIAA Paper 90-1630.

Saxer A.P. (1992)
A Numerical Analysis of 3-D Inviscid Stator/Rotor Interactions Using Non-Reflecting Boundary Conditions. MIT Gas Turbine Laboratory Report No.209, Massachusetts Institute of Technology, March 1992.

Schlichting H. (1968)
Boundary Layer Theory, 6th ed., McGraw-Hill.

Schlichting H., Das A. (1970)
On the Influence of Turbulence Level on the Aerodynamic Losses of Axial Turbomachinery. Flow Research on Blading, L.S. Dzung ed., Elsevier Publishing Company, 1970.

Schulz H.D., Gallus H.E., Lakshminarayana B. (1990a)
Three-Dimensional Separated Flow Field in the Endwall Region of An Annular Compressor Cascade in the Presence of Rotor-Stator Interaction. Part 1: Quasi-Steady Flow Field and Comparison With Steady-State Data. ASME Journal of Turbomachinery, 112, October 1990.

Schulz H.D., Gallus H.E., Lakshminarayana B. (1990b)
Three-Dimensional Separated Flow Field in the Endwall Region of An Annular Compressor Cascade in the Presence of Rotor-Stator Interaction. Part 2: Unsteady Flow and Pressure Field. ASME Journal of Turbomachinery, 112, October 1990.

Sedlar M. (1993)
Using Quasi-3D Viscous Flow Modeling in Pump Design. Numerical Methods in Laminar and Turbulent Flow, Vol 8, Part II. Pineridge Press Ltd.

Shang T., Epstein A.H., Giles M.B., Sehra A.K. (1993)
Blade Row Interaction Effects on Compressor Measurements. ASME Journal of Propulsion and Power, 9, No.4.

Sharma O.P., Ni R.H., Tanrikut S. (1994)
Unsteady Flows in Turbines - Impact on Design Procedure, in "Turbomachinery Design Using CFD". AGARD Lecture Series No.195.

Silkowski P.D. (1995)
Measurements of Rotor Stalling in Matched and Mismatched Multistage Compressor. MIT Gas Turbine Report No.221, Massachusetts Institute of Technology.

Smith L.H. (1996)
Discussion of ASME Paper 96-GT-029 Birmingham, United Kingdom, June 1996.

Smith L.H. (1970)
Casing Boundary Layers in Multistage Axial Flow Compressors. Flow Research on Blading,
L.S. Dzung ed., Elsevier Publishing Company, 1970.

Smith L.H. (1966)
Wake Dispersion in Turbomachines. ASME Journal of Basic Engineering, September 1966.

Speidel L. (1951, 1952, 1953)
Untersuchungen uber die Verwendung von Laminar-Profilen in einer Reaktionsturbine. Berichten
51/5, 52/11 und 53/14, Institut fur Stronmungsmechanik der Technischen Hochschule Braun-
schweig, FRG.

Stauter R.C., Dring R.P., Carta F.O. (1991)
*Temporally and Spatially Resolved Flow in a Two-Stage Axial Flow Compressor: Part 1-
Experiment.* ASME Journal of Turbomachinery, 113, April 1991.

Storer J.A., Cumpsty N.A. (1991)
Tip Leakage Flow in Axial Compressors. ASME Journal of Turbomachinery, 113, April 1991.

Storer J.A. (1991)
Tip Clearance Flow in Axial Compressors. Doctoral Dissertation, Department of Mechanical
Engineering, Cambridge University, January 1991.

Tan C.S. (1989)
*A Multi-Domain Spectral Computation of Three-Dimensional Laminar Horseshoe Vortex
Flow Using Incompressible Navier-Stokes Equations.* Journal of Computational Physics, 85,
No.1.

Tan C.S., Greitzer E.M. (1986)
Nonaxisymmetric Compressible Swirling Flows in Turbomachine Annuli. AIAA Journal, 24,
No.1, January 1986.

Taylor E.S. (1971)
Boundary Layers, Wakes and Losses in Turbomachines. MIT Gas Turbine Laboratory Report
No.105, Massachusetts Institute of Technology, April 1971.

Tennekes H. and Lumley J.L. (1972)
A First Course in Turbulence, Massachusetts Institute of Technology, 1972.

Valkov T. (1992)
*Control of the Unsteady Flow in a Stator Blade Row Interacting with Upstream Moving
Wakes.* M.S. Thesis, Department of Aeronautics and Astronautics, Massachusetts Institute
of Technology, 1995.

Valkov T. (1995)
Progress Report to NASA Lewis Research Center. , August 1995.

Vaughan C.M., Turner A.B. (1987)
*Numerical Prediction of Axisymmetric flow in a Rotor/Stator System with an External Main-
stream.* Numerical Methods in Laminar and Turbulent Flow, Vol 5, Part II. Ed. C.S. Taylor,
W.G. Habachi, M.M. Hafez.

Von Karman T., Sears W.R. (1938)
Airfoil Theory For Non-Uniform Motion. J.Aero.Sci., 1938, 5.

Von Karman Institute for Fluid Dynamics (1987)
Finite element calculation methods and their application to turbomachinery flows. VKI
Lecture series 1987-05,

Wagner J.H., Dring R.P., Joslyn H.D. (1983)
Axial Compressor Middle Stage Secondary Flow Study. NASA CR-3701.

Waitz I.A. (1996)
Private Communication. Massachusetts Institute of Technology, June 1996.

Walker G.J. (1993)
The Role of Laminar-Turbulent Transition in Gas Turbine Engines: A Discussion. ASME
Journal of Turbomachinery, 115, April 1993.

Walker G.J., Gostelow J.P. (1990)
Effects of Adverse Pressure Gradients on the Nature and Length of Boundary Layer Transition. ASME Journal of Turbomachinery, 112.

Walker G.J. (1974)
The Unsteady Nature of Boundary Layer Transition on an Axial-Flow Compressor Blade.
ASME Paper 74-GT-135.

Wisler D.C., Bauer R.C., Okiishi T.H. (1987)
Secondary Flow, Turbulent Diffusion and Mixing in Axial-Flow Compressors. ASME Journal
of Turbomachinery, 109.

Wisler D.C. (1985)
Loss Reduction in Axial-Flow Compressors Through Low-Speed Model Testing. ASME Journal of Turbomachinery, 107, April 1985.

White F.M. (1974)
Viscous Fluid Flow, McGraw-Hill Book Company.

Whitehead D.S. (1987)
Classic Two Dimensional Methods, in "Aeroelasticity in Axial-Flow Turbomachines". AGARD-
AG-298, 1, eds. M. Platzer and F.O. Carta.

Zierke W.C., Okiishi T.H. (1982)
Measurement and Analysis of Total-Pressure Data From an Axial-Flow Compressor Stage.
ASME Journal of Turbomachinery, 104.

Appendix A

Geometry and Units

A.1. Compressor Geometry Used.

The geometry used in the present investigation is based on the General Electric Company Low Speed Research Compressor configuration, as described by Wisler (1985). This configuration is an aerodynamically scaled model of stage VII of the 10-stage, 23:1 pressure ratio NASA/GE E^3 compressor. Its blading is characterized by tailored loading, high hub/tip ratio, low aspect ratio and high solidity (**Table A.1**).

Parameter	Present stator	Stage VII high speed stator
Inlet Mach Number	0.11	0.55
Reynolds Number	247,000	n/a
Stage Reaction	63 %	68%
Hub/Tip Ratio	0.85	0.89
Solidity	1.67	1.67
Aspect Ratio	1.34	1.37
Stagger	32°	n/a

Table A.1. Stator geometry in the present investigation (left) and for stage VII of the 23:1 pressure ratio NASA/GE core compressor. After Wisler (1985).

The design LSRC rotor tip clearance is 1.35% of height (Wisler, 1985), which works out to 1.8% of chord. The tip leakage vortex used herein is from a Navier-Stokes simulations of rotor flow with a clearance of 3.0% chord. This clearance is larger than the design value, but still representative.

Axial spacing between rotor and stator is represented here in an implicit manner, by prescribing the velocity amplitude of wake and tip vortex disturbances. Two axial spacings are represented: 0.37 and 0.07 chords. These values correspond to the ones used for Smith (1970) data. The 0.37 chords axial spacing is considered nominal. This is reflected in placing the computational domain inlet boundary at 0.185 chords upstream of the leading edge.

A 1:1 blade ratio is used in the present investigation. This is in contrast to the non-integer blade ratios used in practice (54:74 rotor-stator blade ratio in Manwaring and Wisler's 1992 work). This simplification is justified, given that the unsteady flow mechanisms identified here take place on lengthscales local to the passage.

Recent stator designs are able to eliminate corner stall, and yield a locally two-dimensional attached flow over the entire stator span (LeJambre, 1995). A departure from the stacking used in the LSRC has been made here to arrive at steady (base) stator flows that corresponds to this description. For this purpose, a straight (non-twisted) stator blade is employed in the present investigation. For the sensitivity study, radial gradients and secondary flows are induced instead by varying the base flow inlet profile to the stator (cf.§6.2.2).

A.2. Operating Points Considered.

The present investigation considers design-point and high-loading operating conditions, as shown in **Figure A.1** and **Table A.2**. Low-loading calculations were not deemed necessary.
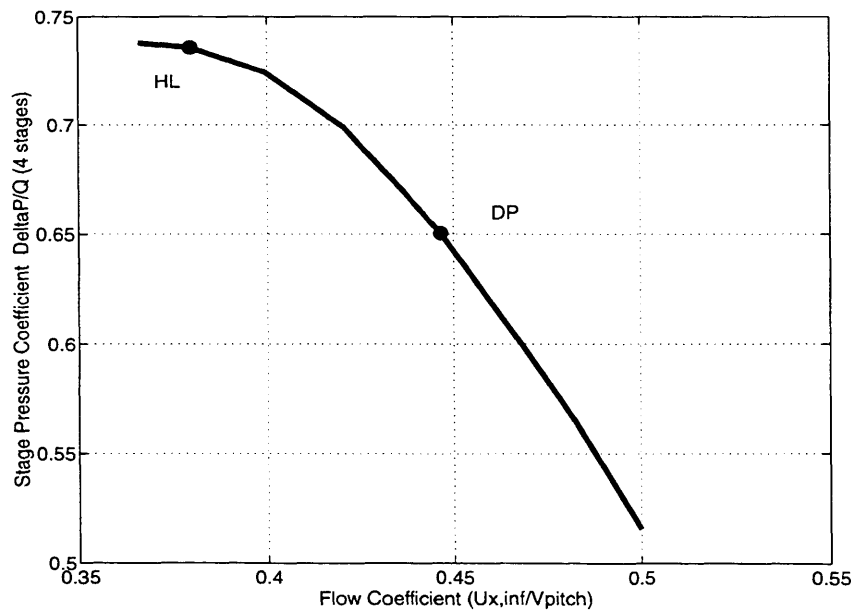
Figure A.1. Location of the DP (design) and HL (high-loading) stator operating points on the stage-average pressure rise characteristic (Manwaring and Wisler, 1992).

Figure of merit	Design Point	High-Loading
Flow coefficient ϕ	0.45	0.38
Stage pressure coefficient ψ	0.65	0.73
Stator inlet air angle θ_1	46.0	50.7
Stator exit air angle θ_2	21.0	n/a
Stator diffusion factor	0.41	0.51

Table A.2. Pitchline stator operating parameters (Manwaring and Wisler 1992).

The GE/LSRC has been extensively used to tackle a variety of compressor flow problems (Wisler, 1985). Insofar unsteady flow is concerned, Manwaring and Wisler (1992) used the facility to characterize the first rotor wakes by means of hot-wire transducers in the first stage rotor/stator gap. The authors also instrumented the midspan of the first-stage stator pressure transducers, and used the unsteady pressure data to evaluate the ability of CFD codes to predict the harmonic content of the unsteady aerodynamic loading induced by the wakes. Silkowski (1995) measured rotor stall characteristics and visualized the rotor exit flowfield over a wide range of flow conditions. Recently, Halstead et al. (1995) obtained detailed transitional data on the midspan boundary layers throughout the compressor.

A.3. Coordinate System.

A Cartesian coordinate system originating at the midspan leading edge, is used throughout this investigation (**Figure A.2**).
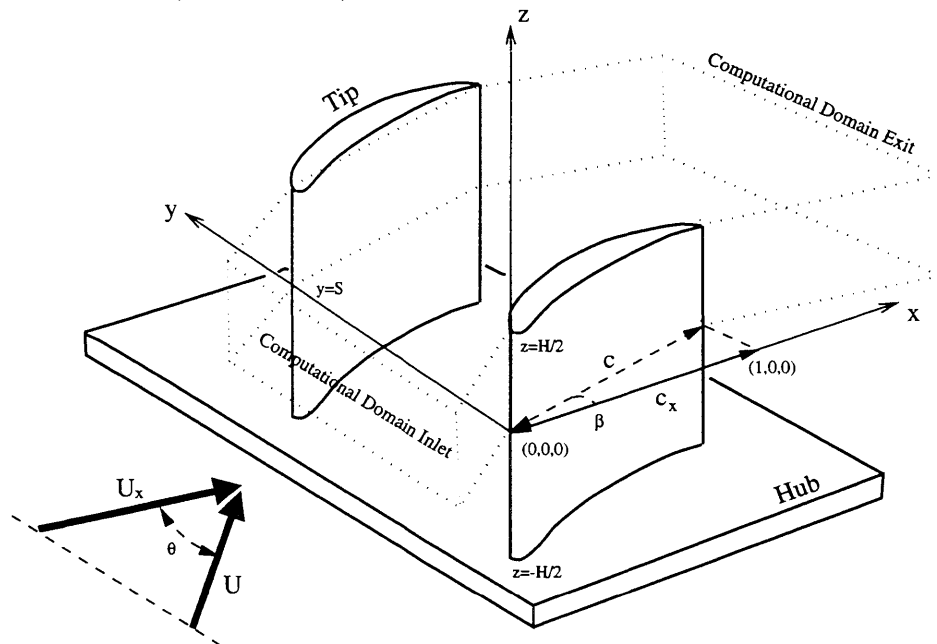
Figure A.2. Coordinate system, computational domain, and flow/geometry scales used to make the problem dimensionless.

Full-span calculations (not discussed here) have shown that the flow in the lower half of the stator passage is virtually free of unsteadiness. Changes in overall performance come from the unsteady flow induced by the upstream rotor vortices near the extremity of the blade. For this reason, the computational domain covers only half of the stator span. The "full-passage" unsteady figures of merit are inferred from the "half-passage" computed figures of merit by means of proportionality :

$$\mathcal{Y}_{s,\text{full}} = 2\mathcal{Y}_{s,\text{half}}$$

$$\mathcal{Y}_{u,\text{full}} = \mathcal{Y}_{s,\text{half}} + \mathcal{Y}_{u,\text{half}}$$

$$\Pi_{s,\text{full}} = 2\Pi_{s,\text{half}} \qquad\qquad (A.01)$$

$$\Pi_{u,\text{full}} = \Pi_{s,\text{half}} + \Pi_{u,\text{half}}$$

In the blade-to-blade plane (xy-plane), the computational domain extends for 0.2 axial chord units upstream of the stator blade trailing edge (mid-gap between rotor and stator), and 0.6 chord units downstream of the stator blade trailing edge. The latter distance is sufficient to prevent interference between the outflow boundary and the blade.

A.4. Dimensionless Units.

Dimensionless units are used throughout this work to present both the computed results and the flow models. The following reference quantities have been used for making the problem dimensionless.

- **Distances.** All distances are scaled with respect to the axial projection "c_x" of the stator blade chord "c". For the present blading, this distance is 2.85 inches. It is related to the blade chord and stagger by

$$c_x = c \cos \beta \qquad\qquad (A.02)$$

- **Velocities.** All velocities are scaled with respect to the pitchline circumferentially-averaged axial velocity component $U_{x,\infty}$ at the mid-gap axial location. At design point, this velocity is estimated at 93 ft/s.

- **Times.** The reference time, $t_{ref} = c_x/U_{x,\infty}$ follows from the above. A unit of dimensionless time corresponds roughly to the time required for a particle to traverse the stator passage, and is thus referred as a *convective time unit* (CTU). At baseline ($\phi = 0.446$), the rotor blade passing period is approximately 0.35 CTUs.

- Densities. The density of the fluid is normalized by the pitchline circumferentially-averaged density ρ_∞ at the mid-gap axial location. Given the incompressible flow assumption, the dimensionless density throughout the flowfield is unity. For this reason, the density symbol is omitted from some equations.

- Pressures. Technically, the reference dynamic head follows from the above selection of reference velocity and density. Thus the raw pressures computed from the NS3D code are in units of $\rho_\infty U_{x,\infty}^2$. It is however common practice to normalize pressures by the total dynamic head upstream of the cascade $\rho_\infty U_\infty^2$. To conform to this practice, all pressure coefficients throughout this work are computed according to :

$$C_t = 2\frac{[p_t - p_{t,avg}]_{\text{code}}}{\rho_\infty \cos\theta_1^2 U_{x,\infty}^2}$$

$$(A.03)$$

$$C_p = 2\frac{[p - p_{avg}]_{\text{code}}}{\rho_\infty \cos\theta_1^2 U_{x,\infty}^2}$$

In this manner, the loss coefficients computed based on the above C_p and C_t also conform to cascade conventions.

- Viscosities. The baseline Reynolds number of the stator is Re=247,000, based on midspan inlet velocity and chord. In light of the above reference velocity and chord however, it follows that the internal computational Reynolds number $R = 1/\nu_i$ is not equal to this value. A careful reader might notice that, internally to the NS3D computational procedure, the passage is scaled so that the hub and casing endwalls are located at $z = \pm 1$. It follows that R is given by:

$$R = \frac{H}{2C}\cos\beta\cos\theta_1 Re \qquad (A.04)$$

The transformations of raw computational units implied by (A.02)-(A.04) have been carried out "transparently", so that the results conform to the cascade design practice. However, future users of the NS3D family of computational tools should be aware of these internal conventions.

Appendix B

Selection and Validation
of the Computational Approach

The quality of the present computational experiments depends on three factors – underlying assumptions, modeling of turbulence and intrinsic accuracy of the method. The effect of these factors shall be examined after a brief introduction of the computational method.

B.1. Selection of Computational Method.

The central problem of computational fluid mechanics is the accurate representation and operation upon continuous fields characterized by high-gradient regions such as boundary layers or shock waves. Several methods have been devised for this purpose :

- Probabilistic methods, illustrated by Monte-Carlo or particle-path simulations. These are rarely used in turbomachinery CFD.

- Finite element/volume/difference methods (Book 1981, Girault 1986, VKI 1987). These use expansions in local, low-order basis functions over small subdomains. A solution to the problem is obtained by means of a weighted-residual or a variational formulation applied to the discrete values of the flow variables at the collocation points. The strength of these methods lies in their geometric flexibility. The low-order expansions however result in a low-order (algebraic) convergence, and are associated with artificial dissipation of energy (numerical viscosity).

- Fully spectral methods (Gottlieb and Orszag, 1977), where an expansion in truncated global functions over the entire computational space is employed. The problem is solved by finding the series coefficients by means of weighted-residual techniques applied at properly selected collocation points. Spectral methods are characterized by a convergence rate that is exponential in the order of the expansion. However, the computational domain is limited to simple geometries.

- Hybrid methods divide the computational domain into a number of regularly-sized regions. A high-order expansion of the flowfield within each region is then carried out, thus achieving both geometric flexibility and high accuracy.

The NS3D computational procedure is based upon a *spectral element* method which belongs to the last category. The base algorithm was developed by Patera (1984) and Korczak (1985). Tan (1989) used a spanwise eigenvalue decomposition allowing to represent three-dimensional internal laminar flows as series of independent two-dimensional problems in modal space. Renaud (1991) applied this method in an investigation of loss mechanisms in turbines. Reynolds-averaging and unsteadiness were included by Valkov (1992). Recent work at the M.I.T. Gas Turbine Laboratory has extended the computational procedure to address rotating centrifugal geometries, density fluctuations, and direct simulations of turbine airfoils at high Reynolds numbers ($\sim$100,000).

B.2. Assessment of Intrinsic Accuracy.

Intrinsic accuracy is the ability to obtain a correct discretized solution to the Navier-Stokes equations for representative conditions. Since no exact analytical solutions are available for turbomachinery unsteady flow, the intrinsic accuracy is verified in three steps. Section B.2.1 establishes the accuracy of the computational procedure basic building blocks for simple cases with known analytical solution. Section B.2.2 demonstrates the local accuracy in a typical unsteady flow situation. Section B.2.3 demonstrates the global accuracy of the scheme in terms of passage figures of merit.

B.2.1. Comparison to steady analytical solutions.

Three cases are considered : (1) fully developed 2D steady laminar Poiseuille flow between two parallel plates, (2) turbulent 2D flow in a convergent-divergent sinusoidal channel, and (3) fully developed 3D steady laminar Poiseuille flow in a straight rectangular passage.

Case 1. The computational grid employed for the first case consists of an array of 15x30 7-th order spectral elements. The plate separation is 1 unit, and the length of the computational domain is 3 units. The dimensionless computational viscosity, ν, is 0.001 units. The analytical solution is (in dimensionless units) :

$$u = y(1 - y); \quad v = 0; \quad \frac{dp}{dx} = -8\nu \qquad (B.01)$$

Using fully-developed flow as inlet boundary conditions, the computed velocity flowfields agree with (B.01) within a global RMS error of 6.2×10^{-5} units. The pressure is constant within 5.9×10^{-2} percent in the plate-to-plate direction, and the axial pressure gradient is

equal to -0.00798 units (0.25% off the analytical value). This test establishes that the planar direct solver (a basic building block of the full unsteady 3D code) is capable of accurately obtaining viscous flows driven by pressure gradients.

Case 2. The computational grid and geometry for 2D turbulent flow in a convergent-divergent channel is shown in **Figure B.1**. The turbulence model employed in the calculation is that of van Driest (White, 1974)

$$\nu = \nu_i + k^2 y^2 \omega^2 \qquad (B.02)$$

which is essentially the inner part of Baldwin-Lomax' algebraic model (**Appendix B**). An intrinsic viscosity of 1/75,000 is used. The computed profiles are compared in **Figure B.1** to the following analytical representation of the "law-ot-the-wall"

$$n^+ = u^+ + e^{-5k}\left[e^{ku^+} - 1 - ku^+ - \frac{(ku^+)^2}{2} - \frac{(ku^+)^3}{6}\right] \qquad (B.03)$$
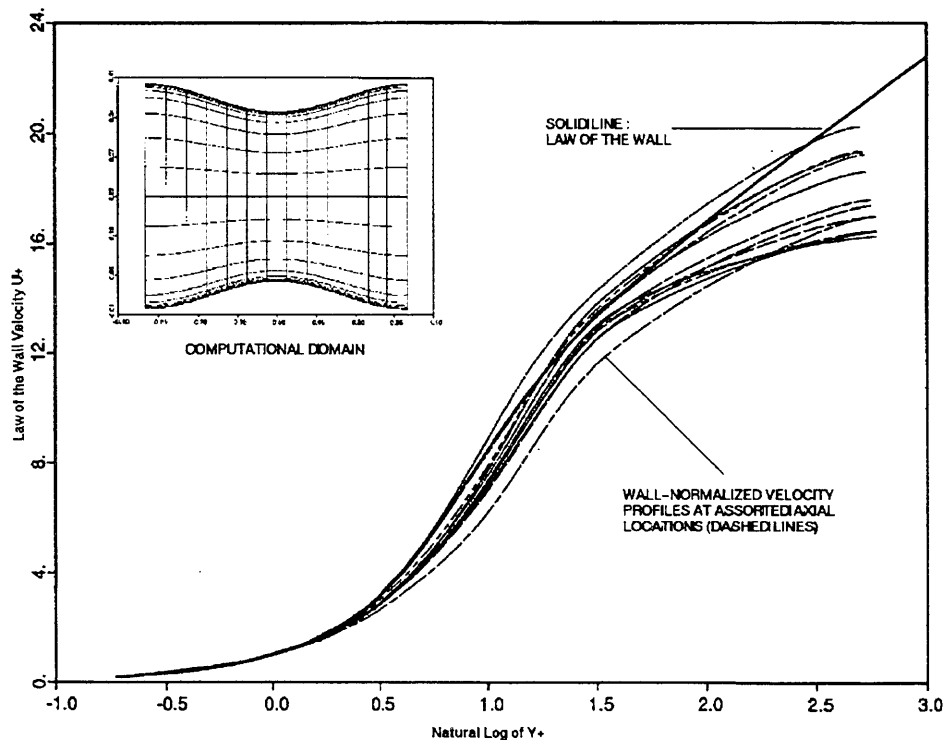
Figure B.1. Computational domain (inset) and comparison between computed and "law-of-the-wall" turbulent profiles at assorted axial locations in a 2D convergent-divergent channel.

Equation (B.03) is a generalized composite formula for the inner and the logarithmic region of a turbulent boundary layer, derived first by Spalding (1961). It is in agreement

with pipe-flow velocity measurements (White, 1974). **Figure B.1** shows how the computed turbulent solution for a channel compares to (B.03) at various axial locations. The agreement is excellent to fairly good far away from the wall. Therefore, the turbulent viscous solver is capable of reproducing the characteristic profiles of a generic turbulent boundary layer.

Case 3. The three-dimensional capabilities of the new code were tested by comparison with the analytical solution for a fully-developed steady laminar Poiseuille flow in a rectangular channel with a cross-section of 1×1 distance units

$$u = -\frac{4\nu}{\pi^3}\frac{dp}{dx}\sum_{k=1,3,5\ldots}\frac{(-1)^{(k-1)/2}}{k^3}\left[1 - \frac{\cosh(k\pi z)}{\cosh(k\pi/2)}\right]\cos(k\pi y) \qquad (B.04)$$

The computational domain contains an 12×24 array of spectral elements and 17 spanwise modes. The analytical and computed velocity fields agree to 3.8×10^{-4} units of global RMS error. This indicates that the spanwise eigenvalue block of the 3D solver is also functioning correctly. Having verified the accuracy of the basic building blocks of the NS3D computational procedure (planar, eddy-viscosity and spanwise solvers) in relatively simple situations, we shall focus on the performance of the whole in a representative unsteady flow situation.

B.2.2. Dynamic consistency of the unsteady solution.

This test shows that the discretized inertial, pressure and viscous force terms sum out to zero in the case of a two-dimensional cascade interacting with upstream wakes. These force terms are obtained in the following manner:

$$\mathbf{a}_{i,jk}^{(1)} = \left.\frac{\partial \mathbf{u}}{\partial t}\right|_{jk,i} = \frac{1}{12\Delta t}\left[\mathbf{u}(t-2\Delta t) - 8\mathbf{u}(t-\Delta t) + 8\mathbf{u}(t+\Delta t) - \mathbf{u}(t+2\Delta t)\right]_{jk,i}$$

$$\mathbf{a}_{i,jk}^{(2)} = -(\mathbf{u}\times\omega)_{jk,i} = \frac{\mathbf{k}\times\mathbf{u}_{jk,i}}{J_{jk,i}}\sum_{r}\sum_{s}\left[\nabla_{jkrs,i}^{x}v_{rs,i}\nabla_{jkrs,i}^{y}u_{rs,i}\right]$$

$$\hspace{11cm}(B.05)$$

$$\mathbf{a}_{i,jk}^{(3)} = (\nabla C_t)_{jk,i} = \frac{1}{J_{jk,i}}\sum_{r}\sum_{s}\nabla_{jkrs,i}C_{trs,i}$$

$$\mathbf{a}_{i,jk}^{(4)} = -(\nabla^2\mathbf{u})_{jk,i} = \frac{1}{J_{jk,i}}\sum_{r}\sum_{s}\mathbf{L}_{jkrs,i}\mathbf{u}_{rs,i}$$

If the solution satisfies the unsteady Navier-Stokes equations, and if the discretized differentiation operators in (B.05) are "exact", the sum of these terms should be nil everywhere. Therefore, the norm of the discretized relative residual error can be used as an indicator of the numerical accuracy of the unsteady solution :

$$\epsilon_{i,jk} = \frac{||\mathbf{a}^{(1)} + \mathbf{a}^{(2)} + \mathbf{a}^{(3)} + \nu\mathbf{a}^{(4)}||_{i,jk}}{\sum_t ||\mathbf{a}^{(t)}||_{i,jk}} \qquad (B.06)$$

Figure B.2 shows the distribution of this residual at the moment of wake interception, when unsteady pressures are at their peak. The peak residuals occur in the free-stream uniform flow, where the denominator of (B.06) is virtually zero. In regions of vortical flow, $\epsilon_{i,jk}$ is usually less than 0.01 percent. The overall residual error is in accordance with the global accuracy of the fractional time-stepping scheme, which is of $\mathcal{O}(\Delta t)$. The residuals near the blade are in accordance with the boundary error of the scheme, which is of $\mathcal{O}(\nu\sqrt{\Delta t})$.
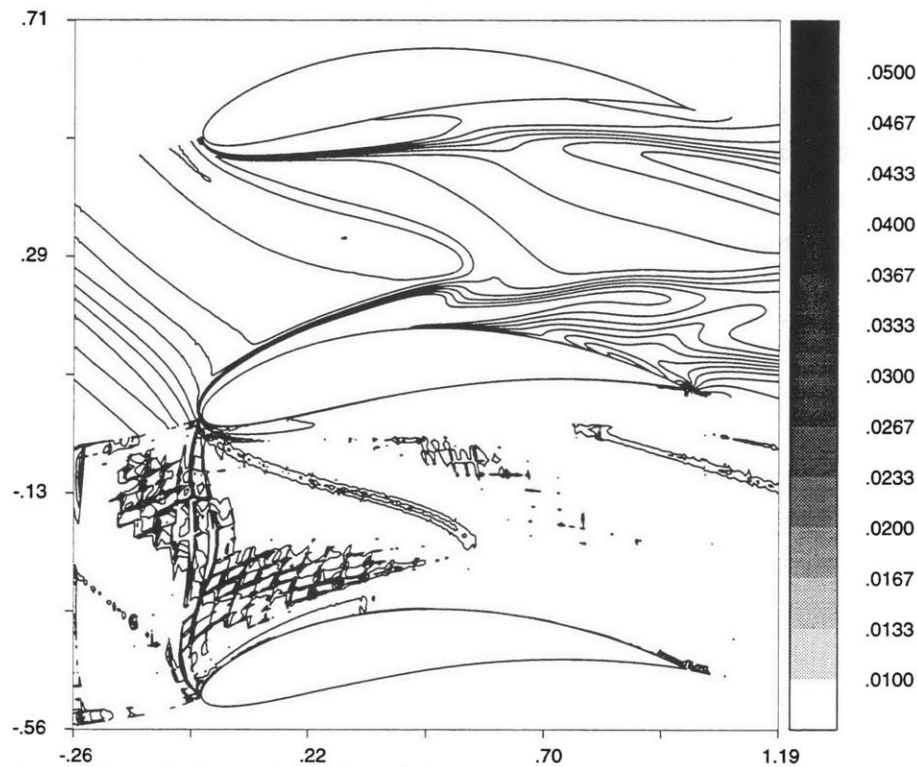
Figure B.2. The relative residual (B.06) in a typical unsteady flow problem is virtually zero in regions of vortical flow. The residual may be larger in regions of uniform flow where (B.06) assumes un undeterminate form of the type 0/0. Top passage : vorticity contours at the moment of wake impingement. Bottom passage : contours of residual $\epsilon_{i,jk}$ at the same time. Scale at right applies to residuals and is in percent. NACA 0812 cascade ($\sigma = 2.0, \beta = 5o, \theta_1 = 13o$). Upstream moving wakes ($V_R = 1, A = 0.5, t = 0.3$). Direct laminar simulation at $R = 1500, \Delta t = 0.001$.

Finally, comparative tests between the full and disturbance formulations of the same unsteady problem (E^3 blade interacting with wakes, $Re = 10^4, \Delta t = 0.001$) have been carried out. The unsteady flowfield from the disturbance NS3D code and the unsteady flowfield from the full Navier-Stokes NS3D code are identical within an absolute RMS error of 1.3×10^{-4}. The material in this section shows that the NS3D computational scheme has a spatial and time accuracy that is appropriate for research purposes.

B.2.3. Time-averaged loss consistency of the unsteady solution.

The purpose of this test is to examine the consistency between time-averaged total pressure losses and vorticity in a representative 3D case. Equation (2.05) states that the time-average rate of loss production should be exactly given by:

$$A\frac{d\mathcal{Y}_p}{dx}(x) = \iint_{x=const.} \overline{\nu\omega^2} dy dz \qquad (B.07)$$

Figure B.3 compares the RHS and LHS of (B.07), based on the computed unsteady total pressure and vorticity fields in a rectangular 3D cascade of unit-length plates ingesting a streamwise vortex. Considering the manner in which (B.07) combines the high gradients of the flow variables, the consistency shown can be qualified as very good. This is especially true around the leading edge, where the rates of loss production are maximum. The consistency in the inlet region is however weaker, due to the presence of some noise. The noise results from the relatively low resolution used in this example. It is not present in the compressor computations to a significant extent.
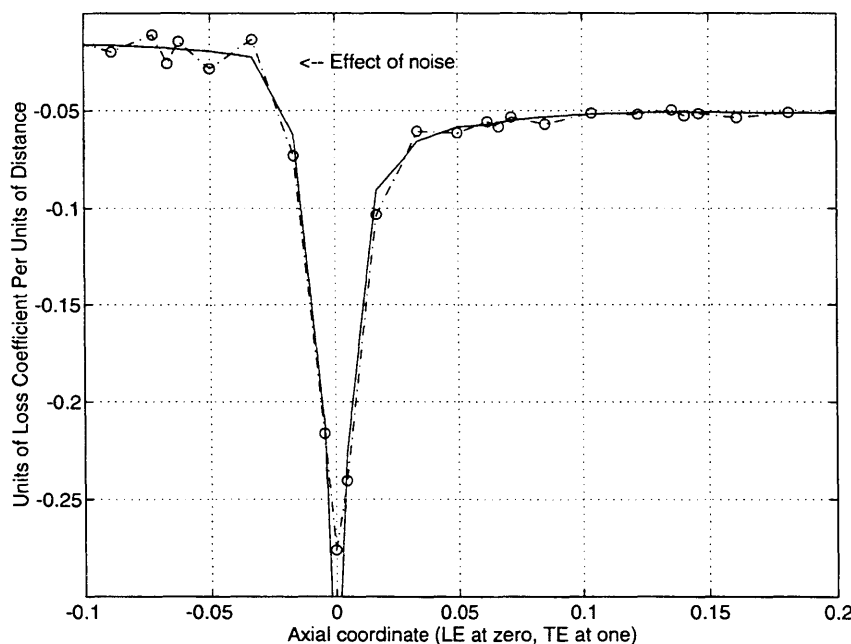
Figure B.3. Solid line: Time-averaged enstrophy integral (RHS of B.07). Dashed lines and dots: Axial derivative of time-averaged loss coefficient (LHS of B.07). Three-dimensional flat plate cascade ($\sigma = 2.0, AR = 0.5$) centrally ingesting a streamwise vortex ($\Gamma = 0.3, r_c = 0.2$). Direct NS3D simulation using a 12x20 blade-to-blade domain and 9 spanwise modes ($\nu = 0.002, \Delta t = 0.005$), no-slip endwalls..

Intrinsic numerical accuracy requirements are met. The effect of turbulence model and assumptions shall be considered next.

B.3. Assessment of the Effects of Eddy Viscosity.

Eddy viscosity effects shall be discussed in four stages. The use of Reynolds averaging in the present unsteady flow situation is examined in §B.3.1. The selection of an algebraic turbulence model is discussed in §B.3.2, while §B.3.3 justifies the use of eddy viscosity over the entire boundary layer. The sensitivity of the unsteady flow features and loss mechanisms to the levels of eddy viscosity is assessed in §B.3.4.

B.3.1. Reynolds averaging in unsteady flow.

Conceptually, the unsteady Navier-Stokes equations, written below in tensor notation, can describe fluid motion across the laminar, transitional and fully turbulent regimes.

$$\frac{\partial u_i}{\partial x_i} = 0 \; ; \qquad \frac{Du_i}{Dt} = -\frac{\partial p}{\partial x_i} + \frac{1}{Re}\frac{\partial}{\partial x_i}\left(\frac{\partial u_i}{\partial x_j} + \frac{\partial u_j}{\partial x_i}\right) \qquad (B.08)$$

In practice however, (B.08) cannot be used to simulate transitional and turbulent flows at high Reynolds numbers. In such flows, energy dissipation takes place at small spatial and time scales (Kolmogoroff microscales) that decrease inversely with the Reynolds number (Tennekes and Lumley, 1972):

$$\begin{aligned}
\eta^* &\sim R^{-3/4} \\
\tau^* &\sim R^{-1/2}
\end{aligned} \qquad (B.09)$$

Therein lies the problem for computation of turbulent and transitional flows such as those in turbomachinery. For instance, a simulation at a Reynolds number of 500,000 needs to be able to resolve flow features as small as 0.00005 chords in order to correctly capture the dynamics of the flow. In practical applications, this problem is circumvened by splitting the flow into two components. The first is a deterministic velocity field U_i of engineering interest. The second component, u'_i, contains the intermittent fluctuations of the turbulence, and satisfies the following criteria with respect to the ensemble-averaging operation :

$$< u'_i > \qquad\qquad = \quad 0$$
$$\qquad\qquad\qquad\qquad\qquad\qquad\qquad\qquad\qquad\qquad (B.10)$$
$$< U_i + u'_i >< U_j + u'_j > \quad = \quad U_i U_j + < u'_i u'_j >$$

Ensemble-averaging the full Navier-Stokes equations yields what is commonly known as the *Reynolds averaged* form of the Navier-Stokes equations :

$$\frac{DU_i}{Dt} = -\frac{\partial P}{\partial x_i} + \frac{\partial}{\partial x_i}\left\{\frac{1}{Re}\left(\frac{\partial U_i}{\partial x_j} + \frac{\partial U_j}{\partial x_i}\right) - < u'_i u'_j >\right\} \qquad (B.11)$$

The closure of (B.11) is provided by expressing the turbulent shear stresses $< u'_i u'_j >$ as the product between the deterministic flow gradients and an eddy viscosity field ν_t:

$$< u'_i u'_j >= \nu_t \left(\frac{\partial U_i}{\partial x_j} + \frac{\partial U_j}{\partial x_i} \right) \qquad (B.12)$$

The Reynolds-averaged Navier-Stokes equations and their derivation are well-known. They have been restated herein for the purpose of questioning the application of the Reynolds-averaged form to a flow where the deterministic components are themselves unsteady. It is straightforward to prove that a sufficient condition for (B.11) is:

$$< U_i u'_j >= U_i < u'_j >= 0 \qquad (B.13)$$

Even when the deterministic component U_i varies in time, (B.13) holds provided that the time scales associated with the unsteady "deterministic" flow are larger than the time scales associated with turbulent fluctuations (B.09). In the case of unsteady flow induced by upstream rotor vortices and wakes, we can distinguish two deterministic time scales. The first is associated with the blade passing period, herein approximately 0.3 convective time units. The second scale is associated with the interception of the vortical disturbance by the stator blade leading edge. It is approximately equal to the thickness of the disturbance divided by the inlet velocity. Herein, this scale is of the order of 0.1 convective time units. Compressor blading Reynolds numbers are usually between 200,000 to 1,000,000 (Mayle, 1991). This corresponds to a turbulence time scale of the order of 0.001 time units, which is much shorter than both of the above deterministic scales. Therefore, the use of Reynolds averaging and turbulent viscosity in the present investigation is justified.

B.3.2. Selection of turbulence model

The use of eddy viscosity makes the Reynolds-averaged Navier-Stokes equations computationally tractable, since $/nu_t$ is usually an order of magnitude or more larger than the physical viscosity $1/Re$. The eddy viscosity is given by semi-empirical relationships involving only the deterministic flow components, and commonly referred to as a *turbulence model*. There is no turbulence model specifically tailored to the unsteady flow from rotor/stator interaction. For this reason, the following two commonly used turbulence models have been considered:

- The Baldwin-Lomax algebraic model (Baldwin and Lomax, 1978).

- The K-ϵ model (e.g. Launder and Spalding 1983; Benocci, 1991).

The K-ϵ turbulence model is based on a rational representation of the dynamics of the turbulent quantities. However, its computational implementation is fragile, and rather sensitive to the several empirical constants appearing in the ϵ equation (Benocci 1983).

The Baldwin-Lomax model is robust. It is based on mixing length and shear layer concepts (Prandtl 1925, White 1974), that seem appropriate for wake and overtip leakage flows. The model has been extensively applied to boundary-layer, separated and shear flow problems with reasonable accuracy (e.g. Sedlar 1993, Degan and Schiff 1986). Since the more complex K-ϵ model offers no particular advantages here, it was decided to use the Baldwin-Lomax formulation for computing the turbulent viscosities.

B.3.3. Time and spatial ranges for eddy viscosity.

In the present work, turbulent viscosity is used at all times and points of the boundary layer. The rationale for this choice is as follows. Experiments by Dong and Cumpsty (1990a), as well as Schlichting and Das (1970), indicate that the entire SS boundary layer may be considered turbulent when the free-stream turbulence level exceeds a certain critical value. For the cascade used by Schlichting and Das (1970), which is fairly similar to the one here, this critical turbulence level is about 2.5 percent (**Figure B.4**).
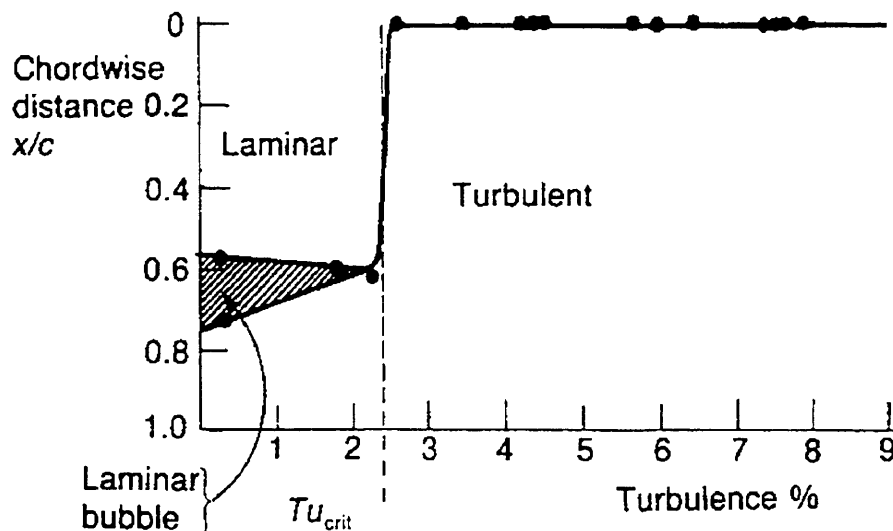
Figure B.4. Positions of separation, reattachment and transition versus free-stream turbulence intensity (Tu) for a NACA65 cascade ($\sigma = 1.0, \theta_1 = 50°, \beta = 40°$). Reynolds number of 160,000. Reproduced from Cumpsty (1989)..

In the multistage environment, free-stream turbulence levels are likely to be above this critical value. Wisler et al. (1987) have measured turbulence levels of 5% in an embedded

stage at design speed away from the casing and the wakes. These levels increase to 10% at reduced mass flow to the left of peak efficiency. Near the endwalls and in the wakes, turbulence levels as high as 20% have been observed. In light of **Figure B.4**, such data indicates that the global use of eddy viscosity is justified for embedded stage simulations.

B.3.4. Sensitivity to eddy viscosity.

The use of turbulence modeling leads to some uncertainty in the computed flows, that stems directly from the empirical nature of the correlations used to compute the eddy viscosity. It is important to assess the degree to which eddy viscosity variations impact the unsteady flow and the loss changes associated with upstream wakes and vortices.

Computational experiments using the baseline turbulence model, indicate that two generic mechanisms are responsible for changes in stator performance. The first is recovery of upstream wakes and tip vortices. The second is normal displacement of boundary layer fluid under the effect of the normal velocity disturbance associated with these wakes and vortices. Both mechanisms are of convective nature. In principle nevertheless, their effect can be influenced by turbulent diffusion. The likelihood for this shall be assessed individually for each mechanism, as follows.

Sensitivity of Recovery. As shown in §**3.3** and §**5.3**, most of the wakes/tip vortex energy is recovered, because recovery occurs over a shorter distance than required for dissipation with the present turbulence model (based on mixing-length/shear layer concepts). Hypothetically, recovery benefits might be reduced if turbulent diffusion rates are sufficiently high.

This possibility has been assessed by carrying a calculation of tip leakage vortex interaction identical in all points to case ID/TL of **Chapter 4**, except that the overall eddy viscosity level is held to 1/1000. This corresponds to approximately two-fold increase in turbulent diffusion rates with respect to the calculation used to demonstrate tip vortex recovery. This constitutes a sufficient upper bound for the uncertainty. The performance effects of recovery in the high-diffusivity case are compared to the baseline ID/TL case in **Table B.1**.

The passage loss numbers in **Table B.1** indicate that a two-fold increase in diffusivity with respect to the value given by the Baldwin-Lomax model does not prevent the recovery of the tip vortex. This low sensitivity is due to the short lengthscale over which recovery occurs ($\sim$0.25 chords) relative to turbulent diffusion. As discussed in §**3.3**, experimental data indicates that diffusion lengthscales at a representative distance behind the rotor are larger than this value. Therefore, our findings with respect to recovery are not dependent

upon the particular turbulence model used.

Loss effect	Baseline ID/TL (**Chapter 4**)	Increased diffusivity $\nu_t = 10^{-3}$
Passage loss increase $\Delta \mathcal{Y}_p$	-0.06 pts	-0.08 pts
Mixing loss difference $\Delta \mathcal{Y}_m$	+0.28 pts	+0.29 pts

Table B.1. Passage loss increase and inlet-to-exit mixing loss difference for baseline and increased-diffusivity ID/TL cases. A low-diffusivity calculation is not necessary for the purpose of assessing the sensitivity of recovery to the turbulence model.

Sensitivity of Boundary Layer Distortion. As shown in §3.3 and §5.2, the performance effect of boundary layer response is tied to the magnitude of the spanwise vortical disturbances induced by the wakes/tip vortex. The term-by-term examination in §5.1 indicates that turbulent diffusion plays almost no role in the production of these disturbances. Normal displacement of vortex lines is the primary mechanism for disturbance production.

In this light, there is an indirect connection between eddy viscosity and vortical disturbances. Eddy viscosity determines the amount and distribution of base vorticity in the steady flow boundary layers. In turn, this determines the magnitude of vortical disturbances arising in the boundary layers. This dependence is captured for instance by the high-loading computational experiment in §6.2.1.

The insensitivity of boundary layer response to the choice of turbulence model (base flow being held constant) is shown by a numerical experiment identical to the baseline VD/TL case except that (a) eddy viscosity is reduced by 50% with respect to the baseline; and (b) the density of the computational grid has been increased by a similar factor. The increase in grid resolution was not sufficient to prevent aliasing noise from the lowered diffusivity. This noise prevents exact comparison of losses, but not of unsteady flow features, which are virtually identical to those from the baseline calculation. This can be appreciated by comparing **Figure B.5** to **Figure 5.3**. Because of the increased resolution, this computational experiment represents a substantial investment in computational resources, and could not be repeated to eliminate the noise.

In summary, boundary layer response effects are not influenced by the choice of turbulence model, provided the base flows used have realistic boundary layers. This has been verified in **Appendix H**.
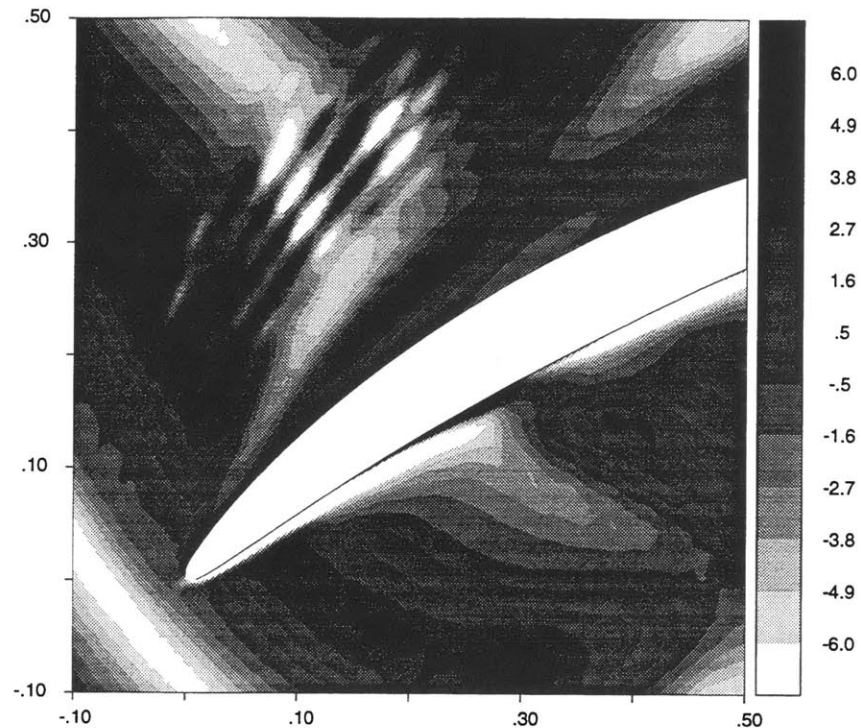
Figure B.5. Disturbance spanwise vorticity $\Delta\omega_z$ on the 91% span blade-to-blade plane from a 50% decreased-diffusivity, increased-resolution calculation otherwise identical to VD/TL. This case: 585 element, 33 plane grid. Case VD/TL: 380 element, 17 plane spectral grid.

B.4. Assessment of the Constitutive Assumptions.

A number of assumptions have been made that allows to reduce the problem of interaction with upstream rotor vortices to its essentials. These are (1) planar stator cascade. (2) rotor-stator blade ratio of 1:1, (3) incompressible flow, and (4) straight stator blades.

Since these assumptions constitute a departure from the environment in aeronautical compressors, their impact on the computed changes in performance shall be considered in the same order. The use of a straight stator is a constraint imposed by the computational approach. The flow angle at the inlet is set to maintain constant incidence to the stator blade. The resulting base flow is free of corner separation, while retaining features typical of 3D compressor flows (spanwise velocity component, streamwise vorticity). These are discussed in **Appendix G**.

B.4.1. Annulus curvature.

Swirl and annulus curvature in typical compressor take values that make centrifugal and Coriolis forces important in general terms. The role of these forces in the interaction

between stator and wakes/tip vortices is a priori unknown. The use of a planar cascade in the present investigation precludes explicit consideration of centrifugal and Coriolis effects. The computed results can be however interrogated to indicate their significance.

In an annular coordinate system (r, θ, x), the centrifugal and Coriolis accelerations acting on a fluid particle are :

$$a_{\text{centrifugal}} = -\frac{v_\theta^2}{r}; \qquad a_{\text{coriolis}} = +\frac{v_r v_\theta}{r} \qquad (B.14)$$

The centrifugal and Coriolis forces associated with the presence of unsteady flow can be expressed in terms of disturbance flow quantities :

$$\Delta a_{\text{centrifugal}} = -\frac{2v_\theta \Delta v_\theta + (\Delta v_\theta)^2}{R_a} \mathbf{e}_r$$

$$\qquad (B.15)$$

$$\Delta a_{\text{coriolis}} = +\frac{\Delta v_r v_\theta + v_r \Delta v_\theta + \Delta v_r \Delta v_\theta}{R_a} \mathbf{e}_\theta$$

Equation (B.15) states that regions of non-uniform swirl, such as wakes and tip vortices, are subjected to additional radial forces. Radial motion of fluid in these regions causes tangential drift by virtue of Coriolis forces. The disturbance centrifugal and Coriolis forces are largest at the inlet of the stator (highest base flow swirl). Their magnitude can be estimated using (B.15) and the unsteady flowfield computed with a planar cascade (This involves the assumption that curvature effects do not lead to radical changes in the unsteady flowfield). **Figures B.6a-b** show the magnitude of these disturbance centrifugal and Coriolis forces. An aggressive value of 5.0 chords for the annulus curvature radius R_a is used in this estimate ($R_a = 10$ for the LSRC).

Figure B.6a indicates that the disturbance centrifugal force is the largest in the tip vortex core (as expected). The force is however too small to substantially affect recovery (which occurs over a distance of 0.25-0.33 chords) or boundary layer response (which occurs on a scale local to the boundary layer). **Figure B.6b** indicates that the disturbance Coriolis force is even smaller. Therefore. the planar cascade assumption is adequate for the flow problem under consideration.

It is to be noted that swirling flows also exhibit other dynamic phenomena of interest. Kerrebrock (1977) has shown that small-amplitude shear disturbances in strongly rotating flows are not convected; rather they propagate slowly and exhibit oscillations with a period comparable to the rotation period of the bulk flow. At high subsonic Mach numbers, Greitzer and Tan (1986) have shown the presence of significant non-convected disturbances coupled to circumferential non-uniformities such as wakes.
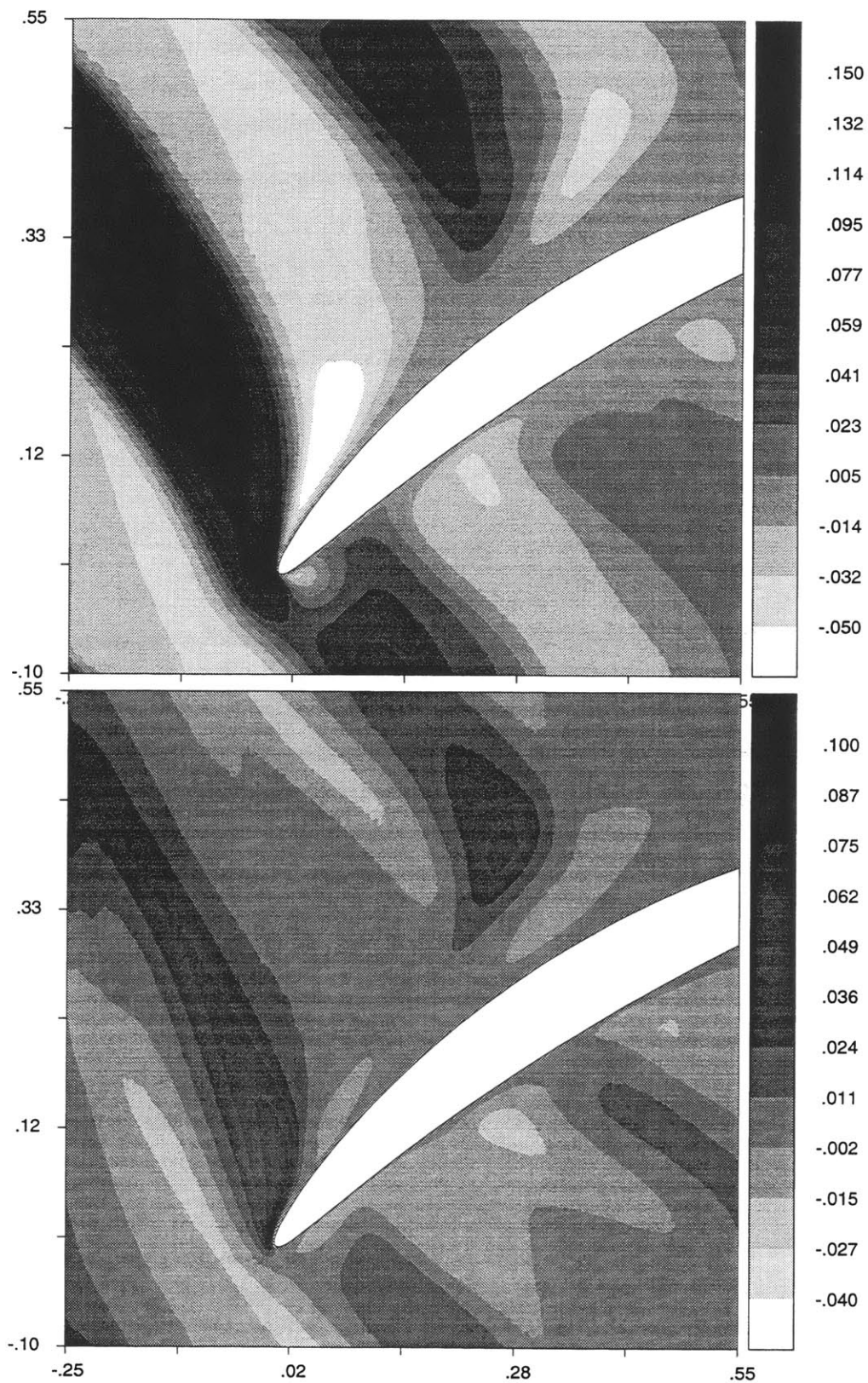
Figure B.6a/B.6b. Estimate of $\Delta a_{centrifugal}$ (top) and $\Delta a_{coriolis}$ (bottom) on the 91% span blade-to-blade plane. This plane passes approximately through the center of the tip vortex (thus showing the strongest disturbance accelerations associated with radius curvature). Estimates are based on the disturbance flowfield from case VD/TL.

B.4.2. Blade count ratio.

With a 1:1 rotor-stator blade count, every stator passage "sees" a single, identical rotor disturbance at any given time. This allows clear identification of the unsteady phenomena, with a minimum of computational effort. Aeronautical compressors however, have non-integer blade ratios for the purpose of reducing tonal noise. The unsteady flow in this case is different from the 1:1 case, because of a circumferential variation in the timing of wake interception. This leads to a pattern of unsteady flow over the annulus, that has a period that is a multiple of the blade passing frequency.

The unsteady flow mechanisms shown here to cause a change in performance are however of a local nature. Individual unsteady flow features (boundary layer vortices, vortex cores) do not interacting with each other, or with those in the next blade row, to a significant extent. Therefore, the performance impact of each individual wake (or a vortex) is not influenced by that of the other wakes (or vortices).

As a result, the changes in performance for non-integer blade ratios can be inferred from those computed for an 1:1 ratio by simply accounting for the different average number of unsteady features per stator passage. This is equivalent to scaling the results computed here by the blade ratio N_R/N_S.

B.4.3. Compressibility.

The present investigation assumes incompressible flow. The flow in the embedded stages of core compressors of interest here, is usually subsonic (Wisler 1985, $M_1=0.55$ for stator VII of the E^3 engine). In the subsonic regime ($M_1 \leq 0.7$), cascade losses are practically independent of the Mach number (Cumpsty, 1989). Actual pressure and potential fields can be inferred from the incompressible solution by means of the Prandtl-Glauert transform. For compressor stages operating in this range, incompressible flow constitutes a valid approximation.

However, for engine components operating in the transsonic/supersonic regime (front compressor stages, turbines), shocks can bring aspects of blade row interaction not captured in the present study.

.

Appendix C

The NS3D Computational Procedure :

Time and Spatial Discretization

Appendices C to F describe an efficient and accurate computational method, referred to as NS3D, for solving the unsteady, three-dimensional incompressible Navier-Stokes equations

$$\frac{\partial \mathbf{u}}{\partial t} - \mathbf{u} \times \boldsymbol{\omega} = -\nabla p_t + \nabla(\nu \nabla \mathbf{u})$$

$$\nabla \cdot \mathbf{u} = 0$$

$$(C.01)$$

Subject to the following boundary conditions :

$$
\begin{array}{lll}
\text{solid surfaces} & : & \mathbf{u} = \mathbf{u}_s(s) \\
& & \nabla p_s \cdot \mathbf{n} = 0 \\
\\
\text{inlet boundary} & : & \mathbf{u} = \mathbf{u}_i(y, z, t) \\
& & \nabla p_s \cdot \mathbf{n} = 0 \\
\\
\text{periodic boundary} & : & \mathbf{u}(x, y + S, z, t) = \mathbf{u}(x, y, z, t) \\
& & p_t(x, y + S, z, t) = p_t(x, y, z, t) \\
\\
\text{exit boundary} & : & \nabla p_s \cdot \mathbf{n} = 0
\end{array}
$$

$$(C.02)$$

Equation (C.01) encompasses both the Reynolds-averaged and direct-simulation cases by representing the viscosity field as follows:

$$\nu = \frac{1}{R} + \mathcal{M}(\mathbf{u}, p, t) \qquad\qquad (C.03)$$

Where $\mathcal{M}$ is an algebraic turbulence model used to calculate the eddy viscosity in the case a Reynolds-averaged solution is desired. Setting $\mathcal{M} = 0$ executes a direct simulation of the full Navier-Stokes equations. Available computational resources limit the Reynolds number that can be achieved in direct simulations. To date, 3D stator unsteady flow direct simulations have been carried for Reynolds numbers up to 10,000.

The NS3D computational procedure can also perform two-dimensional simulations as a special case (§C.17). Direct 2D flow simulations have been carried out for Reynolds numbers of up to 100,000 in compressors (wake-stator interaction, Valkov 1995) and 80,000 in turbines (steady flow, Bury 1996). Extensions of the NS3D computational procedure have been used in studying blade loading response to upstream density non-uniformities (Deregel 1995, Ramer 1996), and simulating micro-engine passage flows using a cylindrical coordinate system formulation.

The NS3D computational procedure is described in four appendices. **Appendix C** presents the time and spatial discretization upon which the procedure is based. **Appendix D** describes implementation innovations that allow turbulent and direct 2D/3D simulations to be performed using modest computational resources. **Appendix E** outlines the algebraic turbulence model used to study the problem of vortex(wake)-blade interaction. Finally, **Appendix F** presents a disturbance technique for unsteady problems that is equivalent to solving the Navier-Stokes equations (C.01), but provides better insight and control of the flow mechanisms.

C.1. Distinctive Features of the NS3D Procedure.

The NS3D method is based on the isoparametric spectral element scheme developed by Patera (1984) and Korczak (1985) for direct solution of the two-dimensional Navier-Stokes equations, and later extended by Tan (1989) to laminar three-dimensional flows. The new method builds upon this previous work in two respects :

- **Size and efficiency.** A relatively large number of x-y spectral elements (300 $\sim$ 600) and spanwise planes (17 $\sim$ 33), is necessary to capture the details of the highly three-dimensional unsteady flow under investigation. Traditional spectral element algorithms require substantial computer resources for problems of this size. This is due to the large operator matrices present in the traditional formulation.

The NS3D method reduces the memory requirements by a factor of N^2, and the number of FLOPs by a factor of N, thereby making the present study feasible from a practical standpoint. The memory savings are illustrated in the following table

Operator matrix class	Traditional implementation	NS3D implementation
Elemental operators	size $\sim 8N_E N^4$	not required
Condensed matrices	size $\sim 6N_Z N_E N^4$	size $\sim 5N_E N^4$
Solver matrices	size $\sim 8N_Z(N_E N)^2$	size $\sim 4(N_E N)^2$

- **Variable viscosity.** The formulations of Korczak (1985), Patera (1984) and Tan (1989) assume that the viscosity of the fluid is constant. This is adequate for direct flow simulations. However, when solving the Reynolds-averaged equations of motion, the viscosity field may vary by several orders of magnitude over short distances. The NS3D method takes this variation into account.

In order to reduce the complexity of the presentation, we shall assume a priori knowledge of the viscosity field "ν", until the turbulence model is introduced in **Appendix E**. We shall first focus on the spanwise discretization of the flowfield, which has two distinct stages – a fully spectral expansion in the spanwise direction, followed by a spectral element discretization in the $x - y$ plane (**Figure C.1**). The spanwise discretization takes advantage of the lack of geometric variation along the span of the blades (cf.§**A.1**), and shall be described first.

C.2. Spanwise Discretization.

The spanwise discretization is based on a fully spectral eigenfunction expansion of the flow variables (Tan, 1989):

$$\mathbf{u}(x,y,z) = \sum_{m}^{N_Z-2} \tilde{\mathbf{u}}_m(x,y)F_m(z)$$

$$p(x,y,z) = \sum_{m}^{N_Z-2} \tilde{p}_m(x,y)G_m(z)$$

$(C.04)$

This expansion allows to reduce the three-dimensional Navier-Stokes problem into a set of independent two-dimensional problems that are less intensive numerically. For this purpose, the modal functions F_m and G_m are chosen to be solutions of a classical Sturm-Liouville problem :

$$\frac{d^2 F_m}{dz^2} = \lambda_m^2 F_m \qquad\qquad (C.05)$$

with the appropriate boundary conditions

$$F_m = 0 \qquad z = \pm 1.$$

$$\frac{dG_m}{dz} = 0 \qquad z = \pm 1. \qquad\qquad (C.06)$$

The analytical solutions of (C.05)/(C.06) are the ordinary sine and cosine functions. The positive sign on the right-hand side of (C.05) requires to cast these in complex notation :

$$
\begin{aligned}
F_m(z) &= \cosh(\lambda_{m,v} z) & m \geq 0 \\
\lambda_{m,v} &= \imath(\tfrac{\pi}{2} + m\pi) & m \geq 0 \\[2mm]
G_m(z) &= \cosh(\lambda_{m,p} z) & m \geq 0 \\
\lambda_{m,p} &= \imath m\pi & m \geq 0
\end{aligned}
\qquad\qquad (C.07)
$$

A transformation to extract the modal content from a given spanwise distribution is necessary to use the expansion (C.04). This implies the use of a Fast Fourier transform applied to a set of collocation planes that are uniformly spaced in the z-direction. Instead, it is desirable to cluster the collocation planes near $z = \pm 1$ in order to resolve the endwall unsteady boundary layer in a more efficient way. Given this consideration, it is more appropriate to expand the modal functions themselves in series of Chebycheff polynomials :

$$F_m(z) = \sum_{i=1}^{N_Z} f_{im} T_{i-1}(z) \qquad\qquad (C.08)$$

Under this expansion, a choice of collocation planes that satisfies the discretization error minimax criterion (Korczak, 1985), is the set of Gauss-Lobatto Chebycheff points in the $[-1; 1]$ interval. The Gaussian point distribution is illustrated in **Figure C.01** and computed according to :

$$z_l = -\cos\frac{(l-1)}{(N_Z-1)}\pi; \qquad l = 1 \dots N_Z \qquad\qquad (C.09)$$
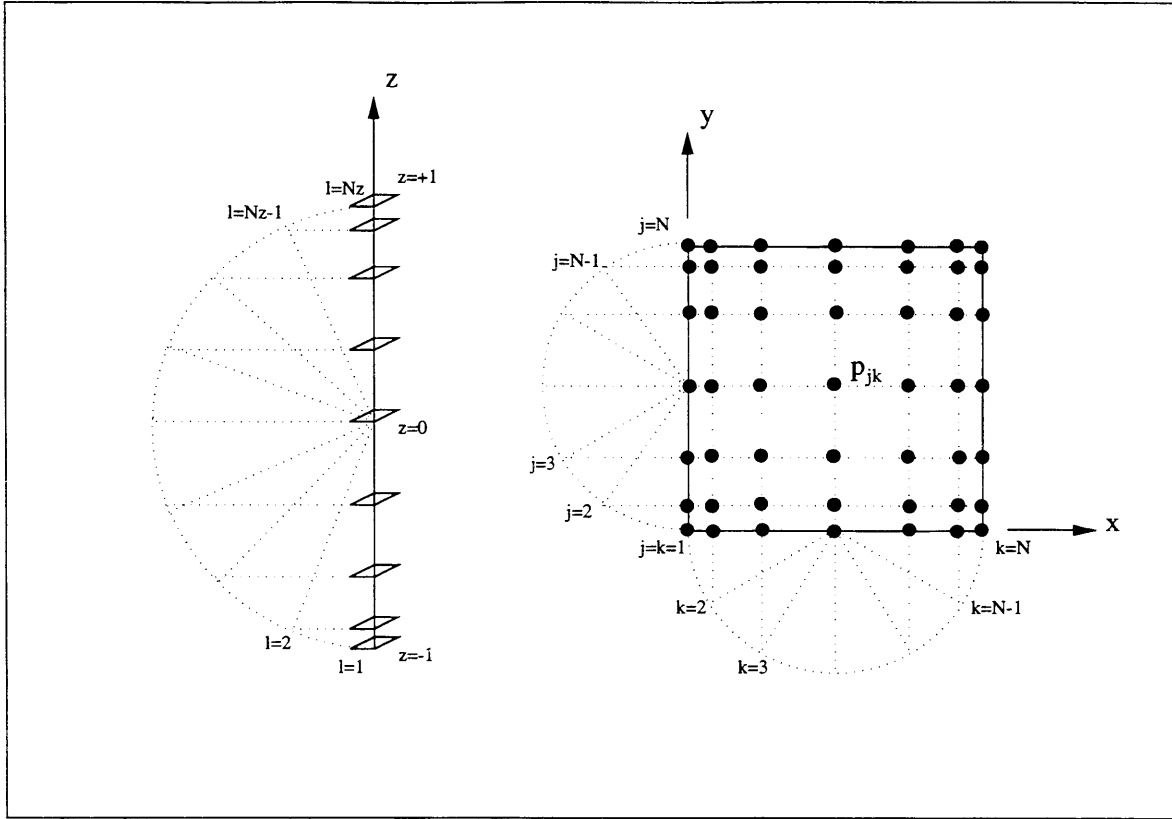
Figure C.1. Gauss-Lobatto Chebycheff distribution in one dimension (left,z-axis,index $"l"$) and in two dimensions (right,x-y plane,index $"jk"$).

Taking the the value of a given flowfield variable $u_l(x,y)$ on the N_Z collocation planes z_l, makes it possible to determine the $N_Z - 2$ spanwise modes $\tilde{u}_m(x,y)$ in (C.04) by means of an FFT-based linear transformation (Tan, 1989). In shorthand, this transformation shall be represented by the operator $\Im_m$. When applied to a collection of discretized values along the spanwise direction, $\Im_m$ returns the m-th mode of the distribution. The entire collection of modes can be obtained according to :

$$\begin{pmatrix} \tilde{\mathbf{u}}_1 \\ \vdots \\ \tilde{\mathbf{u}}_m \end{pmatrix}_{m=1..N_Z-2} = \sum_l \Im_{lm} \begin{pmatrix} \mathbf{u}_1 \\ \vdots \\ \mathbf{u}_l \end{pmatrix}_{l=1..N_Z} \qquad (C.10)$$

The above operation shall be referred to as real-to-modal transformation, and can be implemented as a fast $[\Im]$ matrix-times-vector multiplication. The inverse, or modal-to-real transformation allows to obtain the values of $\mathbf{u}$ at the collocation planes from the modes :

$$\{\mathbf{u}_l\} = \left[\Im^{-1}\right] \{\tilde{\mathbf{u}}_m\} \qquad (C.11)$$

For reasons of computational efficiency, it is necessary to use $N_z = 2^n + 1$ collocation planes in the spanwise direction. In general, 17 to 33 collocation planes are required for representing the unsteady flow of interest here. It is to be noted that the number of z-modes is equal to the number of planes less two, since the two endwall boundary conditions have already been accounted for by an appropriate choice of the modes (C.06).

C.3. X-Y Plane Discretization.

To represent the distribution of a given flow variable $u_l(x, y)$ over a computational x-y plane, the latter is divided into a number of sub-elements of approximately regular shape. These elements are clustered in regions of high flow and geometrical gradient. A local curvilinear coordinate system $(\zeta, \eta)^i$ is associated with each element, as shown in **Figure C.02**.

Inside each such element, the distribution of the flow variable is represented as a direct expansion in series of N-th order Lagrangian interpolants :

$$\mathbf{u}(\zeta, \eta) = \sum_{j=1}^{N} \sum_{k=1}^{N} \bar{\bar{u}}_{jk,i} h_j(\zeta) h_k(\eta) \qquad (C.12)$$

To determine the series coefficients $\bar{\bar{u}}_{jk,i}$, an array of $N \times N$ collocation points $(\zeta, \eta)_{jk,i}$ is used within each element. Although the placement of these points can be arbitrary, the use of the Gaussian distribution shown in **Figure C.02** results in the following property :

$$h_m(\zeta_n) = h_m(\eta_n) = \delta_{mn}; \qquad \begin{cases} \delta_{ij} = 1 & i = j \\ \delta_{ij} = 0 & i \neq j \end{cases} \qquad (C.13)$$

Equation (C.13) implies that :

$$\bar{\bar{u}}_{jk,i} = \mathbf{u}(\zeta_j, \eta_k)_i \qquad (C.14)$$

i.e., that the coefficient of the (j, k) mode is equal to the value of the variable at the local coordinate point (ζ_j, η_k). This is a very useful result, which allows to cast the x-y expansions in terms of real values. Thus, real-to-modal transformations are not required on the x-y planes. Property (C.14) also guarantees a C^0 continuity between adjacent elements, and allows to interpolate geometry and flow variables in the same fashion.
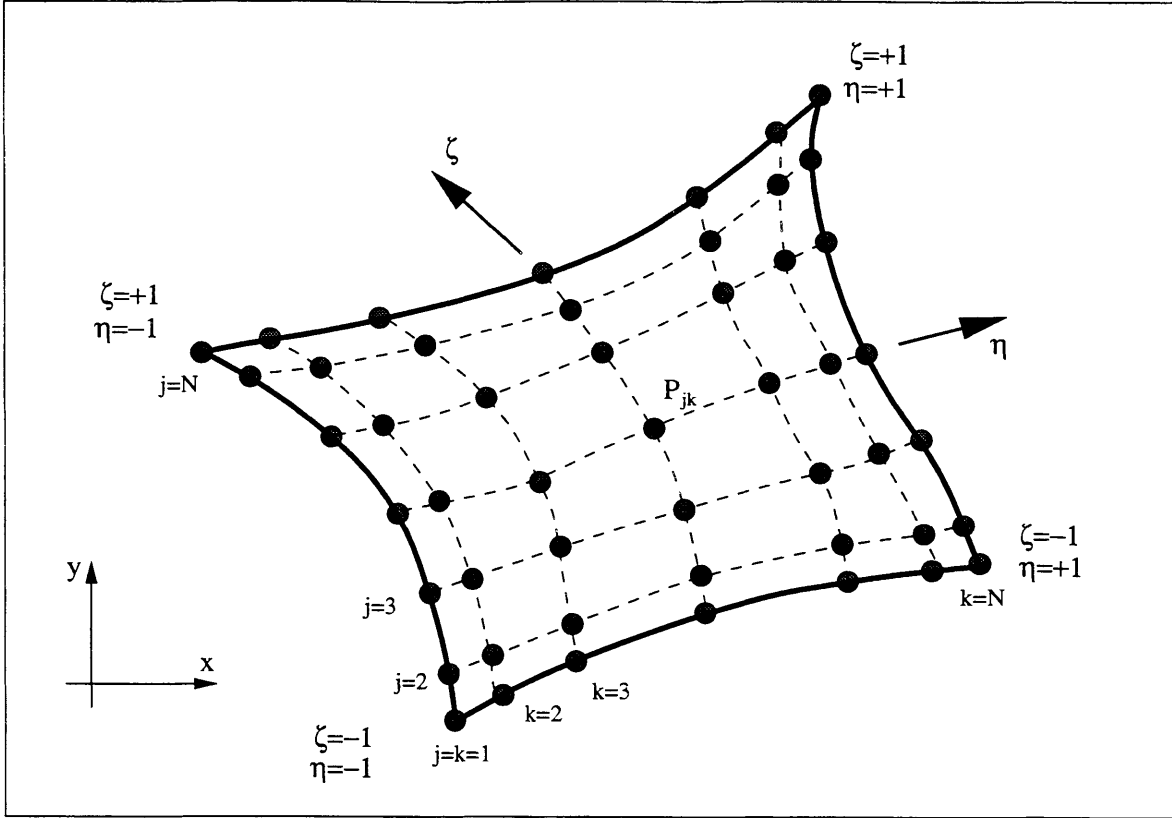
Figure C.2. Collocation points and local coordinate system used for expansion of the flow variables inside a spectral element.

Since the collocation points follow a Gaussian distribution, the Lagrangian interpolants can be constructed as series of orthogonal Chebycheff polynomials :

$$h_m(\zeta) = \sum_{n=1} t_{mn} T_{n-1}(\zeta) \qquad (C.15)$$

where :

$$t_{mn} = \frac{2}{(N-1)C_m C_n} T_{n-1}(\zeta_m) \quad ; \quad C_i = \begin{cases} 1 & m \neq 1, N \\ 2 & m = 1, N \end{cases} \qquad (C.16)$$

It can be shown that the above discretization has a convergence rate that is still exponential in N, albeit slower than that of a fully spectral expansion (Korczak, 1985). In practice, the best results are achieved when the order of the elemental expansion, N, is odd and comprised between $N = 5$ and $N = 9$. For $N \leq 3$, the convergence rate becomes algebraic. For values of N of 11 or more, high-order terms truncation error compromises the accuracy. In the present work, a seventh-order expansion has been used throughout.

C.4. Construction of a Spectral Element Grid.

The accuracy of low-order methods such as finite-element (FE) or finite-volume (FV) is strongly dependent on the density of the grid over which the flowfield is being discretized. Therefore, it is not surprising that traditional mesh generation has been extensively studied as a means to obtain more accurate and efficient solutions. With the present method, proper spectral element gridding of the x-y plane is equally important, albeit for subtler reasons.

The behavior of the spectral element method versus grid resolution is quite different from that of FE/FV methods. In simple terms, one can distinguish between "good" and "bad" spectral grids. At a given Reynolds number, any "good" grid leads to the same solution, which attests for the accuracy of the method. As the Reynolds number is increased, a "good" grid becomes "bad". This can be easily detected by visual inspection, which shows saw-tooth oscillations at the element boundaries. This phenomenon, shown in **Figure C.03** is due to the aliasing of high-order modes, which are necessary to resolve increasingly smaller flow scales at high Reynolds numbers.
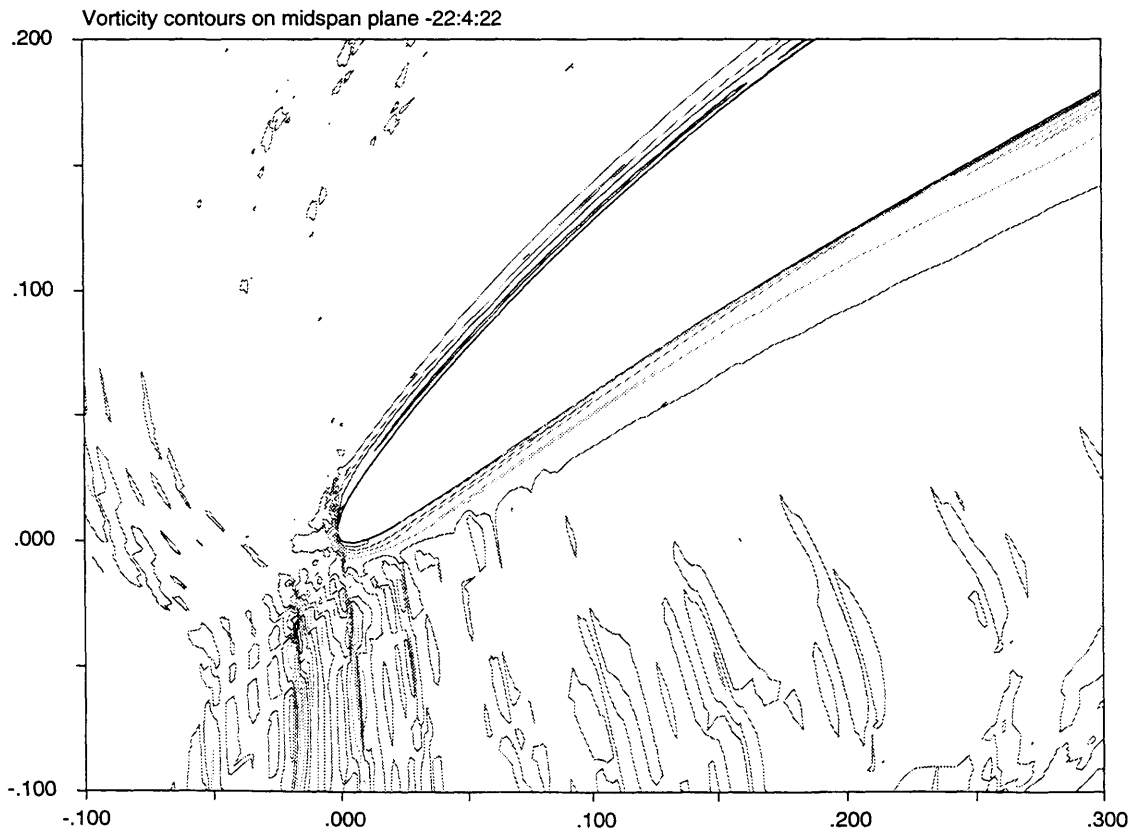
Figure C.3. Aliasing noise resulting from insufficient spectral resolution at a given Reynolds number (direct simulation, Re=10,000).

"Bad" grids cannot be improved by simply increasing the order of the local expansion beyond $N = 7$. Such an increase affects mostly the intrinsic accuracy at the element boundaries, but does little for the resolution at the element center. Instead, it is necessary to cluster the elements in regions of high gradient, and reduce the elemental size overall.

Conceptually, it is possible to produce a "good" grid by simple "proliferation" of spectral elements. In practice, one is limited by the available computational resources. Thus, it becomes increasingly difficult to adequately subdivide the computational domain into spectral elements at high Reynolds numbers. The following set of rules can help with this task:

- Use small, clustered elements in regions of high geometrical gradient such as the leading edge. The characteristic element size "ϱ" there should be comparable to r_{le}, where r_{le} is the radius of curvature of the leading edge.

- Use thin layers of elements in the boundary layer region. The elemental thickness at the surface should be comparable to that of the viscous sublayer, i.e. $\varrho^+ \sim 10$.

- In the Reynolds-averaged case, use a characteristic size of the order of r_d for the rest of the elements (r_d is the smallest macroscopic length scale present in the upstream disturbance, i.e. wake thickness). For rotor vortices and wakes, an r_d between $0.05c$ and $0.10c$ is usually adequate to resolve the bulk flow.

- Keep the element edge angles as close to 90 degrees as possible. This requirement is especially important in regions of high gradients.

- Use an orderly arrangement of the elements, based on the presence of common boundaries. This is necessary to minimize the size of the condensed system matrices (cf. §D.5).

- Use the same abscissa for opposite collocation points on the upper and lower periodic boundaries. This allows to implement the periodicity boundary conditions by using the same global node index for such points.

The spectral grid used in the NS3D computational scheme is based on an arrangement known as H-grid. The alternative "C" and "O" arrangements cannot be made to meet rule # three above. Hybrid arrangements do not allow efficient ordering of the elements.

A grid generation package, NG2, has been developed that automatically generates spectral H-grids around a variety of compressor and turbine geometries according to the foregoing rules. The grid generation package is an essential element of the NS3D computational procedure. It uses a fast, robust and original algorithm, based on metric-preserving Euclidean transformations, rather than on conformal mappings or Laplace solvers. Thus, it is of interest to describe the NG2 algorithm, which proceeds as follows :

A) Specify the computational domain dimensions and boundary geometry. Specify the desired grid density in the four major domain regions : inlet, blade-to-blade, exit and boundary layer.

B) Construct a rectangular template having N_H vertical and N_V horizontal dividers as shown in **Figure C.04a**. The vertical dividers cut the horizontal dividers into into $N_H \times N_V$ horizontal segments of length $\ell_{H,i,j}$. Reciprocally, the horizontal dividers cut the vertical dividers into into $N_V \times H_V$ vertical segments of length $\ell_{V,i,j}$. Within a rectangular template, it is easy to position the dividers in such a manner that the matrices of segment arclength ratios :

$$[\Xi_H^*]_{i,j} = \ell_{H,i,j} / \sum_i \ell_{H,i,j}$$

$$[\Xi_V^*]_{i,j} = \ell_{V,i,j} / \sum_j \ell_{V,i,j}$$

$$(C.17)$$

corresponding to the desired spectral element densities in each of the four major domain regions. The periodicity boundary condition requirements are met by setting :

$$[\Xi_H^*]_{i,1} = [\Xi_H^*]_{i,N_H} \qquad\qquad (C.18)$$

C) Make an arbitrary $N_H \times N_V$ meshing of the computational domain, such as the one shown in **Figure C.04b**.

D) Determine a set of points $Q_{i,j}$ along each vertical divider "j", such that the arclength ratio matrix of the resulting vertical arcs

$$[\Xi_V^Q]_{i,j} = \ell_{V,i,j}^Q / \sum_j \ell_{V,i,j}^Q \qquad\qquad (C.19)$$

is equal to $[\Xi_V^*]$. Reconstruct the "i" horizontal dividers along the set of points $Q_{i=c,j}$ using cubic spline interpolation (**Figure C.04c**).

E) Determine a set of points $P_{i,j}$ along each horizontal divider "i", such that the arclength ratio matrix of the resulting horizontal arcs

$$[\Xi_H^P]_{i,j} = \ell_{H,i,j}^P / \sum_i \ell_{H,i,j}^P \qquad\qquad (C.20)$$

is equal to $[\Xi_H^*]$. Reconstruct the "j" vertical dividers along the set of points $P_{i,j=c}$ using cubic spline interpolation (**Figure C.04d**).

F) Calculate the arclength ratio matrix for the new horizontal segments $[\Xi_H^Q]$. Repeat steps (D), (E) and (F) until the following criteria are satisfied :

$$\| \, [\Xi_H^*] - [\Xi_H^Q] \, \| \;\; \leq \;\; \epsilon$$

$$(C.21)$$

$$max([\Xi_H^*] - [\Xi_H^Q]) \;\; \leq \;\; \epsilon_m$$
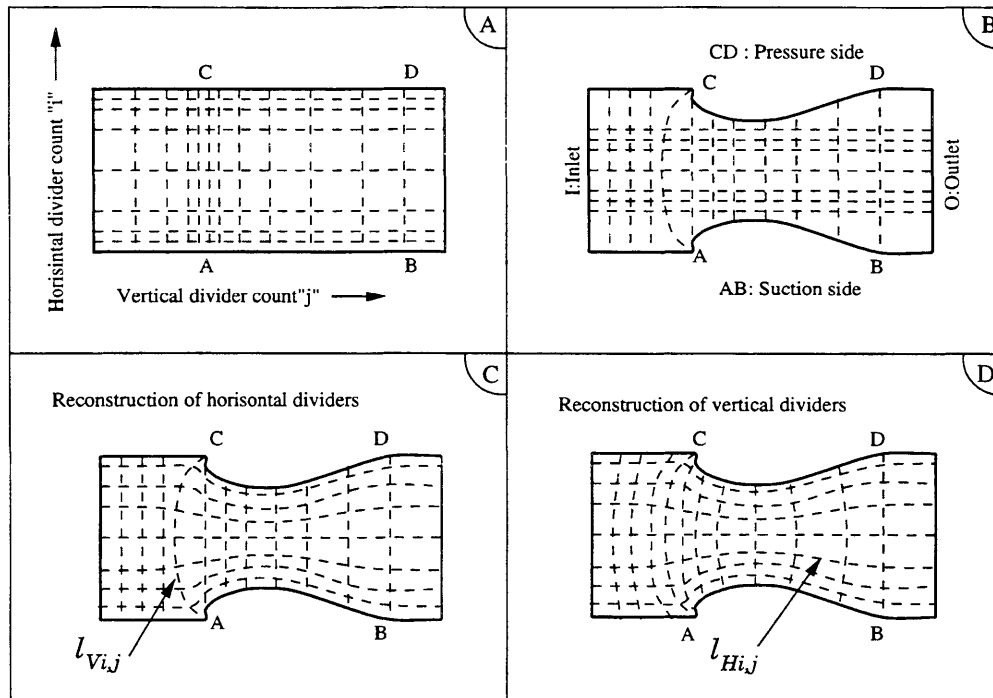
Figure C.4. Metric-preserving algorithm for the subdivision of the computational domain into spectral elements.

Usually, this scheme converges to residuals of 10^{-5} to 10^{-4} in a few iterations. It has also the extra benefit of weakly preserving the right angles in the template, thereby resulting in spectral elements that are rectangular nearly everywhere.

The second stage of the spectral gridding is to position the collocation points $(P)_{jk,i}$ inside the elements. This operation is no less critical, because if a collocation point lies a few percent off its exact Gauss-Lobatto Chebycheff locus in the local coordinate system, there will be similar error in the calculation of the local first-order derivatives. This renders the intrinsic accuracy of the spectral expansion meaningless, and can be easily observed in numerical tests.

While it is straightforward to position the collocation points in rectangular elements (cf. **Figure C.01**), there is no direct analytical way to do so for a general element. The NG2 package solves this problem by applying the above metric-preserving technique within

each spectral element. In this case, the target arclength ratio matrices are set to contain a Gaussian distribution scaled from the $[-1, +1]$ interval to the $[0, 1]$ interval :

$$[\Xi_H^*]_{i,j} = \frac{1}{2} - \frac{1}{2}\cos\frac{(i-1)\pi}{(N-1)}$$

$$[i, j] \in [1, N]^2 \qquad (C.22)$$

$$[\Xi_V^*]_{i,j} = \frac{1}{2} - \frac{1}{2}\cos\frac{(j-1)\pi}{(N-1)}$$

The final stage of the spectral gridding is to index the ensemble of collocation points. In the following, collocation points shall be referred to as nodes. Five indexes are constructed, according to a scheme illustrated in **Figure C.05** :
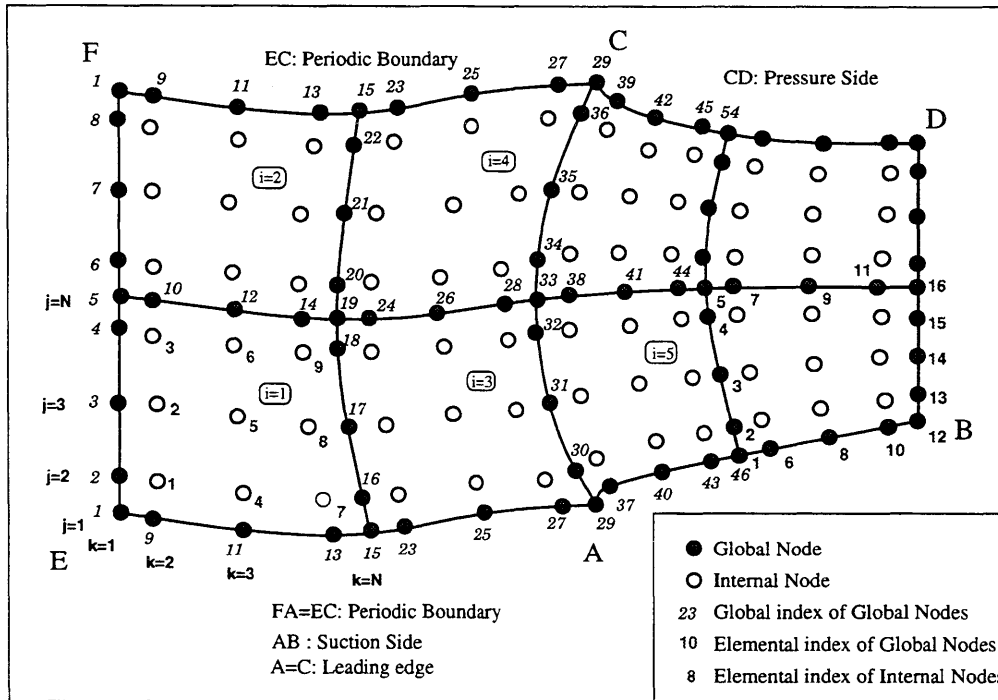
Figure C.5. Indexing scheme for elements, nodes, global nodes and internal nodes. Note the indexing of the periodic boundary.

- An elemental index $()^i_{jk}$ referring to the (ζ_j, η_k) node on the i-th spectral element. This index provides the most direct manner to access a spectrally discretized value. The size of this index is $N_E N^2$.

- An elemental global node index $()^i_g$, referring to the g-th global node on any element i. Global nodes are nodes on the element boundaries, and are shared between two and four elements. The size of this index is approximately $4N - 4$.

- An elemental internal node index $()^i_e$, referred to the e-th internal node on any element i. Internal nodes are local to the elements. The size of this index is $(N - 2)^2$.

- A global index of global nodes $()_G$, which provides a unique pointer to each global node. The size of this index is approximately $2N_E N$.

- A pointer table $(G)_{g,i}$, linking the the elemental global node index $()_g^i$ on element i to the global index of global nodes $()_G$.

- An index, $()_s$, containing the indices of those global nodes at which velocity Dirichlet boundary conditions shall be prescribed. Such nodes usually belong to the blade surface and the inlet. The size of this index is approximately $(2N_P + N_I)(N - 1)$.

The last five indexes are used for static condensation and for efficiently solving the global system equations (cf. §D.1-D.4). The global node indexing scheme shown in **Figure C.05** serves the purpose of minimizing the diagonal bandwidth of the global system matrices. More efficient, but complex, indexing schemes are possible.

C.5. Three-Step Time-Marching Technique.

A fractional time-splitting scheme (Orszag and Kells [34]) is used to advance the Navier-Stokes equations forward in time. Using the flowfield $\mathbf{u}^n$ at time t, the scheme permits to obtain the flowfield $\mathbf{u}^{n+1}$ at time $t + \Delta t$ in three fractional steps :

(1) Convective step, which extrapolates the change in velocity from time t to time $t + \Delta t$ due to convective effects only :

$$\mathbf{u}^* = \mathbf{u}^n + \int_t^{t+\Delta t} \mathbf{u} \times \boldsymbol{\omega} dt \qquad (C.23)$$

(2) Pressure step, which corrects the velocity update from the convective step

$$\mathbf{u}^{**} = \mathbf{u}^* - \int_t^{t+\Delta t} \nabla p \, dt \qquad (C.24)$$

using a pressure field p^{n+1} such that the updated velocity satisfies continuity.

(3) Viscous step, which corrects the velocity update from the pressure step to take into account dissipation effects, and which imposes the Dirichlet boundary conditions.

$$\mathbf{u}^{n+1} = \mathbf{u}^{**} + \int_t^{t+\Delta t} \nabla(\nu \nabla \mathbf{u}) dt \qquad (C.25)$$

A solution of the Navier-Stokes equations is obtained by starting from an approximate velocity field $\mathbf{u}^0$, and advancing the solution with a global time step Δt until a steady state or a periodic unsteady flow is achieved.

The time error of the fractional scheme depends upon the accuracy with which the individual integrals in (C.23) to (C.25) are evaluated in the time domain. The NS3D computational

procedure uses a time discretization scheme which provides an accuracy of order $\mathcal{O}(\nu\sqrt{\Delta t})$ near the boundaries, and of order of $\mathcal{O}(\Delta t)$ elsewhere.

The time step used in the present work is dictated by the need to resolve motion at the fine scales. For Reynolds-averaged simulations, Δt must be an order of magnitude less than the leading edge radius of curvature r_{le}. This results in time steps between 10^{-3} to 2×10^{-3}. The viscosity field "ν" takes values of the order of 10^{-4} to 10^{-3}. Consequently, the time error in the NS3D solutions is within acceptable ranges. Therefore, it was not deemed necessary to use higher-order time discretization for the pressure and viscous steps.

C.6. Time Discretization of the Convective Step.

A fourth-order Runge-Kutta scheme is used to evaluate the integral in equation (C.23). This allows to calculate the spatially-discretized updated velocity, $u^*_{jk,i,l}$ over all the nodes $(P)_{jk,i}$ and planes $(z)_l$, in an explicit manner :

$$\mathbf{u}^{n+1/4}_{jk,i,l} = \mathbf{u}^n_{jk,i,l} + \frac{\Delta t}{2}(\mathbf{u}^n \times \boldsymbol{\omega}^n)_{jk,i,l}$$

$$\mathbf{u}^{n+1/2}_{jk,i,l} = \mathbf{u}^n_{jk,i,l} + \frac{\Delta t}{2}(\mathbf{u}^{n+1/4} \times \boldsymbol{\omega}^{n+1/4})_{jk,i,l} \qquad (C.26)$$

$$\mathbf{u}^{n+3/4}_{jk,i,l} = \mathbf{u}^n_{jk,i,l} + \Delta t(\mathbf{u}^{n+1/2} \times \boldsymbol{\omega}^{n+1/2})_{jk,i,l}$$

$$\mathbf{u}^*_{jk,i,l} = \mathbf{u}^n_{jk,i,l} + \frac{\Delta t}{6}\left\{(\mathbf{u} \times \boldsymbol{\omega})^n + 2(\mathbf{u} \times \boldsymbol{\omega})^{n+1/4} + 2(\mathbf{u} \times \boldsymbol{\omega})^{n+1/2} + (\mathbf{u} \times \boldsymbol{\omega})^{n+3/4}\right\}_{jk,i,l}$$

Given that the spectral expansion in the x-y plane is continuous to order $\mathcal{C}^0$, the vorticity at the element boundaries might present a discontinuity. In practice, this is overcome by averaging the x and y partial derivatives at the boundary between two adjacent elements.

C.7. Time Discretization of the Pressure Step.

A backward Euler scheme is used to evaluate the time integral in the pressure step (C.24)

$$\mathbf{u}^{**} = \mathbf{u}^* - \Delta t \nabla p^{n+1} \qquad (C.27)$$

The pressure field in (C.27) is determined by the requirement for the updated velocity to satisfy the continuity equation :

$$\nabla \cdot \mathbf{u}^{**} = 0 \qquad (C.28)$$

In practice, $\mathbf{u}^{**}$ cannot be obtained explicitly since the pressure does not appear in the continuity equation. The lack of coupling between velocity and pressure is one of the major issues in solving the incompressible Navier-Stokes equations. One way around it is to use of a control volume technique, which is based on the following identity :

$$\iiint_V \nabla \cdot (p\mathbf{u}^{**})dV = \iiint_V p\nabla \cdot \mathbf{u}^{**}dV + \iiint_V \mathbf{u}^{**} \cdot \nabla p dV \qquad (C.29)$$

By virtue of the continuity equation, the first right-hand term of (C.29) is identically zero. The C^0 integrand continuity, allows to apply the divergence theorem to the left-hand side of (C.29), thereby yielding:

$$\iiint_V \mathbf{u}^{**} \cdot \nabla p dV = \oiint_{\delta V} p\mathbf{u}^{**} \cdot \mathbf{dS} \qquad (C.30)$$

By substituting the expression for $\mathbf{u}^{**}$ from equation (C.27) into the above, we obtain a well-posed, three-dimensional integral equation for the pressure field :

$$-\iiint_V \Delta t(\nabla p^{n+1})^2 dV =$$
$$\qquad\qquad\qquad\qquad\qquad\qquad\qquad\qquad\qquad\qquad (C.31)$$
$$-\iiint_V \mathbf{u}^* \cdot \nabla p^{n+1} dV + \oiint_{\delta V} p^{n+1}\mathbf{u}^* \cdot \mathbf{dS} - \Delta t \oiint_{\delta V} p^{n+1}\nabla p^{n+1} \cdot \mathbf{dS}$$

Equation (C.31) is subject to the boundary conditions (C.02), which basically make the last left-hand term drop out. It is furthermore possible to reduce this problem to a set of N_M independent two-dimensional problems by using the eigenfunction expansion of the flow variables in the spanwise direction from §C.2. For this purpose, components of (C.32) containing spanwise derivatives shall be first integrated by parts :

$$-\iiint_V \left(\frac{\partial p}{\partial z}\right)^2 dV = -\left[\iint_S p\frac{\partial p}{\partial z}dxdy\right]_{z=-1}^{z=+1} + \iiint_V p\frac{\partial^2 p}{\partial z^2}dV$$
$$\qquad\qquad\qquad\qquad\qquad\qquad\qquad\qquad\qquad\qquad\qquad (C.32)$$
$$-\iiint_V w\frac{\partial p}{\partial z}dV = -\left[\iint_S wp\,dxdy\right]_{z=-1}^{z=+1} + \iiint_V p\frac{\partial w}{\partial z}dV$$

It is to be noted that the terms in square parenthesis above drop out by virtue of the boundary conditions (C.02). Substituting (C.32) into (C.31) allows to write the 3D integral equation for the pressure in the following form :

$$-\int dz \iint_S \Delta t \left\{ \left(\frac{\partial p^{n+1}}{\partial x}\right)^2 + \left(\frac{\partial p^{n+1}}{\partial y}\right)^2 - p\frac{\partial^2 p^{n+1}}{\partial z^2} \right\} dxdy =$$

$$(C.33)$$

$$-\int dz \iint_S \left\{ u\frac{\partial p^{n+1}}{\partial x} + v\frac{\partial p^{n+1}}{\partial y} + p^{n+1}\frac{\partial w}{\partial z} \right\} dxdy + \int dz \oint_{I,O} p^{n+1} \mathbf{u}^* \cdot \mathbf{dn}$$

Substituting the expansion (C.04) into (C.33), and multiplying the resulting equation by the $\mathfrak{S}_m$ operator defined in (C.10), casts the pressure integral equation into the modal domain. Using the fact that the expansion modal functions $G_m(z)$ are eigensolutions of (C.05) allows one to factor out from this equation the z-summation term :

$$\sum_{m1}^{N_M}\sum_{m2}^{N_M} \int G_{m1}G_{m2}(z)dz...$$

$$(C.34)$$

Owing to the orthogonality of the modal functions, this term is non-zero only when $m_1 = m_2 = m$. As a result, the modal-domain 3D pressure integral equation can be collapsed into a set of N_M independent two-dimensional integral equations for the modes "p_m" of the pressure variable, taken over the spectral x-y plane "S":

$$\forall m = 1..N_M;$$

$$-\iint_S \Delta t \left\{ \left(\frac{\partial \tilde{p}_m^{n+1}}{\partial x}\right)^2 + \left(\frac{\partial \tilde{p}_m^{n+1}}{\partial y}\right)^2 - \lambda_{m,p}^2 (\tilde{p}_m^{n+1})^2 \right\} dxdy =$$

$$(C.35)$$

$$\iint_S \left\{ \tilde{u}_m\frac{\partial \tilde{p}_m^{n+1}}{\partial x} + \tilde{v}_m\frac{\partial \tilde{p}_m^{n+1}}{\partial y} + \tilde{p}_m^{n+1}\frac{\partial \tilde{w}}{\partial z}|_m \right\} dxdy + \oint_{I,O} \tilde{p}_m^{n+1} \tilde{\mathbf{u}}_m^* \cdot \mathbf{dn}$$

These equations shall be spatially discretized in §C.15 and solved for the modes of the pressure variable. Using the inverse transformation $\mathfrak{S}^{-1}$ allows to map the modes back in the real domain and obtain the spatially discretized total pressure distribution $p_{jk,i,l}$. Albeit somewhat complex, this method offers a substantial computational advantage in comparison to solving (C.33) directly.

C.8. Time Discretization of the Viscous Step.

In previous work (Tan 1989), the time-discretized viscous step has been implemented using an implicit Crank-Nicholson scheme. However, an explicit forward Euler scheme was found to be just as adequate. It was thereby used in the NS3D code, where it offers substantial streamlining of the computational process. With a forward-time Euler discretization, to

obtain $\mathbf{u}^{n+1}$ one needs to solve the following three-dimensional vector diffusion PDE, subject to the Dirichlet boundary conditions (C.02) :

$$\mathbf{u}^{n+1} = \mathbf{u}^{**} + \nabla\left(\nu^n\nabla\mathbf{u}^{n+1}\right)\Delta t \qquad (C.36)$$

In practice, a standard variational formulation (Jeffreys & Jeffreys, 1972) of (C.36) allows to improve the the global accuracy of the discretized velocity update in the sense of the minimax criterion. Thus, the NS3D computational procedure solves, for each component "u^{n+1}" of the velocity vector "$\mathbf{u}^{n+1}$", the following problem :

$$\delta\iiint_V \left\{\nu^n\Delta t\left(\nabla u^{n+1}\right)^2 + (u^{n+1})^2\right\}dV = \delta\iiint_V 2u^{n+1}u^{**}dV \qquad (C.37)$$

The direct solution of this equation is quite a formidable task from a computational standpoint. In the NS3D computational procedure this is accomplished by casting the problem in the modal domain and, reducing it to a set of N_M two-dimensional variational problems for the velocity modes u_m^{n+1}. This process is very similar to the one employed in the pressure step. It starts by the following sequence of integration by parts, the purpose of which is to make the first left-hand side term of (C.37) amenable to an eigenmode expansion :

$$\iiint_V \nu\left(\nabla u^{n+1}\right)^2 dV = \int dz\iint_S \nu\left(\frac{\partial u^{n+1}}{\partial x}\right)^2 dxdy$$
$$+\int dz\iint_S \nu\left(\frac{\partial u^{n+1}}{\partial y}\right)^2 dxdy + \int dz\iint_S \nu\left(\frac{\partial u^{n+1}}{\partial z}\right)^2 dxdy \qquad (C.38)$$

$$\int dz\iint_S \nu\left(\frac{\partial u^{n+1}}{\partial z}\right)^2 dxdy = -\int dz\iint_S \nu u^{n+1}\frac{\partial^2 u^{n+1}}{\partial z^2}dxdy$$
$$-\int dz\iint_S u^{n+1}\frac{\partial\nu}{\partial z}\frac{\partial u^{n+1}}{\partial z}dxdy \qquad (C.39)$$

$$\int dz\iint_S u^{n+1}\frac{\partial\nu}{\partial z}\frac{\partial u^{n+1}}{\partial z}dxdy = -\frac{1}{2}\int dz\iint_S (u^{n+1})^2\frac{\partial^2\nu}{\partial z^2}dxdy \qquad (C.40)$$

Equations (C.39) and (C.40) allow to re-write the variational form of the viscous step (C.37) as follows :

$$\delta\iiint_V \left\{\nu\Delta t\left(\frac{\partial u^{n+1}}{\partial x}\right)^2 +\nu\Delta t\left(\frac{\partial u^{n+1}}{\partial y}\right)^2 - \nu\Delta t u^{n+1}\frac{\partial^2 u^{n+1}}{\partial z^2}\right.$$

$$\left. + \left(1 + \frac{\Delta t}{2}\frac{\partial^2\nu}{\partial z^2}\right)(u^{n+1})^2\right\}dV = \delta\iiint_V 2u^{n+1}u^{**}dV$$

$$(C.41)$$

The integrands in the above shall be expanded in terms of spanwise modes using equation (C.04). Using the fact that the modal functions satisfy (C.05) allows to rewrite (C.41) in the following manner :

$$
\delta \sum_{m1}^{N_M} \sum_{m2}^{N_M} \sum_{m3}^{N_M} \int_{-1}^{+1} F_{m1}(z) F_{m2}(z) F_{m3}(z) dz \iint_S \Delta t \left\{ \tilde{\nu}_{m1} \frac{\partial \tilde{u}_{m2}^{n+1}}{\partial x} \frac{\partial \tilde{u}_{m3}^{n+1}}{\partial x} \right.
$$

$$
+ \qquad \tilde{\nu}_{m1} \frac{\partial \tilde{u}_{m2}^{n+1}}{\partial y} \frac{\partial \tilde{u}_{m3}^{n+1}}{\partial y} + \left(\frac{1}{\Delta t} - \tilde{\nu}_{m1} \lambda_{m2,v}^2 + \frac{1}{2} \tilde{\nu}_{m3}'' \right) \tilde{u}_{m2}^{n+1} \tilde{u}_{m3}^{n+1} \left. \right\} dx dy \qquad (C.42)
$$

$$
= \qquad \delta \sum_{m2}^{N_M} \sum_{m3}^{N_M} \int_{-1}^{+1} F_{m2}(z) F_{m3}(z) dz \delta \iiint_V 2 \tilde{u}_{m2}^{n+1} \tilde{u}_{m3}^{**} dx dy
$$

It is not as straightforward as in (C.34) to factor-out the summations along of the eigenmodes F_m. The complication arises from the presence of the triple product between modes in the L.H.S. of (C.42), which makes it impossible to exploit eigenmode orthogonality. On the other hand, the integral of this triple product satisfies the relationship :

$$
\int_{-1}^{+1} F_{m1}(z) F_{m2}(z) F_{m3}(z) dz \quad \left\{ \begin{array}{ll} \neq 0 & m_1 = \pm m_2 \pm m_3; m_1 \geq 1 \\ = 0 & \text{otherwise} \end{array} \right. \qquad (C.43)
$$

Inserting (C.43) into (C.42) and factoring out the orthogonal terms on the right-hand side yields a set of N_M independent variational problems for each of the unknown velocity modes u_m^{n+1} :

$$
\forall m = 1..N_M;
$$

$$
\delta \iint_S \Delta t \left\{ \overline{\nu} \left(\frac{\partial \tilde{u}_m^{n+1}}{\partial x} \right)^2 + \overline{\nu} \left(\frac{\partial \tilde{u}_m^{n+1}}{\partial y} \right)^2 + \left(\frac{1}{\Delta t} - \overline{\nu} \lambda_{m,v}^2 + \frac{1}{2} \overline{\nu}_m'' \right) (\tilde{u}_m^{n+1})^2 \right\} dx dy \qquad (C.44)
$$

$$
= \delta \iint_S 2 \tilde{u}_m^{n+1} \tilde{u}_m^{**} dx dy
$$

Where the term

$$
\overline{\nu} = \sum_{m2} \sum_{m3} \int_{-1}^{+1} \nu_{\pm m2 \pm m3} F_{m2}(z) F_{m3}(z) dz \left[\int_{-1}^{+1} \sum_m F_m^2(z) \right]^{-1} \qquad (C.45)
$$

can be recognized as being the spanwise mean value of the viscosity field at the particular (x,y) location. The modal-domain viscous step equation (C.44) basically states that the

higher modes diffuse at a faster rate, as given by the term $\bar{\nu}\lambda_{m,v}^2$. Any spanwise variation of the viscosity field also modifies the diffusion rate of the m-th mode via the term $\bar{\nu}_m''$.

Before applying the x-y spatial discretization to the set of minimax problems in (C.44), it is convenient to take the variational operator δ inside the integrals. This yields the following set of integral equations :

$$\forall m = 1..N_M;$$

$$\iint_S \Delta t \left\{ \bar{\nu}\frac{\partial \delta \tilde{u}_m^{n+1}}{\partial x}\frac{\partial \tilde{u}_m^{n+1}}{\partial x} + \bar{\nu}\frac{\partial \delta \tilde{u}_m^{n+1}}{\partial y}\frac{\partial \tilde{u}_m^{n+1}}{\partial y} \right. \tag{C.46}$$

$$\left. + \left(\frac{1}{\Delta t} - \bar{\nu}\lambda_{m,v}^2 + \frac{1}{2}\bar{\nu}_m''\right) \delta\tilde{u}_m^{n+1}\tilde{u}_m^{n+1} \right\} dxdy = \delta \iint_S \delta\tilde{u}_m^{n+1}\tilde{u}_m^{**}dxdy$$

After solving (C.46), the velocity modes are mapped back to the computational domain using modal-to-real transformation $\Im^{-1}$. This yields the discretized velocity distribution $\mathbf{u}_{jk,i,l}^{n+1}$ at time $t + \Delta t$ and completes one time cycle.

C.9. Spatial Discretization: Partial Derivatives.

To implement numerically the time-marching algorithm outlined in §C.6 to §C.8, one must address the issue of spatial discretization. This issue has two distinct aspects :

- Calculation of the discretized partial derivatives, needed for the convective step (C.26).

- Calculation of the various integral forms in (C.35) and (C.44) on the x-y spectral plane in terms of discretized variables.

The approximation of the integral forms shall be dealt with in §C.10-§C.14. The partial derivatives in the spanwise direction can be directly found based on (C.04) and our explicit knowledge of the eigenmodes F_m :

$$\frac{\partial \mathbf{u}}{\partial z}\Big|_{jk,i,l} = \sum_{m}^{N_z-2} \tilde{\mathbf{u}}_{jk,i,m}F_m'(z_l)$$

$$\tag{C.47}$$

$$\frac{\partial^2 \mathbf{u}}{\partial z^2}\Big|_{jk,i,l} = \sum_{m}^{N_z-2} \lambda_{m,v}^2\tilde{\mathbf{u}}_{jk,i,m}F_m(z_l); \qquad \nu''\Big|_{jk,i,l} = \sum_{m}^{N_z-2} \lambda_{m,v}^2\tilde{\nu}_{jk,i,m}F_m(z_l)$$

The partial derivatives in the x-y plane must be first calculated in each element's local coordinate system (ζ, η) (cf. **Figure C.02**) and then mapped into the global coordinate frame using :

$$\left\{ \begin{array}{c} \mathbf{u}_x \\ \mathbf{u}_y \end{array} \right\} = \frac{1}{J_i} \left[\begin{array}{cc} y_\eta & -y_\zeta \\ -x_\eta & x_\zeta \end{array} \right]_i \left\{ \begin{array}{c} \mathbf{u}_\zeta \\ \mathbf{u}_\eta \end{array} \right\} \qquad (C.48)$$

This coordinate transform is local to each element "i". Its discretized Jacobian is given by

$$J_{jk,i} = (x_\zeta y_\eta - x_\eta y_\zeta)_{jk,i} \qquad (C.49)$$

The calculation of the partial derivatives in the local coordinate system is relatively straightforward. Using an expansion in local interpolants (C.12), and taking (C.13) and (C.14) into account yields :

$$\frac{\partial \mathbf{u}}{\partial \zeta}\Big|_{jk,i} = \sum_l \sum_m \mathbf{u}_{i,lm} \frac{\partial h_l}{\partial \zeta}(\zeta_j) h_m(\eta_k) = \sum_l \sum_m D_{lj}\delta_{mk}\mathbf{u}_{i,lm}$$

$$\frac{\partial \mathbf{u}}{\partial \eta}\Big|_{jk,i} = \sum_l \sum_m \mathbf{u}_{i,lm} h_l(\zeta_j) \frac{\partial h_m}{\partial \eta}(\eta_k) = \sum_l \sum_m D_{mk}\delta_{lj}\mathbf{u}_{i,lm} \qquad (C.50)$$

$$D_{jk} = \frac{dh_j}{ds}(s_k)$$

The symbol D_{jk} in (C.50) is the *discretized local differential operator*, which need be computed only once as shown in bf §D.8. Using the orthogonality of the Kronecker Delta function, one can eliminate one level of convolution in (C.50). The discretized partial derivatives in the local coordinate system can be then rapidly obtained from :

$$(\mathbf{u}_\zeta)_{jk,i} = \sum_l D_{lj}\mathbf{u}_{i,lk}$$

$$(C.51)$$

$$(\mathbf{u}_\eta)_{jk,i} = \sum_m D_{mk}\mathbf{u}_{i,jm}$$

Since the geometry variables are mapped in the same manner as the flow variables, the discretized coordinate transform matrix in (C.48) can be also calculated using (C.51). For a static grid, this needs to be done only once according to :

$$[T]_{i,jk} = \frac{1}{J_{i,jk}} \left[\begin{array}{cc} \sum_m D_{mk} y_{i,jm} & -\sum_l D_{lj} y_{i,lk} \\ -\sum_m D_{mk} x_{i,jm} & \sum_l D_{lj} x_{i,lk} \end{array} \right] \qquad (C.52)$$

Using (C.51) and (C.52), the discretized partial derivatives in the spectral plane can be obtained in the following straightforward and efficient manner :

$$
\left\{ \begin{array}{c} \left(\dfrac{\partial \mathbf{u}}{\partial x}\right)_{i,jk,z} \\[2mm] \left(\dfrac{\partial \mathbf{u}}{\partial y}\right)_{i,jk,z} \end{array} \right\} = [T]_{i,jk} \left\{ \begin{array}{c} \displaystyle\sum_{l} D_{lj}\mathbf{u}_{i,lk,z} \\[2mm] \displaystyle\sum_{m} D_{mk}\mathbf{u}_{i,jm,z} \end{array} \right\} \qquad (C.53)
$$

Traditionally, the calculation of partial derivatives has been based on the following *global partial differential operators* (Tan 1989):

$$
\nabla^x_{jkrs,i} = D_{rj}\delta_{sk}(y_\eta)_{jk} + D_{sk}\delta_{rj}(-y_\zeta)_{jk}
$$

$$
\nabla^y_{jkrs,i} = D_{rj}\delta_{sk}(-x_\eta)_{jk} + D_{sk}\delta_{rj}(x_\zeta)_{jk}
$$
$$
(C.54)
$$

The set of operators $\nabla_{jkrs,i}$ allows to calculate the partial derivatives directly in the x-y coordinate system according to :

$$
\left(\frac{\partial \mathbf{u}}{\partial *}\right)_{jk,i,l} = \frac{1}{J_{jk,i}} \sum_r \sum_s \nabla^*_{jkrs,i} \mathbf{u}_{rs,i,l} \qquad (C.55)
$$

From a symbolic standpoint, (C.55) is simpler than (C.53), despite the fact that the two forms are algebraically identical. In addition, the use of (C.55) for deriving discretized approximations allows to reduce algebraic complexity significantly. For instance, the discretized 3D Laplacian can be simply written as :

$$
\left(\nabla^2 \mathbf{u}\right)_{jk,i,l} = \frac{1}{J_{jk,i}} \sum_p \sum_q L_{jkpq,i}\mathbf{u}_{pq,i,l} + \sum_m^{N_z-2} \lambda^2_{m,v}\tilde{u}_{jk,i,m}F_m(z_l) \qquad (C.56)
$$

where the *global x-y Laplacian operator* is shortly :

$$
\mathbf{L}_{pqlm,i} = \sum_j \sum_k \frac{1}{J_{jk,i}} \left\{ \nabla^x_{pqjk,i}\nabla^x_{jklm,i} + \nabla^y_{pqjk,i}\nabla^y_{jklm,i} \right\} \qquad (C.57)
$$

Calculation of the discretized Laplacian is required for some high-order formulations of the viscous and pressure steps. It is also a commonly used test to assess the discretisation error associated with a particular scheme. To illustrate the accuracy of the spectral expansion, it is sufficient to mention that (C.56) yields $\nabla^2 f$ within machine precision for exponential polynomials of degree up to $N \times N$ in the x-y plane, and degree N_Z in the z-direction. The Laplacian of "difficult" non-polynomial test functions be calculated with precisions ranging from 10^{-11} to 10^{-4} for $N = 7$ to $N = 11$.

From computational standpoint, (C.55), (C.57), as well as other subsequent expansions based on (C.54), are inefficient and wasteful. For this reason, (C.54) will be used only

as a means to reduce algebraic complexity. The NS3D computational scheme uses (C.53) exclusively. **Appendix D** presents the basis for the NS3D computational efficiency.

C.10. Spatial Discretization: Line Integrals.

The following type of line integrals, where "L" is part of the x-y spectral plane boundary, appears at the right-hand side of the pressure equation (C.35) :

$$\Phi^L(p_m, \mathbf{u}_m) = \oint_L p_m \mathbf{u}_m \cdot d\mathbf{n} = \int_L p_m u_m dy - \int_L p_m v_m dx \qquad (C.58)$$

The evaluation of such integrals is based on integration in the local coordinate system for each element belonging to "L", followed by a elementwise summation. With the spectral grid constructed as shown in **Figure C.04**, there are four distinct cases, determined by the nature of "L" :

$$
\begin{array}{lll}
\mathcal{L} & \text{is the inlet boundary } \mathcal{I}: & k = 1, \zeta = -1 \\
\mathcal{L} & \text{is the exit boundary } \mathcal{O}: & k = N, \zeta = +1 \\
\mathcal{L} & \text{is the suction side } \mathcal{S}: & j = 1, \eta = -1 \\
\mathcal{L} & \text{is the pressure side } \mathcal{P}: & j = N, \eta = +1
\end{array}
\qquad (C.59)
$$

To begin, let's consider the first case. Along $\mathcal{I}$, the integrands can be locally expanded as follows :

$$u_m(x, y) = \sum_j \sum_k u_{jk,i,m} h_j(-1) h_k(\eta) = \sum_k u_{1k,i,m} h_k(\eta)$$

$$dy = \frac{\partial y}{\partial \eta} d\eta; \qquad dx = \frac{\partial y}{\partial \eta} d\eta \qquad (C.60)$$

$$\frac{\partial f}{\partial \eta}(-1, \eta) = \sum_k \left(\frac{\partial f}{\partial \eta}\right)_{1k} h_k(\eta) = \sum_k (\sum_m D_{mk} f_{1m}) h_k(\eta)$$

Substituting into (C.58) yields :

$$\Phi^I(p_m, \mathbf{u}_m) = \sum_{i \in N_I} \int_{-1}^{+1} \sum_r u_{1r,i,m} h_r(\eta) \sum_a p_{1a,i,m} h_a(\eta) \sum_k \sum_m D_{mk} y_{1m} h_k(\eta) d\eta$$

$$- \sum_{i \in N_I} \int_{-1}^{+1} \sum_r v_{1r,i,m} h_r(\eta) \sum_a p_{1a,i,m} h_a(\eta) \sum_k \sum_m D_{mk} x_{1m} h_k(\eta) d\eta$$

$$\qquad (C.61)$$

The introduction of the *local third-order integral operator* :

$$\tilde{B}_{abc} = \int_{-1}^{+1} h_a(\zeta) h_b(\zeta) h_c(\zeta) d\zeta \tag{C.62}$$

allows one to express (C.58) as a convolution sum of local operators and discrete values at the collocation nodes :

$$\Phi^I(p_m, \mathbf{u}_m) = \sum_{}^{i \in N_I} \int_{-1}^{+1} \sum_r \sum_a \sum_k \sum_m p_{1a,i,m} D_{mk} \tilde{B}_{rak} \{u_{1r} y_{1m} - v_{1r} x_{1m}\}_{i,m} \tag{C.63}$$

Approximations to (C.58) for the remaining three cases are obtained in a similar manner:

$$\Phi^O(p_m, \mathbf{u}_m) = \sum_{}^{i \in N_O} \int_{-1}^{+1} \sum_r \sum_a \sum_k \sum_m p_{Na,i,m} D_{mk} \tilde{B}_{rak} \{u_{Nr} y_{Nm} - v_{Nr} x_{Nm}\}_{i,m}$$

$$\Phi^S(p_m, \mathbf{u}_m) = \sum_{}^{i \in N_S} \int_{-1}^{+1} \sum_r \sum_a \sum_k \sum_m p_{a1,i,m} D_{mk} \tilde{B}_{rak} \{u_{r1} y_{m1} - v_{r1} x_{m1}\}_{i,m} \tag{C.64}$$

$$\Phi^P(p_m, \mathbf{u}_m) = \sum_{}^{i \in N_S} \int_{-1}^{+1} \sum_r \sum_a \sum_k \sum_m p_{aN,i,m} D_{mk} \tilde{B}_{rak} \{u_{rN} y_{mN} - v_{rN} x_{mN}\}_{i,m}$$

Although (C.63) and (C.64) constitute an efficient manner to calculate line integrals per se, they cannot be directly used in the spatial discretization of the pressure step. Indeed, the structure of the convolution sums in (C.63) and (C.64) does not allow one to construct a well-posed linear equation for the pressure variable. As it shall become apparent in §C.15, proper convolution sums exhibit the following structure :

$$\sum_j \sum_k p_{jk,i,m} \cdots (\sum \cdots) \tag{C.65}$$

The Kronecker Delta function can be used to convert (C.63) and (C.64) to the proper form above. This yields :

$$\Phi^I(p_m, \mathbf{u}_m) = \sum_{}^{i \in N_I} \sum_j \sum_k p_{jk,i,m} \left\{ \delta_{k1} \sum_r \sum_p \sum_q D_{qp} \tilde{B}_{rjp} (u_{r1} y_{q1} - v_{r1} x_{q1})_{i,m} \right\}$$

$$\Phi^O(p_m, \mathbf{u}_m) = \sum_{}^{i \in N_O} \sum_j \sum_k p_{jk,i,m} \left\{ \delta_{kN} \sum_r \sum_p \sum_q D_{qp} \tilde{B}_{rjp} (u_{rN} y_{qN} - v_{rN} x_{qN})_{i,m} \right\}$$

$$\tag{C.66}$$

$$\Phi^S(p_m, \mathbf{u}_m) = \overset{i \in N_S}{\sum} \sum_j \sum_k p_{jk,i,m} \left\{ \delta_{1j} \sum_r \sum_p \sum_q D_{qp} \tilde{B}_{rkp} (u_{1r} y_{1q} - v_{1r} x_{1q})_{i,m} \right\}$$

$$\Phi^P(p_m, \mathbf{u}_m) = \overset{i \in N_P}{\sum} \sum_j \sum_k p_{jk,i,m} \left\{ \delta_{Nj} \sum_r \sum_p \sum_q D_{qp} \tilde{B}_{rkp} (u_{Nr} y_{Nq} - v_{Nr} x_{Nq})_{i,m} \right\}$$

$$(C.66)$$

For later use, it is convenient to factor out the quantities in braces, and use the following shorthand notation :

$$\Phi^I(p_m, \mathbf{u}_m) = \overset{i \in N_I}{\sum} \sum_j \sum_k p_{jk,i,m} M^I_{jk,i,m}; \quad \Phi^O(p_m, \mathbf{u}_m) = \overset{i \in N_O}{\sum} \sum_j \sum_k p_{jk,i,m} M^O_{jk,i,m}$$

$$\Phi^S(p_m, \mathbf{u}_m) = \overset{i \in N_S}{\sum} \sum_j \sum_k p_{jk,i,m} M^S_{jk,i,m}; \quad \Phi^P(p_m, \mathbf{u}_m) = \overset{i \in N_P}{\sum} \sum_j \sum_k p_{jk,i,m} M^P_{jk,i,m}$$

$$(C.67)$$

It is to be noted that factored-out $M_{jk,i,m}$ are directly related to the mass fluxes $\mathcal{M}$ through the four physical boundaries of the computational domain :

$$\mathcal{M}^I = \int_{-1}^{+1} \overset{i \in N_I}{\sum} \sum_j \sum_k M^I_{jk,i,m} F_m(z) dz; \quad \mathcal{M}^O = \int_{-1}^{+1} \overset{i \in N_O}{\sum} \sum_j \sum_k M^O_{jk,i,m} F_m(z) dz$$

$$\mathcal{M}^S = \int_{-1}^{+1} \overset{i \in N_S}{\sum} \sum_j \sum_k M^S_{jk,i,m} F_m(z) dz; \quad \mathcal{M}^P = \int_{-1}^{+1} \overset{i \in N_P}{\sum} \sum_j \sum_k M^P_{jk,i,m} F_m(z) dz$$

$$(C.68)$$

In order to prevent deterioration of global mass flow conservation due to accumulation of truncation errors over time, the computational procedure imposes an additional constraint :

$$\mathcal{M}^I + \mathcal{M}^O + \mathcal{M}^S + \mathcal{M}^P = 0 \qquad (C.69)$$

Since the fluxes at the inlet, pressure and suction side boundaries are fixed in practice, this constraint is met by by adding a small, constant term to $M^O_{jk,i,m}$ before using (C.67).

C.11. Spatial Discretization: Type I Surface Integrals.

The following type of integrals, where "S" is the entire x-y spectral plane, appears on both sides of the discretized pressure and viscous steps.

$$\Psi^I(\mathbf{u}_m, p_m) = \iint_S \mathbf{u}_m(x,y) p_m(x,y) dx dy \qquad (C.70)$$

The evaluation of such integrals is based on an integration in the local coordinate system, followed by elementwise summation. This is implemented by means of a change of variable

$$dx dy = |J| d\zeta d\eta \qquad i = 1..N_E \qquad (C.71)$$

After expansion of the integrand in terms of local interpolants, (C.70) becomes :

$$
\begin{aligned}
\Psi^I(\mathbf{u}_m, p_m) = \sum^{i\in N_E} \int_{-1}^{+1} \int_{-1}^{+1} \sum_j \sum_k \mathbf{u}_{jk,i,m} h_j(\zeta) h_k(\eta) \sum_p \sum_q p_{pq,i,m} h_p(\zeta) h_q(\eta) \\
\times \sum_r \sum_s |J|_{rs,m} h_r(\zeta) h_s(\eta) d\zeta d\eta
\end{aligned}
\qquad (C.72)
$$

Rearrangement of the terms and introduction of the *local integral operator* (C.62) yields :

$$\Psi^I(\mathbf{u}_m, p_m) = \sum^{i\in N_E} \sum_j \sum_k \sum_p \sum_q \sum_r \sum_s \left\{ \mathbf{u}_{jk} |J|_{rs} \tilde{B}_{jpr} \tilde{B}_{kqs} p_{pq} \right\}_{i,m} \qquad (C.73)$$

Further manipulations of forms like (C.73) shall be motivated by the need to reduce them to the "proper" convolution structure of (C.65) that is required to obtain well-posed discretized pressure and viscous step equations. In previous work, this has been accomplished by introducing the *elementwise surface integral operator* $B^+_{jpkq,i}$:

$$B^+_{jpkq,i} = \sum_r \sum_s |J_{rs,i}| \tilde{B}_{jpr} \tilde{B}_{kqs} \qquad (C.74)$$

Storage of this operator requires $N_E N^4$ memory units, and allows to calculate Ψ_m using $3N_E N^4$ operations :

$$\Psi^I(\mathbf{u}_m, p_m) = \sum^{i\in N_E} \sum_j \sum_k \sum_p \sum_q \mathbf{u}_{jk,i,m} B^+_{jpkq,i} p_{pq,i,m} \qquad (C.75)$$

Although operators like (C.74) are not used in the NS3D computational procedure (cf. **Appendix D**), they shall be retained for a while for the sake of algebraic simplicity.

C.12. Spatial Discretization: Type II Surface Integrals.

The following type of integrals, where "S" is the entire x-y spectral plane, appears on the left-hand side of the discretized viscous step.

$$\Psi^{II}(\nu, \mathbf{u}_m, p_m) = \iint_S \nu(x,y)\mathbf{u}_m(x,y)p_m(x,y)dxdy \qquad (C.76)$$

The approximation of "Ψ_m^{II}" is similar to that of "Ψ_m^I" above. The difference lies in the expansion in interpolants, which combines $|J|$ and $/nu$ in order to conserve proper nesting of the convolution sums.

$$\Psi^{II}(\nu, \mathbf{u}_m, p_m) = \sum^{i\in N_E} \int_{-1}^{+1} \int_{-1}^{+1} \sum_j \sum_k \mathbf{u}_{jk,i,m} h_j(\zeta)h_k(\eta) \sum_p \sum_q p_{pq,i,m} h_p(\zeta)h_q(\eta)$$
$$\times \sum_r \sum_s \nu_{rs,i}|J|_{rs,i}h_r(\zeta)h_s(\eta)d\zeta d\eta \qquad (C.77)$$

The *elementwise surface integral operator* now depends on the scalar field distribution "ν". In principle, it must now be evaluated for each mode at each time step during the course of the simulation :

$$B_{jpkq,i}^+(\nu) = \sum_r \sum_s \nu_{rs,i}|J_{rs,i}|\tilde{B}_{jpr}\tilde{B}_{kqs} \qquad (C.78)$$

Given (C.78), discretized type II surface integrals can be considered as a generalization of type I surface integral :

$$\Psi^{II}(\nu, \mathbf{u}_m, p_m) = \sum^{i\in N_E} \sum_j \sum_k \sum_p \sum_q \mathbf{u}_{jk,i,m} B_{jpkq,m}^+(\nu)p_{pq,i,l} \qquad (C.79)$$

Although operators like (C.78) are not used in the NS3D computational procedure (cf. **Appendix D**), they shall be retained for a while for the sake of algebraic simplicity.

C.13. Spatial Discretization: Type III Surface Integrals.

The following type of integrals, where "S" is the entire x-y spectral plane, appears on the right-hand side of the discretized pressure step.

$$\Psi^{III}(u_m, v_m, p_m) = \iint_S \left(u_m \frac{\partial p_m}{\partial x} + v_m \frac{\partial p_m}{\partial y} \right) dxdy \qquad (C.80)$$

Using the local coordinate system transforms (C.48) and (C.71) allows to cast (C.80) in the following form :

$$\Psi^{III}(u_m, v_m, p_m) = \sum^{i \in N_E} \int_{-1}^{+1} \int_{-1}^{+1} \frac{|J|}{J} \left\{ u(y_\eta p_\zeta - y_\zeta p_\eta) + v(-x_\eta p_\zeta + x_\zeta p_\eta) \right\}_{i,m} d\zeta d\eta \quad (C.81)$$

The expansion in local interpolants of (C.81) can be simplified by introducing the *global partial differential operators* defined in (C.54). This yields :

$$\Psi^{III}(u_m, v_m, p_m) = \sum^{i \in N_E} \int_{-1}^{+1} \int_{-1}^{+1} \sum_a \sum_b \text{sign}(J_{ab,i}) h_a h_b$$

$$\left\{ \sum_p \sum_q u_{pq,i,m} h_p h_q \sum_j \sum_k \sum_r \sum_s \nabla^x_{i,jkrs} p_{rs,i,m} + \right. \qquad (C.82)$$

$$\left. \sum_p \sum_q v_{pq,i,m} h_p h_q \sum_j \sum_k \sum_r \sum_s \nabla^y_{i,jkrs} p_{rs,i,m} \right\} d\zeta d\eta$$

As before, this particular expansion has been selected because it satisfies the requirement for a proper convolution structure (C.65). In raw discretized form, (C.82) can be written as

$$\Psi^{III}(u_m, v_m, p_m) = \sum^{i \in N_E} \sum_j \sum_k \sum_p \sum_q \sum_r \sum_s \sum_a \sum_b \text{sign}(J_{ab,i}) \tilde{B}_{apj} \tilde{B}_{bqk}$$

$$\times \left\{ \nabla^x_{i,jkrs} u_{pq,i,m} + \nabla^y_{i,jkrs} v_{pq,i,m} \right\} p_{rs,i,m} \qquad (C.83)$$

A direct application of (C.83) requires of the order of N^8 operations to estimate Ψ^{III}_m. The raw form is also unsuitable for further algebraic use due to its complexity. However, it is straightforward to reduce (C.83) into a N^4 convolution structure similar to that used for Ψ^{II} and Ψ^I.

$$\Psi^{III}(u_m, v_m, p_m) = \sum^{i \in N_E} \sum_j \sum_k \sum_p \sum_q \left\{ p_{pq,i,m} A^{ox}_{pqjk,i} u_{jk,i,m} + p_{jk,i,m} A^{oy}_{pqjk,i} v_{pq,i,m} \right\} \qquad (C.84)$$

The *global integro-differential operators* A^{ox} and A^{oy} appearing in (C.84) are constructed themselves as convolutions of the *global pseudointegral operator* $B^o_{rpsq,i}$

$$A^{os}_{pqjk,i} = \sum_r \sum_s B^o_{rpsq,i} \nabla^s_{rsjk,i}$$

$$\qquad (C.85)$$

$$B^o_{rpsq,i} = \sum_a \sum_b \text{sign}(J_{ab,i}) \tilde{B}_{apj} \tilde{B}_{bqk}$$

Equation (C.85) is an example of intermediate convolution that leads to a reduction of the number of operations required to evaluate a discretized term. The principle of intermediate convolutions is used to an extreme in the NS3D computational procedure, which bypasses completely the use of operators such as (C.85) to achieve both speedup and reduction in storage.

C.14. Spatial Discretization: Type IV Surface Integrals.

The following type of integrals, where "S" is the entire x-y spectral plane, appears on the left-hand side of the discretized viscous and pressure steps.

$$\Psi^{IV}(\nu, u_m, u_m) = \iint_S \nu \left\{ \left(\frac{\partial u_m}{\partial x}\right)^2 + \left(\frac{\partial u_m}{\partial y}\right)^2 \right\} dx dy \qquad (C.86)$$

Using the local coordinate system transforms (C.48) and (C.71) allows to cast (C.86) in the following form :

$$\Psi^{IV}(\nu, u_m, u_m) = \sum^{i \in N_E} \int_{-1}^{+1} \int_{-1}^{+1} \frac{\nu}{|J|} \left\{ (y_\eta u_\zeta - y_\zeta u_\eta)^2 + (-x_\eta u_\zeta + x_\zeta u_\eta)^2 \right\}_{i,m} d\zeta d\eta \qquad (C.87)$$

Again, the expansion in local interpolants of (C.81) can be simplified by introducing the *global partial differential operators* (C.54). This yields :

$$\Psi^{IV}(\nu, u_m, u_m) = \sum^{i \in N_E} \int_{-1}^{+1} \int_{-1}^{+1} \sum_a \sum_b \frac{\nu_{ab,i}}{|J|_{ab,i}} h_a h_b d\zeta d\eta$$

$$\left\{ \sum_r \sum_s \sum_p \sum_q \nabla^x_{rspq,i} u_{pq,i,m} h_r h_s \times \sum_c \sum_d \sum_j \sum_k \nabla^x_{cdjk,i} u_{jk,i,m} h_j h_k + \right. \qquad (C.88)$$

$$\left. \sum_r \sum_s \sum_p \sum_q \nabla^y_{rspq,i} u_{pq,i,m} h_r h_s \times \sum_c \sum_d \sum_j \sum_k \nabla^y_{cdjk,i} u_{jk,i,m} h_j h_k \right\}$$

As before, this particular expansion has been selected because it satisfies the requirement for a proper convolution structure (C.65). In raw discretized form (C.88) can be written as :

$$\Psi^{IV}(\nu, u_m, u_m) = \sum^{i \in N_E} \sum_r \sum_s \sum_p \sum_q \sum_c \sum_d \sum_j \sum_k \sum_a \sum_b u_{pq,i,m} u_{jk,i,m}$$

$$\times \left\{ \nabla^x_{rspq,i} \nabla^x_{cdjk,i} + \nabla^y_{rspq,i} \nabla^y_{cdjk,i} \right\} \frac{\nu_{ab,i,l}}{|J|_{ab,i}} \tilde{B}_{rja} \tilde{B}_{skb} \qquad (C.89)$$

The raw form of Ψ^{IV} presents the same problem as (C.83) – too much complexity and too many algebraic operations required. Likewise, it is relatively straightforward to reduce (C.89) into a proper N^4 convolution structure similar to that used for the other integral forms :

$$\Psi^{IV}(\nu, u_m, u_m) = \sum_j^{i\in N_E} \sum_k \sum_p \sum_q u_{jk,i,m} A(\nu)_{pqjk,i} u_{pq,i,m} \qquad (C.90)$$

This is accomplished by means of introducing the *global quadratic integro-differential operator* $A(\nu)_{pqjk,i}$, constructed as follows :

$$A(\nu)_{pqjk,i} = \sum_r \sum_s \sum_c \sum_d \left\{ \nabla^x_{rspq,i} B^-(\nu)_{rscd,i} \nabla^x_{cdjk,i} + \nabla^y_{rspq,i} B^-(\nu)_{rscd,i} \nabla^y_{cdjk,i} \right\} \qquad (C.91)$$

$$B^-(\nu)_{rscd,i} = \sum_a \sum_b \frac{\nu_{ab,i}}{|J|_{ab,i}} \tilde{B}_{rja} \tilde{B}_{skb} \qquad (C.92)$$

Although operators like (C.91) are not used in the NS3D computational procedure (cf. **Appendix D**), they allow to reduce the algebraic complexity when writing the fully discretized pressure and viscous equations.

From a numerical standpoint, the approximation of type IV integrals is the stage that is most sensitive to (1) machine precision; and (2) to errors in the placement of the collocation points away from their exact Gaussian loci (cf. **Figure C.01**). This is due to matrices such as $\nabla^x \times \nabla^x$, which are intrinsically ill-conditioned. Simple caution is however sufficient to avoid numeric problems. For instance, using double precision instead of single precision arithmetic can reduce the discretization error by four orders of magnitude for a given Ψ^{IV}.

The full discretization of the convective step (C.26) is trivial, since it only involves explicit invocation of (C.53) to calculate the vorticity. This is not the case for constructing a fully discretized representation of the pressure (C.35) and viscous step (C.46). This is the subject of the remainder of **Appendix C**.

C.15. Spatial Discretization: Pressure Step.

The pressure step equation (C.35) can be written in terms of the above integral forms. After multiplying both sides by -1, this yields :

$$\forall m = 1..N_M$$

$$\Psi_4(1, \tilde{p}_m, \tilde{p}_m) - \lambda^2_{m,p} \Psi_1(\tilde{p}_m, \tilde{p}_m) = \Psi_3(\tilde{u}^*_m, \tilde{v}^*_m, \tilde{p}_m) - \Psi_1(\frac{\partial \tilde{w}^*}{\partial z}|_m, \tilde{p}_m) - \Phi(\tilde{p}_m, \tilde{u}^*_m) \qquad (C.93)$$

Substituting the discrete approximation derived in §C.10-§C.14 into (C.95) yields a set of fully discretized quadratic forms for the pressure modes :

$$\forall m = 1..N_M$$

$$\overset{i\in N_E}{\sum}\sum_j\sum_k\sum_p\sum_q \tilde{p}_{jk,i,m}A(1)_{pqjk,i}\tilde{p}_{pq,i,m} - \overset{i\in N_E}{\sum}\lambda^2_{m,p}\sum_j\sum_k\sum_p\sum_q \tilde{p}_{jk,i,l}B^+_{jpkq,i}\tilde{p}_{pq,i,l} =$$

$$\overset{i\in N_E}{\sum}\lambda^2_{m,p}\left\{\sum_j\sum_k\sum_p\sum_q \tilde{p}_{jk,i,m}A^{ox}_{pqjk,i}\tilde{u}^*_{pq,i,m} + \sum_j\sum_k\sum_p\sum_q \tilde{p}_{jk,i,m}A^{oy}_{pqjk,i}\tilde{v}^*_{pq,i,m}\right\} \qquad (C.94)$$

$$- \overset{i\in N_E}{\sum}\sum_j\sum_k\sum_p\sum_q \tilde{p}_{jk,i,m}B^+_{jpkq,i}\frac{\partial\tilde{w}^*}{\partial z}|_{pq,i,m} - \overset{A\in[I,O,S,P]}{\sum}\overset{i\in N_A}{\sum}\sum_j\sum_k \tilde{p}_{jk,i,m}M^A_{jk,i,m}$$

Equation (C.94) is not suitable for numerical implementation. However, it can be reduced to a linear form by factoring out the (j,k) convolution sums in the following manner :

$$\overset{i\in N_E}{\sum}\sum_j\sum_k\sum_p\sum_q \tilde{p}_{jk,i,m}*_{pqjk,i,m} = \overset{i\in N_E}{\sum}\sum_j\sum_k \tilde{p}_{jk,i,m}\left(\sum_p\sum_q ...\right)_{jk,i,m} \qquad (C.95)$$

In the general case, $p_{jk,i,m}$ is not identically zero. This implies that the quantities within parenthesis on the left and right-hand sides of (C.95) must be equal for all indexes $()_{jk,i,m}$. Therefore, the discretized spanwise modes of the pressure variable can be obtained by solving the following set of N_M independent linear systems :

$$\forall m = 1..N_M$$

$$\overset{i\in N_E}{\sum}\sum_p\sum_q [C_{jkpq,i,m}]\tilde{p}_{pq,i,m} = \tilde{\sigma}^P_{jk,i,m} \qquad (C.96)$$

Equation (C.96) above constitutes the *system equation* for the pressure step, as implemented in the NS3D computational procedure. The *elemental system matrices*, $C_{jkpq,i,m}$, are constructed as follows :

$$C_{jkpq,i,m} = A(1)_{pqjk,i} - \lambda^2_{m,p}B^+(1)_{jpkq,i} \qquad (C.97)$$

The right-hand side term of (C.96), $\sigma^P_{jk,i}$, also referred to as *pressure source term*, is constructed based on the convective step velocity update u* :

$$\tilde{\sigma}^P_{jk,i,m} = \overset{i\in N_E}{\sum} \sum_p \sum_q \left\{ A^{ox}_{pqjk,i} \tilde{u}^*_{pq,i,m} + A^{oy}_{pqjk,i} \tilde{v}^*_{pq,i,m} - B^+(1)_{jpkq,i} \frac{\partial \tilde{w}^*}{\partial z}_{pq,i,m} \right\}$$

$$+ \overset{A\in[I,O,S,P]}{\sum} \overset{i\in N_A}{\sum} M^A_{jk,i,m}$$

(C.98)

Solving (C.96) numerically yields the N_M discretized spanwise modes of the pressure variable. The modes are then mapped into real space using the modal-to-real transform $\mathfrak{S}^{-1}$ (C.11). The resulting discretized static pressure distribution $p^{n+1}_{jk,i,l}$ is used to obtain the pressure step velocity update $\mathbf{u}^{**}_{jk,i,l}$ by means of an an explicit implementation of (C.27) :

$$\mathbf{u}^{**}_{jk,i,l} = \mathbf{u}^*_{jk,i,l} - \Delta_t \left(\frac{\partial p}{\partial x}\right)_{jk,i,l} \mathbf{i} - \Delta_t \left(\frac{\partial p}{\partial y}\right)_{jk,i,l} \mathbf{j} - \Delta_t \left(\frac{\partial p}{\partial z}\right)_{jk,i,l} \mathbf{k} \qquad (C.99)$$

The partial derivatives appearing in (C.99) are calculated using (C.47) and (C.53). It is to be noted that the NS3D computational scheme does not use the $A(1)_{jkpq,i}$ and $B^+(1)_{jpkq,i}$ operators to construct the pressure equation elemental matrices $C_{jkpq,i}$ (cf. **Appendix D**). Nevertheless, they are convenient from a conceptual standpoint.

C.16. Spatial Discretization: Viscous Step.

The viscous step equation (C.46) can be also written in terms of the foregoing integral forms. This yields :

$$\forall m = 1..N_M$$

(C.100)

$$\Psi_4(\nu\Delta t, \delta\tilde{u}^{n+1}_m, \tilde{u}^{n+1}_m) + \Psi_2(1 - \bar{\nu}\Delta t\lambda^2_{m,v} + \frac{\Delta t}{2}\tilde{\nu}''_m, \delta\tilde{u}^{n+1}_m, \tilde{u}^{n+1}_m) = \Psi_1(\delta\tilde{u}^{n+1}_m, \tilde{u}^{**}_m)$$

Substituting the discrete approximation derived in §**C.10**-§**C.14** into (C.95) yields a set of fully discretized quadratic forms for the new velocity modes :

$$\forall m = 1..N_M$$

$$\overset{i\in N_E}{\sum} \sum_j \sum_k \sum_p \sum_q \delta\tilde{u}^{n+1}_{jk,i,m} \left\{ A_{jkpq,i}(\nu\Delta t) + B^+_{jkpq,i}(1 - \bar{\nu}\lambda^2_{m,v}\Delta t + \frac{\Delta t}{2}\tilde{\nu}''_m) \right\} \tilde{u}^{n+1}_{pq,i,m} \qquad (C.101)$$

$$= \overset{i\in N_E}{\sum} \sum_j \sum_k \sum_p \sum_q \delta\tilde{u}^{n+1}_{jk,i,m} B^+_{jkpq,i}(1)\tilde{u}^{**}_{pq,i,m}$$

Calculus of variations states that the variation δu^{n+1} is not identically zero. This allows to factor out the convolution term $\sum_j \sum_k \delta u^{n+1}_{jk,\ldots}$ and eliminate it in a manner similar to that employed for (C.95). Therefore, the discretized spanwise modes of the new velocity can be obtained by solving the following set of N_M independent linear systems :

$$\forall m = 1..N_M$$

$$\sum^{i \in N_E} \sum_p \sum_q C_{jkpq,i,m} \tilde{u}^{n+1}_{pq,i,m} = \tilde{\sigma}^V_{jk,i,m} \tag{C.102}$$

Equation (C.102) above constitutes the *system equation* for the viscous step, as implemented in the NS3D computational procedure. The *elemental system matrices*, $C_{jkpq,i,m}$, are constructed for each mode in the following manner :

$$C_{jkpq,i,m} = A_{jkpq,i}(\nu \Delta t) + B^+_{jkpq,i}(1 - \bar{\nu}\lambda^2_{m,v}\Delta t + \frac{\Delta t}{2}\bar{\nu}''_m) \tag{C.103}$$

The right-hand side term of (C.102), $\sigma^V_{jk,i}$, also referred to as *viscous source term*, is constructed based on the pressure step velocity update $\mathbf{u}^{**}$:

$$\tilde{\sigma}^V_{jk,i,m} = \sum^{i \in N_E} \sum_p \sum_q B^+_{jkpq,i}(1)\tilde{u}^{**}_{pq,i,m} \tag{C.104}$$

It is to be noted that the NS3D computational scheme does not use the $A(\nu)_{jkpq,i}$ and $B^+(*)_{jpkq,i}$ operators to construct the pressure equation elemental matrices $C_{jkpq,i}$ (cf. **Appendix D**). Nevertheless, they are convenient from a conceptual standpoint.

Solving (C.102) for each velocity component yields the N_M discretized spanwise modes of the new velocity. The modes are then mapped into real space using the modal-to-real transform $\mathfrak{S}^{-1}$. This completes one cycle of the time-marching scheme, and advances the velocity forward to time "$t + \Delta t$". A new cycle can be started by using this velocity as an input to the convective step (cf. §C.5).

C.17. Obtaining Two-Dimensional Flow Solutions.

Two-dimensional flow solutions can be obtained as a special case of the spanwise discretization algorithm, where

$$\begin{aligned} N_Z &= N_M = 1 \\ \lambda_{1,p} &= \lambda_{1,v} = 0 \end{aligned} \tag{C.105}$$

This eliminates the need for working in the modal domain. For reference, the resulting integral forms of the pressure and viscous steps are :

$$\iint_S \Delta t \left\{ \left(\frac{\partial p}{\partial x} \right)^2 + \left(\frac{\partial p}{\partial y} \right)^2 \right\} dx dy = -\iint_S \left\{ u \frac{\partial p}{\partial x} + v \frac{\partial p}{\partial y} \right\} dx dy - \oint_{I,O} p\mathbf{u}^* \cdot \mathbf{dn} \quad (C.106)$$

$$\delta \iint_S \left\{ \nu \Delta t (\nabla \mathbf{u}^{n+1})^2 + (\mathbf{u}^{n+1})^2 - 2\mathbf{u}^{n+1} \cdot \mathbf{u}^{**} \right\} dx dy = 0 \quad (C.107)$$

The corresponding discretized pressure step system equation is :

$$\sum_{}^{i \in N_E} \sum_p \sum_q A_{jkpq,i}(1) p_{pq,i} = \sigma_{jk,i}^P$$

$$(C.108)$$

$$\sigma_{jk,i}^P = -\frac{1}{\Delta t} \sum_{}^{i \in N_E} \sum_p \sum_q \left\{ A_{pqjk,i}^{ox} u_{pq,i}^* + A_{pqjk,i}^{oy} v_{pq,i}^* \right\} - \frac{1}{\Delta t} \sum_{}^{A \in [I,O,S,P]} \sum_{}^{i \in N_A} M_{jk,i}^A$$

The corresponding discretized viscous step system equation is :

$$\sum_{}^{i \in N_E} \sum_p \sum_q \left\{ A_{jkpq,i}(\nu \Delta t) + B_{jpkq,i}^+(1) \right\} u_{pq,i}^{n+1} = \sigma_{jk,i}^V$$

$$(C.109)$$

$$\sigma_{jk,i}^V = \sum_{}^{i \in N_E} \sum_p \sum_q B_{jkpq,i}^+(1) u_{pq,i}^{**}$$

It is to be noted that the NS3D computational scheme does not use the $A(\nu)_{jkpq,i}$, $B^+(*)_{jpkq,i}$ or $C_{jkpq,i}$ matrices. Although such matrices are useful from a conceptual standpoint, in practice their use is wasteful. **Appendix D** shall describe the efficient implementation behind the NS3D computational procedure.

Appendix D

The NS3D Computational Procedure : Numerical Implementation

This appendix describes the improvements made to the numerical implementation of the spectral element method. These improvements accelerate the solution procedure by an order of magnitude, and reduce memory requirements by two orders of magnitude with respect to previously used methods (Tan 1989, Renaud 1991). The resulting computational procedure, referred to as NS3D, allows unsteady turbulent 3D simulations to be carried out on an average engineering workstation (IBM RS/6000 models 550/370).

D.1. Overview of the NS3D Algorithm.

The major improvements in the NS3D computational procedure are (1) the use of an iterative "matrixless" static condensation technique to solve the system equations and (2) local assembly of the spectral operators and source terms via minimally-mapped convolutions. These improvements are tied to the following algorithm.

[0] **Precomputing stage:**

> *Construct the D_{ij} and $\tilde{B}_{ijk}$ operators.*
> *Construct the $\mathfrak{S}$ and $\mathfrak{S}^{-1}$ mapping matrices.*
> *Construct the transformation $[T]_{i,jk}$ and Jacobian $J_{i,jk}$ matrices.*
> *Construct the initial velocity flowfield $u^0_{jk,i,l}$.*

[1] **Turbulence model:**

> Construct $\nu_{jk,i,l}$ based on $\mathbf{u}_{jk,i,l}$.

[2] Convective Step:

> *For each element (along index $()_i$).*
> *For each node (along indexes $()_{jk}$).*
>> *Apply (C.26) along the spanwise D.O.F. (along index l).*
>> *Local storage required is thus only $(N_Z N^2)$.*
>> *Store results back into $\mathbf{u}_{jk,i,l}$ once done with element.*
> *At the end, $\mathbf{u}_{jk,i,l}$ contains $\mathbf{u}^*_{jk,i,l}$.*
> *Average $\mathbf{u}_{jk,i,l}$ across adjacent boundaries.*
> *Prescribe inlet boundary conditions.*
> *Prescribe blade surface boundary conditions.*

[3] Pressure Step:

> *Calculate source term $\sigma_{jk,i,l}$ in real space using $\mathbf{u}_{jk,i,l}$*
> *For each element (along index i).*
> *For each node (along indexes jk).*
>> *Apply (C.10) along the spanwise D.O.F. (along index l).*
>> *Store results back into $\sigma_{jk,i,m}$ once done with element.*
> *At the end, $\sigma_{jk,i,l}$ contains the modes $\sigma^p_{jk,i,m}$.*

> *For each odd mode (along index m).*
>> *For each element (along index i).*
>>> *Calculate the operator $B^+(1)_{jpkq}$ locally*
>>> *Calculate the operator $A(1)_{jkpq}$ locally*
>>> *Calculate the elemental system matrix C_{jkpq} for this mode.*
>>> *Perform x-y static condensation on C_{jkpq} locally.*
>>> *Store the results into $[\mathbf{C}_g]_i$, $[\mathbf{C}_{pp}]_i$ and $[\mathbf{C}_{ee}]_i$.*
>> *Perform x-y static condensation on the source term for mode m.*
>> *Solve the system equation at the global nodes (mode m).*
>> *Solve the system equation at the internal nodes (mode m).*
> *At the end, the modes $p_{jk,i,m}$ are obtained.*

> *For each element (along index i).*
> *For each node (along indexes jk).*
>> *Apply (C.11) along the spanwise D.O.F. (along index l).*
>> *Store results back into $p_{jk,i,m}$ once done with element.*
> *At the end, $p_{jk,i,m}$ contains the real pressures $p_{jk,i,l}$.*

> *For each element (along index i).*
> *For each node (along indexes jk).*
>> *Apply (C.99) along the spanwise D.O.F. (along index l).*
>> *Local storage required is thus only $(N_Z N^2)$.*
>> *Store results back into $\mathbf{u}_{jk,i,l}$ once done with element.*
> *At the end, $\mathbf{u}_{jk,i,l}$ contains $\mathbf{u}^{**}_{jk,i,l}$.*
> *Average $\mathbf{u}_{jk,i,l}$ across adjacent boundaries.*

[4] Viscous Step:

> *For each velocity component $C = u, v, w$*
> *Calculate source term $\sigma_{jk,i,l}$ in real space using $C_{jk,i,l}$*
> *For each element (along index i).*
> *For each node (along indexes jk).*
>
> > *Apply (C.10) along the spanwise D.O.F. (along index l).*
> > *Store results back into $\sigma_{jk,i,m}$ once done with element.*
>
> *Store $\sigma_{jk,i,m}$ into $C_{jk,i,l}$.*
> *At the end, $C_{jk,i,l}$ contains the modes $\sigma^C_{jk,i,m}$.*

> *Compute the field $F_{jk,i,m} = (1 - \bar{\nu}\lambda^2_{m,v}\Delta t + \frac{\Delta t}{2}\bar{\nu}''_m)_{jk,i}$*
> *For each mode (along index m).*
>
> > *For each element (along index i).*
> >
> > > *Calculate the operator $B^+(F)_{jpkq}$ locally*
> > > *Calculate the operator $A(\bar{\nu}\Delta t)_{jkpq}$ locally*
> > > *Calculate the elemental system matrix C_{jkpq} for this mode.*
> > > *Perform x-y static condensation on C_{jkpq}.*
> > > *Store the results into $[\mathbf{C}_g]_i$, $[\mathbf{C}_{pp}]_i$ and $[\mathbf{C}_{ee}]_i$.*
> > > *Get the diagonal of the global system matrix D_G.*
> >
> > *For odd modes only:*
> > *Restore $u_{jk,i,l}$ into $\sigma_{jk,i,m}$.*
> > *Perform x-y static condensation on the source term for mode m.*
> > *Solve the system equation at the global nodes (mode m).*
> > *Solve the system equation at the internal nodes (mode m).*
> > *Store the solution in $u_{jk,i,l}$.*
> >
> > *For odd modes only :*
> > *Restore $v_{jk,i,l}$ into $\sigma_{jk,i,m}$.*
> > *Perform x-y static condensation on the source term for mode m.*
> > *Solve the system equation at the global nodes (mode m).*
> > *Solve the system equation at the internal nodes (mode m).*
> > *Store the solution in $v_{jk,i,l}$.*
> >
> > *For even modes only :*
> > *Restore $w_{jk,i,l}$ into $\sigma_{jk,i,m}$.*
> > *Perform x-y static condensation on the source term for mode m.*
> > *Solve the system equation at the global nodes (mode m).*
> > *Solve the system equation at the internal nodes (mode m).*
> > *Store the solution in $w_{jk,i,l}$.*
>
> *At the end, $[u, v, w]_{jk,i,l}$ contains the modes $[u, v, w]^{n+1}_{jk,i,m}$.*

> *For each component $C = u_{jk,i,l} \ v_{jk,i,l} \ w_{jk,i,l}$.*
> *For each element (along index i).*
> *For each node (along indexes jk).*
>
> > *Apply (B.11) along the spanwise D.O.F. (along index l).*
> > *Local storage required is thus only $(N_Z N^2)$.*
> > *Store results back into $C_{jk,i,l}$ once done with element.*
>
> *At the end, $\mathbf{u}_{jk,i,l}$ contains the real $\mathbf{u}^{n+1}_{jk,i,m}$.*

[5] **Control:**

> *Optionally save results.*
> *Increment time counter by Δt and goto step* [1].

The NS3D computational procedure requires the permanent storage of six discretized flowfield variables $[u, v, w, p, \nu, \sigma]_{jk,i,l}$ ($4N_E N^2 N_Z$ reals) and a single set of x-y static condensation matrices ($N_E N^4 + N_E N_I N^2$ reals). The unsteady calculations in **Chapters 4-6** show that rotor vortex interaction effects are localized in the tip region of the stator. For this reason, the NS3D computational procedure assumes that the unsteady flowfield is symmetrical about the midspan plane. This assumption allows to bypass the calculation of the following half of the spanwise modes:

$$\begin{array}{llll} [u,v,p]_m \equiv 0 & \text{if} & m \bmod 2 = 0 \\ w_m \equiv 0 & \text{if} & m \bmod 2 = 1 \end{array} \qquad (D.01)$$

The "full-passage" unsteady time-averaged figures of merit are obtained from the "half-passage" computed figures of merit in the following manner :

$$\mathcal{Y}_{1,\text{full}} = 2\mathcal{Y}_{1,\text{half}}$$

$$\mathcal{Y}_{2,\text{full}} = \mathcal{Y}_{1,\text{half}} + \mathcal{Y}_{2,\text{half}} \qquad (D.02)$$

The following sections describe the constituent elements of the NS3D algorithm. The solution of the pressure (C.97) and viscous (C.102) system equations is described in §**D.2**-§**D.5**. The local assembly of the elemental system matrices is described in §**D.6**, while that of the source terms is covered in §**D.7**. Finally, §**D.8** provides closed-form expressions for the discretized local operators. In the discussion, the terms "elemental" and "local" refer to matrices local to each spectral element.

D.2. Solving the System Equations: Static Condensation.

Consider the example of a medium-sized discretization with 17 collocation planes and 350 7x7 elements per plane. In each system equation, there are 17,150 unknowns per mode. Each time step, 60 such system equations need to be solved (for 15 pressure modes and 3x15 velocity modes). If this problem were treated using simple matrix algebra, 30 distinct system matrices of size 17150×17150 would have to be stored. The problem of matrix storage is even more acute for 2D high Reynolds number direct Navier-Stokes simulations, where up to 150,000 unknowns per system equation may be required (2×10^{10} reals per matrix!). Clearly, a direct approach to solving the system equations (C.97)/(C.102) is not practical.

Static condensation is used as a first step towards reducing the system equations to a tractable size. With this technique, each system equation is solved only for the unknown values at the global nodes $()_G$ (cf. §C.4). The unknown values at the remaining internal nodes $()_e^i$ are inferred on an elemental basis from the values at the global nodes. To illustrate this process, let's consider a system equation for a single-element spectral grid:

$$[C_{jkpq}] \cdot \{u_{pq}\} = \{\sigma_{jk}\} \qquad (D.03)$$

The unknown vector "u_{pq}" and the left-hand side vector "σ_{jk}" shall be partitioned in such a manner that the values associated with the global nodes $()_g$ on this element come first. This partitions the elemental system matrix "C_{jkpq}" into four submatrices as shown below :

$$\begin{bmatrix} C_{jk_g pq_g} & C_{jk_g pq_e} \\ C_{jk_e pq_g} & C_{jk_e pq_e} \end{bmatrix} \cdot \left\{ \begin{array}{c} u_{pq_g} \\ u_{pq_e} \end{array} \right\} = \left\{ \begin{array}{c} \sigma_{jk_g} \\ \sigma_{jk_e} \end{array} \right\} \qquad (D.04)$$

In the above, the sub-indexes $()_{jk_g}$ and $()_{jk_e}$ differentiate between those nodes $()_{jk}$ that are global and internal respectively. For reasons of clarity, the following shorthand notation shall be used onwards in lieu of (D.04) :

$$\begin{bmatrix} \mathbf{C}_{gg} & \mathbf{C}_{ge} \\ \mathbf{C}_{eg} & \mathbf{C}_{ee} \end{bmatrix} \cdot \left\{ \begin{array}{c} u_g \\ u_e \end{array} \right\} = \left\{ \begin{array}{c} \sigma_g \\ \sigma_e \end{array} \right\} \qquad (D.05)$$

An LT decomposition of (D.05) dissociates the unknown values at the global nodes "u_g" from those at the internal nodes "u_e" :

$$\begin{aligned} [\mathbf{C}_{gg} - \mathbf{C}_{ge}\mathbf{C}_{ee}^{-1}\mathbf{C}_{eg}] \cdot \{u_g\} &= \{\sigma_g\} - [\mathbf{C}_{ge}\mathbf{C}_{ee}^{-1}]\{\sigma_e\} \\ \{u_e\} &= [\mathbf{C}_{ee}^{-1}]\{\sigma_e - [\mathbf{C}_{eg}]u_g\} \end{aligned} \qquad (D.07)$$

It is straightforward to prove that the elemental system matrices in (C.97) and (C.103) are symmetric. It follows that :

$$\begin{aligned} [\mathbf{C}_{ge}] &= [\mathbf{C}_{eg}]^T \\ [\mathbf{C}_{ge}\mathbf{C}_{ee}^{-1}] &= [\mathbf{C}_{ee}^{-1}\mathbf{C}_{eg}]^T \end{aligned} \qquad (D.08)$$

Defining the *elementally condensed global system matrix* $[\mathbf{C}_g]$ and the *elementally condensed partitioned matrices* $[\mathbf{C}_{pp}]$ and $[\mathbf{C}_{ee}]^{-1}$ as follows :

$$[\mathbf{C}_{pp}] \;=\; [\mathbf{C}_{ee}\,\mathbf{C}_g]$$

$$[\mathbf{C}_g] \;=\; [\mathbf{C}_{gg} - \mathbf{C}_{ge}\,\mathbf{C}_{pp}]$$

$$(D.09)$$

allows one to rewrite (D.08) using only three submatrices per element :

$$[\mathbf{C}_g] \cdot \{u_g\} \;=\; \{\sigma_g\} - [\mathbf{C}_{pp}]^T \{\sigma_e\}$$

$$\{u_e\} \;=\; [\mathbf{C}_{ee}^{-1}] \{\sigma_e\} - [\mathbf{C}_{pp}]^T \{u_g\}$$

$$(D.10)$$

The partitioning scheme (D.10) can be applied to the ensemble of spectral elements for each eigenmode. Since global nodes may be shared between several elements, the elemental system equation (C.96)/(C.102) coalesces into one linear equation for the unknowns at the global nodes $()_G$

$$\sum\nolimits^{i \in N_E} [\mathbf{C}_g]_i \cdot \{u_g\}_i = \sum\nolimits^{i \in N_E} \left\{ \sigma_g - [\mathbf{C}_{pp}]^T \sigma_e \right\}_i$$

$$\Downarrow \qquad\qquad\qquad (D.11)$$

$$[\mathbf{C}_G]\{u_G\} = \{\wp_G\}$$

The bottom part of (D.11) shall referred to as the *global system equation*, "$[\mathbf{C}_G]$" shall be referred to as the *condensed system matrix*, and "$\wp_G$" shall be referred to as the *condensed source term*. The process leading to (D.11) is known as *static condensation*. It offers the advantage of reducing solver matrix size, while automatically insuring C' continuity between adjacent elements.

To judge the benefits of static condensation, let's re-consider the illustrative example at the beginning of this section. For this case, there are approximately $2N_E(N-1)$ global nodes in the spectral x-y plane. The resulting global system equation has about 4,200 unknowns. Thus, the (symmetric) condensed matrix $[\mathbf{C}_G]$ has $4,200 \times 2,100 \;=\; 8.8810^6$ reals versus 2.9410^8 reals for the uncondensed form.

Although this represents a substantial improvement, the problem is still too large for straightforward implementation. Furthermore, it can be easily seen that for direct 2D simulations ($N_E \sim 10^3$), the statically condensed matrix $[\mathbf{C}_G]$ contains of the order of 10^8 reals. For this reason, an iterative method has been adopted for solving (D.11). The principal advantage of this method is tied to the property that the matrix-times-vector product :

$$\{\mathbf{y}_G\} = [\mathbf{C}_G]\{\mathbf{x}_G\} \qquad\qquad (D.12)$$

can be evaluated without actually knowing the elements of the condensed matrix $[\mathbf{C}_G]$. Since iterative methods use repeated evaluations of such products to solve linear systems, it is possible to solve the system equations without storing the $[\mathbf{C}_G]$ matrix. This ingenious trick is the primary reason for the efficiency of the NS3D computational procedure. The "matrixless" MVM and the particular iterative method used are described in the next section.

D.3. Solving the System Equations: Iterative Approach.

The following diagonally-preconditioned conjugate gradient algorithm is used to solve the global system equations (with the exception discussed in §D.5):

Input the condensed source term vector $\wp_G$
Input the approximate solution $\mathbf{u}^o$ (e.g. from $t - \Delta t$).
Set $\mathbf{r}_1 = \wp - [\mathbf{C}_G]\mathbf{u}^o$
Set $\mathbf{r}_2 = 0.0; quad\mathbf{z}_2 = 0.0; \quad \mathbf{p} = \mathbf{r}_1$
Repeat

> *Calculate $\mathbf{z}_1 = \mathbf{r}_1//\mathbf{D}$*
> *Calculate $T_1 = \mathbf{z}_1 \cdot \mathbf{r}_1$*
> *Calculate $T_2 = \mathbf{z}_2 \cdot \mathbf{r}_2$*
> *Calculate $\beta = T_1/T_2$*
> *Update $\mathbf{p} \leftarrow \mathbf{z}_1 + \beta\mathbf{p}$*
> *Calculate $T_3 = \mathbf{p}[\mathbf{C}_G]\mathbf{p}$*
> *Calculate $\alpha = T_1/T_3$*
> *Calculate $\mathbf{u}^n = \mathbf{u}^o + \alpha\mathbf{p}$*
> *Calculate $\epsilon = |\mathbf{u}^n - \mathbf{u}^o|/|\mathbf{u}^n|$*
> *Update $\mathbf{r}_2 \leftarrow \mathbf{r}_1$*
> *Update $\mathbf{r}_1 \leftarrow \mathbf{r}_1 - \alpha[\mathbf{C}_G]\mathbf{p}$*
> *Update $\mathbf{z}_2 \leftarrow \mathbf{z}_1$*

Until $\epsilon \leq 10^{-7}$.
At this stage $\mathbf{u}^n$ contains the solution to (D.11).

This algorithm converges in about 20 to 50 iterations per system with a typical 400-element, 17-plane grid required for compressor stator turbulent flow simulations. The rapid convergence is due to (1) periodic updates in directions perpendicular to the direction of steepest descent, and (2) preconditioning by the diagonal of the condensed system matrix $\mathbf{D} = D_G$, which reduces the spread in the system matrix eigenvalues.

The iterative algorithm uses repeated evaluations of matrix-times-vector products of the type $\mathbf{y} = [\mathbf{C}_G]\mathbf{x}$. As mentionned above, such products can be evaluated without knowing $[\mathbf{C}_G]$. This is made possible by the indexing scheme, which allows to assemble $\mathbf{y}$ directly

from the *elementally condensed global matrices* $[\mathbf{C}_g]_e$ (D.09). The assembly is performed as follows:

```
Set y_G = 0 ∀G
For all elements (along index i)
For all global nodes on this element only (along index g1)
For all global nodes on this element only (along index g2)
        rows = G(g1,i) (global node index of global node g1 on element i).
        cols = G(g2,i) (global node index of global node g2 on element i).
        y_rows = y_rows + [C_g]_g1,g2,i x_cols
```

The storage of the matrices $[\mathbf{C}_g]_i,[\mathbf{C}_{pp}]_i$ and $[\mathbf{C}_{ee}^{-1}]_i$ is trivial, especially considering that they can be rapidly constructed on an "as-needed" basis. Most important, the above "matrix-less" multiplication algorithm requires only $(4N-2)^2 N_E$ operations to execute what amounts to an $(2N-1)N_E$ matrix-time-vector multiply. Combined with the rapid convergence of the preconditioned C-G iterative scheme, this leads to fast and efficient solution of the pressure (C.96) and viscous (C.102) system equations for the ensemble of global nodes.

The following set of N_E independent linear equations are solved to obtain the solution at the remaining internal nodes. This is trivial in terms of computational resources.

$$\{u_e\}_i = \left[\mathbf{C}_{ee}^{-1}\right]_i \{\sigma_e\}_i - [\mathbf{C}_{pp}]_i^T \{u_g\}_i \qquad i \in [1..N_E] \qquad (D.13)$$

The preconditioner used in the iterative scheme is the diagonal of the condensed system matrix. It can be assembled using a variation of the "matrixless" multiplication algorithm:

```
Set D_G = 0 ∀G.
For all elements (along index i)
For all global nodes on this element only (along index g)
        D_G(g,i) = D_G(g,i) + [C_g]_g,g,i
```

D.4. Solving the System Equations: Boundary Conditions.

The vonNeuman boundary conditions for the pressure step are implicitly contained in the discretized source term (C.98), which "descends" from the integral formulation (C.31) of the problem. However, this is not the case for the viscous step. One simple and efficient way to implement the Dirichlet boundary conditions is during static condensation. This is accomplished by mapping the prescribed velocity values along the inlet boundary and blade surface unto the Dirichlet nodes index $()_s$ defined in §C.4. The elements of the corresponding row of $[\mathbf{C}_G]$ are padded with "0" and "1" accordingly :

$$\wp_s = \mathbf{u}_s; \qquad [\mathbf{C}_G]_{rs} = \delta_{rs} \qquad\qquad (D.14)$$

Since the condensed matrix is not constructed in practice, (D.14) is implemented via the following change into the "matrix-less" multiplication algorithm when solving for velocities :

> *Set $y_G = 0 \; \forall G$*
> *For all elements (along index i)*
> *For all global nodes on this element only (along index $g1$)*
> *For all global nodes on this element only (along index $g2$)*
>
> > *rows $= G(g1,i)$ (global node index of global node $g1$ on element i).*
> > *cols $= G(g2,i)$ (global node index of global node $g2$ on element i).*
> > *if rows $\in$ (), then $\mathbf{y}_{rows} = \mathbf{y}_{rows} + [\mathbf{C}_g]_{g1,g2,i}\mathbf{x}_{cols}$*
>
> *Set $\mathbf{y}_G = \mathbf{u}_G \forall G \in$ (),*

D.5. Solving the System Equations: First Pressure mode.

The convergence rate of iterative methods depends on (1) the size of the matrix (logarithmic dependence in in the case of the above algorithm), and (2) on the ratio R_c between the largest and smallest matrix eigenvalues. Due to the hard-coded Dirichlet boundary conditions, all the N_M viscous step global matrices are well conditioned. On the other hand, the condition number of the pressure matrix increases as the modal number decreases. It is straightforward to demonstrate that the first mode condensed pressure matrix, $[C_G^{p,m=1}]$, is in fact singular. The singularity has a physical basis, since in incompressible flow, the pressure is indeterminate by a constant.

As a result, $\tilde{p}_1$ cannot be obtained by the iterative method. A direct solver, exploiting the band-diagonal structure of the global system matrix, is used for this purpose. **Figure D.01** shows the location of the non-zero elements of $[C_G^{p,m=1}]$. The diagonal bandwidth N_B depends on the largest difference between global node indexes on each side of the periodic boundary. Thus, the bandwidth can be decreased by judicious indexing and ordering of the spectral grid. While the gridding scheme in **Figure C.05** may not be the most efficient in this respect, it is simple to implement and provides an adequate bandwidth of :

$$\frac{N_B}{2} = (N-1)N_I + 1 \qquad\qquad (D.15)$$

Since $[C_G^{p,m=1}]$ is symmetric positive definite, it may be stored in a packed, half-diagonal form $[C_G]^{pd}$, using the algorithm below. The packed form can be prefactored using LIN-PACK's SPBCO, and the the global system equation solved using LINPACK's SPBSL (Dongarra et al. 1979). This requires $2(N-1)^2 N_E N_I$ storage elements. In comparison, the

iterative scheme requires essentially no storage but for the elementally partitioned matrices (D.09). Currently, storing the packed pressure matrix is the limiting factor for 2D direct simulations. In the future, this limitation might be removed by exploiting the sparseness within the diagonal band of the system matrix, or by applying a pressure Dirichlet boundary condition at one node.

$Set\ [C_G]^{pd} = [0]$
For all elements (along index i)
For all global nodes on this element only (along index g1)
For all global nodes on this element only (along index g2)

> $ir = G(g1,i)$ *(global node index of global node g1 on element i).*
> $ic = G(g2,i)$ *(global node index of global node g2 on element i).*
> *If (ir $\leq$ ic) (element above diagonal)*
> $[C_G]^{pd}_{ic-ir+1,ic} = [C_G]^{pd}_{ic-ir+1,ic} + [C_g]_{g1,g2,i}$
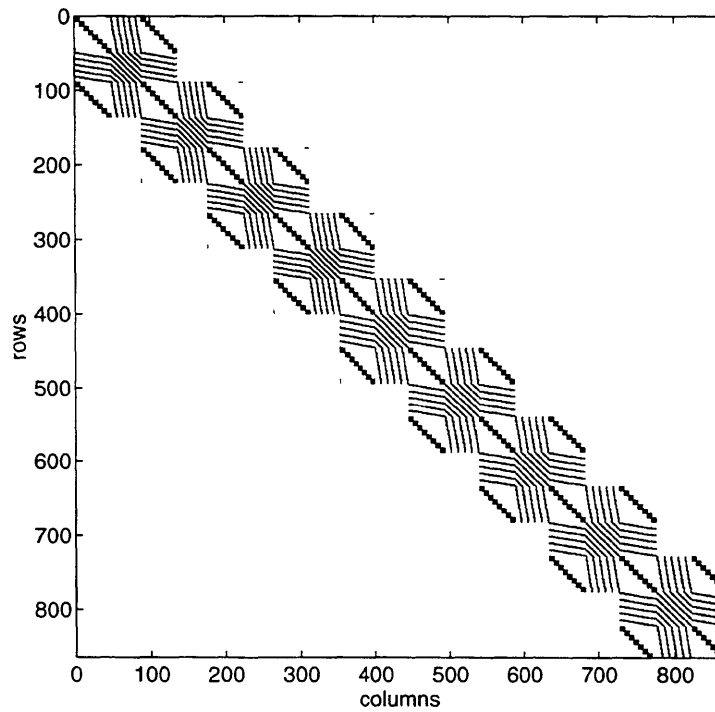
Figure D.01. Distribution of the non-zero elements in the condensed system matrix.

D.6. Efficient Local Assembly of the System Matrices.

The NS3D computational procedure dispenses from storing the elemental system matrices $C_{jkpq,i,m}$ by calculating their constituent operators $A_{jkpq}(\nu)$ and $B^{+}_{jpkq}(\nu)$ for each element on an as-needed basis. The resultant storage savings are particularly important for direct 2D simulations, where the number of elements can be of the order of few thousands.

Unfortunately, equations (C.78) and (C.91) do not provide an efficient basis for such assembly. While simple from a conceptual standpoint, their direct implementation requires N^6 (for C.78) and N^8 (for C.91) floating point operations per element. By going back to the raw convolution forms (C.73) and (C.89), a substantially faster assembly algorithm can be derived. The algorithm is based on intermediate convolutions. It constructs the viscous step elemental system matrix $C^v_{jkpq,i,m}$ in the following manner :

for $m = 1, N_M$

for $i = 1, N_E$

$$
\begin{aligned}
W^+(F)_{pkm} &= \sum_q F_{pq,i}|J|_{pq,i}\tilde{B}_{kmq} \\
W^-(\bar{\nu}\Delta t)_{pkm} &= \sum_q \bar{\nu}_{pq,i}\Delta t|J|^{-1}_{pq,i}\tilde{B}_{kmq} \\
L^+(F)_{jlkm} &= \sum_p W^+(F)_{pkm}\tilde{B}_{jlp} \\
L^-(\bar{\nu}\Delta t)_{jlkm} &= \sum_p W^-(\bar{\nu}\Delta t)_{pkm}\tilde{B}_{jlp} \\
A(\bar{\nu}\Delta t)_{lmrs} &= \sum_j\sum_p D_{lj}D_{rp}L^-(\bar{\nu}\Delta t)_{jpms}\{(y_\eta)_{jm}(y_\eta)_{ps} + (x_\eta)_{jm}(x_\eta)_{ps}\} \\
&\quad + \sum_k\sum_q D_{mk}D_{sq}L^-(\bar{\nu}\Delta t)_{lrkq}\{(y_\zeta)_{lk}(y_\zeta)_{rq} + (x_\zeta)_{lk}(x_\zeta)_{rq}\} \\
&\quad - \sum_j\sum_q D_{lj}D_{sq}L^-(\bar{\nu}\Delta t)_{jrmq}\{(y_\eta)_{jm}(y_\zeta)_{rq} + (x_\eta)_{jm}(x_\zeta)_{rq}\} \\
&\quad - \sum_k\sum_p D_{mk}D_{rp}L^-(\bar{\nu}\Delta t)_{lpks}\{(y_\zeta)_{lk}(y_\eta)_{ps} + (x_\zeta)_{lk}(x_\eta)_{ps}\} \\
C_{jkpq|i,m} &= A(\bar{\nu}\Delta t)_{jkpq} + \Delta t L^+(F)_{jpkq}
\end{aligned}
$$
(D.16)

The same algorithm is used for assembling the pressure step elemental system matrix. Equation (D.16) above is optimal, in the sense that further speed gains cannot be achieved by a different reshuffling of the summation order. The optimal convolution order has been determined via Karnaugh mapping, which is a technique used in the functional optimization of microprocessors. Further acceleration of (D.16) is however still possible. For instance, exploiting the symmetry of elemental matrices, $[*]_{abcd,i,m} = [*]_{cdab,i,m}$, results in a speedup by a factor of two. Likewise, the permutability of the local integral operator:

$$
\tilde{B}_{ijk} = \tilde{B}_{jik} = \tilde{B}_{kji} = \tilde{B}_{ikj} \tag{D.17}
$$

can be leveraged to accelerate (D.16) by 15 percent.

D.7. Efficient Local Assembly of the Source Terms.

The right-hand sides of the pressure (C.98) and the viscous (C.104) step equations contain terms of the form :

$$f^{\oplus}_{jk,i,m} = \sum^{i \in N_E} \sum_p \sum_q +B^{+}_{jpkq,i}(1)u_{pq,i,m}$$

$$(D.18)$$

$$= \sum^{i \in N_E} \sum_a \sum_b \sum_p \sum_q |J|_{ab,i}\tilde{B}_{jpa}\tilde{B}_{kqb}u_{pq,i,m}$$

and of the form :

$$f^{\triangleright|\triangleleft}_{jk,i,m} = \sum^{i \in N_E} \sum_p \sum_q A^{ox|oy}_{pqjk,i}u|v_{pq,i,l}$$

$$(D.19)$$

$$= \sum^{i \in N_E} \sum_p \sum_q \sum_r \sum_s \sum_a \sum_b \nabla^{x|y}_{rsjk,i}\text{sign}(J_{ab,i})\tilde{B}_{apj}\tilde{B}_{bqk}u|v_{pq,i,l}$$

Such terms can be rapidly calculated using intermediate convolutions. An efficient substitute to (D.18) is :

$$\text{for} \quad m = 1, N_M$$
$$\text{for} \quad i = 1, N_E$$

$$W^1_{aqk} \quad = \sum_b |J|_{ab,i}\tilde{B}_{bqk} \qquad\qquad (D.20)$$

$$W^2_{aqj} \quad = \sum_b u_{pq,i,m}\tilde{B}_{apj}$$

$$f^{\oplus}_{jk|i,m} \quad = \sum_a \sum_q W^1_{aqk}W^2_{aqj}$$

An efficient substitute to (D.19) is :

$$\text{for} \quad m = 1, N_M$$
$$\text{for} \quad i = 1, N_E$$

$$
\begin{aligned}
W^0_{aqk} &= \sum_b \text{sign}(J)_{ab,i} \tilde{B}_{bqk} \\
W^1_{aqj} &= \sum_b u_{pq,i,m} \tilde{B}_{apj} \\
W^2_{aqj} &= \sum_b v_{pq,i,m} \tilde{B}_{apj} \\
Q^1_{jk} &= \sum_a \sum_q W^0_{aqk} W^1_{aqj} \\
Q^2_{jk} &= \sum_a \sum_q W^0_{aqk} W^2_{aqj} \\
f^{\triangleright}_{jk|i,m} &= \sum_p \sum_q Q^1_{pk} D_{jp} (y_\eta)_{pk} + \sum_p \sum_q Q^1_{jq} D_{kq} (-y_\zeta)_{jq} \\
f^{\triangleleft}_{jk|i,m} &= \sum_p \sum_q Q^1_{pk} D_{jp} (-x_\eta)_{pk} + \sum_p \sum_q Q^1_{jq} D_{kq} (x_\zeta)_{jq}
\end{aligned}
\qquad (D.21)
$$

The number of floating point operations is reduced thereby by two orders of magnitude, while the need for storing the precomputed $A^{ox/y}$ and B^+ matrices is eliminated.

D.8. Exact Forms of the Local Operators.

The local system differential operator D_{ij} can be constructed analytically. This is accomplished in a more straightforward manner when the indexes are ran from $0..N-1$ rather than $1..N$. With this convention in place, we have :

$$
D_{ij} = \frac{dh_i}{ds} \Big|_{s=\cos\theta_j} =
\begin{cases}
\displaystyle\sum_{m=0}^{m=N-1} mH_{im} \frac{\sin m\theta_j}{\sin \theta_j}; & j \neq 0, N-1 \\
\displaystyle\sum_{m=0}^{m=N} m^2 H_{im}; & j = 0 \\
\displaystyle\sum_{m=0}^{m=N} (-1)^{m+1} mH^2_{im}; & j = N-1
\end{cases}
\qquad (D.22)
$$

Likewise, the local system integral operator $\tilde{B}_{ijk}$ is best constructed in the following manner

$$\bar{B}_{ijk} = \sum_a \sum_b \sum_c H_{ia} H_{jb} H_{kc} \int_0^\pi \cos a\theta \cos b\theta \cos c\theta \sin \theta d\theta$$

$$= \frac{1}{8} \sum_a \sum_b \sum_c H_{ia} H_{jb} H_{kc} \times \left\{ \begin{array}{ll} +\mathcal{F}(a+b+c+1) & -\mathcal{F}(a+b+c-1) \\ +\mathcal{F}(a+b-c+1) & -\mathcal{F}(a+b-c-1) \\ +\mathcal{F}(a-b+c+1) & -\mathcal{F}(a-b+c-1) \\ +\mathcal{F}(a-b-c+1) & -\mathcal{F}(a-b-c-1) \end{array} \right\} \qquad (D.23)$$

where :

$$H_{ij} = \frac{2}{N-1} \frac{1}{C_i C_j} \cos \frac{ij\pi}{N-1} \qquad (D.24)$$

$$\mathcal{F}(n) = \frac{1-(-1)^n}{n}; \qquad \mathcal{F}(0) = 1 \qquad (D.25)$$

Appendix E

The NS3D Computational Procedure :

Turbulence Modeling

This appendix presents a method for estimating the values of the turbulent viscosity field "ν" for a three-dimensional, unsteady, vortex driven flow in a turbomachinery passage. The method is an extension of the original algebraic Baldwin-Lomax turbulence model (1978), modified to account for the fact that distinct turbulent mixing flow processes may be at work in different regions of this complex flowfield.

E.1. Flowfield Regions.

The original Baldwin-Lomax model (1978) cannot be directly used to study the unsteady flow produced by incoming wakes and vortices for the following reasons:

- The presence of free vortical disturbances outside the boundary layer biases the calculation of the thickness parameter n_{max}. This is illustrated in **Figure E.2**, and leads to values of the eddy viscosity that are disconnected from flow physics.

- The original model requires to continuously monitor the location of the wakes/vortex centerline from which the local n coordinates are measured. Given the complex configuration of the flowfield here, such monitoring is not practical.

For this reason, the Baldwin-Lomax model has been modified here to resolve these difficulties, while retaining the physical principles underlying the calculation of eddy viscosity. The modified model distinguishes three flowfield regions shown in **Figure E.1**.

In each region of **Figure E.1**, the calculation of eddy viscosity proceeds differently as described below. It is to be noted that this description is made using the dimensionless convention established in §**A.4**. In contrast, most turbulence models in the literature are formulated in dimensional terms.
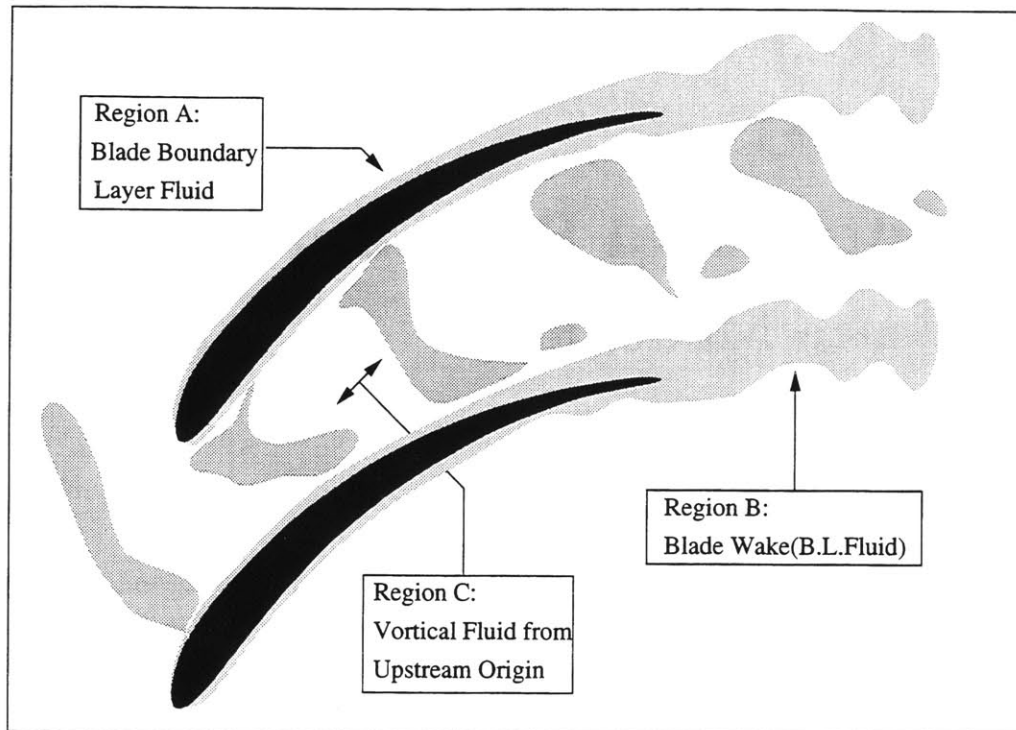
Figure E.1. The turbulence model distinguishes three flowfield regions: boundary layer, wake and free-stream vortical region. The boundary layer region is further divided in two subdomains – inner and outer.

E.2. Eddy Viscosity in the Disturbed Boundary Layer Region.

The calculation of eddy viscosity in the disturbed boundary layer region (Region A in **Figure E.1**) is based upon a coordinate system measuring the distance from the nearest solid wall "n". The use of the quantities at the nearest solid wall for three-dimensional geometries has been suggested by Vaughan and Turner (1987).

The Baldwin-Lomax model divides the boundary layer region into inner and outer subdomains, shown in **Figure E.2**. Different formulas are used to estimate the eddy viscosity in each of the subdomains. To insure a continuous distribution, the eddy viscosity in the inner and outer subdomains is patched according to :
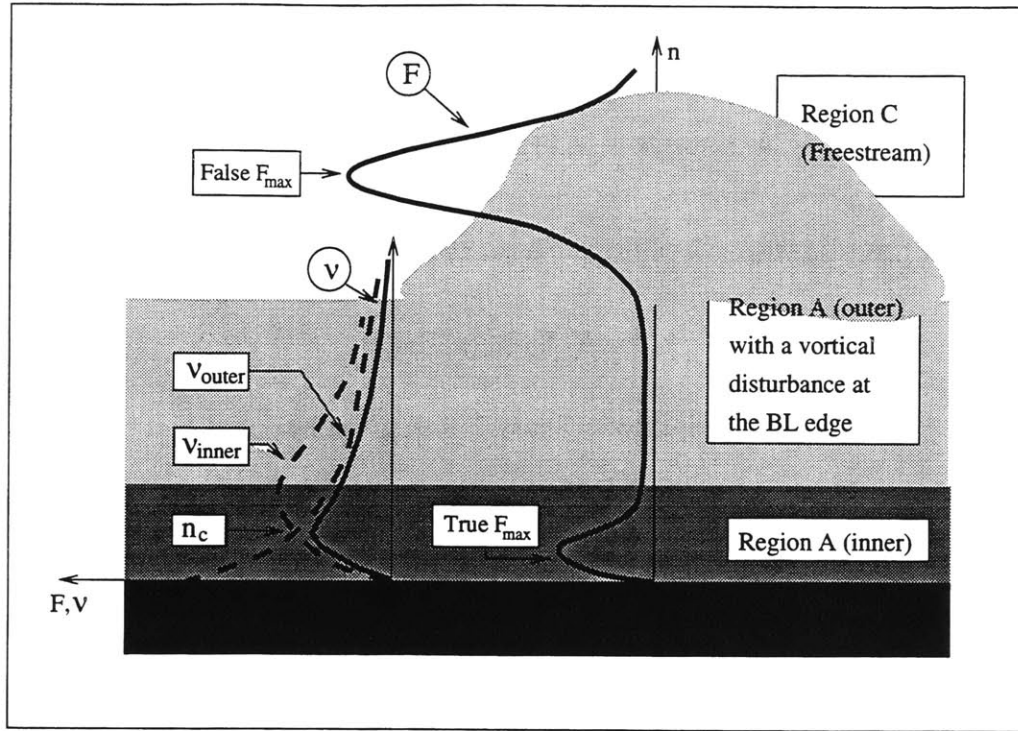
Figure E.2. Nearest-wall based coordinate system used by the modified Baldwin-Lomax model, and typical profiles of F, $\nu_{i,t}$ and $\nu_{o,t}$. The two subdomains of the boundary layer (inner and outer) are shown in gray.

$$\nu_t = \begin{cases} \nu_{t,i} & n \le n_c \\ \nu_{t,o} & n > n_c \end{cases} \qquad (E.01)$$

where the cross-over distance n_c is the smallest distance from the surface at which the values from the inner and from the outer formulas are equal. This is illustrated by the left set of curves in **Figure E.2**. The eddy viscosity in the **inner subdomain** is computed using the Prandtl-Van Driest mixing-length formulation:

$$\nu_{t,i} = l^2 |\omega| \qquad (E.02)$$

The mixing length is calculated according to :

$$l = kn \left[1 - e^{-n^+/A^+} \right] \qquad (E.03)$$

The dimensionless law-of-the-wall coordinate n^+ is given by

$$n^+ = n \sqrt{Re \frac{\partial u}{\partial n}}_{n=0} \qquad (E.04)$$

The function $A^+(s)$ represents the effect of pressure gradients on the boundary layer :

$$A^+(s) = 26\left[1 + 11.8\frac{dp}{ds}\sqrt{Re(\frac{\partial u}{\partial n})^3}\right]_{n=0}^{-1/2} \qquad (E.05)$$

In the **outer subdomain**, the following formula is used for computing the eddy viscosity

$$\nu_{t,o} = K_1 K_2 F_W(s) F_K(n) \qquad (E.06)$$

where the $F_K(n)$ is the Klebanoff intermittency factor, given by

$$F_K(n) = \left[1 + 5.5C_K^6\left(\frac{n}{n_{max}}\right)^6\right]^{-1} \qquad (E.07)$$

and where the wake factor is defined as :

$$F_W(s) = \min\left\{\begin{array}{c} n_{max}F_{max} \\ C_W n_{max} U_D^2/F_{max} \end{array}\right\} \qquad (E.08)$$

The quantity n_{max} is the locus of the <u>closest to the wall</u> maximum F_{max} of the function:

$$F(n) = n|\omega|\left[1 - e^{-n^+/A^+}\right] \qquad (E.09)$$

In the absence of external vortical disturbances, this definition is fully equivalent to that from the classical model. In the presence of these, the use of the first maximum gives a value of n_{max} which is more representative of the physical meaning of this quantity - boundary layer thickness. Had the original formulation been used in presence of wakes, one would obtain a value of n_{max} outside of the boundary layer (cf. **Figure E.2**).

The quantity U_D represents the difference between the maximum and minimum total velocity in the boundary layer profile at that axial location :

$$U_D^2 = \left(|u|_{max} - |u|_{min}\right)^2 \qquad (E.10)$$

For unseparated boundary layers, the $|u|_{min}$ term is taken to be zero. For separated boundary layers, one must take into consideration the change of flow direction in the above definition of $|u|_{min}$. It is to be noted that the product $n_{max}F_{max}$ is equivalent to $\delta^* U_e$ in the Clauser equilibrium formulation (White, 1974). Therefore, $n_{max}(s)$ is physically representative of the local thickness of the region of vortical flow.

E.3. Eddy Viscosity in the Disturbed Wake Region.

The calculation of the eddy viscosity in the disturbed wake region (Region B in **Figure E.1**) proceeds in a manner identical to that in the outer subdomain of the boundary layer (E.06-E.10), except for the manner in which the shape function F is defined :

$$F(n) = n|\omega| \qquad (E.11)$$

In the wake region, the origin for the coordinate n is the center of the wake, and thus lies on the curved sheet formed by the points of largest velocity defect behind the stator blade. Technically, the quantities F_{max} and n_{max} required for the outer eddy viscosity should be calculated based upon this origin. Therein lies a major practical difficulty, since tracking the position of this sheet in unsteady flow is a quite complex task. However, if one assumes a linear disturbance velocity profile (reasonable assumption given the velocity profiles in wakes and tip vortices) n_{max} and F_{max} can be found in a straightforward manner :

$$n_{max} = \frac{t_w}{2}$$
$$F_{max} = |u|_{max} - |u|_{min} \qquad (E.12)$$

where t is the thickness of the wake. Upon substitution of (E.12) into (E.08), the wake factor can be determined in an equally simple manner :

$$F_W(s) = C_W \frac{t_w}{2} U_D = \frac{C_W t_w^2}{4} \omega \qquad (E.13)$$

Examination of the Klebanoff intermittency factor, shown in **Figure E.3** reveals that F_K is essentially unity inside the wake, and decays rapidly to zero outside it. It follows that the eddy viscosity in the wake region is approximately proportional to the local vorticity :

$$\nu_t = K_1 K_2 C_W \frac{t_w^2}{4} \omega \qquad (E.14)$$

Equation (E.14) is efficient, since local vorticity values are readily available in the (x-y-z) stator coordinate system. Before its incorporation in the computational scheme, one needs however to examine the realism of the underlying linear velocity profile assumption. From a physical standpoint, this assumption is equivalent to neglecting the effect of small-scale features in the wake profile upon turbulent diffusion. Valkov (1992) developed a form of (E.14) which assumes a Gaussian velocity profile distribution in the wake. Despite its complexity, this form yields essentially the same values for ν_t as (E.14), provided that the vorticity remains below 30-40 U/c. Above this threshold, (E.14) overpredicts the eddy viscosity. The rotor wakes and vortices used in the present investigation satisfy this limit.
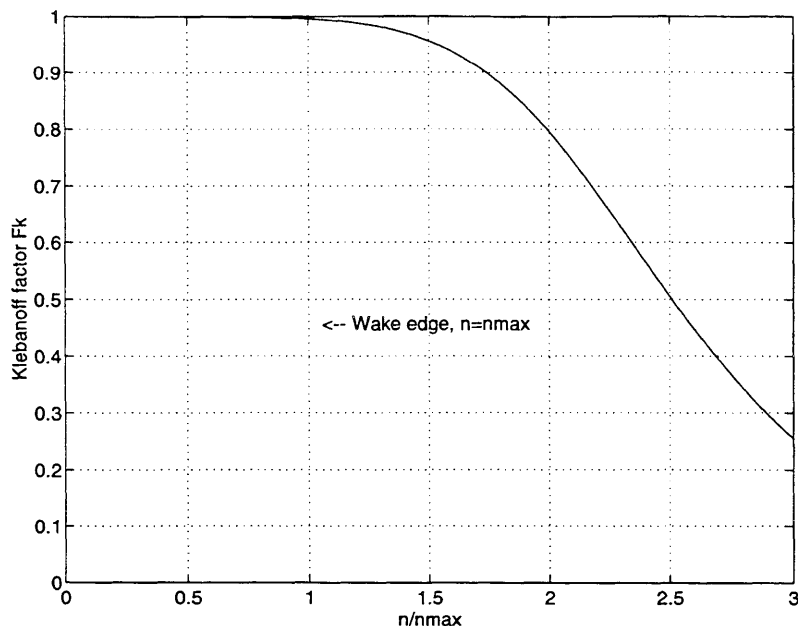
Figure E.3. Variation of the Klebanoff intermittency factor F_K as a function of the normalized distance n/n_{max} from the wake centerline. The edge of the wake is at $n/n_{max} = 1$.

From a different standpoint, Equation (E.14) states that the "mixing length" in the wake region is constant, which is substantiated by experimental evidence (White 1974). In fact, upon closer examination, (E.14) can be found to be equivalent to Clauser's eddy viscosity scaling law for wake-like structures (White 1974, pp.477). Thus, considering the empirical uncertainty underlying the use of turbulence modeling, Equation (E.14) is appropriate for obtaining the eddy viscosity in the wake region.

E.4. Eddy Viscosity in the Freestream Vortical Flow Region.

By analogy, equation (E.14) can be used to calculate the eddy viscosity associated with upstream rotor wakes, provided the appropriate characteristic thickness is used. The upstream rotor tip leakage vortices appear to have a velocity profile similar to thick wake localized near the upper endwall (Khalid 1995). For this reason, the eddy viscosity in the regions external to the blade boundary layer (regions B and C in **Figure E.1**) shall be calculated according to the following approximation of (E.14):

$$\nu_t = 0.0017(t^*)^2 \omega \qquad (E.15)$$

Equation (E.15) is a simplified version of the outer formulation of the Baldwin-Lomax model, valid for regions of free shear flow. It offers the significant advantage of using the readily available local vorticity, instead of tracking the centerlines of the vortical disturbances in the complex flow geometry of our problem.

The characteristic thickness parameter t^* used in (E.15) depends upon the inlet boundary conditions used for a particular simulation. Based on the material in §G.2, $t^* \sim 0.1c$ for upstream rotor wakes. For upstream rotor tip leakage vortices, the spanwise thickness of the total pressure defect region is used, thus $t^* \sim 0.1 - 0.2c$. The constants appearing in (E.01)-(E.15) are those obtained by Cebeci, and used by Baldwin and Lomax (1978) :

Constant	C_W	C_K	k	K_1	K_2
Value	0.25	0.3	0.4	0.0168	1.6

Table E.1. Constants appearing in the Baldwin-Lomax model.

These constants have been empirically determined for the case of compressible flow. No specific values for the case of incompressible flow have been found in the literature. VKI lecture materials (1991) suggest that the values for compressible flow can be used in the incompressible case.

E.5. Patching of Eddy Viscosity between Flow Regions.

The NS3D computational procedure requires a C^0 continuity of the eddy viscosity field between and within the three flow regions shown in **Figure E.1**. Continuity within the disturbed boundary layer region (Region A in **Figure E.1**) is guaranteed by (E.01). Continuity within and between the free shear flow regions (Regions B and C in **Figure E.1**) is ensured by (E.15). Continuity between the free shear flow regions and the disturbed boundary layer region is achieved by patching (E.01) and (E.15) at the closest location n_p to a solid surface where they are of equal value. The free-shear layer flow eddy viscosity approximation (E.15) is used beyond this location.

The foregoing patching process is more flexible than trying to find the edge of the boundary layer. It allows to account for deformation of the boundary layer region envelope under the effect of the upstream rotor disturbances. It also maps the proper values of disturbance vorticity into eddy viscosity, regardless of whether the vortical fluid originated at the stator or at the rotor blade surface.

Appendix F

Disturbance Flow : Concept and Application

This appendix presents the useful concept of disturbance flow and the details of its implementation in the NS3D computational procedure. The use of the disturbance flow technique offers several advantages from both computational and conceptual standpoint, such as:

- Disturbance flow features are easy to visualize and identify.

- Changes in performance can be directly related to disturbance features (**Appendix I**).

- The effects of viscosity, non-linearity, three-dimensionality and other complex factors can be easily separated.

- The solution of the disturbance formulation of the Navier-Stokes equations requires less computational resources.

Given these advantages, the present investigation uses a disturbance formulation of the equations of motion (F.06) that is equivalent to the full Navier-Stokes equations (C.01).

F.1. Disturbance Flow Concept.

The *disturbance flow* is defined as the difference between an unsteady flow and a reference (or *base*) flow taken at all points of the computational domain. Herein, the unsteady flow is due to the interaction with upstream rotor tip leakage vortices or midspan wakes. The base flow is the "steady" flow that would exist in the stator passage had those vortices (or wakes) been mixed out at the mid-gap axial plane.

$$\Delta \mathbf{u}(x, y, z, t) = \mathbf{u}_u(x, y, z, t) - \mathbf{u}_s(x, y, z)$$

$$\Delta p(x, y, z, t) = p_u(x, y, z, t) - p_s(x, y, z) \qquad (F.01)$$

$$\Delta \boldsymbol{\omega}(x, y, z, t) = \boldsymbol{\omega}_u(x, y, z, t) - \boldsymbol{\omega}_s(x, y, z)$$

The disturbance flow contains explicitly those features of the unsteadiness associated with upstream vortices (or wakes) and their interaction with the stator blade. The "steady" base flow can be unsteady itself, for instance owing to vortex shedding from the stator trailing edge. However, unless there is massive boundary layer separation, the unsteadiness in the reference flow is small and its effect negligible. In the present investigation, the base flow is independent of time.

The concept of disturbance can be extended to any other flow quantity of interest. For this purpose, it is convenient to introduce the *disturbance operator* Δ, which can be applied to yield the difference for any flow quantity Q between unsteady and "steady" base flows

$$\Delta Q = Q_u - Q_s \qquad (F.02)$$

For instance, the time-averaged loss in unsteady flow can be expressed as a change in loss with respect to the base flow :

$$\mathcal{Y}_u = \mathcal{Y}_s + \Delta \mathcal{Y} \qquad (F.03)$$

where $\Delta \mathcal{Y}$ is the loss explicitly due to the effect of the upstream rotor disturbances. As shown in **Appendix I**, this term can be directly related to the disturbance vorticity $\Delta \boldsymbol{\omega}$. The disturbance operator introduced above is linear with respect to addition, multiplication by a constant, and other linear operators :

$$\Delta(aP + bQ) = a\Delta P + b\Delta Q \qquad (a, b) \in R^2$$

$$\overline{\Delta P} = \Delta \overline{P}$$

$$\nabla \Delta P = \Delta \nabla P; \qquad \int \Delta P = \Delta \int P \qquad (F.04)$$

However: $\Delta(PQ) \neq \Delta P \Delta Q$!

It is to be noted that in general, the time-average of the disturbance flow quantities is

not zero. This distinguishes the disturbance approach from the conceptually similar linear perturbation techniques.

$$\overline{\Delta \mathbf{u}} \neq 0; \qquad \overline{\Delta p} \neq 0... \qquad\qquad (F.05)$$

As an aside, the disturbance concept can be applied to any situation where one is interested in describing the changes brought by a particular flow phenomenon. One such application is the propagation of density non-uniformities through a blade row.

F.2. Governing Equations.

Using (F.01), the incompressible, Reynolds-averaged Navier-Stokes equations can be cast in a disturbance form that allows to compute the disturbance flow $(\Delta \mathbf{u}, \Delta \boldsymbol{\omega}, \Delta p)$ for a specified (1) steady base flow and (2) inlet disturbance profile:

$$\nabla \cdot \Delta \mathbf{u} = 0$$

$$\frac{\partial \Delta \mathbf{u}}{\partial t} = \underbrace{\mathbf{u}_s \times \Delta \boldsymbol{\omega}}_{I} + \underbrace{\Delta \mathbf{u} \times \boldsymbol{\omega}_s}_{II} + \underbrace{\Delta \mathbf{u} \times \Delta \boldsymbol{\omega}}_{III} - \underbrace{\nabla \Delta p_t}_{IV} + \underbrace{\nabla[(\nu_s + \Delta \nu)\nabla \Delta \mathbf{u}]}_{V} + \underbrace{\nabla(\Delta \nu \nabla \mathbf{u}_s)}_{VI} \qquad (F.06)$$

The boundary conditions to the disturbance equations of motion (F.06) are slightly different from those for the full Navier-Stokes equations :

- Surfaces. The disturbance velocity and pressure gradient at the solid surfaces are nil even in the presence of steady fluid suction/blowing:

$$\begin{aligned} \Delta \mathbf{u} &= 0 \\ \Delta \nabla p \cdot \mathbf{n} &= 0 \end{aligned} \qquad (F.07)$$

- Inlet. The inlet boundary conditions carry information only about the moving disturbances from the upstream rotor:

$$\begin{aligned} \Delta \mathbf{u} &= \mathbf{u}_u(x_i, y, z, t) - \mathbf{u}_s(x_i, y, z) \\ \Delta \nabla p \cdot \mathbf{n} &= 0 \end{aligned} \qquad (F.09)$$

The disturbance inlet boundary conditions are determined based on previous computational and experimental studies of the flow leaving the rotor (discussed in **Appendix G**).

Equations (F.06) is used to obtain the unsteady flows in the present investigation (as a sum of disturbance and base flows). The disturbance formulation of the Navier-Stokes equations is a useful conceptual tools for understanding the mechanics of blade row interaction.

This is due to the presence of base flow and upstream disturbances as two input parameters that completely specify the resulting unsteady flow response in the stator.

For instance, the boundary layers in the base flow can be removed. Comparing the resulting disturbance flow to the disturbance flow obtained with a normal base flow clearly shows the effect boundary layer response. The same approach can be used to identify the role of any parameter, such as stator loading or flow three-dimensionality. The inlet disturbance profile can be also manipulated for this purpose. For instance, the effect of reducing blade row spacing can be simulated by increasing the strength of the upstream disturbances while keeping the base flow constant. The crossflow velocity component of the upstream tip vortex can be removed, to determine which aspect of the vortex vortex structure is responsible for changes in stator performance. Such clear dependencies are difficult to isolate by experimental or traditional computational means, which yield the "complete" flow variables.

F.4. Physical Basis of the Disturbance Equations.

Each individual term in (F.06) represents a specific physical process in the unsteady flow that can be individually examined as follows :

(1) Term I represents the simple convection of the disturbances by the base flow. The transport of the upstream wake fluid by the bulk flow in the stator passage is an example of this mechanism.

(2) Term II represents the distortion of the base flow vorticity by the unsteady disturbance flow. This mechanism is significant in regions where the base flow is rotational. It is responsible for the boundary layer disturbances in described in **Chapters 3-6**.

(3) Term III represents the non-linear self-advective processes affecting the disturbance. The motion of a curved vortex filament under the effect of its self-induced velocity, or the migration of the rotor wakes, are examples of this mechanism.

(4) Term IV accounts for the coupling between pressure and velocity fluctuations. In is to be noted that, since the disturbance flow is incompressible, the base pressure "p_s" does not explicitly influence the unsteadiness.

(5) Term V accounts for the dissipation of the disturbances under the combined effects of the steady and unsteady viscous and turbulent shear stresses. The diffusion of a wake in otherwise uniform flow is an example of this mechanism.

(6) Term VI accounts for the dynamic effects of turbulent eddy viscosity fluctuations. This term is present only in Reynolds-averaged situations, and its effects are negligible in the present case.

Each of these terms can be manipulated to reveal specific mechanistic aspects of blade row interaction. For instance, the disturbances may linearized by setting term III in (F.06) to zero

in the computational procedure. Another simplified instance of the disturbance equations of motion is the *slip-free, non-linear inviscid base flow* formulation used for the results in **Chapter 4**. This formulation is useful for (1) assessing the role of recovery, and (2) isolating the dynamics and impact of boundary layer response:

$$\frac{\partial \Delta \mathbf{u}}{\partial t} = \underbrace{\mathbf{u}_s \times \Delta \boldsymbol{\omega}}_{I} + \underbrace{\Delta \mathbf{u} \times \Delta \boldsymbol{\omega}}_{III} - \underbrace{\nabla \Delta p_t}_{IV} + \bar{\nu} \nabla^2 \Delta \mathbf{u}$$

$$(F.09)$$

$$\text{Surface B.C} : \Delta \mathbf{u} \cdot \mathbf{dn} = 0$$

Term II is absent from (F.09) because the base flow is inviscid. Turbulent diffusion is however retained in the disturbance flow. In this manner, the upstream wakes and vortices are allowed to mix out, while interacting with the stator in an otherwise inviscid setting. The retention of turbulent diffusion in the disturbance flow serves two purposes. First, it suppresses the intrinsic instability of the inviscid equation. Second, it allows to assess the relative importance of recovery in the presence of turbulent diffusion. The latter point is important, since the recovery benefit from purely inviscid models may not be achieved in practice (Smith, 1996).

F.5. Computational Implementation.

The implementation of the disturbance equations of motion (F.06)/(F.09) in the NS3D computational procedure is relatively straightforward. First, no changes in the time discretisation or spatial discretization are required. For this reason, the implementation of the pressure and viscous steps is identical to that discussed in **Appendices C-D**.

The discretized convective step (C.23) is however different as shown below. This is due to (1) the different convective terms in the disturbance equations of motion; and (2) to the presence of the $\nabla(\Delta \nu \nabla \mathbf{u}_s)$ term (term VI of F.06). Although this term is of viscous origin, it acts like a body force from an algebraic standpoint. Therefore, it has been implemented in the convective step by means of an explicit backward-Euler scheme. A fourth-order Runge-Kutta scheme is however used for the purely convective effects.

$$\mathbf{u}_{jk,i,l}^{n+1/4} = \mathbf{u}_{jk,i,l}^{n} + \frac{\Delta t}{2} \mathbf{F}_{jk,i,l}^{n} \quad ...\text{etc.}$$

$$\mathbf{G}_{jk,i,l}^{n} = \nabla(\Delta \nu^{n} \nabla \mathbf{u}_s^{n})_{jk,i,l}$$

$$(F.10)$$

$$\mathbf{u}_{jk,i,l}^{*} = \mathbf{u}_{jk,i,l}^{n} + \frac{\Delta t}{6} \left\{ \mathbf{F}^{n} + \mathbf{F}^{n+1/4} + \mathbf{F}^{n+1/2} + \mathbf{F}^{n+3/4} \right\}_{jk,i,l} + \Delta t \mathbf{G}_{jk,i,l}^{n}$$

The convective forcing function **F** depends on the desired nature of the unsteady solution:

$$\text{Non-linear}: \quad \mathbf{F}^t_{jk,i,l} = \left\{ \mathbf{u}_s \times \Delta\omega^t + \Delta\mathbf{u}^t \times \omega_s + \Delta\mathbf{u}^t \times \Delta\omega^t \right\}_{jk,i,l}$$

$$\text{Linearized}: \quad \mathbf{F}^t_{jk,i,l} = \left\{ \mathbf{u}_s \times \Delta\omega^t + \Delta\mathbf{u}^t \times \omega_s \right\}_{jk,i,l}$$

$$(F.11)$$

Thus, given the appropriate boundary conditions and viscosity field, the NS3D computational procedure described in **Appendices C-D** can be used for solving the disturbance flow equations without modification except as noted above.

F.6. Disturbance Vorticity Dynamics.

The vorticity form of the full Navier-Stokes equations states that there are three mechanisms through which vorticity can be introduced in a flow:

$$\frac{\partial\omega}{\partial t} + \underbrace{(\mathbf{u}\cdot\nabla)\omega}_{\text{Transport}} = \underbrace{(\omega\cdot\nabla)\mathbf{u}}_{D} - \underbrace{\frac{1}{\rho^2}\nabla\rho\times\nabla p}_{B} + \underbrace{\frac{1}{R}\nabla^2\omega}_{V} \qquad (F.12)$$

- Since vortex lines move with the flow, their tilting and stretching introduces new vorticity components or alters the strength of the existing ones. This mechanism, represented by the term labeled "D" in (F.12), does not exist in two-dimensional flows.

- Baroclinic torque, represented by the term labeled "B" in (F.12). This mechanism does not exist in the incompressible flow situation investigated here, and is usually not significant in subsonic flows. Therefore, it shall not be considered further.

- Diffusion of vorticity produced at solid surfaces. This mechanism is represented by the term labeled "V" in (F.12).

In subsonic unsteady flow, changes in time-average loss are directly related to changes in vorticity (§**2.3**). Thus, it is of particular importance to understand the mechanisms through which disturbance vorticity ($\Delta\omega$) is introduced in the flow. The production of *disturbance* vorticity is a more complex phenomenon than described above. For this reason, the simpler two-dimensional situation will be examined first. Three-dimensional effects later shall be added later. In two-dimensional incompressible flow, the disturbance vorticity is is governed by the following equation, derived by applying the Δ operator to (F.12):

$$\frac{\partial\Delta\omega}{\partial t} + \underbrace{(\mathbf{u}_s\cdot\nabla)\Delta\omega}_{\mathbf{T}_{LC}} + \underbrace{(\Delta\mathbf{u}\cdot\nabla)\Delta\omega}_{\mathbf{T}_{NC}} = -\underbrace{(\Delta\mathbf{u}\cdot\nabla)\omega_s}_{\mathbf{T}_1} + \underbrace{\nu\nabla^2\Delta\omega}_{\mathbf{T}_4} \qquad (F.13)$$

The left-hand side of (F.13) represents the transport of disturbance vorticity in unsteady flow by the combination of bulk flow (linear convective term designated by T_{LC}) and disturbance flow (non-linear advective term designated by T_{NC}). The right-hand side represents two distinct mechanisms for introducing *disturbance* vorticity:

- Production of disturbance vorticity by normal "distortion" of existing vortex lines in the base flow. The lines in question are spanwise vortex filaments that are being moved in the blade-to-blade plane by the velocity disturbance. This mechanism, represented by the term T_1 (F.13), has no counterpart in steady flow. Examination of this term indicates that this mechanism is most important in regions regions where the base flow vorticity has large gradients (e.g. boundary layer edges). It has been found that normal distortion is the primary mechanism involved in boundary layer response for the unsteady flow under consideration. Its effects on loss are noticeable.

- Diffusion of disturbance vorticity produced at the solid surfaces (term T_1 in F.13). It is shown in §5.1.3 and §3.1, that this mechanism does not contribute to the change in stator loss in a significant manner.

In three-dimensional unsteady incompressible flow, there are two additional disturbance vorticity production terms, as shown below:

$$\frac{\partial \Delta \omega}{\partial t} + (\mathbf{u}_s \cdot \nabla)\Delta \omega + (\Delta \mathbf{u} \cdot \nabla)\Delta \omega = -(\Delta \mathbf{u} \cdot \nabla)\omega_s + \underbrace{(\omega \cdot \nabla)\Delta \mathbf{u}}_{T_2} + \underbrace{(\Delta \omega \cdot \nabla)(bu_s + \Delta \mathbf{u})}_{T_3} + \nu \nabla^2 \Delta \omega$$

Both of these terms are associated with stretching and tipping of vortex filaments. The term labeled "T_2" accounts for disturbance vorticity introduced by stretching/tipping of base flow vorticity filaments by the action of the disturbance velocity field. On the other hand, the term labeled "T_3" accounts for disturbance vorticity resulting from the stretching/tipping of disturbance vorticity filaments due to non-uniform base velocity (linear effect) and disturbance velocity (non-linear effect) fields.

The distinction between sources of disturbance vorticity in the computed solution is important, since it points to those flow mechanisms responsible for changes in loss. Identification of these mechanisms is useful in proposing design actions that exploit or mitigate the performance effects of upstream rotor disturbances.

Appendix G

Input Elements :

Inlet Boundary Conditions

Wakes, tip leakage vortices and streamwise vortices from the upstream rotor are represented as moving velocity disturbances, prescribed on the inlet boundary of the stator computational domain. This appendix describes the coordinate system ($\S$**G.1**) and the inlet boundary conditions ($\S$**G.2-G.4**) used for this purpose.

G.1. Method of describing rotor vortical disturbances.

Rotor disturbances are specified as a disturbance velocity field $(\Delta u_r, \Delta v_r, \Delta w_r)$ in a yawed frame moving with the rotor. This frame, referred to as REY (rotor exit yawed) frame, is shown in **Figure G.1**. The yaw angle is determined by the velocity triangles at the exit of the rotor.

$$\tan \theta_{2,r} = \frac{V_{\theta 2,r}}{U_x} \qquad (G.01)$$

An intermediate, moving frame is used for the purpose of transferring the disturbances specified in the REY frame, onto the stationary inlet boundary of the computational domain. This frame, referred to as REA (rotor exit axial) frame, is also shown in **Figure G.1**.

The disturbance velocity components in the REA frame, $(\Delta u_t, \Delta v_t, \Delta w_t)$, are obtained from $(\Delta u_r, \Delta v_r, \Delta w_r)$ by means of a linear transformation:
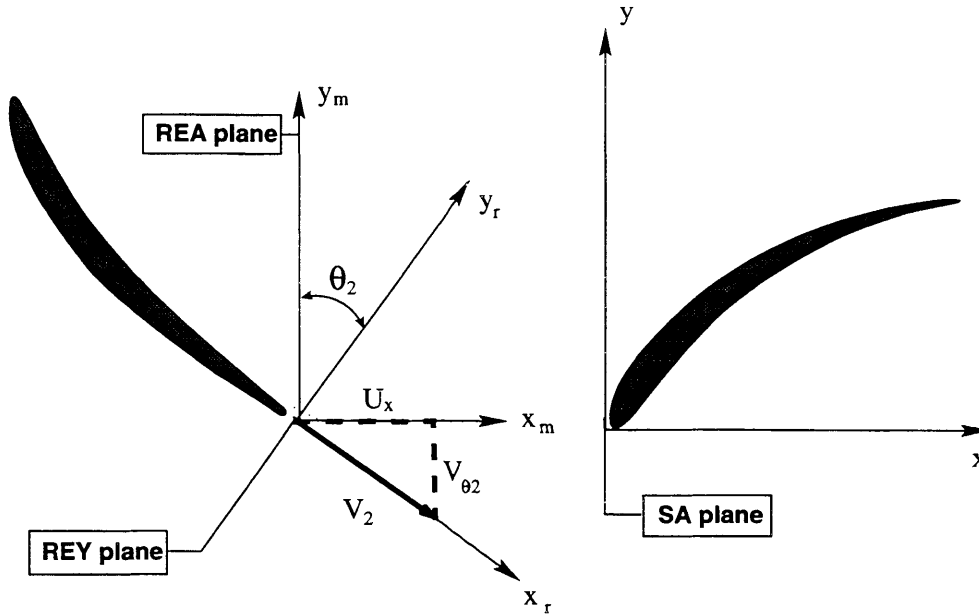
Figure G.1. Data on wakes and tip vortices is usually presented in the rotor relative frame (REY frame). To translate this information into the stator absolute frame (SA frame), an intermediate REA frame is used. This frame is aligned with the SA frame, but moves with the rotor blade.

$$
\begin{matrix}
\Delta u_t(y_r/\cos\theta_{2,r}, z) \\
\Delta v_t(y_r/\cos\theta_{2,r}, z) \\
\Delta w_t(y_r/\cos\theta_{2,r}, z)
\end{matrix}
=
\begin{bmatrix}
\cos\theta_{2,r} & \sin\theta_{2,r} & 0 \\
-\sin\theta_{2,r} & \cos\theta_{2,r} & 0 \\
0 & 0 & 1
\end{bmatrix}
\cdot
\begin{matrix}
\Delta u_r(y_r, z) \\
\Delta v_r(y_r, z) \\
\Delta w_r(y_r, z)
\end{matrix}
\qquad (G.02)
$$

Except for the relative tangential motion between the REA and SA frames, equation (G.02) also describes the disturbance velocity profile at the inlet of the stator $(\Delta u, \Delta v, \Delta w)$. Therefore, the disturbance inlet boundary conditions at the inlet of the stator computational domain are given by:

$$
\begin{aligned}
\Delta u(y, z, t) &= \Delta u_t(y_t, z) + u_s \delta u \\
\Delta v(y, z, t) &= \Delta v_t(y_t, z) + u_s \delta v \\
\Delta w(y, z, t) &= \Delta w_t(y_t, z) + u_s \delta w
\end{aligned}
\qquad (G.03)
$$

In the stator frame, the upstream wakes and vortices appear as a train of periodic disturbances, moving in the tangential direction with speed equal to the rotor wheel speed V_R. Mathematically, this is achieved by means of the following mapping:

$$
y_t = y_i - \min(y_i) - tV_R - S\mathcal{E}\left(\frac{y_i - \min(y_i) - tV_R}{S}\right)
\qquad (G.04)
$$

The adjustment velocities $(\delta u, \delta v, \delta w)$ in (G.03), represent a steady bias added to the disturbance so that the unsteady flow at the inlet has the same time-averaged mass flux and

momentum as the base flow. This satisfies the premise that the base flow is the steady flow that would exist in the stator passage if the upstream disturbances are mixed out between the blade rows. The adjustment velocities are obtained by solving the following system of equations :

$$\iint_{x_i} (\Delta u_t + u_s \delta u) dy dz = 0$$

$$\iint_{x_i} (u_s + \Delta u_t + u_s \delta u)(v_s + \Delta v_t + u_s \delta v) dy dz = \iint_{x_i} u_s v_s dy dz \qquad (G.05)$$

$$\iint_{x_i} (u_s + \Delta u_t + u_s \delta u)(w_s + \Delta w_t + u_s \delta w) dy dz = \iint_{x_i} u_s w_s dy dz$$

The multiplication by u_s in (G.03) and (G.05) allows to satisfy the non-slip endwall boundary conditions (u_s=1 in 2D flow). The adjustments to preserve mass and momentum are applied to the unsteady flow rather than to the base flow, since the base flow velocity forms the basis for non-dimensionalization. The adjustment velocities are typically small (few percent of the free-stream velocity).

The disturbances seen by the stator may appear quite different from their original description in the REY frame locked to the rotor (cf. §2.5, **Figure 2.3**). This is due to the transformation (G.02). The disturbance velocity field is not affected by the transformation between moving and stationary blade rows. The following sections describe the three base-line types of upstream rotor disturbances used in the present investigation (wake, tip leakage vortex, streamwise vortex) in the originating REY frame.

G.2. Description of the upstream rotor wakes.

A relatively large amount of data, obtained primarily in large-scale research compressors, is available for characterizing the ensemble-averaged properties of the rotor wakes. Relative velocity profiles taken in the rotor-stator gap are given by Silkowski (1995), Prato and Lakshminarayana (1993), Wisler (1992), Stauter, Dring and Carta (1991), Zierke and Okiishi (1982), and Gallus (1979) among others. The velocity profile across the wake is generally asymmetric, and reflects the difference in boundary thickness between the rotor blade suction and pressure sides.

Most of these experimental studies indicate that a two-dimensional representation of the wake geometry is adequate over most of the span. For instance, Wisler (1992) and Silkowski (1995) observe that the wake velocity defect is nearly constant between 20-80% of the span (the wakes become stronger near the hub, possibly owing to the higher loads on the rotor

blade there). The wakes appear as relatively straight spanwise columns of lower total pressure fluid. Experiments by Poensgen and Gallus (1991) support this observation.

It is to be noted however that a noticeable radial velocity component is generally present in the wakes (Prato and Lakshminarayana 1993, Kotidis and Epstein 1991, Nurzia and Puddu 1994). The effects of this radial component are not considered in the present study. The objective here is to elucidate the key role of the relative velocity defect. For this reason, the wakes used herein are described by a symmetrical, two-dimensional Gaussian velocity profile in the REY frame:

$$\Delta u_r = -A_r V_2 \exp\left\{-\ln 100 A \left[\frac{2y_r}{t_w}\right]^2\right\} - A_r V_2 \exp\left\{-\ln 100 A \left[\frac{2(S_r - y_r)}{t_w}\right]^2\right\} \tag{G.06}$$

$$\Delta v_r = 0 \quad ; \quad \Delta w_r = 0$$

Table G.1 summarizes ensemble-averaged properties of the wake (relative velocity defect A_r and 99% velocity defect thickness t_w) measured in research compressors. Wake properties depend on design, on how far behind the rotor the data is taken and on operating point. With the present configuration, a relative defect of 20-25% can be considered representative at design point operation.

Source	Axial spacing (% of chord)	Probe location (% of gap)	A_r ($\%V_{2r}$)	t_w (%S)
Stauter, Dring and Carta (1991)	48	4.0-71.0	0.47-0.23	16-25
Manwaring and Wisler (LSRC, DP) (1992)	40	50	0.17	30
Silkowski (LSRC, $\phi = 0.35$, HL) (1995)	40	50	0.30	18
Silkowski (LSRC, $\phi = 0.38$, DP) (1995)	40	50	0.16	20
Silkowski (LSRC, $\phi = 0.31$, LL) (1995)	40	50	0.17	30
Poensgen and Gallus (1991, cylinder rods)	50	50	0.15	30
Capece and Fleeter (1987)	n/a	n/a	0.15-0.30	25-40
Gallus (1979)	50	33	0.20-0.45	15

Table G.1. Ensemble-averaged midpsan wake properties from several experimental studies (DP=design point,HL/LL=high/low loading).

Wake decay as a function of downstream distance behind the rotor, and fluctuations of the wake properties in the time domain, are two other important wake parameters that shall be discussed presently. Wake profile measurements by Stauter et al. (1991) past the second-stage rotor of the UTRC LSRR2 provide information on how fast the rotor wake defect is attenuated in the space between blade rows. This data, shown in **Figure G.2**, is used in

this study to determine the "strength" of the wakes arriving in the stator as a function of the axial spacing between blade rows.
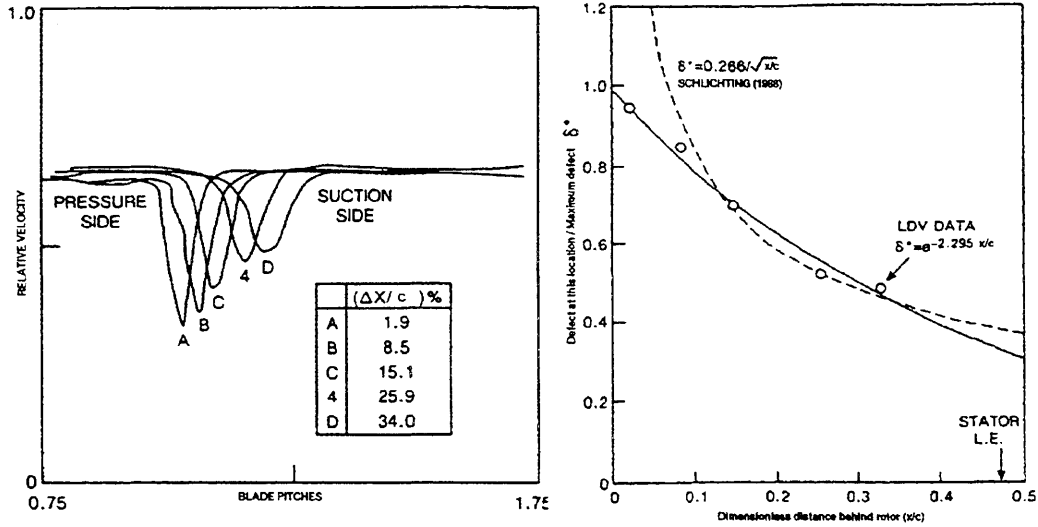

Figure G.2. Left : Measured ensemble-averaged wake profiles at five different locations past the rotor TE. Right : Measured velocity defect decay $A_r/A_{r.max}$ behind the rotor (dots and solid lines) and comparison to Schlichting (1968) correlation (dashed line). Location labeled "4" is near the mid-gap. From Stauter et al. (1991).

The above results are presented on an ensemble-averaged basis. In practice, the wake properties fluctuate in time. There is not sufficient data to characterize these fluctuations fully in terms of frequence and amplitude. In the introduction to his vortex-street model, Gertz (1988) pointed out that such fluctuations are present in some compressors and virtually absent in other designs. Available data indicates that the period of the fluctuations is comprised between 1/8 and 1/3 of the blade passing period (Brookfield 1996, Kotidis and Epstein 1991) and possibly related to the Strouhal number for vortex shedding based on local trailing edge properties. Near the rotor trailing edge, the amplitude of the fluctuations can be as large as the defect itself.

Since the effect of such fluctuations has not been considered in previous studies, the present investigation opens the subject by using a simplified model thereof. In this model, the wake velocity defect A_r is oscillated sinusoidally in the time domain with an amplitude equal to the ensemble-average $\overline{A_r}$, and at a fraction T_i/T_p of the blade passing period T_p.

$$A_r(t) = \overline{A_r}\left[1 + \sin\left(2\pi\frac{T_i}{T_p}T_p t\right)\right] \qquad (G.07)$$

As noted in §2.5, the disturbance velocity associated with the wake appears as a jet is directed against the pressure surface of the stator blades. This jet carries an excess of total

pressure, tangential momentum and incidence relative to the core flow. This can be seen in experiments where the data is taken in the stator frame of reference (e.g. Cherrett et al. , 1994). Compared to the core flow velocity in the stator frame, the wake disturbance can be quite strong. Capece and Fleeter (1987) have measured "gusts" between 20-50 percent of absolute velocity, thereby putting linearized wake interaction theory in question.

G.3. Description of the upstream rotor tip leakage vortex.

The flow near the outer casing behind a compressor rotor is characterized by three-dimensional, low-total pressure structure commonly referred to as a tip leakage vortex. The baseline tip leakage vortex used in the present study is illustrated in **Figure G.3** in terms of crossflow (left) and relative velocity defect (right) in the REY frame. It is based on the computed exit flowfield by Khalid (1995) for an isolated LSRC rotor at design point loading and tip clearance of 0.03 chords. The flowfield shown in **Figure G.3** is representative of ensemble-averaged data taken in research compressors (e.g. Khalid 1995, Wagner 1983).

To obtain the disturbance flow for of the tip vortex, $(\Delta u_r, \Delta v_r, \Delta w_r)$ as required by the code, the flowfield shown in **Figure G.3** is circumferentially mixed out, and the resulting average removed. The wakes are also removed in order to avoid confusing their effects with that of the tip leakage flow. The resulting disturbance flowfield has two components:

- A region of velocity defect Δu_r, qualitatively similar to that in a wake. This region is associated with the low-energy, blockage fluid in the tip leakage vortex.

- A jet-like crossflow disturbance $(\Delta v_r, \Delta w_r)$ associated with the flow from the high-pressure towards the low-pressure side of the overtip clearance.

At the exit of the rotor, the crossflow disturbance is about half as large as that associated with the velocity defect. The studies of Hunter and of Hunter and Cumpsty (1982), Storer (1991), Storer and Cumpsty (1991) and Khalid (1995) among others have contributed towards understanding how the tip leakage vortex arises and what parameters control the process. Khalid (1995) established that the blockage associated with the tip leakage vortex is directly propotional to the tip clearance and varies as a power of the rotor tip net loading parameter. Furthermore, Khalid noted similarities between the tip leakage flow and wake flows. These results are used in the present investigation to approximately scale the tip vortex at operating points and for axial spacings other than the baseline.

It is to be noted that for very small tip clearances (less than a percent) or for no clearance at all, no tip leakage vortex is observed. Instead, the flow in the aft part of the rotor tip separates (Storer and Cumpsty 1991). However, for clearances of engineering interest, the pattern of swirling, low-P_t described above is observed at the rotor exit.
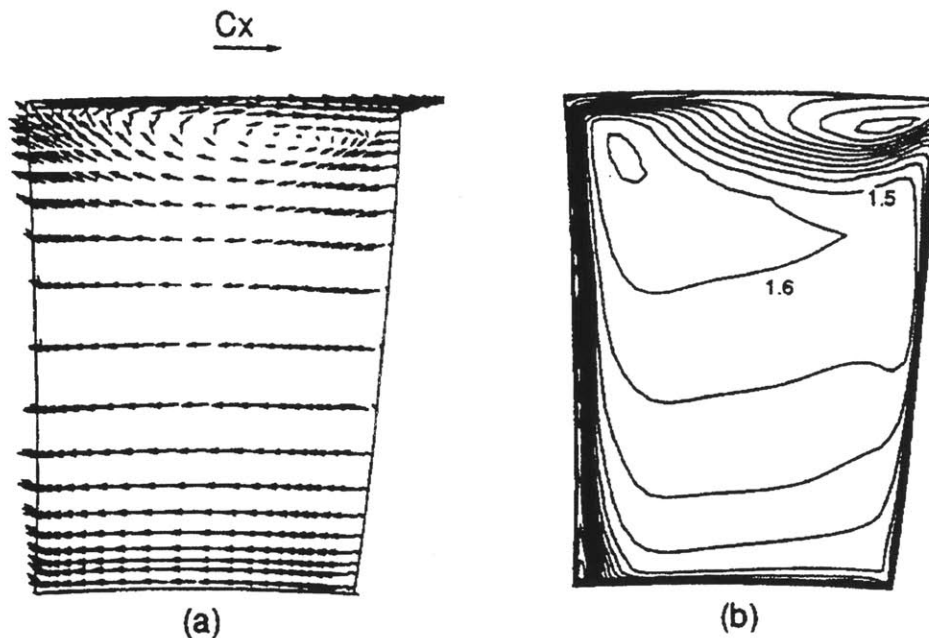
Figure G.3. Tip vortex flowfield in the REY frame used to derive disturbance inlet boundary conditions in the present investigation. Left: crossflow velocity vectors, showing the secondary flow structure associated with the vortex. Right: relative velocity contours, showing the strong velocity defect associated with the vortex. From Khalid (1995) computation for an isolated LSRC rotor at design loading and 0.03c tip clearance. Vortex is assumed to be steady in the rotor frame. This assumption is not necessary correct (Graf, 1996) but its effect can be assessed by examining results from fluctuating wakes.

G.4. Description of the upstream rotor streamwise vortex.

The foregoing tip leakage vortex is quite different from a purely streamwise vortex in the rotor relative frame. A "perfect" streamwise vortex can be described as a a "bundle" of vortex filaments aligned with the flow leaving the rotor, It is associated with a strong swirling point-flow in the rotor exit crossflow plane and no relative velocity defect.

The majority of flow data shows no evidence for such "perfect" streamwise vortices in research compressors (e.g. Silkowski, 1995). In fact, only one investigation shows such a "perfect" streamwise vortex (Nurzia and Puddu, 1994). In this case, the most apparent secondary flow feature at the exit of the rotor is an intense almost-perfect streamwise vortex core at the hub. Nurzia and Puddu's work is on an industrial fan and not on a research compressor. The blading at the hub of this fan is more similar to that of a helicopter rotor than to a compressor, which explains the presence of a well-delineated streamwise vortex.

Despite its limited practical significance, stator interaction with such streamwise vortices is useful from a fundamental standpoint. It showcases differences in the performance effects

of streamwise vortices and tip leakage vortices, and can identify which structural aspects of the tip leakage flow are the important one. For this reason, the third type of upstream rotor disturbance used herein is a vortex with a circular viscous core of streamwise vorticity. The inlet boundary conditions at the inlet of the stator are obtained by considering an array of images of a classical viscous vortex core (White, 1974).

$$\Delta u_r = 0$$

$$\Delta v_r = \frac{\Gamma}{2\pi} \sum_{l=-\infty}^{l=+\infty} \sum_{m=-\infty}^{m=+\infty} \frac{z_r + z_c - (4m+2)H}{r_{lm}^2} \left\{ 1 - e^{-1.26 r_{lm}^2 / r_c^2} \right\}$$

$$- \frac{\Gamma}{2\pi} \sum_{l=-\infty}^{l=+\infty} \sum_{n=-\infty}^{n=+\infty} \frac{z_r - z_c - 4nH}{r_{ln}^2} \left\{ 1 - e^{-1.26 r_{ln}^2 / r_c^2} \right\} \qquad (G.08)$$

$$\Delta w_r = \frac{\Gamma}{2\pi} \sum_{l=-\infty}^{l=+\infty} \sum_{n=-\infty}^{n=+\infty} \frac{y_r - y_c - lS_r}{r_{ln}^2} \left\{ 1 - e^{-1.26 r_{ln}^2 / r_c^2} \right\}$$

$$- \frac{\Gamma}{2\pi} \sum_{l=-\infty}^{l=+\infty} \sum_{m=-\infty}^{m=+\infty} \frac{y_r - y_c - lS_r}{r_{lm}^2} \left\{ 1 - e^{-1.26 r_{lm}^2 / r_c^2} \right\}$$

The index "l" in (E.12) accounts for tangential periodicity, whereas the indexes "m" and "n" account for the CW/CCW images and images-of-images with respect to the hub and casing. The distance offsets r_{lm} and r_{ln} in (G.08) are given by :

$$r_{ln}^2 = (y_r - y_c - lS_r) + (z_r - z_c - 4nH)^2$$

$$\qquad (G.09)$$

$$r_{lm}^2 = (y_r - y_c - lS_r) + (z_r - z_c - 4mH - 2H)^2$$

With the present stage design, the vortex filament described by (G.09) is roughly perpendicular to the main flow streamlines at the entrance of the stator. The core radius r_c of the streamwise vortex is governed by the balance between convective and diffusive time constants. Based on Nurzia and Puddu (1994) data, a vortex core radius of 0.15 blade spans appears to be a reasonable choice. The circulation of the core is taken equal to the rotor blade bound circulation (0.45U/c), based on the similarity between the vortex core visible in Nurzia and Puddu's (1994) data and the trailing hub vortex of a helicopter rotor.

Appendix H

Input Elements :

Steady Base Flows

This appendix describes the base flows used in the present investigation. The base flow is the steady flow that would exist in the stator passage if the upstream rotor disturbances are mixed-out at the inlet. The base flow serves as a propagation and interaction medium for the upstream disturbances. Four different base flows are used:

Base flow	Designation
Inviscid design-point base flow	ID
Viscous design-point base flow	VD
Viscous high-loading base flow	VH
Viscous high-shear base flow flow	VS

H.1. Computational method.

The inviscid base flow is obtained by means of the PCPANEL code developed by McFarland (1984). PCPANEL is based on a discrete singularity representation of a single blade row. Two-dimensional inviscid solutions are obtained at design-point incidence, and stacked in the spanwise direction to obtain an inviscid three-dimensional flowfield without spanwise flow or gradients. This limitation is acceptable, given that the purpose of the inviscid solution is to isolate unsteady flow features associated with the boundary layer response.

The viscous base flows are obtained by means of the Adamczyk et al. (1989) three-dimensional Navier-Stokes flow solver. This is a proven research code that has been successfully employed in several turbomachinery investigations, including Khalid's (1995) study

of tip leakage flow in a compressor rotor. For steady-state flows, this code yields adequate flowfields much faster than the NS3D computational procedure. It solves the steady Reynolds-averaged form of the mass, momentum, energy and state equations discretized on a cell-centered H-grid in the cylindrical-coordinate relative frame of a single stator blade row. The eddy viscosity and heat transfer coefficients are obtained using the Baldwin and Lomax (1978) turbulence model for wall-bounded flows, without special treatment of the wake region. The stability of the scheme is maintained by means of a linear combination of second and fourth order artificial viscosities (Jameson et al. 1981). To preserve the overall incompressible nature of the simulation, the base flows are computed at a Mach number of 0.2 (the lowest Mach number for which a relatively smooth solution can be obtained).

H.2. Inlet Profiles.

The circumferentially-averaged flow properties in turbomachinery may exhibit considerable spanwise gradients, that are associated with the development of endwall boundary layers along the annulus and with the manner in which the rotors transfer energy to the working fluid. Such spanwise profiles are of considerable interest, given their bearing on overall performance and pressure rise. Since the base flows used herein are computed for a single stator blade row, it is particularly important to prescribe inlet spanwise profiles at the entrance of the stator that are representative of the conditions in a typical embedded stage.
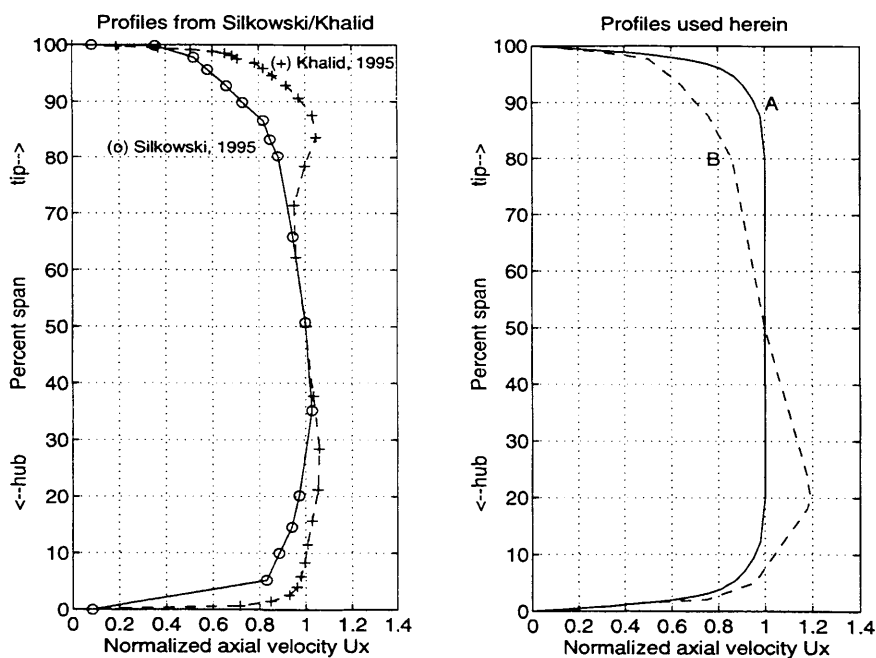

Figure H.1. Left: Normalized axial velocity profile at the inlet of an LSRC stator from Silkowski (1995) measurements and from Khalid (1995) single-rotor computations. Right: Axial velocity profiles used to generate the base flows in the present investigation. The normalization ensures that $U_x = 1$ at midspan (§A.4).

Measurements in modern compressors have shown that spanwise profiles of velocity and temperature settle down to a relatively constant pattern after three or four stages (Cumpsty 1989, Smith 1970). This pattern appears to be composed of (1) casing boundary layer extending over the outer 10-15% of span. (2) a largely inviscid core flow characterized by a velocity gradient such that the axial velocity near the casing is usually smaller than that near the hub, and (3) a hub boundary layer over the inner 10-20% of the span.

Based on this situation, two velocity profiles are used to generate the viscous base flows in the stator passage. The first profile, labeled "A" in the left side of **Figure H.1**, has a uniform core flow. As shown on the right side of **Figure H.1**, this profile is representative of the flow behind an isolated or front-stage rotor The second profile, labeled "B" on the left side of **Figure H.1**, is constructed using the largest velocity gradient found in the surveyed literature (Rhie et al. 1995 multistage calculation for Pratt & Whitney core compressor). The use of these different inlet profiles allows one determine the role of steady flow spanwise gradients on the performance changes brought by upstream wakes and vortices (cf. **§6.2.2**).
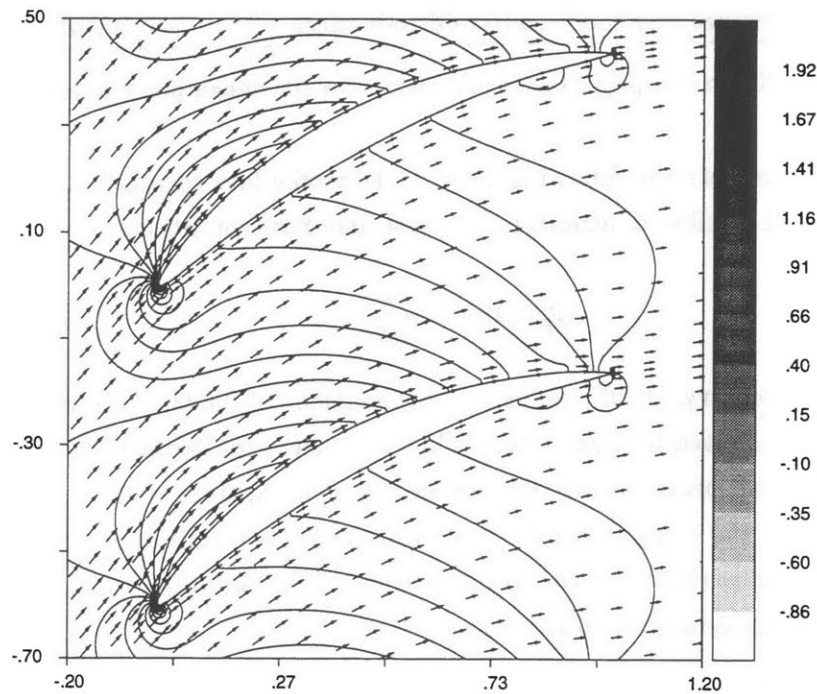

Figure H.2. Isobars of static pressure coefficient and velocity vectors on the midspan blade-to-blade plane in the inviscid (ID) base flow.

H.3. Inviscid base flow (ID).

The inviscid base flow is obtained using a design-point midspan incidence of 46 degrees (Manwaring and Wisler, 1992). The computed flowfield is shown in **Figure H.2**. The

computed stator static pressure coefficient (2.03) is 0.490, which is nearly equal to the exact theoretical value of 0.506. The computed passage and mixing loss coefficients are nil.

H.4. Viscous design point base flow (VD).

The design-point operating conditions for which the VD base flow is obtained are defined in **Appendix A**. Some of the important performance parameters computed at this point are summarized in **Table H.1**. The values of these parameters are comparable to what is currently used in the design practice.

Parameter	Value
Midspan inlet angle	46.0°
Midspan exit angle	21.0°
Midspan diffusion factor	0.41
Net static pressure recovery coefficient (entire passage)	0.402
Total pressure loss coefficient (entire passage)	0.033
Total pressure loss coefficient (midspan only)	0.020

Table H.1. Key stator performance parameters for the design-point base flow.

Cumpsty (1989) presents the following generic 2D profile loss correlation, based on empirical data for several families of airfoils under unstalled flow conditions:

$$y_p \approx 0.007 \frac{2\sigma}{cos\theta_2} \qquad (H.01)$$

For the present geometry, (H.01) yields a loss coefficient of 0.023. This value is in good agreement with the computed midspan passage loss coefficient in **Table H.1**. This indicates that the dissipative flow processes in this region are well captured in the VD base flow. **Figure H.3** compares the computed midspan static pressure distribution with data taken by Manwaring and Wisler (1992) at the same location. The computed loading distribution is in reasonably good agreement with the data.

No experimental data is available for more detailed assessment of the base flow features. Despite this, it is still possible to make a critical examination of the computed base flow. **Figure H.4** shows the midspan velocity contours, revealing a flowfield typical of modern stator blading. The suction side boundary layer progressively thickens, but remains attached almost until the trailing edge.

As shown in **Figure H.5**, the computed boundary layer velocity profile fits the law of the wall (White, 1974) in the unseparated flow region. This is a useful confirmation, given

that the base flow vorticity distribution is an important factor in determining the profile loss (§6.2.1, also **Appendix J**).
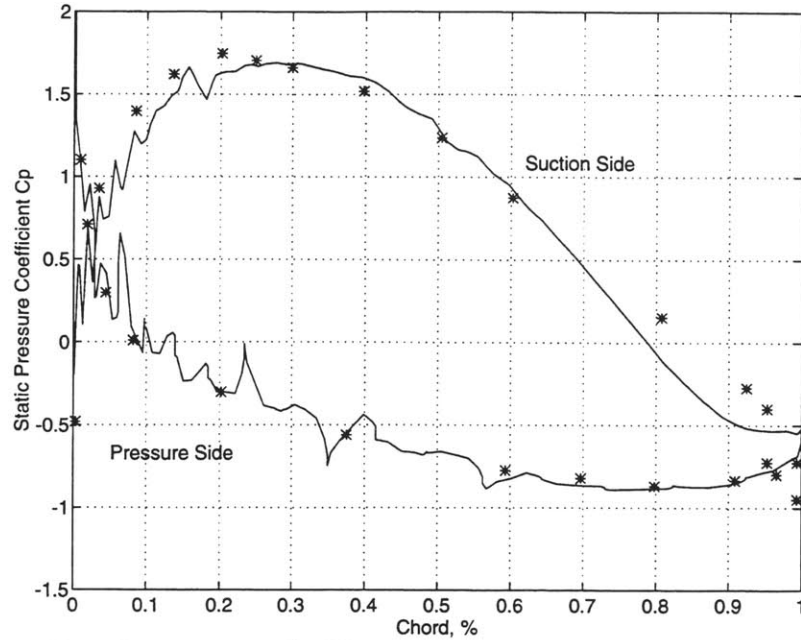

Figure H.3. <u>Dots</u>: Measured midspan static pressure distribution (adapted from Wisler, 1992). <u>Solid line</u>: Computed midspan static pressure distribution. Design-point operation ($\phi=0.45, \psi=0.65$).
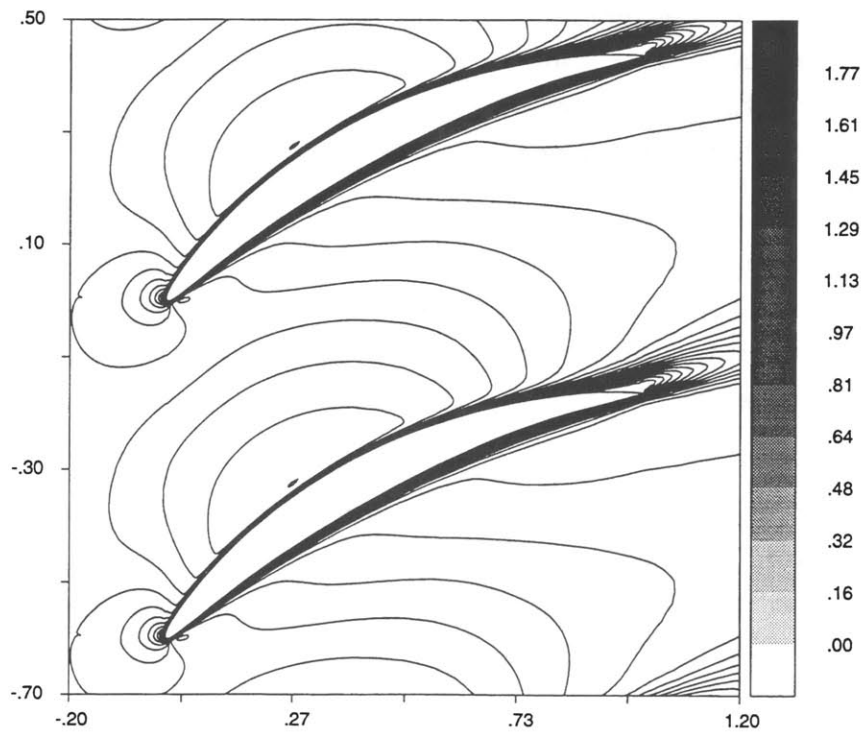

Figure H.4. Isovelocity contours on the mid-span blade-to-blade plane in the computed design-point base flow.
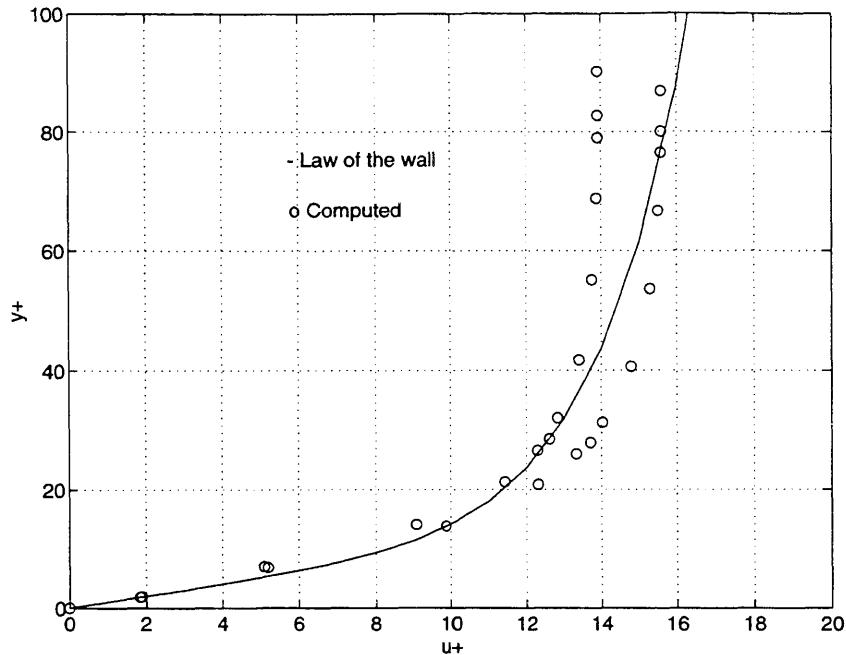
Figure H.5. Dots: Envelope of suction-side boundary layer profiles between 0.2 and 0.5 chords from the computed VD base flow. Solid line: Law of the wall (White, 1974). Design-point operation (ϕ=0.45,ψ=0.65).

The secondary flow vortical structure of the VD (design-point) base flow are shown in **Figure H.6** Near the leading edge, the computed flow is characterized by the two legs of the horseshoe vortex. This feature is normal, and can be explained by the deformation of the endwall boundary layer vortex filaments by the leading edge (**Figure H.7**, left). Further downstream however, the endwall flow streamwise vorticity comes to be dominated by the effects of enwall boundary layer turning (**Figure H.7**, left).

Streamwise vorticity is present in the blade boundary layer as well. Its presence can be explained by the "tilting" of the spanwise vortex filaments therein brought by the slowing of the flow near the casing, which is in turn due to the presence of swirl (**Figure H.7**, right). The magnitude of the computed streamwise vorticity in agreement with the Winter-Squire equation. This reinforces the conclusion that the VD base flow is representative of the actual flow in the stator.

It is to be noted that the base flow streamwise vorticity accounts for only about 15% of the total pressure loss. The remaining 85 percent are due to normal vorticity, under the form of boundary layers on the blade and on the endwalls. Considering the moderate flow turning in the stator, this finding is not surprising.
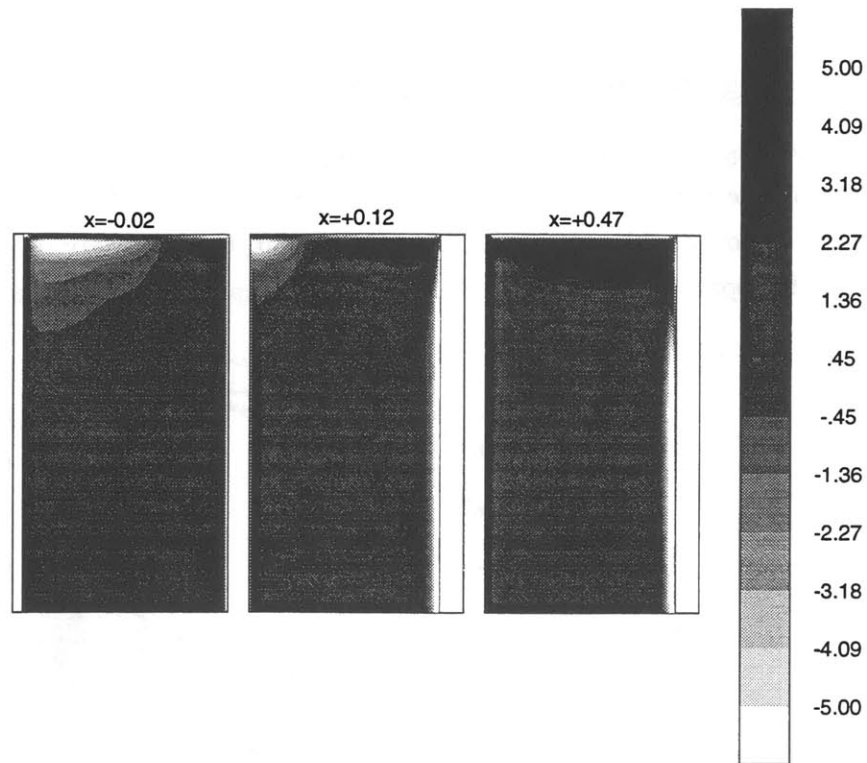
Figure H.6. Design-point base flow streamwise vorticity field in the outer half of the crossflow plane. (left:immediately before the leading edge, center:shortly after the leading edge, right:midchord).
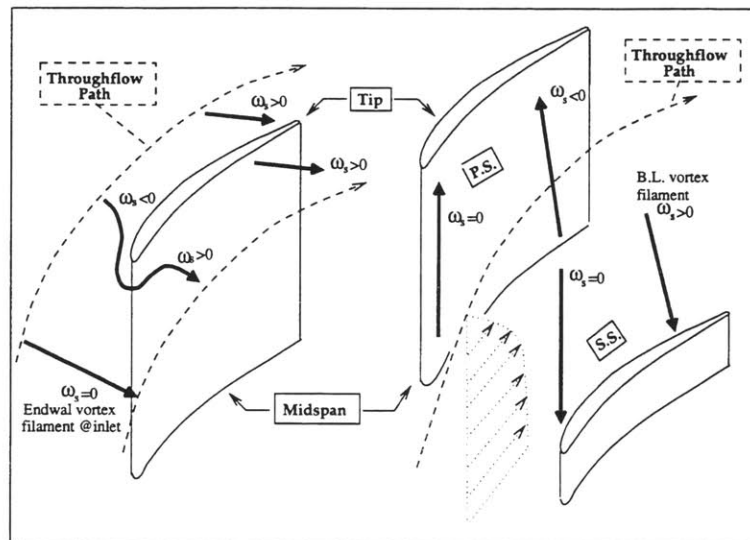
Figure H.7. The streamwise vorticity pattern shown in **Figure H.6** can be explained in terms of turning of the base flow boundary layer vortical filaments.

H.5. Viscous high-loading base flow (VH).

The high-loading point is at the right of the compressor characteristic peak (**Figure A.1, Appendix A**). The midspan flow angle at the inlet of the stator of 51 degrees. As shown in **Figure H.8**, the flow at this point is unstalled. However, the boundary layer thickness and the extent of the separated region have increased with respect to the design point case.
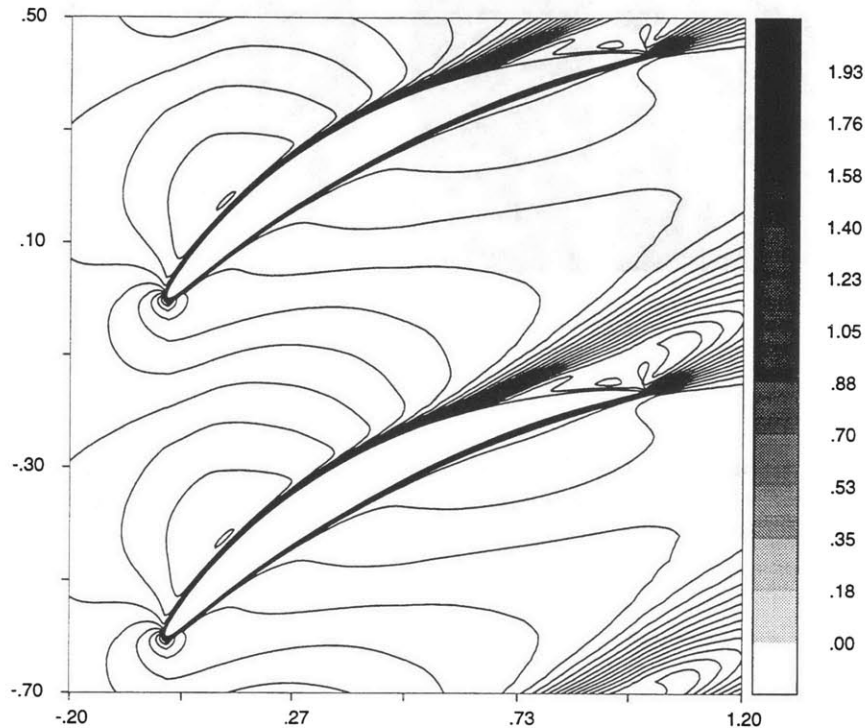
Figure H.8. Isovelocity contours on the mid-span blade-to-blade plane in the computed design-point base flow.

This results in an increased overall passage loss in the stator passage, that can be appreciated by comparing **Tables H.1** and **H.2**. The static pressure recovery coefficient of the stator has also increased. The performance parameters below are representative of a highly-loaded but yet-unstalled blade row.

Parameter	Value
Midspan inlet angle	51.0°
Midspan exit angle	21.0°
Midspan diffusion factor	0.51
Net static pressure recovery coefficient (entire passage)	0.402
Total pressure loss coefficient (entire passage)	0.044

Table H.2. Key stator performance parameters for the high-loading base flow.

H.6. Viscous high-shear base flow (VS).

The most notable feature of the high-shear base flow is a more pronounced secondary flow pattern (**Figure H.9**). This can be explained by the turning of a flow that has increased non-unformity at the inlet. Otherwise, the VS base flow is qualitatively similar to the design-point base flow (the VD and VS base flows are obtained at the same incidence).

Figure H.9. Design-point base flow streamwise vorticity field in the outer half of the crossflow plane. (left:immediately before the leading edge, center:shortly after the leading edge, right:midchord).

Appendix I

Mechanistic Relationships for Unsteady Loss and Pressure Rise

This appendix has a two purposes. The first is to define time-averaged figures of merit for unsteady flow that are (1) physically related to compressor performance and (2) fam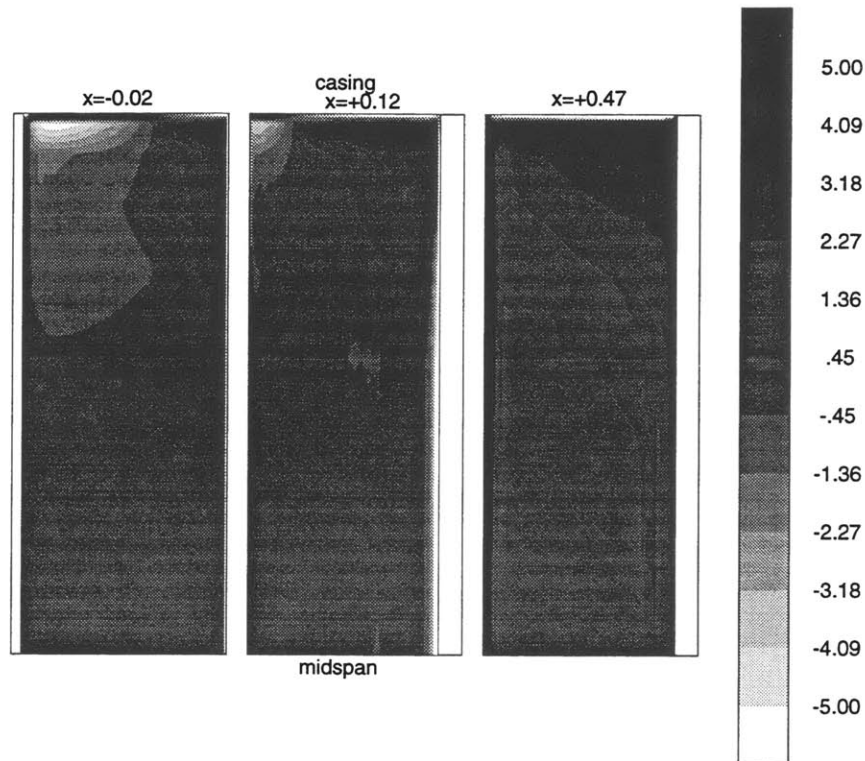iliar to designers. The second is to derive mechanistic relationships between figures of merit and those flowfield features that can be observed by means of computation or experiment.

This study is concerned with subsonic flows. In such flows, compressibility does not exert a radical impact on the flow features or on the production of vorticity and total pressure loss. For this reason, the relationships have been derived on an incompressible basis. This leads to simple expressions that contain the essence of the problem.

I.1. Figures of Merit.

This section derives a loss coefficient related to the time-averaged compressor efficiency:

$$\eta = \frac{\text{Isentropic work of adiabatic compression for a given total pressure ratio}}{\text{Actual work of adiabatic compression for the same total pressure ratio}} \qquad (I.01)$$

For this purpose, the unsteady compression process is treated as a collection of fluid particles undergoing a change in state within an insulated control volume, illustrated in **Figure I.1**. Only the average value of the shaft work is of practical interest. It can be computed by application of the first law to each particle, followed by summation over a large number of particles. If the unsteady process is periodic (i.e. there is no net accumulation of energy or mass in the compressor stage over a given time period), the average work is:
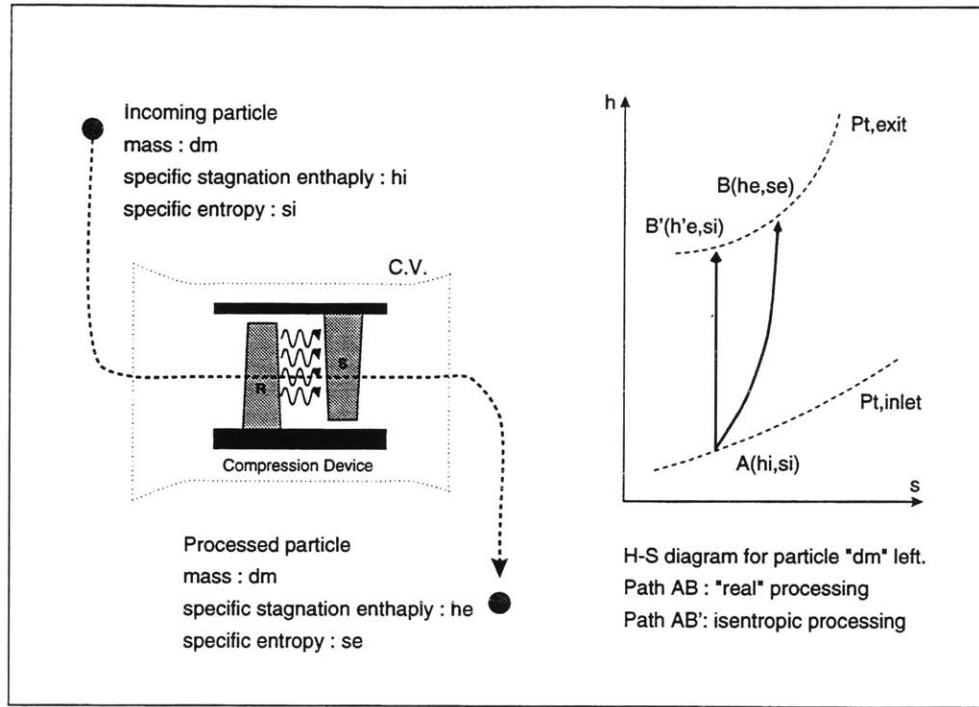
Figure I.1. Processing of fluid particles within a control volume around the device, and associated change of state in the H-S diagram.

$$\dot{\mathcal{W}}_{c.v.} = \oint\!\!\!\oint_{c.v.} \overline{\dot{m}h_t} \cdot \mathbf{dS} = \int\!\!\!\int_{\text{exit}} \overline{\dot{m}h_t} dA - \int\!\!\!\int_{\text{inlet}} \overline{\dot{m}h_t} dA \qquad (I.02)$$

As shown in **Figure I.1** (right), the actual stagnation enthalpy rise for a fluid element "dm" going though the real compression process will be higher than in isentropic compression. If the variations in pressure due to unsteadiness and losses are small relative to the absolute value, one can use the local slope of the P_t lines:

$$\left(\frac{\partial h_t}{\partial s}\right)_{P_t} = T_t \qquad (I.03)$$

to relate the difference between real and ideal exit stagnation enthalpy of a fluid particle to the increase in specific entropy:

$$h_{t,e} - h'_{t,e} = T_{t,e}(s_e - s_i) \qquad (I.04)$$

The above quantity represents the specific power required to bring a fluid particle to its isentropic state. Summation of fluid particles over the flow area and time period, together with (I.02), leads to the following expression for time-averaged efficiency:

$$\eta = 1 - \frac{\iint \overline{\dot{m} T_t (s_e - s_i)} dA}{\iint \overline{\dot{m}(h_{t,e} - h_{t,i})} dA} \qquad (I.05)$$

Equation (2.05) is an extension of the well-known steady formula (Denton 1993, Kerrebrock 1992) for unsteady non-uniform flow. It states that the only rational measure of loss is entropy flux (in this case, mass and time-averaged). Our computational procedure does not provide entropy levels directly, but total pressure distributions are readily available. For this reason, (I.05) shall be cast in terms of P_t by making use of the following perfect gas relationship:

$$s_e - s_i = C_p \ln(T_{t,e}/T_{t,i}) - R \ln(P_{t,e}/P_{t,i}) \qquad (I.06)$$

For adiabatic flow through a stationary blade row the stagnation temperature is constant, and the stagnation pressure ratio is close to unity. A Taylor series expansion of (I.06) yields:

$$T_t(s_e - s_i) \approx \frac{P_{t,i} - P_{t,e}}{\rho_{t,i}} \qquad (I.07)$$

Considering incompressible flow, substitution of (I.07) into (I.05) yields the following relation between the non-uniform total pressure field and the drop in time-averaged stage efficiency associated with entropy rise in the stator:

$$(1 - \eta)_{\text{stator}} \approx \frac{\iint (\overline{U_i P_{t,i} - U_e P_{t,e}}) dA}{UP_{t,\text{stage inlet}} - UP_{t,\text{stage exit}}} \qquad (I.08)$$

A dimensionless loss coefficient shall be used to represent this drop in efficiency:

$$(1 - \eta)_{\text{stator}} \approx \frac{P_{t,\text{stator inlet}} - P_{\text{stator inlet}}}{P_{t,\text{stage inlet}} - P_{t,\text{stage exit}}} \, \mathcal{Y}_{I \to E} \qquad (I.09)$$

where:

$$\mathcal{Y}_{I \to E} = \frac{1}{A} \left[\iint_E \overline{uc_t} dA - \iint_I \overline{uc_t} dA \right] \qquad (I.10)$$

In steady flow, the loss coefficient given by (I.10) is identical to that used in cascade testing and stage design (Lieblein et al. 1953, Cumpsty 1989, Kerrebrock 1992, Denton 1993):

$$\mathcal{Y} = \frac{\text{Mass averaged } \Delta P_t \text{ across cascade}}{Q_{\text{inlet}}} \qquad (Steady Flow) \qquad (I.11)$$

I.2. Connection between Passage Loss and Flow Variables.

To extract $\mathcal{Y}_p$, the full Navier-Stokes equations shall be cast in the following form:

$$\nabla C_t = -2\frac{\partial \mathbf{u}}{\partial t} + 2\mathbf{u}\times\boldsymbol{\omega} - \frac{2}{R}\nabla\times\boldsymbol{\omega} \qquad (I.12)$$

Multiplying both sides by $\mathbf{u}$ and observing that $\mathbf{u}\cdot\mathbf{u}\times\boldsymbol{\omega} \equiv 0$ yields :

$$\mathbf{u}\cdot\nabla C_t = -\frac{\partial \mathbf{u}^2}{\partial t} - \frac{2}{R}\mathbf{u}\cdot(\nabla\times\boldsymbol{\omega}) \qquad (I.13)$$

By virtue of continuity, the left-hand side of (I.13) can be written as :

$$\mathbf{u}\cdot\nabla C_t = \nabla\cdot(\mathbf{u}C_t) - C_t(\nabla\cdot\mathbf{u}) = \nabla\cdot(\mathbf{u}C_t) \qquad (I.14)$$

Integrating (I.14) over the passage control volume, and applying the divergence theorem to the left-hand side of the resulting integral yields:

$$\oiint_{\delta V}(\mathbf{u}C_t)\cdot\mathbf{dn} = -\iiint\left\{\frac{\partial \mathbf{u}^2}{\partial t} + \frac{2}{R}\mathbf{u}\cdot(\nabla\times\boldsymbol{\omega})\right\}dV \qquad (I.15)$$

In absence of fluid suction or blowing from the solid boundaries, the left-hand side of (I.15) has the same form as the dimensionless passage loss coefficient $\mathcal{Y}_p$. Inserting the identity:

$$\nabla\cdot(\mathbf{u}\times\boldsymbol{\omega}) = \boldsymbol{\omega}\cdot(\nabla\times\mathbf{u}) - \mathbf{u}\cdot(\nabla\times\boldsymbol{\omega}) \qquad (I.16)$$

into (I.15), and applying the divergence theorem to the $\nabla\cdot(...)$ terms in the right-hand side thereof, yields:

$$\oiint_{\delta V}(\mathbf{u}C_t)\cdot\mathbf{dn} = -\underbrace{\frac{\partial}{\partial t}\iiint_V \mathbf{u}^2 dV}_{K.E.} + \underbrace{\frac{2}{R}\oiint_{\delta V}(\mathbf{u}\times\boldsymbol{\omega})\cdot\mathbf{dn}}_{F.F.} - \underbrace{\frac{2}{R}\iiint_V \boldsymbol{\omega}^2 dV}_{V.D} \qquad (I.17)$$

Each term in the above can be connected to a particular physical process. The term labeled "KE" represents the rate of change of kinetic energy of the fluid contained in the control volume. The term labeled "FF" represents the net flux of frictional work across the boundaries of the control volume. The term labeled "VD" represents the rate of work done by frictional forces within the control volume. Time-averaging (I.17) yields the passage loss coefficient $\mathcal{Y}_p$ of interest on the left-hand side. On the right-hand side, it is straightforward to show that the time-average of the kinetic energy term is zero for periodic flows. Furthermore, It is easily shown that the FF term in the computed flowfields here is about an order of

magnitude smaller than the VD (viscous dissipation term). As a result, the time-average loss coefficient is function only of the total enstrophy field ω^2 inside the passage:

$$A\mathcal{Y}_p = -\frac{2}{R} \iiint \overline{\omega^2} dV \qquad (I.18)$$

Equation (I.18) is useful. The unsteady flow phenomena here can be described and understood in terms of vorticity redistribution. Equation (G.07) provides the desired direct link between changes in time-averaged loss coefficient and the underlying changes in the flow vortical structure. For instance, the difference in time-average passage loss between the unsteady flow and the steady pre-mixed flow can be written as follows:

$$A\mathcal{Y}_{p,u} - A\mathcal{Y}_{p,s} = -\frac{2}{R} \iiint \overline{(\boldsymbol{\omega}_u + \boldsymbol{\omega}_s) \cdot (\boldsymbol{\omega}_u - \boldsymbol{\omega}_s)} dV \qquad (I.19)$$

The vorticity field of the base flow, $\boldsymbol{\omega}_s$ is essentially constant in time. Using the "Delta" notation, introduced in §F.1 to represent differences between unsteady and steady base flow, allows to write (I.19) in the following manner :

$$A\Delta\mathcal{Y}_p = -\frac{4}{R} \iiint \boldsymbol{\omega}_s \cdot \overline{\Delta\boldsymbol{\omega}} dV - \frac{2}{R} \iiint \overline{(\Delta\omega)^2} dV \qquad (I.20)$$

Equation (I.20) is used to determine the change in passage loss associated with boundary layer disturbances. The first term on its right-hand side represents additional dissipative work due to the presence of vortical disturbances within a vortical base flow. The second (non-linear) term represents the increase in dissipative work associated with the disturbance proper. In the cases examined here, it is found that this term can be neglected.

I.3. Connection between Mixing Loss and Flow Variables.

The loss from mixing the flow at a given axial location to uniform condition, $\mathcal{Y}_m(x)$, is calculated using a constant-area assumption. This assumption has been selected among others because it corresponds to a physically realizable process. The flow at the exit boundary of the mixing control volume is uniform, although it may fluctuate in time. We are interested only in the time-average value of the mixing loss coefficient in the control volume, therefore:

$$A\mathcal{Y}_m(x) = \iint_\infty \left\{ u_D \left(C_{p,\infty} + u_D^2 + v_D^2 + w_D^2 \right) \right\} dydz - \iint_A \left\{ u \left(C_p + u^2 + v^2 + w^2 \right) \right\} dydz \qquad (I.21)$$

It is to be noted that $\rho = 1$ (incompressible flow, dimensionless units) in the above, which allows to simplify the notation. The flow conditions at the far downstream boundary

$(C_{p,\infty}, u_D, v_D, w_D)$ are determined by means of mass and momentum flux conservation:

$$\frac{\partial}{\partial t} \iiint \rho dV + \oiint \rho \mathbf{u} \cdot \mathbf{dn} = 0$$

$$\frac{\partial}{\partial t} \iiint 2\rho u dV + \oiint 2\rho \mathbf{u}\mathbf{u} \cdot \mathbf{dn} = \iiint C_p \mathbf{dn}$$

$$(I.22)$$

The mass conservation equation yields:

$$u_D = M/A \qquad (I.23)$$

where $"M"$ is the mass flux entering the passage, given by the boundary conditions. For two-dimensional flow, $u_D \equiv 1$. The three components of the momentum equation yield:

$$C_{p,\infty} = -2u_D^2 - \frac{2}{A} \iiint_V \frac{\partial u}{\partial t} dV + \frac{1}{A} \iint_A (C_p + 2u^2) dA$$

$$v_D = -\frac{1}{Au_D} \iiint_V \frac{\partial v}{\partial t} dV + \frac{1}{Au_D} \iint_A uv dA \qquad (I.24)$$

$$w_D = -\frac{1}{Au_D} \iiint_V \frac{\partial w}{\partial t} dV + \frac{1}{Au_D} \iint_A uw dA$$

Substituting (I.24) into (G.21) allows (after some algebra) to express the instantaneous flux of total pressure across the boundaries of the control volume in the following form :

$$\oiint_{C.V.} \mathbf{u} C_t \cdot \mathbf{dn} = u_D \iint_A (C_p + 2u^2 - u_D^2) dA - \iint_A u(C_p + u_T^2) dA$$

$$+ \frac{1}{u_D A} \left\{ \iint_A uv dA \right\}^2 + \frac{1}{u_D A} \left\{ \iint_A uw dA \right\}^2 + I(t)$$

$$(I.25)$$

where $"I(t)"$ represents terms containing a time derivative :

$$I(t) = -2u_D \iiint_v \frac{\partial u}{\partial t} dV$$

$$+ \frac{1}{u_D A} \left\{ \iiint_V \frac{\partial v}{\partial t} dV \right\}^2 - \frac{2}{u_D A} \iint_A uv dA \iiint_V \frac{\partial v}{\partial t} dV \qquad (I.26)$$

$$+ \frac{1}{u_D A} \left\{ \iiint_V \frac{\partial w}{\partial t} dV \right\}^2 - \frac{2}{u_D A} \iint_A uw dA \iiint_V \frac{\partial w}{\partial t} dV$$

The time-average of the L.H.S. in (I.25) is the mixing loss coefficient $\mathcal{Y}_m$ sought. The first four R.H.S. terms in (I.25) represent a quasi-steady mixing loss, i.e. the loss that would be

incurred had the flow been "frozen" at this moment and then mixed to a uniform state. On the other hand, the time-average of the last term (I.26) is not identically zero. With some extra algebra, it can be shown that this time-average is:

$$\mathcal{I} = -\frac{1}{u_D A} \left\{ \iiint_V \frac{\partial v}{\partial t} dV \right\}^2 - \frac{1}{u_D A} \left\{ \iiint_V \frac{\partial w}{\partial t} dV \right\}^2 \qquad (I.27)$$

Equation (I.27) indicates that the mixing loss of an unsteady flow not only on the flow profile at the mixing plane, but also on the details of the entire mixing process. The existence of this *non-stationary* term is in principle a major obstacle for calculating the mixing loss, since (I.27) involves an integral over the entire mixing volume (which is infinite) of an unsteady flow field that is a priori unknown. However, for the flow situations examined here, it appears that the non-stationary term is can be neglected compared to the quasi-steady term. This can be shown by plotting the net loss coefficient, $\mathcal{Y}_n$, as a function of the locus of the control plane used to calculate $\mathcal{Y}_n$. As shown in (I.28), the net loss is defined as the passage loss coefficient $\mathcal{Y}_p(x)$ generated from inlet up to the location "x", plus the quasi-steady mixing loss of the flow past this location.

$$\mathcal{Y}_n(x) = \mathcal{Y}_p(x) + \mathcal{Y}_{m,\text{quasi-steady}}(x) \qquad (I.28)$$

Since $\mathcal{Y}_p(x)$ contains both quasi-steady and non-stationary effects, calculating $\mathcal{Y}_n(x)$ in (I.28) at different x locations results into a net loss variation that reflects the importance of the unstationary mixing loss. The result of this experiment is shown in **Figure I.2**.
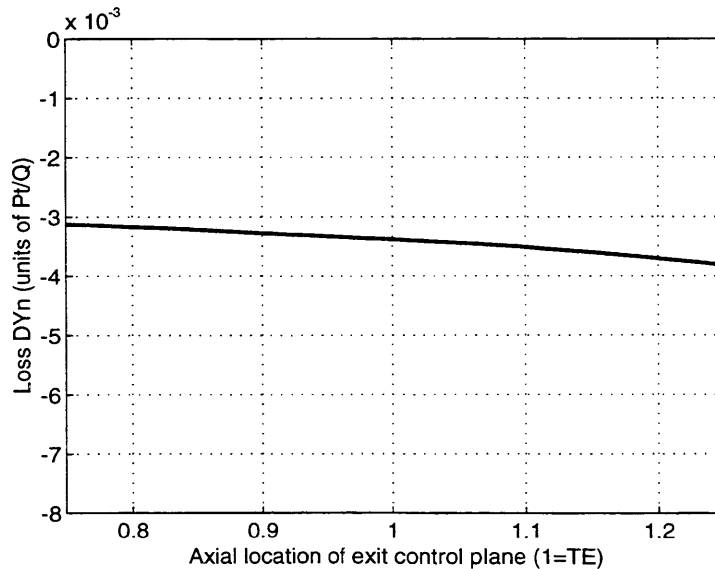

Figure I.02. Distribution of $\Delta\mathcal{Y}_n(x)$ as a function of the axial location of the mixing control plane. Based on the unsteady flowfield from the VD/TL computational experiment (§5.1, tip leakage vortex-stator interaction, $\phi = 0.45$, Re=3.10^4).

The relatively constant value of $\Delta \mathcal{Y}_n(x)$ in **Figure I.2** indicates that the non-steady component of mixing loss is about five times smaller than the quasi-steady component. Only when the flow is massively separated (in 2D direct laminar simulation of wake-stator interaction), we have seen this not to be the case. For this reason, the mixing loss coefficients herein are calculated using the quasi-steady part of (I.25).

$$A\mathcal{Y}_m(A) = u_D \iint_A (\overline{C_p} + \overline{2u^2} - u_D^2)dA - \iint_A \overline{u(C_p + u_T^2)}dA$$

$$+ \frac{1}{u_D A}\overline{\left\{ \iint_A uvdA \right\}}^2 + \frac{1}{u_D A}\overline{\left\{ \iint_A uwdA \right\}}^2$$

$$(I.29)$$

As noted above, (I.29) does not hold true for all types of unsteady flows, but constitutes an adequate approximation for the type of unsteady flow examined here. A possible explanation is that flow unsteadiness is mainly here is due to the convection of disturbances which (local to their own frame) are relatively steady in time.

In the three-dimensional case, the exiting flow does not mix to uniform state due to the presence of endwall boundary layers. Equation (I.29) can be easily modified to account for this phenomenon, since the quasi-steady loss coefficient satisfies the following property :

$$\mathcal{Y}_m(A \to B) = \mathcal{Y}_m(A \to U) - \mathcal{Y}_m(B \to U)$$

$$(I.30)$$

where $(A \to B)$ indicates a mixing process from state "A" to some fully-developed state "B" with endwall boundary layer; $(A \to U)$ indicates the mixing process to a fully uniform state used to derive (I.29); and $(B \to U)$ indicates the mixing loss from the fully-developed state with endwall boundary layers to the hypothetical fully-uniform flow. Equation (I.30) is basically a constant-level shift in the computed mixing loss representing the endwall effect. Since we are interested in the mixing loss *difference* between unsteady and steady reference flows $\Delta \mathcal{Y}_m$, the correction (I.30) is not essential, although it is used in the computed results. The difference in mixing loss is obtained in a straightforward manner by applying the Δ operator to (I.29)/(I.30):

$$A\Delta\mathcal{Y}_m(A) = u_D \iint_A (\Delta\overline{C_p} + \Delta\overline{2u^2})dA - \iint_A \Delta\overline{u(C_p + u_T^2)}dA$$

$$+ \frac{1}{u_D A}\Delta\overline{\left\{ \iint_A uvdA \right\}}^2 + \frac{1}{u_D A}\Delta\overline{\left\{ \iint_A uwdA \right\}}^2$$

$$(I.31)$$

Equation (I.31) is used to compute the mixing loss benefits presented here. However, it is not very informative on their causes. A more suitable expression for explaining changes in mixing

loss can be derived by assuming that (1) $u_D \sim 1$, and (2) upstream rotor non-uniformities are smaller than the lengthscale over which the core base flow properties change. With these, (I.31) can be reduced to:

$$A\Delta\mathcal{Y}_m(A) \approx u_D \iint_A \overline{\Delta u \Delta C_p} dA - \iint_A \overline{(1+\Delta u)(\Delta u^2 + \Delta v^2 + \Delta w^2)} dA$$

$$+\frac{1}{A}\overline{\left\{\iint_A (1+\Delta u)\Delta v dA\right\}}^2 + \frac{1}{A}\overline{\left\{\iint_A (1+\Delta u)\Delta w dA\right\}}^2$$

(I.32)

Equation (I.32) usually approximates (G.31) within 5-10 percent. It provides a useful correlation between (a) the change in mixing loss due to unsteadiness, and (b) the disturbance velocity profile. In physical terms, (I.32) states that the difference in mixing loss between two flows is given by the difference in work done by the pressure force at the mixing plane, plus the difference in kinetic energy flux at this plane.

It is to be noted that one should be careful when making further assumptions (such as $\Delta u << 1$) in an attempt to further simplify (I.32), since the velocity fluctuations are usually in phase. This yields non-negligible third-order terms. It is to be noted that (I.32) also applies to the case of two-dimensional flow by simply letting $w = 0$.

I.4. Connection between Passage Pressure Rise and Flow Variables.

The static pressure coefficient, representing the capacity of the stator to convert kinetic energy in the incoming flow to static pressure, can be expressed in terms of flowfield variables by projecting the momentum conservation principle (I.22) along the axial direction while including friction forces as well. Using a control volume between the inlet and the exit of the stator, this yields:

$$A\Pi_p(x) = \int_{x_{LE}}^{x} \int_{-H/2}^{H/2} \left[(\overline{C_p})_{PS} - \overline{C_p})_{SS}\right] dydz \quad \text{Blade Pressure Force}$$

$$+2\int_{SS}^{PS} \int_{-H/2}^{H/2} \overline{[u^2(x=0) - u^2(x)]} dydz \quad \text{Momentum Recovery}$$

(I.33)

$$-\frac{2}{R}\int_{x_{LE}}^{x} \int_{-H/2}^{H/2} \left[(\overline{\omega_z})_{PS} - \overline{\omega_z})_{SS}\right] dxdz \quad \text{Blade Friction Force}$$

$$-\frac{2}{R}\int_{x_I}^{x} \int_{SS}^{PS} \left[(\overline{\omega_y})_L - \overline{\omega_y})_U\right] dxdy \quad \text{Endwall Friction Force}$$

Equation (I.33) provides a direct connection between the static pressure coefficient of

the stator on one side, and (1) pressure and friction forces on solid surfaces, and (2) flux of kinetic energy on the other. At the exit of the stator, the flow is mixed-out to a uniform state. In addition, a certain amount of static pressure rise occurs when mixing the incoming vortices and wakes. The pressure rise achieved from mixing an unsteady non-uniform flow is related to the axial non-uniformity in the flow :

$$\Pi_m(A) = 2 \iint_A (\overline{u^2} - u_D) dA$$

$$\Delta\Pi_m(A) = 4 \iint_A u\overline{\Delta u} dA + 2 \iint_A \overline{\Delta u^2} dA$$

$$(I.34)$$

Unlike mixing loss, mixing pressure rise does not have an unstationary component. The net static pressure rise is obtained by adding the pressure rise in the stator passage (I.33) and the mixing pressure rise above (I.34). When calculating the difference in net static pressure rise, $\Delta\Pi_n$, the kinetic energy terms cancel. This leaves a particularly simple expression for the effect of unsteadiness on the stator pressure recovery coefficient:

$$\begin{aligned}
\Delta\Pi_n(x) &= \int_{x_{LE}}^{x} \int_{-H/2}^{H/2} \left[(\overline{\Delta C_p})_{PS} - (\overline{\Delta C_p})_{SS} \right] dy\,dz \\
&\quad - \frac{2}{R} \int_{x_{LE}}^{x} \int_{-H/2}^{H/2} \left[(\overline{\Delta\omega_z})_{PS} - (\overline{\Delta\omega_z})_{SS} \right] dx\,dz \\
&\quad - \frac{2}{R} \int_{x_I}^{x} \int_{SS}^{PS} \left[(\overline{\Delta\omega_y})_L - (\overline{\Delta\omega_y})_U \right] dx\,dy
\end{aligned}$$

$$(I.35)$$

Equation (I.35) equates changes in static pressure recovery by the stator to changes in the axial force sustained by the blades. In turn, this force can be related to the blade loading and boundary layer characteristics.

I.5. Reynolds-Averaged Form of the Mechanistic Relationships.

The foregoing relationships are technically valid for both laminar and turbulent unsteady flows. From a computational standpoint however, we lack the resources to resolve turbulent flow dissipative phenomena in a direct manner. This limits the utility of the passage loss equation derived in §I.2.

This difficulty can be overcome by assuming that the Reynolds-averaged form of the Navier-Stokes equations (C.01) accounts correctly for dissipative phenomena taking place at turbulent microscales. Integrating these equations over the control volume in a manner identical to that of §I.1 yields the following expression for the mass-averaged total pressure flux:

$$\oint\!\!\!\oint_{\delta V}(\mathbf{u}C_t)\cdot\mathbf{dn} = -\int\!\!\int\!\!\int_V \frac{\partial \mathbf{u}^2}{\partial t}dV + 2\int\!\!\int\!\!\int_V \mathbf{u}\cdot[\nabla(\nu\nabla\mathbf{u})]dV \qquad (I.36)$$

Using the identity:

$$\nabla(\nu\nabla\mathbf{u}) = -\nu\nabla\times\boldsymbol{\omega} + (\nabla\nu\cdot\nabla])\mathbf{u} \qquad (I.37)$$

yields the following expression for the passage loss coefficient:

$$\oint\!\!\!\oint_{\delta V}(\mathbf{u}C_t)\cdot\mathbf{dn} = -\underbrace{\frac{\partial}{\partial t}\int\!\!\int\!\!\int_V \mathbf{u}^2 dV}_{K.E.} +2\underbrace{\oint\!\!\!\oint_{\delta V}\nu(\mathbf{u}\times\boldsymbol{\omega})\cdot\mathbf{dn}}_{F.F.} -2\underbrace{\int\!\!\int\!\!\int_V \nu\omega^2 dV}_{V.D.} \qquad (I.38)$$

Equation (I.38) is thus the Reynolds-averaged equivalent of (I.17) for turbulent flow. Like in (I.17) the term marked "FF" is negligibly small. Neglecting this term yields an expression for Reynold-averaged loss that is basically identical to (I.18) except for the presence of dimensionless eddy viscosity:

$$\mathcal{Y}_p = -2\int\!\!\int\!\!\int \nu\overline{\omega^2}dV \qquad (I.39)$$

Equation (I.39) is useful in relating the changes in passage loss due to unsteadiness to the disturbance vorticity and eddy viscosity fields:

$$\Delta\mathcal{Y}_p = -4\int\!\!\int\!\!\int \nu_s\boldsymbol{\omega}_s\cdot\overline{\Delta\omega}dV - 2\int\!\!\int\!\!\int \nu_s\overline{(\Delta\omega)^2}dV + 2\int\!\!\int\!\!\int \overline{\Delta\nu(\omega_s+\Delta\omega)^2}dV \qquad (I.40)$$

The first two terms of (I.40) are equivalent to (I.20). They represent the additional dissipative work associated with a vortical disturbance in an underlying vortical field, and the effect of friction within the disturbance itself. The third term represents the effect of the change in turbulent eddy viscosity due to the presence of flow fluctuations. According to the mixing length hypothesis, underlying the turbulence model here, these changes in eddy viscosity are proportional to changes in vorticity:

$$\overline{\Delta\nu} \approx l^2\frac{\boldsymbol{\omega}_s\cdot\overline{\Delta\omega}}{|\boldsymbol{\omega}_s|} \qquad (I.41)$$

Substituting (I.41) into (I.40) yields the following expression for the change in passage loss:

$$\Delta\mathcal{Y}_p \approx -6\int\!\!\int\!\!\int \nu_s\boldsymbol{\omega}_s\cdot\overline{\Delta\omega}dV - 6\int\!\!\int\!\!\int \nu_s\overline{(\Delta\omega)^2}dV - 2\int\!\!\int\!\!\int \overline{\Delta\nu\Delta\omega^2}dV \qquad (I.42)$$

It is instructive to compare (I.42) and (I.20). The leading terms of these equations differ by the coefficient in front of the integral (4 vs. 6). This difference indicates that, in turbulent flow, a vortical disturbance aligned with the mean vorticity shall produce a loss increment that is 50 percent larger than the loss increment that would be created in a laminar flow with the same level of diffusivity. In turbulent flow, the loss effects of vortical disturbances are therefore "amplified".

I.6. Application of the Loss Equation to Three-Dimensional Flow.

It is useful to describe the vortical structure in the flow using the flow-based coordinate system shown in **Figure I.3**. In this system, the vorticity is decomposed in two components: streamwise (in the direction of velocity) and normal (the remainder) in the manner shown in Equation (I.43).
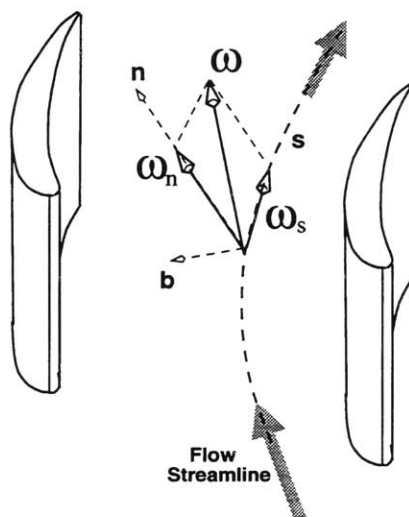
Figure I.3. Coordinate system tied to the decomposition of vorticity into a streamwise and normal components. A binormal direction is also defined, perpendicular to the plane formed by vorticity and velocity. Near the suction surface for instance, the normal direction is spanwise, and the binormal direction is perpendicular to the suction surface of the blade. Note that the vortical normal and binormal directions defined in this manner are not the same as the kinematic normal and binormal directions, which are based on acceleration components.

$$\mathbf{s} = \frac{\mathbf{u}}{|\mathbf{u}|}$$

$$\boldsymbol{\omega}_s = (\mathbf{s} \cdot \boldsymbol{\omega})\mathbf{s} \qquad\qquad (I.43)$$

$$\boldsymbol{\omega}_n = (\mathbf{s} \times \boldsymbol{\omega}) \times \mathbf{s} = \boldsymbol{\omega} - \boldsymbol{\omega}_s$$

The decomposition (I.43) applies to both steady and unsteady flow. Streamwise vorticity in turbomachinery is usually associated with secondary flows. Normal vorticity is primarily present in the blade and endwall boundary layers, as well as in wakes. Inserting (I.43) in (I.39) yields an expression that allows one to assess the relative contribution of streamwise and normal vorticities to passage loss:

$$\mathcal{Y}_p = -2 \iiint \nu \overline{\omega_n \cdot \omega_n} dV - 2 \iiint \nu \overline{\omega_s \cdot \omega_s} dV \qquad (I.44)$$

Streamwise vorticity may be introduced in the flow though several mechanisms, such as turning of boundary layer vortex filaments, leakage flows, baroclinic torque or turbulence. Disturbance streamwise vorticity is defined as the difference in streamwise vorticity between the unsteady and steady flowfields. Inserting this definition into (I.43) yields:

$$\Delta \omega_s = \underbrace{\Delta \omega \cdot \mathbf{s}_s}_{I} + \underbrace{\omega_s \cdot \Delta \mathbf{s}}_{II} + \underbrace{\Delta \omega \cdot \Delta \mathbf{s}}_{III} \qquad (I.45)$$

This equation indicates that unsteadiness can introduce streamwise vorticity in the flow in two manners. The first is associated with fluctuations of the vorticity vector (term I in I.45). The second is associated with instantaneous changes in the flow direction (term II in I.45, term III is a combination of terms I and II). The relative contribution of disturbance streamwise vorticity to the change in loss associated with unsteady flow can be determined by splitting (I.42) along streamwise and normal disturbance components:

$$\Delta \mathcal{Y}_p \approx -\iiint 6\nu_s \left[\omega_{n,s} \cdot \overline{\Delta \omega_n} + \overline{(\Delta \omega_n)^2} \right] dV - \iiint 6\nu_s \left[\omega_{s,s} \cdot \overline{\Delta \omega_s} + \overline{(\Delta \omega_s)^2} \right] dV \quad (I.46)$$

This equation has two interesting implications as far as changes in time-averaged loss are concerned. First, any vortical disturbance in the flowfield is the source of additional loss. Second, vortical disturbances with a non-zero time average, that occur in regions of steady vortical flow where the base vorticity is in the same direction, can be a primary source of additional loss (in particular when $|\Delta \omega| \leq \|bo_s\|$). For instance, spanwise vortical disturbances in the blade boundary layer (which contains primarily spanwise vorticity) are more important than streamwise vortical disturbances in the same location.

I.7. Changes in Total Pressure.

Local changes in total pressure due to unsteady flow can be directly related to changes in the normal and streamwise vorticity fields. To accomplish this, the form (I.12) of the

Navier-Stokes equations is projected in the binormal direction of the flow coordinate system defined in **Figure I.3**. After time-averaging of the periodic flow, this operation yields:

$$\frac{\partial \overline{C_t}}{\partial b} = 2\overline{u\omega_n} - 2R \left(\frac{\partial \overline{\omega_n}}{\partial s} - \frac{\partial \overline{\omega_s}}{\partial n} \right) \qquad (I.47)$$

Provided the steady-flow $(\mathbf{s}, \mathbf{n}, \mathbf{b})$ coordinate system is used to decompose both the steady and unsteady vorticity vectors, an application of the Δ operator to (I.47) yields:

$$\frac{\partial \overline{\Delta C_t}}{\partial b} = 2\overline{\Delta u_{tot}\omega_{n,s}} + 2\overline{u_{tot,s}\Delta\omega_n} + 2\overline{\Delta u_{tot}\Delta\omega_n} - 2R \left(\frac{\partial \overline{\Delta\omega_n}}{\partial s} - \frac{\partial \overline{\Delta\omega_s}}{\partial n} \right) \qquad (I.48)$$

Equation (I.48) is quite useful for describing local changes in the time-averaged total pressure as a consequence of redistribution of vorticity. In the case of wake and tip vortex interaction, the following simplified form of (I.48) can describe these local changes fully:

$$\frac{\partial \overline{\Delta C_t}}{\partial b} \approx +2\overline{u_{tot,s}\Delta\omega_n} \qquad (I.49)$$

Equation (I.49) postulates that changes in time-averaged total pressure due to unsteadiness are due to the redistribution of normal vortical filaments on a time-averaged basis. In the computed solution, such changes are localized near the blade surface. As noted in **Figure I.3**, the normal vorticity there is in the spanwise direction, and the term $\frac{\partial \overline{\Delta C_t}}{\partial b}$ represents variation in the direction normal to the blade surface.

Appendix J

Modeling the Effects of Upstream Wakes and Tip Vortices

This appendix derives simplified models for the performance impact of reversible recovery and non-transitional boundary layer response. The appendix is divided into five sections.

- Section **J.1** presents a method for determining upstream wake and vortex parameters as a function of compressor design. These parameters serve as an input for the models.

- Section **J.2** derives a model for the recovery of the energy of a two-dimensional disturbance jet, such as that associated with an upstream wake.

- Section **J.3** derives a model for the additional loss associated with boundary layer distortion under the effect of the two-dimensional disturbance jet.

- Section **J.4** extends the models to tip vortex interaction, on the basis of similarity with the two-dimensional wake interaction considered in §**J.2-J.3**.

- Section **J.5** presents a summary of the models and of their application.

J.1. Input parameters.

The models are applied in the geometrical context of a repeating-stage, multistage compressor illustrated in **Figure 7.1 (Chapter 7)**. While not all stages in a typical core compressor are identical, this assumption is usually representative for the effect of nearby stages and reduces the number of design variables considered. Since the effects of both upstream wakes and tip leakage vortices can be expressed in the same two-dimensional terms, the stage design is also described in mostly 2D terms. In particular, the design parameters considered

are midspan flow coefficient (ϕ), pressure coefficient (ψ), reaction ($\mathcal{R}$), solidity (σ), blading chord (c), tip clearance (τ), and axial gap (d).

J.1.1. Flow and disturbance angles. The relative flow angles at design are determined by the choice of stage reaction, flow and pressure coefficients:

$$\tan\theta_{1,R} = \frac{1}{\phi}\left(\mathcal{R} + \frac{\psi}{2}\right) \qquad \tan\theta_{1,S} = \frac{1}{\phi}\left(1 - \mathcal{R} + \frac{\psi}{2}\right)$$

$$\tan\theta_{2,R} = \frac{1}{\phi}\left(\mathcal{R} - \frac{\psi}{2}\right) \qquad \tan\theta_{2,S} = \frac{1}{\phi}\left(1 - \mathcal{R} - \frac{\psi}{2}\right) \tag{J.01}$$

The ingestion and discharge angles of vortical disturbances from the upstream blade row in the relative reference frame of the downstream blade row, are obtained based on assuming that these disturbances are simply convected by the core flow:

$$\tan\gamma_{1,S} = \frac{\phi}{\mathcal{R} - 0.5\psi} \qquad \tan\gamma_{1,R} = \frac{\phi}{1 - \mathcal{R} - 0.5\psi}$$

$$\tan\gamma_{2,S} = \frac{\xi_S}{1 - \xi_S \tan\theta_{2,S}} \qquad \tan\gamma_{2,R} = \frac{\xi_R}{1 - \xi_R \tan\theta_{2,R}} \tag{J.02}$$

where (ξ_R, ξ_S) are rather complex functions of cascade angles and solidity derived in §**J.2.2**. It is to be noted that the subscripts $()_R$ and $()_S$ refer to the rotor and stator respectively. The latter subscript should not be confused with $()_s$, which refers to the steady (base) flow in absence of disturbances. Unsubscripted variables apply generically to both fixed and rotating blade rows in the relative frame.

J.1.2. Steady-state loss levels. For each blade row, the steady loss coefficients are estimated using the following expression :

$$\mathcal{Y}_{p,s} = 2\frac{\theta_w}{c}\frac{\sigma}{\cos\theta_2}\left(1 - \frac{\cos\theta_1}{\cos\theta_2}\right)^2 \tag{J.03}$$

which holds for a wide range of blade profiles (NACA-65, C4) in attached subsonic flows at practical Reynolds numbers (Cumpsty, 1989). For diffusion factors (DF) within design limits, steady loss is a weak function of DF, and depends primarily on solidity.

J.1.3. Wake properties. The wake properties used in **Chapter 3** are obtained based on experimental data discussed in the text. The wake properties used in the design study of **Chapter 7** are obtained in the following manner. First, the wake integral momentum thickness in the relative frame is computed from the following least-squares fit of data for NACA-65 and C4 blades at minimum incidence (Cumpsty, 1989):

$$\frac{\theta_w}{c} = 0.006 + 0.032 \mathrm{DF}^2 \qquad (\mathrm{DF} < 0.6) \tag{J.04}$$

where DF is the section diffusion factor (e.g. Cumpsty, 1989)

$$\mathrm{DF} = \left[1 - \frac{\cos\theta_1}{\cos\theta_2}\right] + \frac{\cos\theta_1}{2\sigma}(\tan\theta_1 - \tan\theta_2) \tag{J.05}$$

The following correlation, obtained by Stauter et al. (1991) in a research compressor, is used to estimate the rate of wake decay in the interblade gap.

$$A_r = 0.52\exp\left(-2.295\frac{d}{c}\right); \qquad 0.03 < \frac{d}{c} < 0.5 \tag{J.06}$$

For the purposes of modeling, the wake disturbance in the relative frame of the downstream blade row is approximated by a linear velocity profile "jet" characterized by a peak disturbance velocity "A_j" and a geometrical thickness "t_w". These are readily related to the wake parameters in the upstream relative frame:

$$t_w = \theta_w \left[\frac{A_r}{4}\left(1 - \frac{A_r}{4}\right)\right]^{-1}; \qquad A_j = A_r \;/\; \cos\theta_{2,upstream} \tag{J.07}$$

J.1.4. Tip vortex properties. The tip vortex properties used in **Chapters 4-6** are obtained based on Khalid's (1995) computational study of tip leakage flow for the GE/LSRC rotor. Unlike for the above wakes, there are no correlations that allow to estimate the tip vortex properties in detail for different designs. For the purposes of **Chapter 7**, the velocity field of the tip leakage vortex of the LSRC computational study ($\tau = 0.03, \psi = 0.64$), is scaled using the following relationship proposed by Khalid (1995) for the vortex blockage at the exit of the blade row:

$$\frac{A_b \cos\beta_e}{\tau s / \sin\beta_m} = \mathcal{G}\left(\frac{\overline{\Delta P}^a - \overline{\Delta P_t}^a}{Q_{2\tau}}\right) \tag{J.08}$$

where $\mathcal{G}$ is a quadratic fit of Khalid's (1995) computational experiments. Khalid's (1995) work also suggests a wake representation of the overtip leakage flow can capture the trends in clearance-related blockage. For this reason, it has been assumed that the interblade decay of the TL vortex follows the same relationship as that of a wake (J.06). While crude, this treatment captures to some extent the effect of design point selection on the strength of the tip leakage vortex.

J.2. Recovery of a 2D upstream wake jet.

The recovery model is build by (1) deriving an expression for the mixing loss of an idealized 2D wake disturbance jet, (2) determining the change in wake length and thickness due to transport through the stator, and (3) determining the extent to which these changes reduce the mixing loss relative to that at the inlet. The velocity defect in the wake is considered constant in time.

The model makes a number of assumptions that are justified given the vorticity dynamics observed in the wake interaction simulations of §3.1. The assumptions are as follows: (1) incompressible inviscid flow, (2) wake thickness small compared to the blade chord so that wakes can be represented as a straight thin segment of vortical flow convected by the mean flow in the passage, (3) the vortical flow inside the jet can be approximated by two layers of uniform, opposite-sign vorticity, and (4) at the inlet of ther stator, there is one rotor wake per stator passage. The simplified flow situation is shown in **Figure J.1**. The last assumption corresponds to a 1:1 rotor/stator blade count ratio. Assuming that the individual wakes do not interact with each other, the results from the model can be extended to other blade counts by multiplication by N_R/N_S.
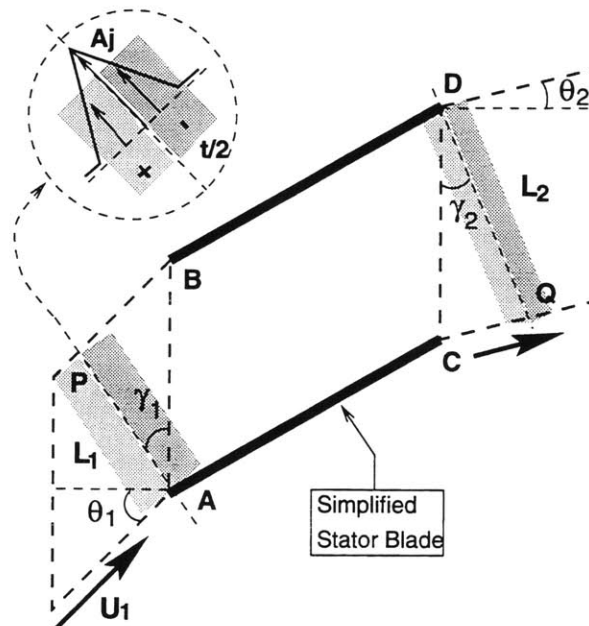
Figure J.1. Simplified model of wake transport through the stator passage. The wake is represented as two sheets of uniform, opposite-sign vorticity. A linear disturbance velocity distribution is associated with this vorticity field (inset). The wake is intercepted at point "A" and time $t_0=0$; it is fully ingested at point "B" and time t_1; it starts leaving the stator at point "C" and time t_2 and is fully discharged at point "D" and time t_3.

J.2.1. Mixing loss of the disturbance jet.

The purpose of this section is to establish an expression for the total pressure loss that would result if the simplified wake jet of **Figure J.1** is mixed out to uniform state. The point of departure is a form of (I.32) that is reduced to a two-dimensional form, and from which the static pressure disturbance is eliminated on the basis that such wakes do not carry a static pressure difference. Given the periodicity of the flow, it is possible to replace time-averaging with spatial integration executed in an (x, y) frame locked to the moving jet. In this frame, the velocity disturbance associated with the jet is steady in time, which yields the follwing expression for the jet mixing loss:

$$S\Delta Y_m(x) \approx -\iint_S \overline{(1 + \Delta u)(\Delta u^2 + \Delta v^2)}dy + \frac{1}{S}\overline{\left\{\iint_S (1 + \Delta u)\Delta v dy\right\}}^2 \qquad (J.09)$$

The velocity disturbance can be described by means of a wake profile shape function, $f(s)$, scaled by the jet velocity excess, A_j, and by the jet thickness, t_w:

$$\Delta u = A_j \sin\gamma \left[m_1 - f(\frac{y\sin\gamma}{t_w})\right]$$

$$\Delta v = A_j \cos\gamma f(\frac{y\sin\gamma}{t_w}) + C \qquad (J.10)$$

Given assumptions (2) and (3) above, the profile function here is piecewise linear:

$$f(s) = (1 - 2|s|)\mathcal{H}(1 - 2|s|)\text{sign}(s) \qquad (J.11)$$

It is to be noted that the axial disturbance velocity component in (J.10) is constructed with a constant bias, in order to satisfy global continuity :

$$\int_0^S \Delta u dy \equiv 0 \qquad (J.12)$$

When condition (J.12) is met, the potential flow bias C in the tangential velocity disturbance (J.10) has no effect on the mixing loss. Therefore, it shall be dropped throughout the rest of this appendix. The parameter m_1 in appearing in (J.10) is the jet displacement thickness, and is the first of a generalized series of profile moments m_n:

$$m_n = \frac{1}{S}\int_0^S f(y)dy = \frac{t_w}{S(n + 1)\sin\gamma} \qquad (J.13)$$

Substituting (J.10) into (J.09) yields, after considerable algebra, the following expression of the mixing loss of the jet as a function of its peak velocity excess A_j, its thickness t_w, and its inclination γ.

$$\frac{\Delta Y_m(x)}{S} = (m_1^2 - m_2)A_j^2 + \sin\gamma(2m_1^3 + r^3 - 3m_1m_2)A_j^3 + \sin^2\gamma\cos^2\gamma(m_1^2 - m_2)^2 A_j^4 \quad (J.14)$$

Equation (J.14) provides a good approximation (within 5-10%) of the numerically integrated mixing loss of the Gaussian profile wake used for the CFD results, thereby indicating that assumption (3) above is justified. It is tempting to eliminate high-order terms from (J.14). However, careful consideration of the high-order term effects leads to the conclusion that second or third-order approximations to (J.14) may be as much as 100% in error for realistic combinations of (A_j, t_w, γ).

J.2.2. Geometry of the jet at the exit of a blade row.

To determine the amount by which the mixing loss of the jet is reduced, it is necessary to estimate the jet parameters $(A_{j,2}, t_{w,2}, \gamma_2)$ at the exit of the blade row. This is done by estimating the transit times $t_{1..3}$ at which the endpoints of the jet enter and leave the blade row, and using the property of vortex lines to travel with the fluid to predict the amount of stretching of the jet.

The transit times are estimated using the geometry of **Figure J.1**, and assuming uniform flow. At time $t_0 = 0$ a wake is intercepted by the leading edge. Because the wake is inclined with respect to the vertical, it will not be cut into a wake segment until time t_1, given by:

$$t_1 \approx \mathrm{PB}\cos\theta_1 \quad (J.15)$$

The suction-side leg of the wake starts leaving the stator passage at a time t_2 given by :

$$t_2 \approx \int_0^c \left\{ U_m + \frac{\Gamma}{2c} \right\}^{-1} dx \quad (J.16)$$

The term "U_m" in (J.16) is the mean dimensionless velocity for a flow without circulation, whereas the term $\Gamma/2c$ represents the acceleration of the flow over the suction surface due to circulation. The pressure side leg of the wake starts leaving the stator passage at a time t_3 given by :

$$t_3 \approx \int_0^c \left\{ U_m - \frac{\Gamma}{2c} \right\}^{-1} dx + t_1 \quad (J.17)$$

After this point in time, the wake is convected by the uniform flow leaving the blade, and no further changes in inclination γ take place. Therefore, the length and orientation of the wake segment leaving the blade can be determined as a function of the difference, Δt, between the times at which the pressure side and the suction side legs of the wake are discharged from the stator.

$$\Delta t = t_3 - t_2 \approx t_1 + \int_0^c \left\{ U_m - \frac{\Gamma}{2c} \right\}^{-1} dx - \int_0^c \left\{ U_m + \frac{\Gamma}{2c} \right\}^{-1} dx \qquad (J.18)$$

Equation (J.18) can be reduced to a closed form by assuming that U_m is constant in the axial direction and equal to the algebraic mean of the inlet and exit velocities.

$$U_m^2 = 1 + \frac{\tan^2 \theta_1 + \tan^2 \theta_2}{2} \qquad (J.19)$$

The dimensionless circulation about the blade can be determined in a simple manner, by considering that the flow within the contour $ABCD$ is irrotational. This yields:

$$\Gamma = S(\tan \theta_1 - \tan \theta_2) \qquad (J.20)$$

It is also convenient to express the dimensionless distance PB in (J.15) in terms of flow and wake inlet angles, using simple trigonometry. In this manner, a closed-form expression for the discharge time difference is obtained:

$$\Delta t = \frac{S}{\cot \gamma_1 + \tan \theta_1} + \frac{\Gamma}{U_m^2 + \Gamma^2/4c^2} \qquad (J.21)$$

Equation (J.21) allows one to estimate the distance already traveled by the suction side leg upon full discharge of the wake from the stator blade row

$$QC = \frac{\Delta t}{\cos \theta_2} \qquad (J.22)$$

This result allows to "close" the triangle CDQ in **Figure J.1**, and thereby determine the inclination γ_2 and the length DQ of the wake segment leaving the blade row:

$$\tan \gamma_2 = \frac{\xi}{1 - \xi \tan \theta_2} \qquad (J.23)$$

$$DQ = AP(\cos \gamma_1 + \tan \theta_1 \sin \gamma_1)\sqrt{\xi^2 + (1 - \xi \tan \theta_2)^2} \qquad (J.24)$$

The factor ξ appearing in the above depends on the discharge time difference and on the interblade spacing, S:

$$\xi = \frac{\Delta t}{S} = \frac{\sin \gamma_1 \cos \theta_1}{\cos \theta_1 - \gamma_1} + \frac{\Gamma/S}{U_m^2 + \Gamma^2/4c^2} \qquad (J.25)$$

Knowing the percentage elongation of the jet allows one to determine the jet velocity excess $A_{j,2}$ and thickness $t_{w,2}$ at the exit of the blade row. Under the inviscid 2D flow assumption, the vorticity of a particular fluid element, and the circulation around a contour traveling with the fluid remain constant. The circulation about one of the vortical layers comprising the wake can be related to A_j in the following manner:

$$\Gamma_W = \oint_W \mathbf{u} \cdot \mathbf{dl} = LA_j = \text{Constant} \qquad (J.26)$$

Equation (H.26) states that the attenuation of the jet velocity due to passing the jet through the blade row is proportional to the stretching of the jet:

$$a_r = \frac{A_{j,2}}{A_{j,1}} = \frac{AP}{DQ} = (\cos \gamma_1 + \tan \theta_1 \sin \gamma_1)\sqrt{\xi^2 + (1 - \xi \tan \theta_2)^2} \qquad (J.27)$$

Since circulation and vorticity are related,

$$\Gamma_W = \iint_W \omega dx dy = \frac{t_w L \omega}{2} = \text{Constant} \qquad (J.28)$$

Equation (J.28) states that the jet thickness also decreases in proportion to the stretching:

$$\frac{t_{w,2}}{t_{w,1}} = a_r \qquad (J.29)$$

For the stator under consideration (26 degrees flow turning) the model predicts an attenuation factor of 1.8^{-1}. This agrees well with the roughly two-fold attenuation seen in the CFD results (**Figure 3.10**). The model also predicts well the geometry parameters of the wake at the exit of the stator, as shown in **Table J.1**

Parameter	Simulation	Kinematic model
Wake inlet inclination, $\gamma_{1,s}$	40.3°	40.7°
Wake exit inclination, $\gamma_{2,s}$	56.0°	52.0°
Exit/Inlet length ratio, L_2/L_1	1.6-1.7	1.8

Table J.1. The present kinematic model compared to the Navier-Stokes simulation for baseline wakes in §3.1.

It is to be noted that Equation (J.27) has been derived assuming a positive inclination of the wake at the inlet. As evidenced by the results on **Figure 7.1**, this is usually the case for wakes coming from the blade row that is directly upstream. On the other hand, wakes originating from the next-to-immediate blade row upstream may have a negative inclination relative to the blade row under consideration. By means of an approach similar to the above, one may demonstrate that (J.27) is valid for both positive and negative wake inclinations, provided that the factor ξ is calculated in the following manner :

$$\xi = \text{sign}(\gamma_1) \left\{ \frac{\sin \gamma_1 \cos \theta_1}{\cos \theta_1 - \gamma_1} + \frac{2\sigma^2(\tan \theta_1 - \tan \theta_2)}{2\sigma^2 + (0.5 + \sigma^2)(\tan^2 \theta_1 + \tan^2 \theta_2) - \tan \theta_1 \tan \theta_2} \right\} \quad (J.30)$$

Equation (J.30) differs from (J.25) by the factor $\text{sign}(\gamma_1)$ which accounts for the fact that the wake inclination at the inlet may be negative. It is to be noted that the expression for the circulation (J.20) is incorporated in (J.30) explicitly.

J.2.3. Model for ideal mixing loss benefit.

When computing the time-averaged mixing loss at the exit of the blade row $\Delta Y_{m,2}$, one has to consider that the length of the wake segments has increased with respect to that at the inlet. Therefore, the loss benefit $\Delta \mathcal{Y}_m$, from passing the wakes through the blade row has to be computed according to:

$$\Delta \mathcal{Y}_m = \Delta Y_{m,1} - a_r^{-1} \Delta Y_{m,2} \quad (J.31)$$

The jet mixing loss coefficient at the inlet, $\Delta Y_{1,m}$ is calculated by inserting the values of $(A_j, t_w, \gamma)_1$ obtained from §J.1, into (J.14). Likewise, $\Delta Y_{2,m}$ at the exit is calculated by inserting the values of $(A_j, t_w, \gamma)_2$ obtained from §J.2.2 into (J.14). The full expression for $\Delta \mathcal{Y}_m$ obtained in this manner is suitable for numerical implementation, but not very insightful. On the other hand, one might note from (J.14) that:

$$\Delta Y_{m,2} \approx a_r^3 \Delta Y_{m,1} \quad (J.32)$$

which leads to the conclusion that the benefit from passing the wake jet is proportional to the energy present in the incoming wake, and quadratically proportional to the attenuation:

$$\Delta \mathcal{Y}_m \approx (1 - a_r^2) \Delta Y_{m,1} \quad (J.33)$$

This result is in agreement with derivations carried out by Adamczyk (1994). As shown in **Figure 3.8**, the predictions from this simplified model agree with the computed benefit

from the Navier-Stokes simulations over the range of wake defects considered. The parameters which determine the degree of attenuation a_r can be determined if one carries out a thought experiment in which the flow angles and wake inlet inclination angle are made independent (instead of being inter-related as per §J.1.1). In this context, the attenuation depends primarily on the flow turning in the blade row. As shown in **Figure J.2**, there is an approximately linear relationship between $\theta_1 - \theta_2$ and a_r, that holds over a wide range of the remaining parameters.
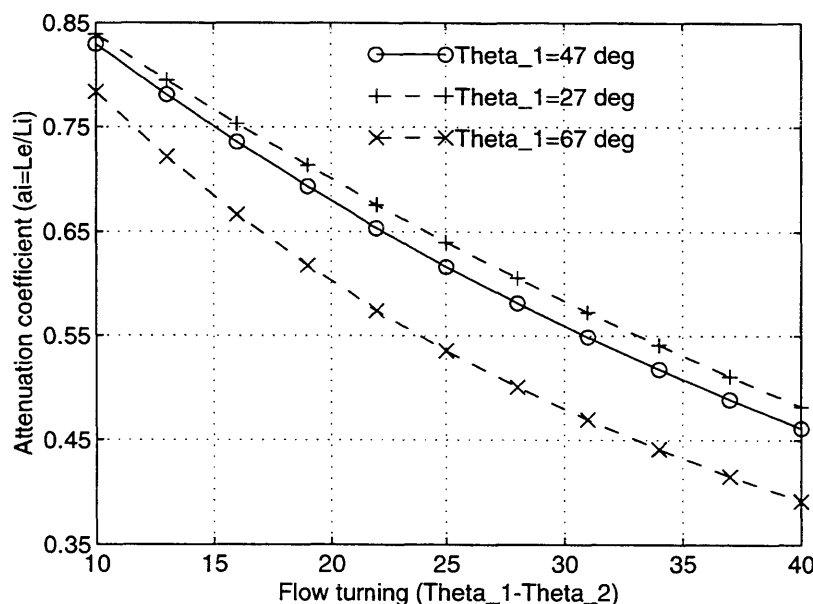

Figure J.2. Velocity attenuation $a_r = L_1/L_2$ of an upstream wake versus flow turning for different inlet angles. Cascade solidity 1.6, wake ingestion angle 43.4°. The curves do not collapse so closely when plotted in terms of diffusion factor or circulation.

The relationship between wake ingestion angle γ_1 and attenuation is more complex. As shown in **Figure J.3**, there is an optimum range of wake ingestion angles, providing high attenuation. This range is quite wide ($40° < \gamma_1 < 80°$ for the cascade considered). Strong attenuation is desirable for closely-spaced blade rows, because it can reduce the entropy rise from wake mixing at an early stage.

Figure J.3 also shows that some ingestion angles result in wake amplification rather than attenuation. This is detrimental for performance, because energy is "extracted" from the flow in order to increase a wake non-uniformity that may be eventually mixed out. **Figure 7.1** shows that this occurs when the wake is aligned with the flow direction at the blade row entrance. Such an orientation is impossible for the wake from the blade row directly upstream. However, wakes from two blade rows upstream may be ingested in this manner for certain compressor designs. This matter is given further consideration in §J.5.
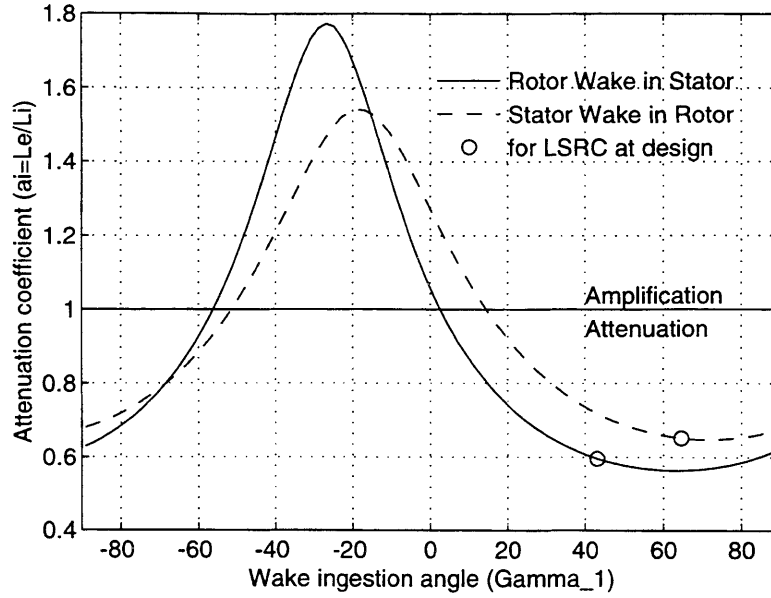
Figure J.3. Velocity Attenuation $a_r = L_1/L_2$ of an upstream wake in a typical stator (solid line) and in rotor (dashed line) across the full range of wake ingestion angles. Not all of those angles actually occur in practice. Cascade parameters: $\theta_{1R} = 59.5°, \theta_{2R} = 44.4°, \sigma_R = 1.25, \theta_{1S} = 47.6°, \theta_{2S} = 21.0°, \sigma_S = 1.66$. Circles show wake ingestion angles by the LSRC stator at design point ($\phi = 0.445, \psi = 0.64, \mathcal{R} = 63\%$). Values of $a_r < 1$ indicate reversible attenuation, and correspond to a loss benefit from processing.

J.2.4. Model for the leading edge pressure pulse.

This section proposes a simplified model for estimating the magnitude of the high-pressure pulse appearing on the leading edge pressure side at the moment of wake interception (cf. §3.1). The model assumes that the high-pressure region is the result from bringing the wake jet to a stagnation point at the surface.

The peak pressure, $(\Delta C_p)^+$, is computed in a quasi-steady manner, i.e. by using the steady form of the Bernoulli's equation along a streamline associated with the jet. Let $()_o$ and $()_f$ denote the stagnation and free-stream ends of the streamline respectively. The velocity vector at the $()_o$ end is $\mathbf{u}_o = u_s\mathbf{i} + v_s\mathbf{j}$ (only the disturbance jet is brought to rest, not the base flow itself). The velocity vector at the $()_f$ end is $\mathbf{u}_f = u_s\mathbf{i} + (v_s + A_j)\mathbf{j}$. The peak pressure pulse is approximated by the difference in static pressure between these two points on the same streamline. In quasi-steady-terms, this yields:

$$(\Delta C_p)^+ \approx 2(p_o - p_f)\rho U^2 \approx (u_s\mathbf{i} + (v_s + A_j)\mathbf{j})^2 - (u_s\mathbf{i} + v_s\mathbf{j})^2$$

$$(J.34)$$

$$\approx 2v_s A_j + A_j^2$$

This estimate of $(\Delta C_p)^+$ does not include the time-dependent term of the unsteady Bernoulli equation. However, the good agreement between (J.34) and the CFD results in **Figure 3.2**, suggests that this term is not important for the flow under consideration.

J.3. Boundary layer response to a 2D upstream wake jet.

The points of departure for calculating the increase in passage loss $\Delta \mathcal{Y}_p$, due to boundary layer distortion by the wake jet, are (1) a linearized two-dimensional form of the mechanistic relationship between total pressure loss and vorticity (2.07)/(I.42):

$$\Delta \mathcal{Y}_p \approx -6 \int\int \nu_s \omega_s \overline{\Delta \omega} dx dy \qquad (J.35)$$

and (2) a two-dimensional linearized inviscid form of the equation governing the disturbance vorticity in the flow (F.13):

$$\frac{\partial \Delta \omega}{\partial t} + (\mathbf{u}_s \cdot \nabla)\Delta \omega = -(\Delta \mathbf{u} \cdot \nabla)\omega_s \qquad (J.36)$$

The use of the linearized form (J.35) is based on the observation that $\Delta \omega < \omega$ in the disturbed boundary layer region contributing to increased loss in the CFD solution. The inviscid form (J.36) of the vorticity equation is used because the computational experiments discussed at the end of §3.1 indicate that viscous terms are not a significant factor in the response of the boundary layer to the jet (it is to be noted that the base flow is viscous and rotational though, thus $\omega_s \neq 0$). The vorticity equation (J.36) is also linearized, since computations with linearized slip-free disturbance flow about a viscous base flow yield boundary layer vortical disturbances similar to those from the full Navier-Stokes simulations. In summary, the simplifications behind (J.36) ensure that the only source of disturbance vorticity is the distortion of base flow boundary layer vortex filaments by the velocity field of the jet.

In addition, these equations are applied to a simplified representation of the suction side boundary layer, shown in **Figure J.4**, that makes the problem of calculating $\Delta \mathcal{Y}_p$ mathematically tractable. This representation neglects the curvature of the surface, and assumes a thin boundary layer in which the streamwise variation of base and disturbance flow quantities occurs on a much longer scale than the one associated with transverse variation. Removal of high-order terms from (J.36) in virtue of the latter assumption, yields the following equation for the disturbance vorticity:

$$\underbrace{\frac{\partial \Delta \omega}{\partial t} + U\frac{\partial \Delta \omega}{\partial x} + V\frac{\partial \Delta \omega}{\partial y}}_{\text{transport}} \approx - \underbrace{\Delta v \frac{\partial \Omega}{\partial y}}_{\text{production}} \qquad (J.37)$$

Equation (J.37) embodies the balance between production (right-hand side) and convective transport (left-hand side) of disturbance vorticity. It is to be noted that capital letters have been used to denote the steady base flow velocity components (U, V) and vorticity Ω in the context of the simplified geometry in **Figure J.4**. Examination of (J.37) reveals that disturbance vorticity is produced in regions of high base flow vorticity gradient. For law-of-the wall profiles, "$\frac{\partial \Omega}{\partial y}$" is positive and takes its largest value where the boundary layer is thinnest (leading edge), and at the "knee" of the velocity profile (near the edge of the boundary layer). This explains why the boundary layer vortical disturbances described in §3.1 and in §5.1.2 appear to be produced at the leading edge upon wake interception. Equation (J.37) also explains why these disturbances contain negative-sign spanwise vorticity (Δv and $d\Omega/dy$ are both positive).
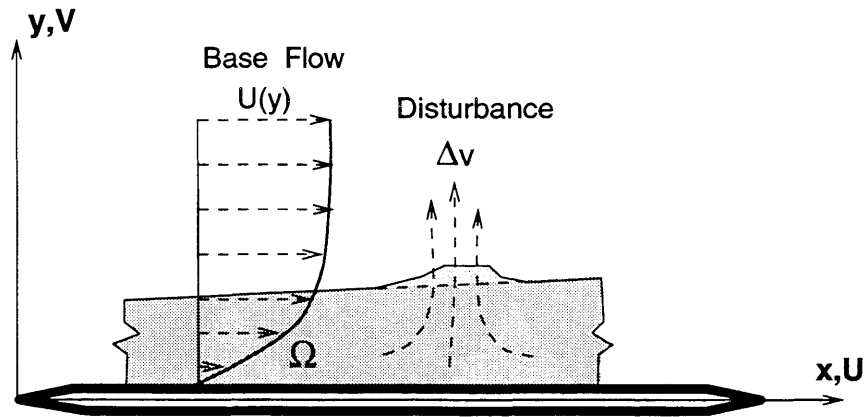

Figure J.4. Simplified representation of boundary layer distortion under the effect of a wake jet. The boundary layer (BL) is approximated by a uniform sheet of spanwise vorticity. The highest vorticity gradients are at the knee of the BL profile. This is in accordance with the law-of-the wall velocity profile.

Although (J.37) is analytically tractable, four further simplifications thereof have been made. First, one may set $V = 0$ while retaining the essence of the mechanism that is being modeled (motion of boundary layer vortex filaments under the effect of Δv). Second, to determine the change in loss due to the wake jet (J.35), only the time-average of $\Delta \omega$ is required and not the time-accurate solution. Since (J.37) is linear, $\overline{\Delta \omega}$ can be obtained by first time-averaging the equation and then solving it. In combination with $V = 0$, time-averaging (J.37) yields the following equation:

$$\frac{d\overline{\Delta \omega}}{dx} \approx -\frac{\overline{\Delta v}}{U}\frac{d\Omega}{dy} \qquad (J.38)$$

Despite its appearance (J.38) is a partial differential equation given the relationship be-

tween $\Delta\omega$ and Δv. The third simplification consists in prescribing a simplified profile for Δv. Noting that at the surface $\Delta v=0$, and that at the edge of the boundary layer $\Delta v=v_n(t)$ (where $v_n(t)$ is the velocity imposed by the wake jet), a linear profile is used for Δv:

$$\overline{\Delta v} = \frac{y}{\delta}\Delta V_n \qquad (J.39)$$

where δ is the thickness of the boundary layer; and where ΔV_n is the time-averaged transverse velocity imposed by the wake jet at the edge of the boundary layer:

$$\Delta V_n = \overline{v_n(t)} \approx \frac{A_j t_w \sin\chi}{2S} \qquad (J.40)$$

The resulting differential equation for $\overline{\Delta\omega}$:

$$\frac{d\overline{\Delta\omega}}{dx} \approx -\frac{y\Delta V_n}{\delta U}\frac{d\Omega}{dy} \qquad (J.41)$$

can be solved by assuming a given profile for the steady (base) flow boundary layer. The profile assumed here is linear, and one in which the boundary layer thickness varies as $\sqrt{(x)}$. This yields:

$$\Omega \sim \Omega_{\mathrm{ref}}x^{-\frac{1}{2}} \qquad (J.42)$$

Inserting (J.42) in (J.41) and integrating yields:

$$\overline{\Delta\omega} = -\frac{2y\Delta V_n}{\delta U}x\frac{d\Omega}{dy} + \text{constant} \qquad (J.43)$$

Both sides of $(J.43)$ shall be multiplied by $6\nu_s\Omega$ and integrated over the boundary layer with respect to the normal coordinate y. This yields:

$$6\int_0^\delta \nu\Omega\overline{\Delta\omega}dy \approx -12x\frac{\Delta V_n}{U}\int_0^\delta \nu_s\Omega\frac{d\Omega}{dy}\frac{y}{\delta}dy + \text{constant} \qquad (J.44)$$

In light of (J.35), the LHS of (J.44) can be recognized as the rate of increase of the additional passage loss induced by the wake jet:

$$6\int_0^\delta \nu\Omega\frac{d\overline{\Delta\omega}}{dx}dy = -\frac{d\Delta\mathcal{Y}_p}{dx} \qquad (J.45)$$

After integration by parts, the RHS can be recognized to be proportional to the rate of increase of the steady (base) flow passage loss in the axial direction:

$$-12\frac{\Delta V_n}{U}\int_0^\delta \nu_s\Omega\frac{d\Omega}{dy}\frac{y}{\delta}dy = -6x\frac{\Delta V_n}{U}\frac{d\mathcal{Y}_{p,s}}{dx} \qquad (J.46)$$

Equating (J.45) and (J.46) and integrating with respect to x yields:

$$\Delta\mathcal{Y}_p = 6\frac{\Delta V_n}{U}\int_0^1 x\frac{d\mathcal{Y}_{p,s}}{dx}dx + \text{constant} \qquad (J.47)$$

The integration constant is zero, since $\Delta\mathcal{Y}_p = 0$ when $\Delta V_n = 0$ by definition (no increase in loss in absence in wakes). Equation (J.47) states that the increase in profile loss due to the upstream wake jet/boundary layer interaction depends only on the chordwise distribution of profile losses of the steady flow, and is proportional to the average transverse velocity imposed by the wake jet on the edge of the boundary layer. This is a useful and insightful relationship that is not qualitatively affected by the foregoing assumptions. It can be further simplified by assuming a linear rate of increase of the base flow loss. This yields the following simplified relationship:

$$\Delta\mathcal{Y}_p \approx 2\frac{\Delta V_n}{U}\mathcal{Y}_{p,s} \qquad (J.48)$$

As shown in **Figure 3.7**, equation (J.48) agrees to a reasonable extent with the CFD results for the geometry and operating point considered. In particular, the CFD results also show a proportional relationship between $\Delta\mathcal{Y}_p$ and ΔV_n. However, the material in §6.2 indicates that (J.48) may fail when a different loading distribution is considered. In this case, only the complete equation (J.47) is capable of capturing the trends in the Navier-Stokes simulation.

J.4. Three-dimensional aspects of tip vortex processing.

J.4.1. Transport of a streamwise vortex lines.

The purpose of this section is to quantify the changes in streamwise and blade-to-blade vortex lines as they pass through the stator. An inviscid-flow diffuser analogy, illustrated in **Figure J.5**, is employed for this purpose.

Streamwise vortex filament. The evolution of vorticity in the vortex line at the left side of **Figure J.5** can be represented by the following form of (F.12):

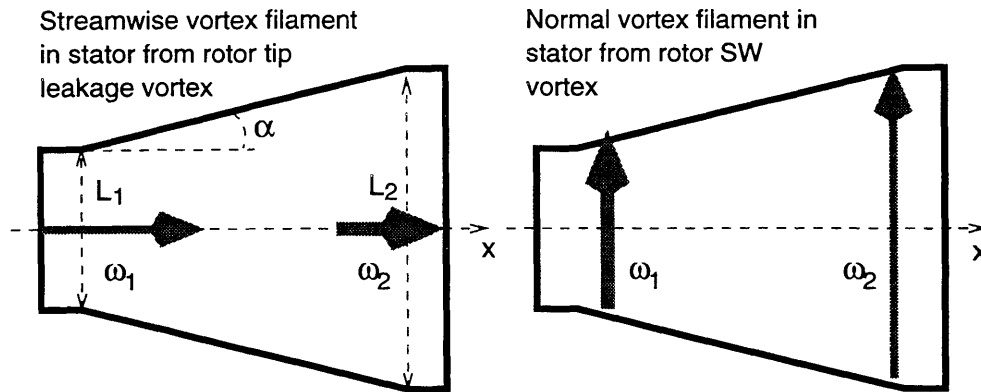$$\frac{D\omega}{dt} = \omega\frac{\partial U}{\partial x} \qquad (J.49)$$

Figure J.5. Diffusor analogy for the transport of vortex filaments through the stator. Left: Streamwise vortex filaments (vorticity decreases). Right: Blade-to-blade vortex filaments (vorticity increases).

Given the geometry of the diffuser:

$$U = U_1 \left[1 + \tan\alpha \frac{x}{L_1} \right]^{-1}$$

$$\tag{J.50}$$

$$\frac{\partial U}{\partial x} = -\frac{\tan\alpha U_1}{L_1} \left[1 + \tan\alpha \frac{x}{L_1} \right]^{-2}$$

Using (J.50) and $t = dx/U$ allows to re-write (J.49) as:

$$\frac{d\omega}{d\dot{x}} = -\frac{\tan\alpha}{L_1} \left[1 + \tan\alpha \frac{x}{L_1} \right]^{-1} \omega$$

$$\tag{J.51}$$

Solving this equation yields:

$$\ln\omega = -\ln\left(1 + \tan\alpha \frac{x}{L_1} \right) + \text{constant}$$

$$\tag{J.52}$$

Which is equivalent to:

$$\frac{\omega_2}{\omega_1} = \frac{L_1}{L_2}$$

$$\tag{J.53}$$

Equation (J.53) indicates that the slowing of the flow in the stator causes the vorticity in an upstream streamwise vortex line to decrease in proportion to the stretching that an upstream wake perpendicular to the incoming flow would undergo. This implies that the

velocity field associated with this vortex filament is also attenuated in the same manner. Therefore, the jet associated with the simplified tip leakage vortex structure shown in **Figure 4.11** is attenuated to the same extent as a 2D wake passing through the same stator. Thus, the fraction of energy recovered from such a vortex and from a 2D wake are the same, and should scale in the same manner.

Blade-to-blade vortex filament. When the vortex filament is perpendicular to the streamlines, as shown at the right of **Figure J.5**, the vorticity is amplified instead. Such vortex filaments are associated with pure streamwise vortices in the upstream rotor frame. In the simplified case here, the vorticity is governed by:

$$\frac{D\omega}{dt} = \omega \frac{\partial V}{\partial y} \tag{J.54}$$

Given the geometry of the diffuser:

$$V = U \tan \alpha \frac{y}{L} \tag{J.55}$$

Using (J.55), (J.50) and $t = dx/U$ allows to solve (J.54) and obtain:

$$\frac{\omega_2}{\omega_1} = \frac{L_2}{L_1} \tag{J.56}$$

In this case, the vorticity is amplified in proportion to the vortex stretching, and the loss associated with mixing of the vortex increases in a quadratic manner. This result is in agreement with remarks by Denton (1993).

J.4.2. Boundary layer response.

Section **5.2.1** established that the increase in loss due to tip vortex/boundary layer interaction occurs through the same mechanisms involved in 2D wake/boundary layer interaction. This result was further confirmed in §**6.4**, which shows that the disturbance vortical flow can be described in the blade-to-blade plane on a locally 2D manner. Therefore, the increase in passage loss due to the upstream tip leakage vortex can be estimated by dividing the blade in individual sections of thickness dz, and by applying the 2D model of §**J.3** to each section considering the jet parameters at the immersion under consideration. This yields the following extension of (J.47):

$$\Delta \mathcal{Y}_p = 6 \int \frac{\Delta V_n(z)}{U} \int_0^1 x \left. \frac{d\mathcal{Y}_{p,s}(z)}{dx} \right|_{2D} dx\, dz \tag{J.57}$$

The simplified form of (J.57) is identical to (J.48):

$$\Delta \mathcal{Y}_p \approx 2 \frac{\Delta V_n}{U} c Y_{p,s} \qquad (J.58)$$

In the case of (J.58), the transverse disturbance velocity, ΔV_n, comprises a spanwise as well as a time average. Based on continuity, it is possible to relate ΔV_n to the tip leakage blockage $\frac{A_b}{A_e}$ in the rotor frame as defined by Khalid (1995). This yields:

$$\Delta V_n = \frac{A_b}{A_e} \frac{\sin \chi}{\cos \theta_{2r}} \qquad (J.59)$$

J.5. Synthesis.

This section summarizes how the foregoing expressions are applied in the context of the multistage interaction model of **Figure 7.1 (Chapter 7)**, to estimate the change in efficiency due to blade row interaction for different designs.

The first step of the model is to estimate the "strength" of the upstream wakes and vortices using the material in §**J.1**. This is followed by computing the attenuation coefficient a_r for the design under consideration in the following manner:

$$a_r = (\cos \gamma_1 + \tan \theta_1 \sin \gamma_1)\sqrt{\xi^2 + (1 - \xi \tan \theta_2)^2}$$

where:

$$\xi = \text{sign}(\gamma_1) \left\{ \frac{\sin \gamma_1 \cos \theta_1}{\cos \theta_1 - \gamma_1} + \frac{2\sigma^2(\tan \theta_1 - \tan \theta_2)}{2\sigma^2 + (0.5 + \sigma^2)(\tan^2 \theta_1 + \tan^2 \theta_2) - \tan \theta_1 \tan \theta_2} \right\} \qquad (J.60)$$

$$\tan \gamma_2 = \frac{\xi}{1 - \xi \tan \theta_2}$$

The loss benefit from recovering upstream wakes in the frame of the downstream blade row is then estimated using:

$$\Delta \mathcal{Y}_m = \Delta Y_m(A_{j,1}, t_{w,1}, \gamma_1) - a_r^{-1} \Delta Y_m(a_r A_{j,1}, a_r t_{w,1}, \gamma_2) \qquad (J.61)$$

where ΔY_m is the function embodied by (J.14). The loss benefit from recovery of the tip vortex is computed according to

$$\Delta \mathcal{Y}_m \approx (1 - a_r^2)\Delta \mathcal{Y}_i \qquad (J.62)$$

The increase in passage loss from each wake/boundary layer and tip leakage vortex/boundary layer interaction is computed according to the simplified form of (J.47):

$$\Delta \mathcal{Y}_p \approx \frac{2\Delta V_n}{U_m} \mathcal{Y}_{p,s} \qquad\qquad (J.63)$$

where:

$$\begin{aligned}
\Delta V_n &= \frac{A_j t_w \sin \chi}{2S} \quad \text{Wake} \\
\Delta V_n &= \frac{A_b}{A_e} \frac{\sin \chi}{\cos \theta_{2r}} \quad \text{TL vortex}
\end{aligned} \qquad\qquad (J.64)$$

The above loss changes are computed in loss coefficient relative to the reference frame of the downstream blade row. They are converted to efficiency figures by using the relative dynamic head in front of each cascade and the stage pressure coefficient: (note that the flow is considered incompressible)

$$\Delta \eta = \frac{\phi^2}{2\psi} \left[\frac{(\Delta \mathcal{Y}_p + \Delta \mathcal{Y}_m)_{rotor}}{\cos \theta_{1,R}} + \frac{(\Delta \mathcal{Y}_p + \Delta \mathcal{Y}_m)_{stator}}{\cos \theta_{1,S}} \right] \qquad\qquad (J.65)$$

The equations derived in this Appendix implicitly assume a 1:1 rotor-to-stator blade count ratio. In this case, there is one rotor wake entering a stator passage per wake passing period. Given that wakes and vortices do not appear to interact strongly with each other in the CFD simulations, and under the assumption that wakes and vortices do not interact with annulus-scale unsteady flow phenomena, the change in loss for other blade count ratios $q = N_R/N_S$ is related to the time averages for 1:1 blade count by means of:

$$\overline{\Delta \mathcal{Y}_q} = q\overline{\Delta \mathcal{Y}_{1:1}} \qquad\qquad (J.66)$$

As noted in §J.2.3, wake-like disturbances originating in the second upstream blade row can be amplified for certain compressor configuration (e.g. third rotor wake can be amplified in the fourth rotor passage). Figure J.6 shows that such amplification occurs in designs with low pressure rise and high flow coefficient. A reaction of 50% minimizes the extent of unconstrained design space where amplification can occur. As reaction increases, there is a wider range of designs in which the stator wakes may be amplified in the next stator. If reaction is decreased, the same can be said about the rotor wakes processing in the next rotor. Overall however, the amount of amplification is not sufficient to cancel the benefits of attenuation in the preceding stage.
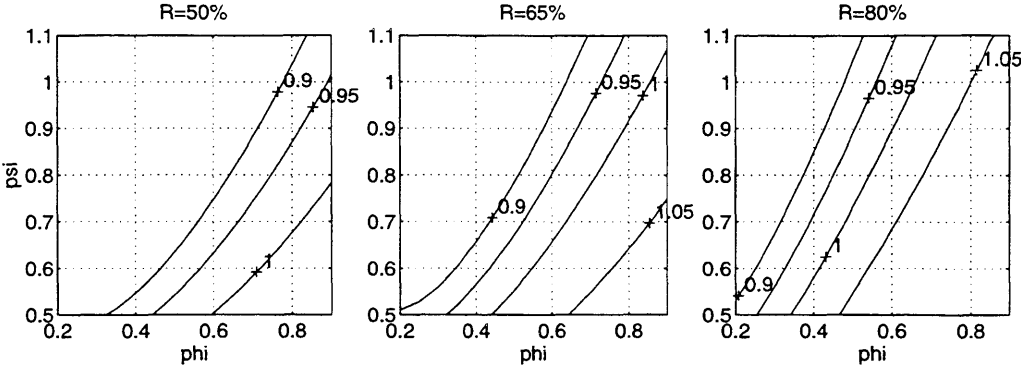
Figure J.6. Isocontours of $\max(a_{\tau,R}, a_{\tau,S})$ of wakes from blade row N into blade row N+2. Values above 1.0 correspond to wake amplification, and occur at high flow coefficients and low pressure coefficients. The plots have a symmetry about the 50% reaction point.

For the compressor considered here, such amplification does not occur, but neither is there much attenuation by the second blade row. Since most of the wake energy is recovered in the first downstream blade row, the lack of subsequent attenuation in the second blade row is not important from loss standpoint.